SCUOLA NORMALE SUPERIORE - PISA

Perfezionamento in Fisica

Many-body physics with Ytterbium Fermi gases in optical lattices: from one-dimensional systems to orbital magnetism

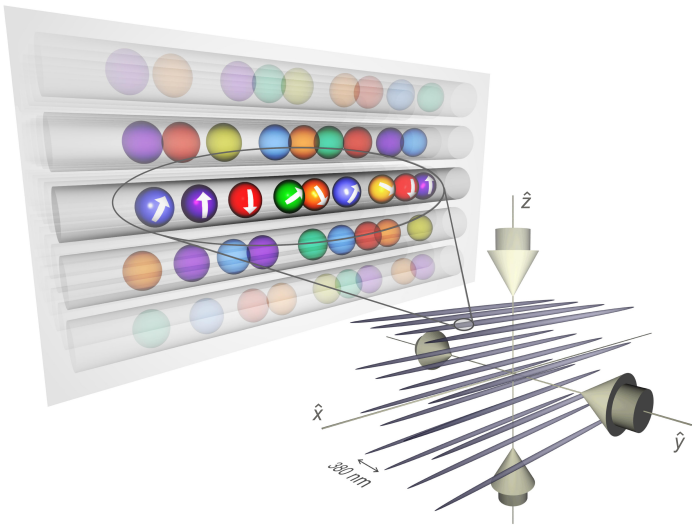

Relatore interno: **Prof. Rosario Fazio**
Relatore esterno: **Prof. Massimo Inguscio**

Guido Pagano
A.A. 2011/2014

Abstract

Ultracold atoms provide a powerful platform to address fundamental problems in many-body quantum physics. Owing to their rich electronic structure, ultracold two-electron atoms offer new exciting possibilities, enlarging the range of physical phenomena that it is possible to investigate with these atomic systems.

This thesis reports on the experimental investigation of ultracold fermionic Ytterbium atoms in optical lattices. These alkaline-earth-like atoms are characterized by purely nuclear spin, completely decoupled from the electronic degrees of freedom. Consequently their low-energy scattering properties are independent of the nuclear spin orientation, giving rise to a $SU(N)$ symmetry class, where N is the number of nuclear spin components. These features allowed us to demonstrate the first experimental realization of one-dimensional quantum gases of ultracold fermions interacting within the $SU(N)$ symmetry class, where N can be adjusted from 2 to 6. The findings of this work are interpretable in the framework of the Tomonaga-Luttinger liquid model, which is the paradigmatic description for one-dimensional interacting quantum systems. By tuning the number of spin components, we observed that the static and dynamic properties of the system deviate from those of ideal fermions and, for $N > 2$, from those of a spin-1/2 Luttinger liquid. In particular, we validated for the first time the prediction that, in the large-N limit, one-dimensional Fermi gas exhibits properties of a bosonic spinless liquid. All the experimental results have been enabled by the construction of a versatile setup that makes possible the manipulation of atomic clouds of fermionic ^{173}Yb in optical lattices as well as the optical detection and accurate control of the number of nuclear spin components by means of optical pumping processes.

Moreover, atomic Ytterbium provides the possibility to engineer coherent Raman couplings between different nuclear spin states. By studying and implementing such Raman processes, we paved the way to the investigation of spin-orbit physics and artificial gauge fields with multi-component fermions.

In addition to their nuclear spin, two-electron fermions offer experimental access to long-lived electronically-excited states. Coherent control of Ytterbium clock transition $^1S_0 \rightarrow {}^3P_0$ in three-dimensional optical lattices has led to the first observation of fast, coherent spin-exchange oscillations between two ^{173}Yb atoms in different electronic orbitals. These experiments show that two-electrons atoms in optical lattices can be used as novel quantum simulators of unique many-body phenomena such as $SU(N)$ orbital magnetism.

Contents

Introduction

In the late '90s, owing to remarkable advances in atom manipulation techniques with laser light, it became possible to cool atomic gases down to the quantum degeneracy regime, highlighting the effects of quantum statistics both in Bose [1, 2] and in Fermi [3, 4] gases. This important result opened the door to a new field, the ultracold quantum gases, where the unprecedented degree of control on the experimental parameters yielded the opportunity to use these system as a versatile tool for quantum simulation [5], following the famous intuition of Richard Feynman [6]. Proceeding on this line of research, the realization of optical lattices [7, 8] and the possibility to control the interaction parameters between the ultracold atoms [9] paved the way to quantum simulation of condensed-matter models [10] and enabled the realization of strongly-correlated many-body systems [11, 12].

In this context, this work aims to use quantum degenerate Ytterbium (^{173}Yb) Fermi gases [13] in optical lattices to explore and investigate a large variety of physical systems. Ytterbium is an alkaline-earth-like two-electrons atom, which has a completely diamagnetic ($J = 0$) ground state and, in the case of fermionic isotopes, presents purely nuclear spin, completely decoupled from the electronic degrees of freedom. Consequently, the interaction between ultracold ^{173}Yb atoms is independent of the nuclear spin orientation. This invariance is the manifestation of an intrinsic $SU(N)$ symmetry of two-electron fermionic atoms [14], where N is the number of nuclear spin components. This high degree of symmetry in the interaction leads to the absence of spin-relaxation mechanisms, which implies the possibility to realize a degenerate Fermi gas with a tunable number N of spin components, accurately controlled by means of optical manipulation techniques. The presence of the $SU(N)$ symmetry drastically modifies the low-energy properties of lattice models where exotic ground states are predicted, e.g. chiral spin liquids [15–18]. The emergent $SU(N)$ symmetry is of interest also for other fields of physics outside atomic and condensed-matter physics. For example, $SU(3)$ color symmetry has a central role in quantum chromodynamics, where the forces between quarks are mediated by $SU(3)$ gauge bosons, known as gluons. These analogies already stimulated several proposals [19–23] that aim to bridge atomic quantum gases and high-energy lattice gauge theories.

Another key feature of alkaline-earth-like atoms is the presence of electronically-excited long-lived states, which can be coherently addressed using ultra-narrow lasers. In particular, the metastable $^3P_0$ state has a lifetime of the order of tens of seconds and thus can be considered as an alternative ground state of the system, nevertheless separated by an optical energy from the absolute ground state. The precision measurements of these ultra-narrow optical transitions have stimulated a flourishing field of research aiming to improve the current frequency standard with a new generation of atomic clocks [24–28]. Furthermore, this spectroscopic tool is also a powerful resource for quantum simulation purposes, to explore paradigmatic condensed-matter models [14] and realize artificial gauge fields [29, 30].

Outline

This PhD thesis has been carried out at the European Laboratory for Non-Linear Spectroscopy (LENS) in the Ytterbium lab, under the supervision of Prof. Massimo Inguscio and Prof. Leonardo Fallani. The thesis is organized as follows:

Chapter 1 reviews the theoretical and experimental tools used to manipulate and control both the atomic motion and the internal degrees of freedom of the atoms. We briefly outline the atom-laser interaction, focusing on optical potentials for multilevel atoms such as Ytterbium. An in-depth description is devoted to the optical lattices and Raman transitions, highlighting the points in common between these atomic physics tools. Finally, the theory of low-energy scattering is reviewed, with a focus on ultracold atomic clouds confined in one dimension and on $SU(N)$-symmetric interactions.

Chapter 2 is devoted to the description of the experimental apparatus and of the procedures used in this work. Indeed in the first part of my PhD, I contributed to the construction of the Ytterbium vacuum system and of the laser setup, which are both presented in detail. The second part of this chapter concerns the experimental procedures to achieve the quantum degeneracy regime of both the bosonic ^{174}Yb and the fermionic ^{173}Yb isotopes. We also describe the characterization of the optical lattices and the development of the all-optical techniques to detect and manipulate the nuclear spin population. The construction of such a versatile experimental apparatus led to three different lines of research, respectively developed in the three following chapters:

- Chapter 4: In the first experiment [31], which forms the main topic of this thesis, we studied the static and dynamic properties of multi-component spin mixtures of ultracold fermions confined in one dimension. Indeed, one-dimensional (1D) systems of spinful fermions have been the subject of intense studies in theoretical physics

over the past fifty years [32, 33]. In these systems, low dimensionality amplifies quantum fluctuations and enhance correlations, leading to the failure of the Landau-Fermi liquid theory and to the emergence of a different phenomenological paradigm, namely the Tomonaga-Luttinger liquid model. This model is reviewed in Chapter 3, starting from the case of spinless fermions, and it is generalized to the "spinful" two-component and multi-component cases.

Ultracold fermionic gases offer a unique opportunity to investigate the low-energy physics of these models in a clean and controllable fashion. In particular, this is the first experimental investigation of the role of spin multiplicity in fermionic one-dimensional quantum liquids, especially with more than two spin components. By directly comparing systems with different number of spin components N, we highlighted how repulsive interactions between particles cause static and dynamic properties of one-dimensional fermions to differ significantly from those of an ideal Fermi gas, as expected from the Luttinger theory for a liquid of spin-1/2 fermions. Moreover, stronger deviations, not accounted for by the spin-1/2 theory, were measured when the fermionic liquid is prepared in more than two spin states. In particular, we verified the prediction [34] that, for a large number of spin components, a system of one-dimensional fermions exhibits properties of a bosonic spinless liquid. Our results pave the way to the observation of fundamental aspects of one-dimensional systems of spinful particles such as spin-charge separation in ultracold atomic systems.

- Chapter 5: In the second experiment [35], we coherently addressed the metastable $^3P_0$ state by using an ultra-narrow laser system developed by my coworker Giacomo Cappellini [36]. We studied binary collisions between atoms in different nuclear spin and electronic states. Because of the fermionic anti-symmetrization of the global wavefunction, it is possible to define two collisional channels associated to symmetric and anti-symmetric electronic states, which are separated by an exchange energy. This system has been recently investigated in several labs around Europe [37–39]. In particular, at the LMU [40] the scattering length associated to the anti-symmetric electronic state has been measured using spectroscopic techniques and the $SU(N)$ symmetry of this collisional channel has been tested. Following a different approach, we observed for the first time spin-exchange oscillations that witness the coherent nature of the magnetic interaction between two atoms in different electronic states. This observation allowed us to fully characterize the inter-orbital two-body collisions between Ytterbium atoms in the low-lying electronic states. The demonstration of coherent spin exchange interactions is a milestone in the route to quantum simulation of orbital magnetism models, e.g. the Kondo lattice model [14], where localized magnetic moments interact with mobile fermions.

- Chapter 6: In a third set of experiments we engineered coherent Raman couplings between different nuclear spin states. We discovered that ^{173}Yb provides a wealth of different Raman configurations that can be used for the investigation of spin-orbit physics [41, 42] and artificial gauge fields [43–46] with multi-component fermions. During this PhD thesis, we built the Raman optical setup and learned how to exploit light shifts and Rabi couplings to tune the number of spin components that are resonantly coupled. The possibility to create coherent couplings between more than two internal states provides an additional synthetic dimension [47] to the system, where the nuclear spin states are interpreted as singly-addressable sites among which a coherent tunneling is provided by the Raman transitions. Combining velocity-dependent Raman couplings with this brand new approach, it is possible to realize a synthetic gauge field in a hybrid two-dimensional lattice [48], which will be the focus of the PhD thesis of my coworker Marco Mancini [49]. In such a system, one dimension is defined by a standard optical lattice and the other is implemented by the synthetic dimension encoded by the Raman couplings in the internal state of the atoms. After the completion of this thesis, this set of experiments eventually led to the first observation [50] of chiral edge states with neutral atoms.

Publications

The results shown in this thesis are reported in the following references:

- *"A one dimensional liquid of fermions with tunable spin"*
  G. Pagano, M. Mancini, G. Cappellini, P. Lombardi, F. Schäfer, H. Hui, X. J. Liu, J. Catani, C. Sias, M. Inguscio and L. Fallani, Nature Physics **10**, 198 (2014).

- *"Direct Observation of Coherent Inter-orbital Spin-Exchange Dynamics"*
  G. Cappellini, M. Mancini, **G. Pagano**, P. Lombardi, L. Livi, M. Siciliani de Cumis, P. Cancio, M. Pizzocaro, D. Calonico, F. Levi, C. Sias, J. Catani, M. Inguscio, and L. Fallani, Physical Review Letters **113**, 120402 (2014).

- *"Observation of chiral edge states with neutral fermions in synthetic Hall ribbons"*
  M. Mancini, **G. Pagano**, G. Cappellini, L. Livi, M. Rider, J. Catani, C. Sias, P. Zoller, M. Inguscio, M. Dalmonte, L. Fallani, arXiv:1502.02495v1 (2015), Science (to be published).

- *"A compact ultranarrow high-power laser system for experiments with 578 nm Ytterbium clock transition"*
  G. Cappellini, P. Lombardi, M. Mancini, **G. Pagano**, M. Pizzocaro, L. Fallani, J. Catani, Review of Scientific Instruments **86**, 073111 (2015).

Chapter 1

A Toolbox for ultracold Ytterbium Fermi gases

This chapter is a brief summary of the basic concepts and experimental tools used in atomic physics, focusing in particular on the aspects more closely related to ultracold Ytterbium Fermi gases and to the research topics covered in this PhD thesis. Section 1.1 introduces the theory of ultracold degenerate Fermi gas trapped in a harmonic potential of arbitrary dimensions and focuses on the experimental methods to measure physical observables such as temperature, density and momentum distributions. Section 1.2 introduces the atom-light interaction, which has a central role in atomic physics experiments as it allows the manipulation of both the *atomic motion* using far-off resonant dipole traps and optical lattices and the *atomic internal state* by means of stimulated Raman transitions. An in-depth description is devoted to optical potentials for multilevel atoms such as Ytterbium. In section 1.3 an introduction to the low-energy scattering properties of ultracold clouds is given, highlighting in particular how interactions depend on the dimensionality of the system. Finally the relation between the atomic internal states and two-body collisions is discussed, describing the emergence of $SU(N)$-symmetric interaction in Ytterbium ultracold Fermi gases.

1.1 Degenerate Fermi gases in harmonic potential

The ideal case of non-interacting Fermi gases subjected to a harmonic potential in D dimensions is described by the single-particle Hamiltonian:

$$\hat{H} = \frac{\hat{\mathbf{p}}^2}{2m} + \sum_{\alpha=1}^{D} \frac{1}{2} m\omega_\alpha^2 \hat{x}_\alpha^2, \tag{1.1}$$

where $\hat{\mathbf{p}}$ and $\hat{x}_\alpha$ are respectively the particle momentum and position operators along direction $\alpha = x, y, z$. Even if in ultracold atoms experiments the system is well isolated from the environment, it is convenient to consider the system in contact with a reservoir and then to fix the chemical potential μ such that the average number of particle $\langle N \rangle$ is fixed to N. The grand canonical partition function for a harmonically confined Fermi gas is

$$Z_{GC} = \prod_{\mathbf{n}} \left(1 + \mathcal{F}^{-1} e^{\beta \epsilon_{\mathbf{n}}}\right), \tag{1.2}$$

where $\beta = 1/k_B T$, with k_B being the Boltzmann constant and T being the temperature, $\mathcal{F} = e^{\beta\mu}$ is the fugacity and $\epsilon_{\mathbf{n}} = \sum_{\alpha=1}^{D} \hbar\omega_\alpha (n_\alpha + 1/2)$ is the single-particle energy of a trapped fermion in D dimensions. The quantity $g_{\mathbf{n}} = \frac{1}{1+\mathcal{F}^{-1} e^{\beta\epsilon_{\mathbf{n}}}}$ is the Fermi-Dirac factor and it gives the probability of the state described by quantum numbers $\mathbf{n} = \{n_1, n_2, \ldots, n_D\}$ to be occupied. The relevant thermodynamic physical variables can be computed from the quantity:

$$\begin{aligned} \log Z_{GC} &= \sum_{\mathbf{n}} \log\left(1 + \mathcal{F}^{-1} e^{\beta \sum_{\alpha=1}^{D} \hbar\omega_\alpha (n_\alpha + 1/2)}\right) \\ &= \int d\epsilon \, g(\epsilon) \log\left(1 + \mathcal{F}^{-1} e^{\beta\epsilon}\right) \\ &\simeq \left(\frac{k_B T}{\hbar\bar{\omega}}\right)^D \mathrm{Li}_{D+1}(-\mathcal{F}), \end{aligned} \tag{1.3}$$

where $\bar{\omega} = (\prod_{\alpha=1}^{D} \omega_\alpha)^{1/D}$ is the geometric average of the harmonic oscillator frequencies,

$$g(\epsilon) = \frac{\epsilon^{D-1}}{(D-1)!(\hbar\bar{\omega})^D}, \tag{1.4}$$

is the density of states in D dimensions and

$$\mathrm{Li}_D(z) = \sum_{k=1}^{\infty} \frac{z^k}{k^D}, \tag{1.5}$$

is the Polylogarithmic function in D dimensions, which converges for all complex numbers with $|z| \leq 1$. From the partition function, the total number of atoms can be computed from the thermodynamic relation:

$$\langle N \rangle = -\frac{1}{\beta}\frac{\partial \log(Z_{GC})}{\partial \mu} = -\mathcal{F}\frac{\partial \log(Z_{GC})}{\partial \mathcal{F}} = -\left(\frac{k_B T}{\hbar\bar{\omega}}\right)^D \mathrm{Li}_D(-\mathcal{F}). \tag{1.6}$$

The Fermi energy can be calculated by fixing the total number of atoms at $T = 0$:

$$N = \int_0^{E_F} g(\epsilon) d\epsilon \longrightarrow k_B T_F = (D!N)^{1/D}\hbar\bar{\omega}. \tag{1.7}$$

By substituting this expression in Eq.(1.6), the relation between the fugacity and the temperature is

$$\mathrm{Li}_D(-\mathcal{F}) = -\frac{1}{D!}\left(\frac{T_F}{T}\right)^D. \tag{1.8}$$

1.1.1 Thomas-Fermi approximation

Since typically in ultracold atoms experiments the thermal energy $k_B T \equiv 1/\beta$ is higher than the quantum mechanical level spacing[1], it is convenient to use a semiclassical approach in order to find the density of a trapped Fermi gas in real and momentum space. Indeed, it is possible to apply a local density approximation incorporating the harmonic potential $V(\mathbf{r})$ in the Fermi factor of a homogeneous gas, obtaining an occupation number for a phase-space cell centered at $\{\mathbf{r}, \mathbf{p}\}$:

$$f(\mathbf{r}, \mathbf{p}) = \frac{1}{1 + e^{\beta\left(\frac{\mathbf{p}^2}{2m} + V(\mathbf{r}) - \mu\right)}}. \tag{1.9}$$

By integrating over the phase-space density (normalized by the volume $(2\pi\hbar)^D$) on the real or momentum space, the momentum and density distributions can be computed as:

$$\begin{aligned} n(\mathbf{r}) &= \int \frac{d^D\mathbf{p}}{(2\pi\hbar)^D} f(\mathbf{r}, \mathbf{p}) = -\frac{1}{\lambda_{dB}^D}\mathrm{Li}_{D/2}\left(-\mathcal{F}e^{-\beta V(\mathbf{r})}\right), \\ n(\mathbf{p}) &= \int \frac{d^D\mathbf{r}}{(2\pi\hbar)^D} f(\mathbf{r}, \mathbf{p}) = -\frac{1}{m^D\bar{\omega}^D}\frac{1}{\lambda_{dB}^D}\mathrm{Li}_{D/2}\left(-\mathcal{F}e^{-\beta\frac{\mathbf{p}^2}{2m}}\right), \end{aligned} \tag{1.10}$$

[1] Typical trap frequency are of the order of 100 Hz whereas typical thermal energies are $T \sim 1\ \mu\mathrm{K} \sim h/k_B \times 20$ kHz.

where $\lambda_{dB} = \sqrt{2\pi\hbar^2/mk_BT}$ is the de-Broglie wavelength. At $T = 0$, the phase-space occupation becomes simply:

$$f(\mathbf{r},\mathbf{p}) = \Theta\left(\frac{\mathbf{p}^2}{2m} + V(\mathbf{r}) - \mu\right), \tag{1.11}$$

where $\Theta(x)$ is the Heaviside function and the density distribution is

$$n(\mathbf{r}) = \int_{|\mathbf{p}|<\sqrt{2m(\mu-V(\mathbf{r}))}} \frac{d^D\mathbf{p}}{(2\pi\hbar)^D} = \frac{1}{(2\pi\hbar)^D}\frac{\Omega_D}{D}\left[2m(\mu - V(\mathbf{r}))\right]^{D/2}, \tag{1.12}$$

where Ω_D is the surface of the D-dimensional unit sphere. From Eq. (1.12) we can determine the Thomas-Fermi radius along the i-th dimension, $R_i^{TF} = \sqrt{2\mu/m\omega_i^2}$, that at low temperature is a good estimate of the cloud size. An important observation is that, in the Thomas-Fermi approximation, the momentum distribution $n(\mathbf{p})$ is always isotropic as evident from Eq. (1.10). Consequently, as it will be shown in the next section, the aspect-ratio of a fermionic cloud that is suddenly released from a harmonic trap, always approaches one for sufficiently long times of ballistic expansion.

1.1.2 Time-of-flight momentum distribution of a Fermi gas

One of the most important observable of a degenerate quantum gas is its the column-integrated density $n_c(x,y)$, which is typically imaged either in situ or after a ballistic expansion induced by a sudden switch-off of all the trapping potentials. The expression of the expanded cloud density $n(\mathbf{r},t)$ can be found through the semiclassical approach, by adding the contributions from particles at all points $\mathbf{r}_0$ that had the correct initial momentum $\mathbf{p}_0 = m(\mathbf{r}-\mathbf{r}_0)/t$. Hence in the case of a three-dimensional harmonic trapping potential[2]:

$$\begin{aligned} n(\mathbf{r},t) &= \int d\mathbf{r}_0 \int \frac{d\mathbf{p}_0}{(2\pi\hbar)^3} f(\mathbf{r}_0,\mathbf{p}_0)\delta(\mathbf{r}-\mathbf{r}_0-\frac{\mathbf{p}_0}{m}t) \\ &= \int \frac{d\mathbf{p}_0}{(2\pi\hbar)^3}\frac{1}{1+\exp\left(\beta\left[\frac{\mathbf{p}_0^2}{2m}+V(\mathbf{r}-\frac{\mathbf{p}_0}{m}t)-\mu\right]\right)} \\ &= -\frac{1}{\lambda_{dB}^3}\prod_{\alpha=1}^{3}\frac{1}{\sqrt{1+\omega_\alpha^2 t^2}}\mathrm{Li}_{3/2}\left(-\mathcal{F}\exp\left[-\beta\frac{m}{2}\sum_{\alpha=1}^{3}\frac{\omega_\alpha^2}{1+\omega_\alpha^2t^2}x_\alpha^2\right]\right). \end{aligned} \tag{1.13}$$

[2] In the harmonic potential case, the integral can be computed analytically.

This result is more concisely written by introducing the factors $b_\alpha(t) = \sqrt{1+\omega_\alpha^2 t^2}$ and stressing that the density distribution is simply related to the one at $t = 0$ as:

$$n(\mathbf{r},t) = \frac{1}{b_x(t)b_y(t)b_z(t)}\, n\left(\frac{x}{b_x(t)}, \frac{y}{b_y(t)}, \frac{z}{b_z(t)}, t=0\right).$$

It is important to note that for long ballistic expansion times ($t \gg 1/\bar{\omega}$), the density distribution becomes isotropic reflecting the isotropy of the momentum distribution in trap:

$$n(\mathbf{r}, t \gg 1/\bar{\omega}) = -\frac{1}{\lambda_{dB}^3(\bar{\omega}t)^3}\mathrm{Li}_{3/2}\left(-\mathcal{F}\exp\left[-\beta\frac{m}{2}\frac{\mathbf{r}^2}{t^2}\right]\right). \tag{1.14}$$

Since the observable in the experiments is the column integrated density, namely $n_c(x,y) = \int dz\, n(x,y,z)$, Eq. (1.13) has to be integrated along the imaging axis z using the integral property of polylogarithmic function:

$$\int_{-\infty}^{+\infty} dx\, \mathrm{Li}_n(ze^{x^2}) = \sqrt{\pi}\ \mathrm{Li}_{n+1/2}(z), \tag{1.15}$$

yielding the formula:

$$n_c(x,y) = -\frac{m(k_BT)^2}{2\pi\hbar^3\omega_z}\prod_{\alpha=x,y}\frac{1}{\sqrt{1+\omega_\alpha^2t^2}}\ \mathrm{Li}_2\left(-\mathcal{F}\exp\left[-\beta\frac{m}{2}\sum_{\alpha=x,y}\frac{\omega_\alpha^2}{1+\omega_\alpha^2t^2}x_\alpha^2\right]\right). \tag{1.16}$$

More details on the imaging of a harmonically trapped Fermi gas can be found in the imaging section 2.3.7.

1.2 Laser cooling and optical potentials

The atom-light interaction is the fundamental tool used to manipulate and interrogate the atomic system. In general, an atom interacting with light represents an *open quantum system* since it is always coupled with the electromagnetic vacuum field[3], which acts as a thermal reservoir and causes spontaneous emission. A common formalism to describe such a system is the *master equation*, that rules the time evolution of the density matrix

[3] The vacuum electromagnetic field formulation in second quantization is

$$\hat{\mathbf{E}}_\perp(\mathbf{r},t) = i\sum_{\mathbf{k},\lambda}\sqrt{\frac{\hbar\omega_\mathbf{k}}{2\epsilon_0 V}}\boldsymbol{\varepsilon}_{\mathbf{k}_\lambda}\left[\hat{a}_{\mathbf{k}_\lambda}e^{i(\mathbf{k}_\lambda\cdot\mathbf{r}-\omega_{\mathbf{k}_\lambda}t)} - \hat{a}^\dagger_{\mathbf{k}_\lambda}e^{-i(\mathbf{k}_\lambda\cdot\mathbf{r}-\omega_{\mathbf{k}_\lambda}t)}\right] \tag{1.17}$$

where V is the integration volume, ϵ_0 the vacuum dielectric constant, $\omega_{\mathbf{k}_\lambda} = c|\mathbf{k}_\lambda|$ is the optical frequency and $\boldsymbol{\varepsilon}_{\mathbf{k}_\lambda}$ is the polarization vector with $\lambda = 1, 2$ the polarization index.

$\hat{\rho}$ of the atomic system [51, 52]:

$$\begin{aligned} \frac{d\hat{\rho}}{dt} &= \frac{1}{i\hbar}\left[\hat{H},\hat{\rho}\right], \\ \hat{H} &= \hat{H}_A + \hat{H}_R + \hat{H}_I, \end{aligned} \tag{1.18}$$

where $\hat{H}_A$ and $\hat{H}_R$ are, respectively, the atomic system and radiation field Hamiltonians and

$$\hat{H}_I = -\hat{\mathbf{d}} \cdot [\mathbf{E}(\mathbf{r},t) + \mathbf{E}_\perp(\mathbf{r},t)] \tag{1.19}$$

describes the interaction between the atomic dipole $\hat{\mathbf{d}}$ and the electromagnetic field. The latter takes into account the vacuum electromagnetic field $\mathbf{E}_\perp(\mathbf{r},t)$ and a laser field $\mathbf{E}(\mathbf{r},t)$ of wavelength λ_L, assumed to be a plane wave:

$$\mathbf{E}(\mathbf{r},t) = \boldsymbol{\varepsilon} E_0 \cos(\mathbf{k}_L \cdot \mathbf{r} - \omega_L t) \tag{1.20}$$

where $\boldsymbol{\varepsilon}$ the polarization vector and $|k_L| = 2\pi/\lambda_L$ is the wavevector. This interaction term gives rise to both a dissipative and a conservative force:

- The **dissipative force** is related to cycles of absorption from the laser field and spontaneous emission in the reservoir vacuum field. In particular, considering a two-level atom with the excited $|e\rangle$ and ground state $|g\rangle$ separated by an energy $\hbar\omega_0$, the spontaneous scattering rate can be calculated from first principles [53] as:

$$\Gamma = \frac{|\hat{\mathbf{d}}_{eg}|^2 \omega_0^3}{3\pi\epsilon_0 \hbar c^3} \tag{1.21}$$

  where $\hat{\mathbf{d}}_{eg} = \langle e|\hat{\mathbf{d}}|g\rangle$. Absorbing and spontaneously emitting photons, the atomic dipole oscillates out of phase with respect to the incoming electromagnetic field. As a result, the atomic motion can be damped out by the average net momentum transfer resulting from the absorption of a laser photon with momentum $\hbar\mathbf{k}_L$ and the subsequent spontaneous emission over the whole solid angle. This mechanism, often referred to as *radiation pressure*, is at the basis of laser cooling techniques such as Zeeman slowing (section 2.3.1) and magneto-optical trapping (section 2.3.2), which can be used to trap and cool an atomic cloud down to temperatures of the order of tens of micro-Kelvin. The expression of the dissipative force can be derived from the master equations of a two-level atom interacting with a laser field (optical Bloch equations [51]) by using the rotating wave approximation[4] (RWA). In particular, a plane wave of intensity I, frequency ω_L and detuning $\Delta = \omega_L - \omega_0$ exerts on an

[4] Given a laser field $\mathbf{E}(\mathbf{r},t) = \boldsymbol{\varepsilon} E_0 \cos(\mathbf{k}_L \cdot \mathbf{r} - \omega_L t)$, the rotating wave approximation consists in transforming into the reference frame co-rotating with the optical field at angular frequency ω_L in which the

atom at rest the following force:

$$\mathbf{F}_{diss} = \hbar \mathbf{k}_L \frac{\Gamma}{2} \left(\frac{I/I_s}{1 + (2\Delta/\Gamma)^2 + I/I_s} \right) \tag{1.22}$$

where $I_s = 4\pi^2 \hbar c \Gamma / 6\lambda_L^3$ is defined as the saturation intensity. In the saturation regime at $I/I_s \gg 1, \Delta/\Gamma$ we have $\mathbf{F}_{diss} = \hbar \mathbf{k}_L \Gamma/2$ where it appears evident that the force stems from the momentum transfer $\hbar \mathbf{k}_L$ induced by scattered photons at rate $\Gamma/2$. This holds for near resonant light ($\Delta \sim \Gamma$), where the RWA is a good approximation. In the limit of far-detuned light ($\Delta \sim \omega_0 \gg \Gamma$), the counter-rotating wave term can not be neglected and the effective scattering rate can be calculated [8] as:

$$\Gamma_{sc} = \frac{3\pi c^2}{2\hbar\omega_0^3} \left(\frac{\omega_L}{\omega_0} \right)^3 \left(\frac{\Gamma}{\omega_0 - \omega_L} + \frac{\Gamma}{\omega_0 + \omega_L} \right)^2 I. \tag{1.23}$$

- The **conservative force** relies on the interaction with the laser field itself and it is unrelated to the electromagnetic vacuum reservoir. It relies on cycles of absorption and stimulated emission in which the atomic dipole oscillates in phase with the incident electromagnetic field. Using the optical Bloch equation in rotating wave approximation, the expression for the conservative force is [51]:

$$\mathbf{F}_{cons}(\mathbf{r}) = -\frac{\hbar\Delta}{2} \frac{\nabla I(\mathbf{r})/I_s}{1 + (2\Delta/\Gamma)^2 + I(\mathbf{r})/I_s}. \tag{1.24}$$

  The dependence on the intensity gradient makes evident that this force relies on the beam profile inhomogeneity as the atomic dipole redistributes photons between different plane waves at the same energy but at different momenta. Moreover the sign of the detuning Δ determines if the atoms will be attracted ($\Delta < 0$) or repelled ($\Delta > 0$) from the intensity maximum. In the limit of far-detuned light ($\Delta \sim \omega_0 \gg \Gamma$), the potential energy (also called dipole potential), that gives rise to the force (1.24) is

$$V_{dip}(\mathbf{r}) = \frac{3\pi c^2}{2\omega_0^3} \left(\frac{\Gamma}{\omega_0 - \omega_L} + \frac{\Gamma}{\omega_0 + \omega_L} \right) I(\mathbf{r}). \tag{1.25}$$

In the regime $\omega \gg \Delta \sim \Gamma$ where we can neglect the counter-rotating term, Eqs. (1.23) and (1.25) imply $\Gamma_{sc} \sim (\Gamma/\Delta)^2$ and $V_{dip} \sim \Gamma/\Delta$. This scaling suggests that the effective scat-

interaction Hamiltonian

$$\hat{H}_I \sim \underbrace{\left(|e\rangle\langle g| e^{-i(\omega_L - \omega_0)t} + |g\rangle\langle e| e^{+i(\omega_L - \omega_0)t} \right)}_{\text{resonant}} + \underbrace{\left(|e\rangle\langle g| e^{+i(\omega_L + \omega_0)t} + |g\rangle\langle e| e^{-i(\omega_L + \omega)t} \right)}_{\text{anti-resonant}}$$

is made of two slowly varying resonant terms, to be retained, and two anti-resonant components rapidly oscillating at $\omega_L + \omega_0$, which are neglected.

tering rate could be efficiently suppressed compared to the conservative dipole potential by choosing a large detuning. Indeed in order to efficiently trap and cool atomic clouds down to quantum degeneracy, it is crucial to minimize the inelastic scattering events that would lead to strong heating (one photon energy recoil is $E_R = \hbar^2 k_L^2/2m \sim k_B \times 100$ nK) by implementing conservative optical dipole traps with far-detuned light, compatibly with laser power. If the laser detuning allows us to neglect inelastic scattering, we can move from a master equation formalism to a Hamiltonian framework to describe atom-light interaction. In particular in the rotating-frame, the atomic wavefunction $|\Psi(t)\rangle = \psi_e(t)|e\rangle + \psi_g(t)|g\rangle$ evolution is described by the following Hamiltonian:

$$\hat{H} = \hat{H}_A + \hat{H}_I = \left[\frac{p^2}{2m} - \hbar\Delta\,\hat{\sigma}^\dagger\hat{\sigma}\right] + \frac{\hbar}{2}\left[\Omega(\mathbf{r})\hat{\sigma}^\dagger + \Omega^*(\mathbf{r})\hat{\sigma}\right] \tag{1.26}$$

where we have defined the Rabi frequency and the raising/lowering operators as:

$$\Omega(\mathbf{r}) = -\frac{\mathbf{d}_{eg}\cdot\mathbf{E}(\mathbf{r})}{\hbar}, \qquad \hat{\sigma}^\dagger = |e\rangle\langle g|, \qquad \hat{\sigma} = |g\rangle\langle e|. \tag{1.27}$$

Since the atomic motion evolves on the characteristic timescales $T_R = \hbar/E_R$ of the recoil energy, we have $\Delta \gg \Gamma \gg E_R/\hbar$. Therefore the atomic internal state is damped instantaneously to equilibrium when compared to the external motion[5]. This results in a negligible excited state population which leads to an effective Hamiltonian for the ground-state population [54]:

$$\hat{H}_{\text{eff}} = \frac{p^2}{2m} + \frac{\hbar|\Omega(\mathbf{r})|^2}{4\Delta} \tag{1.28}$$

It shall be noted that the expression for the effective potential is the same as Eq. (1.25) without the counter-rotating wave term:

$$V_{dip} = \frac{\hbar\Omega^*(\mathbf{r})\Omega(\mathbf{r})}{4\Delta} = \frac{3\pi c^2}{2\omega_0^3}\left(\frac{\Gamma}{\Delta}\right) I(\mathbf{r}). \tag{1.29}$$

This formulation more clearly highlights the nature of optical trapping as a second order process with $|e\rangle$ playing the role of the intermediate state. Indeed in this picture, $\Omega \propto \mathbf{d}_{eg}$ and $\Omega^* \propto \mathbf{d}_{ge}$ refer respectively to the absorption and the stimulated emission processes which dress the atomic ground-state motion. This framework will be useful in formulating the theory of optical lattices and Raman processes. Nevertheless these results are to be taken with a grain of salt because they are valid in the ideal case of a two-level atomic system. In the next section we will extend these results to the case of multi-level atoms focusing on the specific case of the optical transitions of ^{173}Yb.

[5]The results of this approximation are the conditions $\dot{\psi}_e(t) = 0$ which leads to $\psi_e(t) = (\Omega^*/2\Delta)\psi_g(t)$.

Optical potentials for ^{173}Yb

In the case of multilevel atoms, light-atom interaction does not change qualitatively with respect to the ideal two-level case. In this section we will focus on the particular case of ^{173}Yb, whose ground state has zero electronic angular momentum $J_g = 0$ and purely nuclear spin $I = F_g = 5/2$. We consider the case of an excited P state with $J_e = 1$ and total angular momentum $|I - J_e| \leq F_e \leq I + J_e = 3/2, 5/2, 7/2$ (see Fig. 1.1 for the $^3P_1$ manifold).

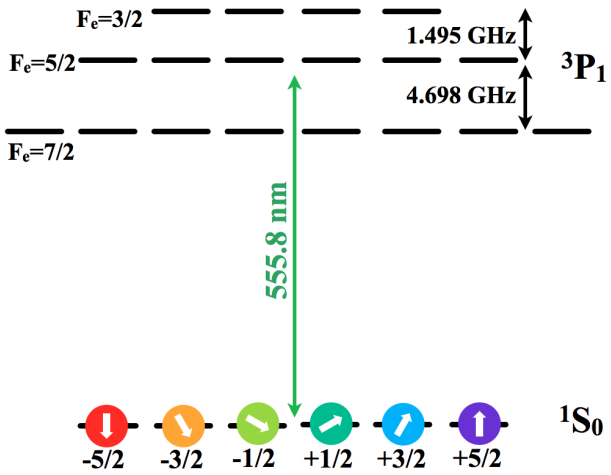

Figure 1.1: Hyperfine structure of the $^1S_0 \rightarrow {}^3P_1$ transition.

Considering the angular momentum projections along the quantization axis $-F_{g(e)} \leq m_{g(e)} \leq F_{g(e)}$, we can define the following projection operators that span the whole Hilbert space:

$$\begin{aligned} \hat{P}_e &= \sum_{F_e, m_e} |F_e, m_e\rangle\langle F_e, m_e|, \\ \hat{P}_g &= \sum_{m_g} |F_g, m_g\rangle\langle F_g, m_g|. \end{aligned} \tag{1.30}$$

Assuming no external fields, so that all the excited and ground sublevels are degenerate in energy, the atomic Hamiltonian in the rotated frame is

$$\hat{H}_A = -\hbar \sum_{F_e, m_e} \Delta_{F_e} |F_e, m_e\rangle\langle F_e, m_e|, \tag{1.31}$$

where $\Delta_{F_e} = \omega_L - \omega_{F_e}$ is the detuning from the hyperfine resonance at ω_{F_e}. On the other hand, in order to evaluate the interaction Hamiltonian it is helpful to conveniently use

operators (1.30) to decompose the q-component of the dipole operator in lowering and raising operators [54]:

$$\hat{d}_q = \hat{P}_e \hat{d}_q \hat{P}_g + \hat{P}_g \hat{d}_q \hat{P}_e = \hat{d}_q^{(+)} + \hat{d}_q^{(-)}. \tag{1.32}$$

Here $q = -1, 0, 1$ is the index labeling the dipole operator component in the spherical basis. In this notation, $q = \pm 1$ couple to $\boldsymbol{\sigma}^{\mp}$-polarized electric fields whereas $q = 0$ couples $\boldsymbol{\pi}$-polarized light. In order to factor out the angular dependence, we can use the Wigner-Eckart theorem to decompose the dipole matrix element connecting $|F_g, m_g\rangle$ to $|F_e, m_e\rangle$ in a reduced matrix element and a Clebsch-Gordan coefficient

$$\langle F_e, m_e | d_q | F_g, m_g \rangle = \langle F_e || \mathbf{d} || F_g \rangle \langle F_e, m_e | F_g, m_g; 1, q \rangle, \tag{1.33}$$

where the Clebsch-Gordan coefficients take into account the angular momentum conservation selection rules $m_g - m_e = q$ and $F_e = F_g \pm 1, F_g$. The reduced matrix element can be further simplified by noting that the dipole operator acts on the electronic angular momentum J. Since $F_{g(e)} = I + J_{g(e)}$, we can use Wigner 6-j symbols to write

$$\langle F_e || \mathbf{d} || F_g \rangle = \langle J_e || \mathbf{d} || J_g \rangle (-1)^{F_g + J_e + 1 + I} \sqrt{(2F_g + 1)(2J_e + 1)} \begin{Bmatrix} J_e & J_g & 1 \\ F_g & F_e & I \end{Bmatrix}. \tag{1.34}$$

Using symmetry properties of Clebsch-Gordan and Wigner 6-j with Eqs. (1.33) and (1.34), we can derive an important property of the q-component of the dipole operator [54], namely:

$$\left(\hat{d}_q^{(+)}\right)^\dagger = (-1)^q \hat{d}_{-q}^{(-)}, \tag{1.35}$$

The physical implication of this relation is that the operator associated to the process $m_g \to m_e - q$ is not the *hermitian conjugate* of the one associated with $m_e \to m_g + q$ process in terms of matrix element unless the polarization is $\boldsymbol{\pi}$ ($q = 0$). In other words, for a given ground-state sublevel m_g, the probability amplitude of a $\boldsymbol{\sigma}^{\pm}$ photon absorption process has the same absolute value but opposite phase of the $\boldsymbol{\sigma}^{\pm}$ photon emission process. As shown below, this phase relation is irrelevant to calculate optical potentials, as only matrix element absolute values are involved, but it will be crucial to correctly assess the values and the phases of the two-photon Raman couplings in chapter 6. With this compact notation we can generalize the interaction Hamiltonian (1.26) as

$$\hat{H}_I = \frac{\hbar}{2} \sum_q \left[\Omega_q \hat{\Sigma}_q^\dagger + \Omega_{-q}^* \hat{\Sigma}_{-q} \right], \tag{1.36}$$

where

$$\Omega_q(\mathbf{r}) = -\frac{\langle J_e||\mathbf{d}||J_g\rangle E_q(\mathbf{r})}{\hbar}, \qquad \hat{\Sigma}_q^\dagger = \sum_{F_e}\sum_{m_e m_g} \mathcal{S}^{(q)}_{m_e m_g}(F_e)|F_e, m_e\rangle\langle F_g, m_g| \tag{1.37}$$

are respectively the Rabi frequency associated at the field with polarization q and the raising operator. The coefficient

$$\mathcal{S}^{(q)}_{m_e m_g}(F_e) = \langle F_e, m_e|F_g, m_g; 1, q\rangle(-1)^{F_g+J_e+1+I}\sqrt{(2F_g+1)(2J_e+1)}\left\{\begin{array}{ccc} J_e & J_g & 1 \\ F_g & F_e & I \end{array}\right\} \tag{1.38}$$

takes into account the angular part of the matrix element[6]. In this theoretical framework we can use Eq. (1.29) to work out the optical potential generated by a q-polarized light for a specific ground-state sublevel m_g, simply summing over the excited state weighted for their detuning [8]:

$$\begin{aligned} V^{(q)}_{m_g}(\mathbf{r}) &= \frac{\hbar|\Omega_q(\mathbf{r})|^2}{4}\left(\sum_{F_e}\frac{|\mathcal{S}^{(q)}_{m_g}(F_e)|^2}{\Delta_{F_e}}\right) \\ &= \frac{3\pi c^2}{2\omega_0^3}\Gamma_{J_e J_g}\left(\sum_{F_e}\frac{|\mathcal{S}^{(q)}_{m_g}(F_e)|^2}{\Delta_{F_e}}\right) I_q(\mathbf{r}), \end{aligned} \tag{1.39}$$

where the spontaneous decay rate $\Gamma_{J_e J_g}$ is defined in terms of reduced matrix element as

$$\Gamma_{J_e J_g} = \frac{3\pi\epsilon_0\hbar c^3}{\omega_0^3}\left(\frac{2J_g+1}{2J_e+1}\right)|\langle J_g||\mathbf{d}||J_e\rangle|^2. \tag{1.40}$$

Analogously it is possible to compute the scattering rate by generalizing Eq. (1.23):

$$\Gamma^{(q)}_{m_g} = \frac{3\pi c^2}{2\hbar\omega_0^3}\Gamma^2_{J_g J_e}\left(\sum_{F_e}\frac{|\mathcal{S}^{(q)}_{m_g}(F_e)|^2}{\Delta^2_{F_e}}\right) I_q(\mathbf{r}). \tag{1.41}$$

As an example, the optical potential and the scattering rate near the ^{173}Yb resonance $^1S_0 \rightarrow {}^3P_1$ at 556 nm is shown in Fig. 1.2 for polarization $\boldsymbol{\sigma}^-$. It is interesting to note how the symmetry properties of the Clebsch-Gordan coefficients determine the following relations:

$$V^{\pi}_{m_g} = V^{\pi}_{-m_g}, \quad V^{\sigma^+}_{m_g} = V^{\sigma^-}_{-m_g}, \qquad \Gamma^{\pi}_{m_g} = \Gamma^{\pi}_{-m_g}, \quad \Gamma^{\sigma^+}_{m_g} = \Gamma^{\sigma^-}_{-m_g}. \tag{1.42}$$

[6] From now on we omit the index m_e in the coefficients $S^{(q)}_{m_e m_g}$ since it is unambiguously determined by the angular momentum conservation $m_g = m_e - q$.

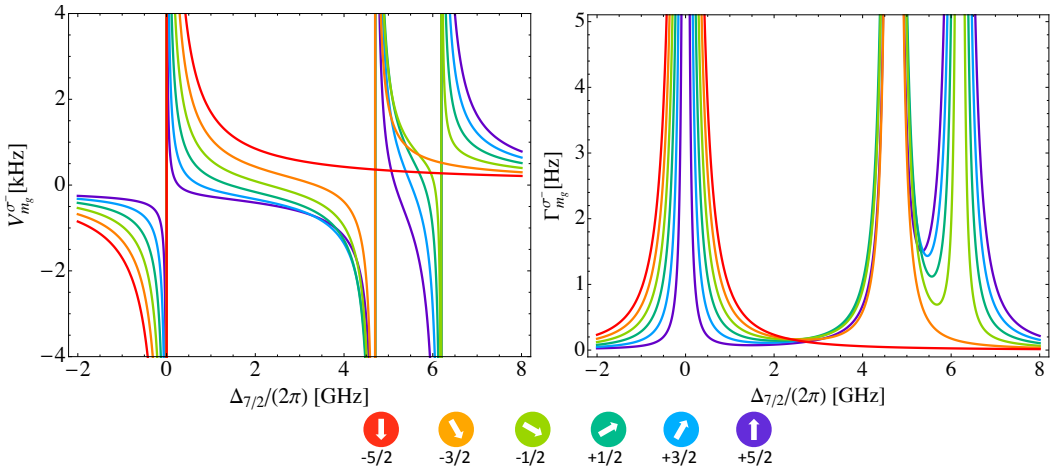

Figure 1.2: Optical potential $V^{\sigma^-}_{m_g}$ and scattering rate $\Gamma^{\sigma^-}_{m_g}$ for laser light close to the $^1S_0 \rightarrow {}^3P_1$ transition in ^{173}Yb. The peak intensity is $I_{\sigma^-} = 50$ mW/cm^2 and the detuning $\Delta_{7/2}$ on the x-axis is with respect to the $F_e = 7/2$ resonance. The other two resonances (see also Fig. 1.1) refer to $F_e = 5/2$ ($\Delta^{7/2-5/2}_{hfs} = 4698$ MHz) and $F_e = 3/2$ ($\Delta^{7/2-3/2}_{hfs} = 6193.5$ MHz).

Because of these symmetry relations, the light shift V_{tot} induced by a "isotropic" polarization $\hat{\varepsilon} = 1/\sqrt{3}(\hat{\varepsilon}_+ + \hat{\varepsilon}_- + \hat{\varepsilon}_\pi)$ is independent from the specific spin state. This property arises from the relation

$$\sum_q |\mathcal{S}^{(q)}_{m_g}(F_e)|^2 = (2F_e+1)(2J_g+1)\left\{ \begin{array}{ccc} J_e & J_g & 1 \\ F_g & F_e & I \end{array} \right\}^2 \equiv S_{F_e,F_g}, \quad \forall m_g, F_e. \tag{1.43}$$

This means that with an isotropic polarization every excited state contributes with the same weight to the light shift independently from the specific m_g considered. This weight is a purely geometrical factor S_{F_e,F_g}, which is usually referred to as relative strength of the transition $F_g \rightarrow F_e$.

Since light shifts and scattering rates depend on the specific nuclear spin components, it is useful to investigate how an external magnetic field bias modify these quantities. In the specific case of the $^3P_1$ excited state, for the typical magnetic field achievable in the current experimental setup (at most 150 Gauss), the weak field regime applies apart from small corrections (see Fig. 1.3). Therefore the total angular momentum F is still a good quantum number and the matrix elements in numerators of each term in Eq. (1.39) are not significantly modified. Nevertheless, in the denominators of the same equation the degeneracy lifting operated by the magnetic field on the $^3P_1$ sublevels needs to be properly

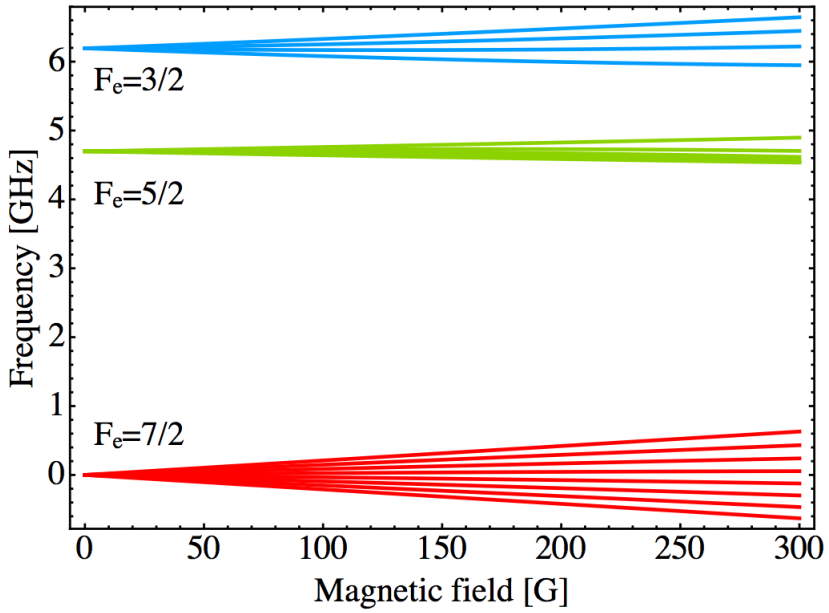

Figure 1.3: Exact diagonalization of the hyperfine Hamiltonian of the $^3P_1$ state as a function of magnetic field. The magnetic dipole $A_{hfs} = 1094.2$ MHz and quadrupole $B_{hfs} = -827.2$ MHz hyperfine couplings are reported in [55].

taken into account by the substitution $\Delta_{F_e} \to \Delta_{F_e} - E^{m_e}_{F_e}(B)$, with $E^{m_e}_{F_e}(B)$ being the magnetic splitting reported in Fig. 1.3. For this reason light shifts and scattering rates are modified with respect to the zero magnetic field case and the symmetry relations (1.42) are broken.

it is worth noting that, for large detuning $\Delta \gg \Delta_{hfs}$, with Δ_{hfs} being the typical separation between different hyperfine transitions, we can approximate $\Delta_{F_e} \sim \Delta$ and factor it out from the summation over the $\mathcal{S}^{(q)}_{m_g}$ coefficients. Then by using the property $\sum_{F_e} |\mathcal{S}^{(q)}_{m_g}(F_e)|^2 = 1/3$, $\forall m_g, q$ we find:

$$V^{(q)}(\mathbf{r}) \sim \frac{1}{3} V_{dip}(\mathbf{r}), \qquad \Delta \gg \Delta_{hfs} \tag{1.44}$$

The physical intuition is that, at large detuning, the electric field does not "resolve" the hyperfine structure and since the light is polarized it interacts on average with only one component $\hat{d}_q$ of the dipole operator, which amounts for 1/3 of the total matrix element.

On the same line of reasoning, in order to calculate optical potentials for detunings $\Delta \sim \omega_L$, we need to consider all the different electronic levels as possible intermediate states, neglecting their hyperfine splittings. As a consequence, the light shift on a generic

electronic state $|a\rangle$ is a straightforward extension of Eq. (1.25), namely:

$$V_a(\mathbf{r}) = \sum_{b\neq a} \frac{3\pi c^2}{2\omega_b^3} \left[\frac{\Gamma_b}{(\omega_b - \omega_a) - \omega_L} + \frac{\Gamma_b}{(\omega_b - \omega_a) + \omega_L} \right] I(\mathbf{r}), \tag{1.45}$$

where ω_b identifies the resonance frequency of the transition $|a\rangle \to |b\rangle$ with its respective linewidth Γ_b. This formulation will be used in chapter 5 to evaluate the light shift potential of the electronic states $|a\rangle = |^1S_0\rangle, |^3P_0\rangle$ as a function of the frequency ω_L.

This formalism highlights how the optical potential results from a two-photon coupling that acts on *one* specific ground-state m_g. However two-photon processes can give rise also to Raman stimulated transitions in which *two* different ground states are coherently coupled without a significant population of the excited state. This will be the topic of the next section.

1.2.1 Raman processes

Let us consider, for simplicity sake, a Λ-configuration (see Fig. 1.4) with a three-level atom with an excited state $|e\rangle$ and two ground states $|g_1\rangle$ and $|g_2\rangle$ corresponding to the atomic resonances ω_{01} and ω_{02} respectively [54]. Considering a total electric field:

$$\mathbf{E}(\mathbf{r}, t) = \boldsymbol{\varepsilon}_1 E_{01} \cos(\mathbf{k}_1 \cdot \mathbf{r} - \omega_1 t) + \boldsymbol{\varepsilon}_2 E_{02} \cos(\mathbf{k}_2 \cdot \mathbf{r} - \omega_2 t), \tag{1.46}$$

we can define a rotating-frame where the free atomic Hamiltonian is

$$\hat{H}_A = \frac{\hat{p}^2}{2m} + \Delta_1 |g_1\rangle\langle g_1| + \Delta_2 |g_2\rangle\langle g_2|, \tag{1.47}$$

where $\Delta_1 = \omega_1 - \omega_{01}$ and $\Delta_2 = \omega_2 - \omega_{02}$ are the detunings with respect to relative transitions. Considering Eq. (1.46), we can generalize the two-level interaction RWA Hamiltonian (1.26) as:

$$\hat{H}_I = \frac{\hbar}{2} \left[\Omega_1 e^{i\mathbf{k_1}\cdot\mathbf{r}} \hat{\sigma}_1^\dagger + \Omega_1^* e^{-i\mathbf{k_1}\cdot\mathbf{r}} \hat{\sigma}_1 \right] + \frac{\hbar}{2} \left[\Omega_2 e^{i\mathbf{k_2}\cdot\mathbf{r}} \hat{\sigma}_2^\dagger + \Omega_2^* e^{-i\mathbf{k_2}\cdot\mathbf{r}} \hat{\sigma}_2 \right], \tag{1.48}$$

where $\hat{\sigma}_1 = |g_1\rangle\langle e|$ and $\hat{\sigma}_2 = |g_2\rangle\langle e|$. Using the ansatz $|\Psi\rangle = \psi_{g_1}|g_1\rangle + \psi_{g_2}|g_2\rangle + \psi_e|e\rangle$, we can use the same adiabatic approximation as for the two-level case, imposing $\partial\psi_e/\partial t = 0$, which leads to:

$$\psi_e(t) = \frac{\Omega_1}{2\Delta}\psi_{g_1}(t) + \frac{\Omega_2}{2\Delta}\psi_{g_2}(t), \tag{1.49}$$

where we defined $\Delta = \Delta_1 + \Delta_2$ assuming $|\Delta_1 - \Delta_2| \ll \Delta$, namely that the difference in energy between the two ground states is much lower than the detuning from the excited

state. Plugging Eq. (1.49) in the Schrödinger equation leads to a two-level effective

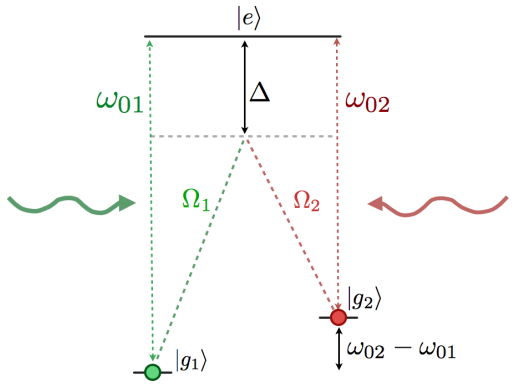

Figure 1.4: Level scheme of a Raman transition. $|g_1\rangle$ and $|g_2\rangle$ are coupled resonantly via a two-photon process.

Hamiltonian with coherent couplings between the ground states:

$$\hat{H}_R = \begin{pmatrix} \dfrac{\hat{p}^2}{2m} + \hbar\omega_{LS_1} & \dfrac{\hbar\Omega_R}{2}\, e^{i2\mathbf{k}_R\cdot\mathbf{r}} \\ \dfrac{\hbar\Omega_R^*}{2}\, e^{-i2\mathbf{k}_R\cdot\mathbf{r}} & \dfrac{\hat{p}^2}{2m} + \hbar\omega_{LS_2} - \delta \end{pmatrix}, \tag{1.50}$$

where $2\mathbf{k}_R = \mathbf{k}_1 - \mathbf{k}_2$ is the momentum transfer acquired by the atom that undergoes a "spin-flip" process from $|g_1\rangle$ to $|g_2\rangle$ and viceversa, $\delta = \Delta_1 - \Delta_2 = (\omega_1 - \omega_2) - (\omega_{01} - \omega_{02})$ is the detuning with respect the two-photon resonance and

$$\Omega_R = \frac{\Omega_1\Omega_2^*}{2\Delta}, \qquad \omega_{LS_\alpha} = \frac{|\Omega_\alpha|^2}{4\Delta}, \tag{1.51}$$

are respectively the effective two photon Rabi frequency and the light shift on $|g_\alpha\rangle$ with $\alpha = 1, 2$. Assuming Ω_R real and choosing a reference frame such that $\mathbf{k}_R \cdot \mathbf{r} = k_R x$, it is particularly useful to express the Raman Hamiltonian in terms of Pauli matrices:

$$\hat{H}_R = \frac{\hat{p}^2}{2m}\hat{\mathbb{1}} + \frac{\hbar\Omega_R}{2}\left[\hat{\sigma}_x \cos(2k_R x) - \hat{\sigma}_y \sin(2k_R x)\right] + \frac{\delta'}{2}\hat{\sigma}_z \tag{1.52}$$

where we inserted the differential light shift in $\delta' = \delta - (\omega_{LS_2} - \omega_{LS_1})$. it is worth noting that by applying the unitary transformation $\hat{U} = e^{ik_R\hat{x}\hat{\sigma}_z}$ (which is basically a gauge

transformation) we obtain:

$$\hat{H}'_R = \hat{U}\hat{H}_R\hat{U}^\dagger = \begin{pmatrix} \dfrac{(p-\hbar k_R)^2}{2m} + \dfrac{\delta'}{2} & \dfrac{\hbar\Omega_R}{2} \\ \dfrac{\hbar\Omega_R^*}{2} & \dfrac{(p+\hbar k_R)^2}{2m} - \dfrac{\delta'}{2} \end{pmatrix} \tag{1.53}$$

This form will be particularly useful in the next section where optical lattices and Bragg dynamics will be interpreted as a particular case of Raman process.

1.2.2 Optical lattices

Optical lattices are a fundamental tool in the context of quantum simulation as they provide an ideal realization of the periodic potentials that play a central role in solid state physics. Such optical structures can be obtained from two counter-propagating plane-waves with the same polarization, creating a stationary interference pattern along the z propagation direction:

$$\mathbf{E}_L(\mathbf{r}) = \boldsymbol{\varepsilon} E_0 \left[\cos(k_L z - \omega_L t) + \cos(k_L z + \omega_L t)\right] = \boldsymbol{\varepsilon} E_0 \cos(k_L z)(e^{i\omega_L t} + e^{-i\omega_L t}). \tag{1.54}$$

Following Eq. (1.26), this beam configuration results in the rotating-frame Hamiltonian:

$$\hat{H} = \hat{H}_A + \hat{H}_I = \left[\frac{p^2}{2m} - \hbar\Delta\,\hat{\sigma}^\dagger\hat{\sigma}\right] + \hbar\Omega_0\cos(k_L z)\left[\hat{\sigma}^\dagger + \hat{\sigma}\right]. \tag{1.55}$$

Following the adiabatic approximation (Eq. 1.28), we obtain:

$$\hat{H}_{\text{eff}} = \frac{p^2}{2m} + V_0\cos^2(k_L z), \tag{1.56}$$

where $V_0 = \hbar|\Omega_0|^2/4\Delta$. Experimentally, optical lattices are obtained by superimposing two counter-propagating Gaussian beams such that, beside the periodic pattern, there is also an additional external confinement term in the potential:

$$V_{1D}(r,z) = V_0 e^{-2\frac{r^2}{w^2(z)}}\cos^2(k_L z) \simeq V_0\cos^2(k_L z) + \underbrace{\frac{1}{2}m\omega_r^2 r^2 + \frac{1}{2}m\omega_z^2 z^2}_{V_{ext}}. \tag{1.57}$$

The depth of an optical lattice is naturally defined in units of recoil energy $E_R = \hbar^2 k_L^2/2m$ through the dimensionless parameter $s = V_0/E_R$. By making a harmonic approximation around $r = 0$ and $z = 0$, it is possible to distinguish the radial frequency and the longitudinal frequency due to the Gaussian envelope of the counter-propagating beams and

express them in terms of recoil units:

$$\begin{aligned} \omega_r &= \sqrt{\frac{4V_0}{mw_0^2}} = \sqrt{\frac{4E_R}{mw_0^2}}\sqrt{s}, \\ \omega_z &= \sqrt{\frac{2V_0}{mz_R^2}} = \sqrt{\frac{2E_R}{mz_R^2}}\sqrt{s}. \end{aligned} \tag{1.58}$$

By expanding the co-sinusoidal term in Eq. (1.57) around $z = 0$, we obtain the harmonic frequency associated to the lattice sites created by the interference pattern along the z-axis, namely:

$$\omega_\perp = \sqrt{\frac{2k_L^2}{m}V_0} = \frac{2E_R}{\hbar}\sqrt{s}. \tag{1.59}$$

Optical lattices are a versatile and maneuverable tool not only to build perfect periodic potentials but also to tune the dimensionality of the system. Indeed in this thesis, 2D optical lattices have been used to study the physics of one-dimensional systems (see chapter 4) and 3D optical lattices have been used to investigate two-body collisions between different electronic states in "zero-dimensional" traps (see chapter 5). In the former case, an array of one-dimensional wires along the x-direction is created by retro-reflecting two orthogonal beams along z and y-axis. By making the same harmonic approximation of Eq. (1.57), the resulting potential can be written as:

$$V_{2D}(x, y, z) = V_0 \cos^2(k_L z) + V_0 \cos^2(k_L y) + \frac{1}{2}m\left(\omega_x^2 x^2 + \omega_y^2 y^2 + \omega_z^2 z^2\right), \tag{1.60}$$

where:

$$\begin{aligned} \omega_x^2 &= \frac{4E_R}{mw_{0y}^2}s_y + \frac{4E_R}{mw_{0z}^2}s_z, \\ \omega_y^2 &= \frac{2E_R}{mz_{Ry}^2}s_z + \frac{4E_R}{mw_{0z}^2}s_z, \\ \omega_z^2 &= \frac{4E_R}{mw_{0y}^2}s_y + \frac{2E_R}{mz_{Rz}^2}s_z, \end{aligned} \tag{1.61}$$

where s_y and s_z are the lattice depths along y and z respectively.

In the next two sections we will neglect the external harmonic confinement to focus on two different aspects of the physics of optical lattices: the band structure and the exact eigenfunctions of a particle in a periodic potential in one, two and three dimensions, and the dynamics of a particle subjected to a periodic potential.

Band structure and Bloch functions

The problem of a single particle in a periodic potential has been extensively studied in the last century in solid state physics [56]. The discrete translational symmetry simplifies significantly the problem imposing, through the Bloch theorem, a specific form of the eigenfunctions $\psi_k^{(n)}(z)$ which are associated to an infinite discrete series of dispersion relations $E^{(n)}(k)$:

$$\hat{H}\psi_k^{(n)}(z) = E^{(n)}(k)\psi_k^{(n)}(z), \qquad \psi_k^{(n)}(z) = e^{ikz}u_k^{(n)}(z), \tag{1.62}$$

where $u_k^{(n)}(z)$ is a function with the same periodicity $d = \lambda_L/2$ of the potential, that is $u_k^{(n)}(z+d) = u_k^{(n)}(z)$. In the specific case of a perfect sinusoidal potential along z, the Schrödinger equation for a single particle moving can be solved exactly in terms of Mathieu functions. In particular, Eq. (1.62) can be recast as:

$$\left[\frac{d^2}{dw^2} + \left(\frac{E}{E_R} - \frac{s}{2}\right) - 2\left(\frac{s}{4}\right)\cos(2w)\right]\psi(w) = 0, \quad w = k_L z, \tag{1.63}$$

which is the well-known Mathieu equation with parameters[7] $a = E/E_R - s/2$ and $q = s/4$. As expected from the Bloch theorem, the eigenenergies are an infinite discrete series of dispersion relations $E^{(n)}(k)$ that can be written in terms of Mathieu Characteristic values $\mathcal{A}[k/k_L, -s/4]$:

$$\begin{aligned} E^{(n)}(k) &= \mathcal{A}\left[\frac{k}{k_L} + 2\,\mathrm{Sign}\left(\frac{k}{k_L}\right)\left(\frac{n+1}{2} - 1\right), -\frac{s}{4}\right] + \frac{s}{2}, \quad n = 1, 3, 5, \ldots, \\ E^{(n)}(k) &= \mathcal{A}\left[\frac{k}{k_L} - 2\,\mathrm{Sign}\left(\frac{k}{k_L}\right)\left(\frac{n+2}{2} - 1\right), -\frac{s}{4}\right] + \frac{s}{2}, \quad n = 2, 4, 6, \ldots, \end{aligned} \tag{1.64}$$

where $k \in (-k_L, +k_L)$ and n is the band index in the reduced zone scheme. The eigenenergies for different values of s are plotted in Fig. 1.5. It shall be noted that, as the depth of the potential grows, the band gaps increase accordingly. Moreover, for high values of s, the lower bands flatten out and are well approximated by the harmonic oscillator levels (see dashed line in Fig. 1.5) and consequently the band gap can be approximated as $\hbar\omega_\perp$, where $\omega_\perp$ defined in Eq. (1.59). The Bloch functions (Fig. 1.6) can be recast in analytical

[7] The Mathieu equation is defined as:

$$y'' + [a - 2q\,\cos(2z)]y = 0.$$

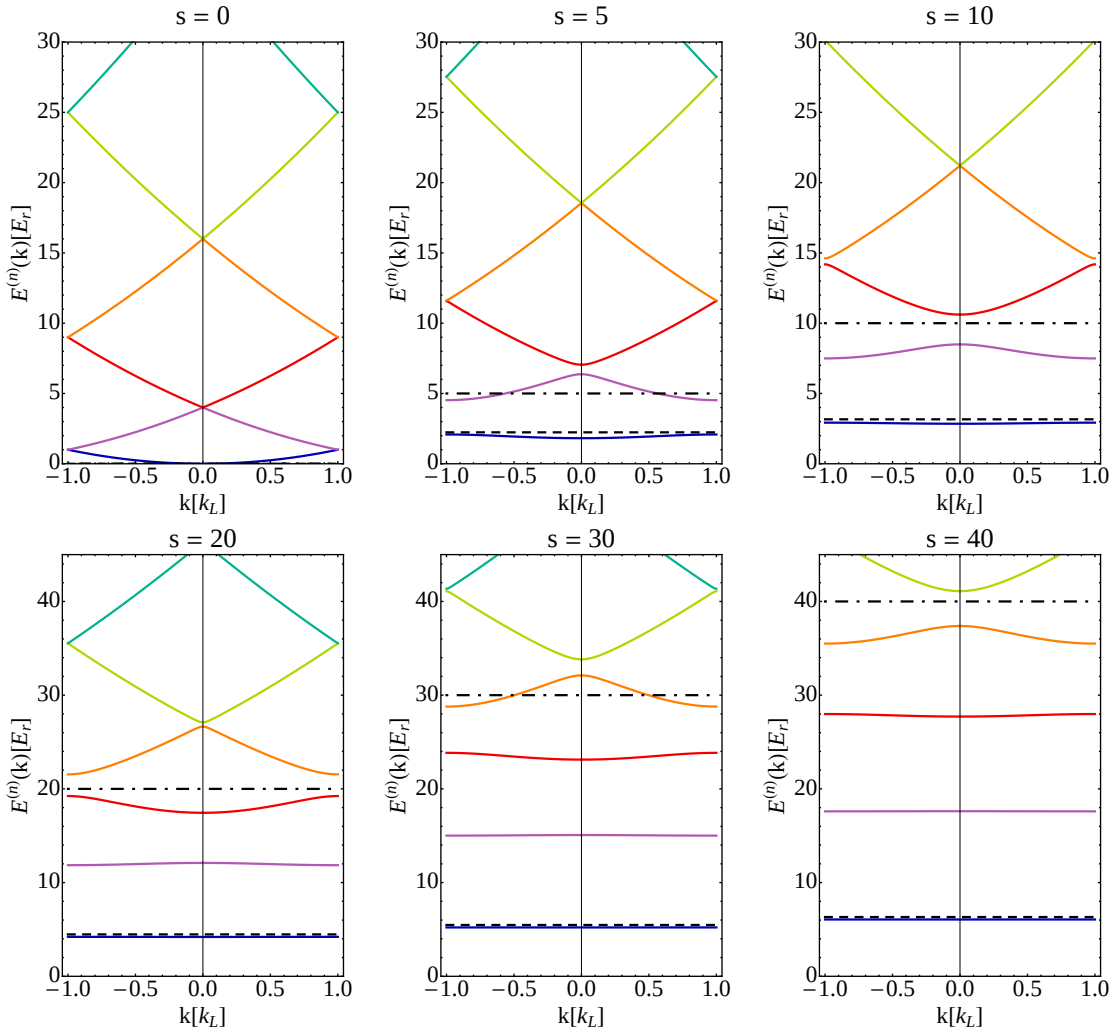

Figure 1.5: Spectrum of a single particle in a periodic potential for different values of s calculated solving the Mathieu differential equation. The different bands are labeled with different colors. The black dash-dotted line is the value of s and the black dashed line is the zero-point harmonic oscillator energy $\hbar\omega_\perp/2$. As the lattice depth increases, the band gaps grow accordingly and the lowest band approaches the harmonic oscillator energy.

form [57] in terms of Mathieu functions as:

$$\psi_k(w) = \mathcal{C}\left(E(k) - \frac{s}{2}, -\frac{s}{4}, w\right) + i\,\mathrm{Sign}(k)\;\mathcal{S}\left(E(k) - \frac{s}{2}, -\frac{s}{4}, w\right), \tag{1.65}$$

where $\mathcal{C}$ and $\mathcal{S}$ denote respectively the even and odd Mathieu functions, which form a complete orthogonal set. Within this formalism, it is possible to define a tunneling energy

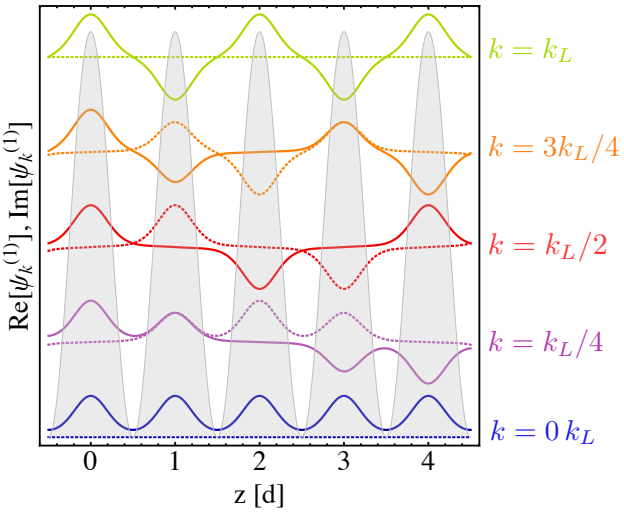

Figure 1.6: Real (solid line) and imaginary part (dashed line) of Bloch eigenfunctions $\psi_k^{(1)}(z)$ in the lowest band for $s = 8$. The shaded area represents the periodicity of the potential. For clarity sake, the wavefunctions have an artificial offset.

J associated to the probability of the particle to tunnel from site to site. In a tight-binding approximation [11], this quantity is related to the kinetic energy of the particle in a given band of index n and it is proportional to the width of the band itself:

$$J^{(n)} = \frac{E^{(n)}(k_L) - E^{(n)}(0)}{4} \tag{1.66}$$

In the case of 3D lattices with three retro-reflected beams forming the periodic potential, the particles are confined in all directions and the eigenenergies and the eigenfunctions are easily computed since the problem is separable:

$$\begin{aligned} E^{(n_x,n_y,n_z)}(\mathbf{k}) &= E^{(n_x)}(k_x) + E^{(n_y)}(k_y) + E^{(n_z)}(k_z), \\ \Psi_{\mathbf{k}}(\mathbf{r}) &= \psi_{k_x}^{(n_x)}(x)\psi_{k_y}^{(n_y)}(y)\psi_{k_z}^{(n_z)}(z). \end{aligned} \tag{1.67}$$

It shall be noted that, in a one-dimensional band structure, the gap between the lowest and

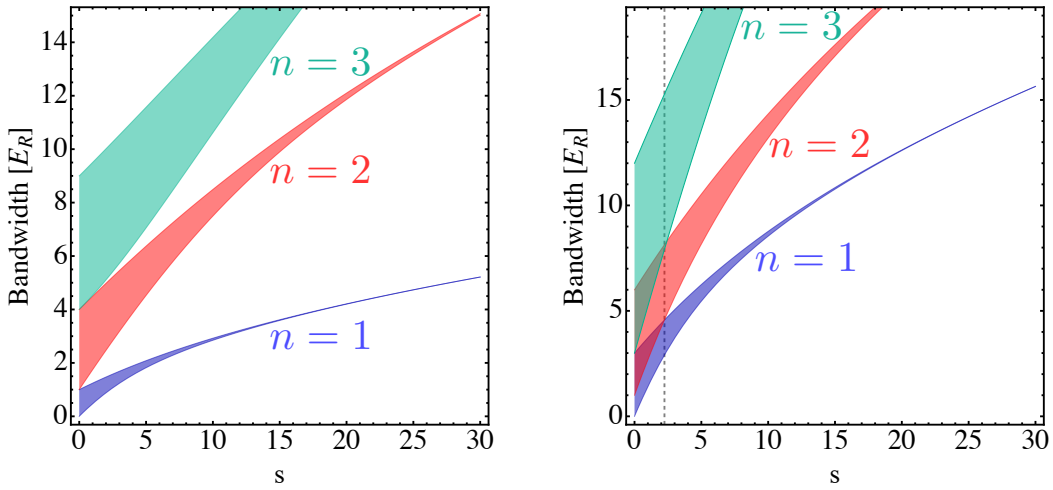

(a) 1D lattice **(b)** 3D lattice

Figure 1.7: Bandwidth of lowest, first and second excited band as function of lattice depth s for 1D lattice **(a)** and 3D lattice **(b)**. Note that in the 3D case the gap opens up only for $s \gtrsim 2.24$ which is represented as the dotted line in **(b)**.

the first excited band opens as long as $s > 0$, but in a three-dimensional lattice structure the gap opens for $s \gtrsim 2.24$ (Fig. 1.7). This happens because, in three dimensions, the first excited state corresponds to the eigenenergy $E^{(2,1,1)}(\mathbf{k})$, which at low s and for some quasi-momentum $\mathbf{k}$, can be smaller than the lowest band energy $E^{(1,1,1)}(\mathbf{k})$.

Besides 3D and 1D optical lattices, the geometry with just two retroreflected beams (see Eq. 1.60) constitutes the ideal playground to investigate one-dimensional systems. A single particle moving in a 2D homogeneous optical lattice displays a free particle dispersion along the x-direction of the tubes. In this case the eigenenergies and the associated eigenfunction are:

$$\begin{aligned} E^{(n_y,n_z)}(\mathbf{k}) &= \frac{\hbar^2 k_x^2}{2m} + E^{(n_y)}(k_y) + E^{(n_z)}(k_z), \\ \Psi_{\mathbf{k}}(\mathbf{r}) &= e^{ik_x x}\psi_{k_y}^{(n_y)}(y)\psi_{k_z}^{(n_z)}(z). \end{aligned} \tag{1.68}$$

However to be fully one-dimensional only the lowest band in both y and z directions ($n_y = n_z = 1$) has to be occupied and the dynamics along y and z needs to be completely "frozen". This condition is fulfilled if:

$$E_F \ll \hbar\omega_\perp(s), \tag{1.69}$$

that is, for high enough values of s, the Fermi energy E_F of the harmonically trapped gas is much lower than the band gap between the lowest and the first excited band; moreover the tubes are completely decoupled from each on the time-scale of the experiment (for further details, see section 4.1).

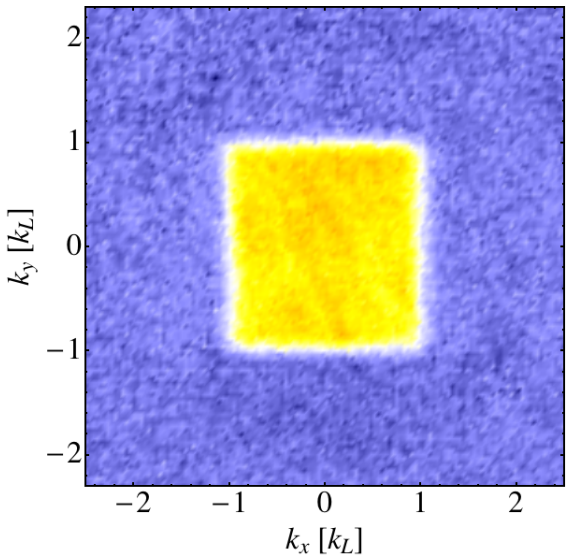

Figure 1.8: False-color time-of-flight image of the lattice momentum distribution of spin-polarized fermions in a 3D optical lattice at $s_x = s_y = s_z = 30$. With $N_{at} = 2 \cdot 10^4$ and $(\omega_x, \omega_y, \omega_z) = 2\pi \times (50, 53, 51)$ Hz, only the lowest band is populated.

All the results illustrated in this section concern the equilibrium state in an optical lattice in which the atoms occupy the lowest band of the lattice. The equilibrium state is prepared by adiabatically ramping up the intensity of the lattice beams, typically using an exponential ramp, to avoid atoms to Landau-Zener tunnel in the excited bands. In order to visualize the band population, a useful observable is the lattice momentum distribution of a Fermi gas in a optical lattice (Fig. 1.8), which can be measured by band mapping [58, 59]. This technique consists in switching off the lattice beams adiabatically with respect to the timescale $1/\omega_\perp$, related to the lattice band gap, but faster than $1/\omega_{trap}$, associated to the external trap frequencies. In this way we map the lattice momentum onto the atomic velocity distribution, measured by absorption imaging after ballistic expansion. Conversely, another way to understand optical lattice properties is to switch on abruptly the lattice beams (faster than every other energy scale) and study the dynamics of the atoms in periodic potentials, which will the be the topic of the next section.

Dynamics in optical lattices

In order to study the dynamics of a particle in a perfect periodic potential, we can use the time-dependent version of the Schrödinger equation shown in Eq. (1.63), expressed in recoil units:

$$i\frac{\hbar}{E_R}\frac{\partial}{\partial t}\psi = \left[\left(-\frac{d^2}{dw^2}+\frac{s}{2}\right)+\frac{s}{4}\left(e^{i2w}+e^{-i2w}\right)\right]\psi. \tag{1.70}$$

Defining a dimensionless variable $\tau = t/\tau_R$ in unit of recoil time $\tau_R = \hbar/E_R$ and writing Eq. (1.70) in momentum space (in k_L units), we get the following set of equations for a given momentum k:

$$i\frac{\partial}{\partial\tau}\psi_k = (k^2+\Omega)\psi_k + \frac{\Omega}{2}(\psi_{k+2}+\psi_{k-2}),\ \forall k, \tag{1.71}$$

where we defined $\Omega = s/2$, which is nothing else than the Raman coupling (see Eq. (1.51)) $\Omega_0^2/4\Delta$ between different momentum states in recoil units. Depending on the time and power broadening, this simple equation individuates two different regimes:

- **Bragg regime:** for long interaction times ($t \gg 1/\sqrt{2\Omega\omega_R}$) [60], the kinetic energy acts as an effective detuning with respect to the resonant dynamics. In this weak-coupling regime, power broadening is not enough to balance out the kinetic energy difference and the dynamics resemble the one of a two-level system. In case of non-zero momentum initial state ($k_i = \pm nk_L$) energy conservation favors dynamical tunneling processes from $-nk_L$ to nk_L in which the atoms exchange coherently with the electromagnetic field $2n$ photons via n negligibly-populated intermediate states (see Fig. 1.9a). By adiabatic elimination of the intermediate states, it is possible to compute the expression for the n-th order process effective Rabi frequency:

$$\Omega_n^{\text{eff}} = \frac{\Omega^n}{(8\omega_R)^{(n-1)}(n-1)!}. \tag{1.72}$$

  In other words, energy and momentum conservation allow only resonant transitions between selected momentum classes whose difference is $k_f - k_i = 2nk_L$. On the other hand, if the initial state is at zero momentum $k = 0$ (Fig. 1.9b), the dynamics is blocked by the kinetic energy offset. In this case, in order to observe a coherent dynamics, the electric field defined in Eq. (1.54) needs to have two frequency components to match the $\Delta E = 4E_R$ energy difference between the two momentum states. In this regime the process can be described as a two-photon Raman oscillation described by the Hamiltonian (1.53) where $k_R = k_L$, the two internal atomic states correspond to the two momentum states $k = 0$ and $k = 2k_L$ and $\Omega_{1(2)}$ recall the single-photon Rabi frequencies associated to the two different electric fields in

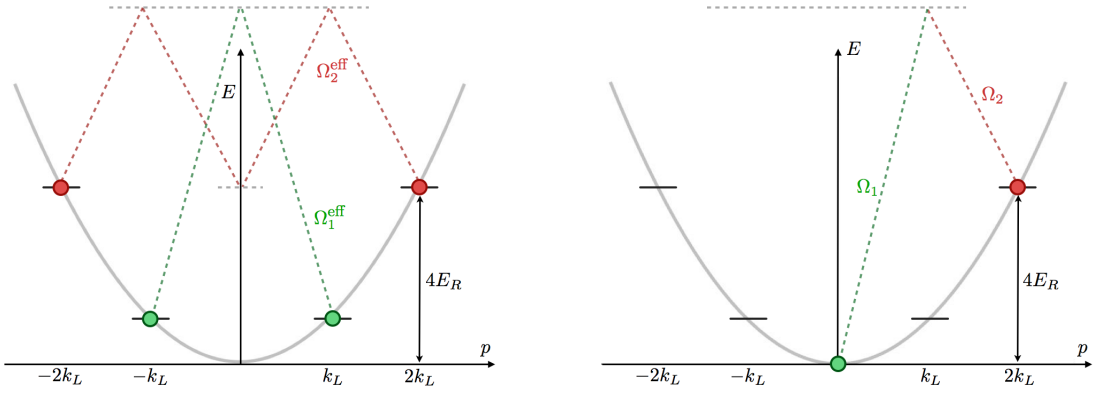

(a) Dynamical tunneling **(b)** Two-frequency Bragg

Figure 1.9: Bragg processes starting from different initial states: **(a)** Bragg processes of the first (green) and second order (red) processes. **(b)** Bragg oscillations between $k = 0$ and $k = 2k_L$ where $\Omega_{1(2)}$ are single-photon Rabi frequency.

Eq. (1.46).

- **Raman-Nath regime**: Often called Kapitza-Dirac, it holds for very short interaction time ($t \ll 1/\sqrt{2\Omega\omega_R}$), such that the kinetic energy term can be neglected leading to a coupling between several nk_L diffraction orders. In this case the Schrödinger equation (1.71), without kinetic term and after a $-\Omega$ shift of the energy scale, reduces to:

$$i\frac{\partial}{\partial\tau}\psi_k = \frac{\Omega}{2}(\psi_{k+2} + \psi_{k-2}). \tag{1.73}$$

As shown in Eq. (1.73), only momentum components that differ by even multiples of k_L are coupled and, considering the initial conditions $\psi_0(0) = 1$, $\psi_{k\neq 0}(0) = 0$, the solutions can be written as:

$$\psi_{2nk_L}(t) = (-i)^n J_n(\Omega t), \tag{1.74}$$

where J_n denotes the n-th order Bessel function. In order to observe Raman-Nath dynamics, a short optical lattice pulse is applied on the atomic cloud. Usually Eq. (1.74) well describes the dynamics of BEC (Bose-Einstein Condensate) in optical lattices since it has a very narrow momentum distribution ($\Delta k \ll k_L$) peaked around $k = 0$. This is also the reason why this regime is used to align and calibrate the optical lattice as the frequency $\Omega = s/2$ is a direct measurement of the lattice depth.

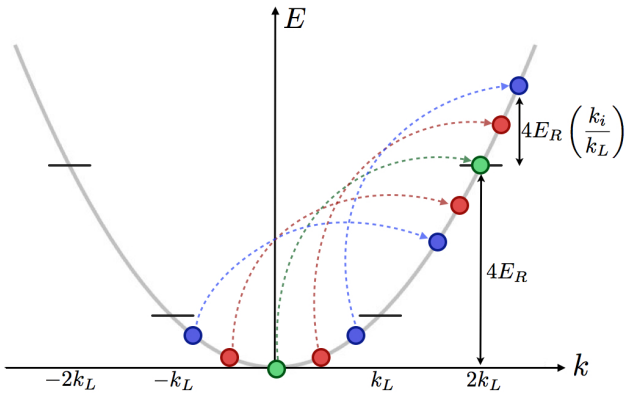

Figure 1.10: Sketch of fermionic Raman-Nath dynamics. Every momentum state k_i of the Fermi sea experiences a different evolution. Only processes to positive momentum are indicated for clarity sake.

It is interesting to analyze the Raman-Nath dynamics of a Fermi sea in optical lattice. In this peculiar case, there are many different initial momentum states k_i ranging from k_F to $-k_F$ that are coupled to $k_f = k_i \pm 2, \ldots, k_i \pm 2n, \ldots$. In particular every momentum component k_i dynamics is ruled by the Hamiltonian [61] in reduced units:

$$\hat{H}_{k_i} = \begin{pmatrix} (k_i - 2)^2 & \Omega/2 & 0 \\ \Omega/2 & k_i^2 & \Omega/2 \\ 0 & \Omega/2 & (k_i + 2)^2 \end{pmatrix}. \tag{1.75}$$

From Eq. (1.75) it is clear that every momentum component k_i oscillates with its own generalized Rabi frequency Ω_{k_i} giving rise to the rather complex dynamics. In Fig. 1.11 it is shown the evolution of a Fermi sea in a optical lattice. In order to extrapolate the momentum distribution evolution along the lattice direction, we integrated the image along the direction orthogonal to the optical lattice. By stacking these one-dimensional time-dependent momentum distributions as a function of the pulse time t, it is possible to visualize the dynamics of the cloud and to compare it with the dynamics of a Gaussian wave-packet with momentum width comparable to the Fermi momentum $k_F \simeq 0.4k_L$. The simulation has been done considering every momentum k_i evolving independently with its own Hamiltonian (1.75). The experimental evolution matches perfectly the theoretical prediction given by the experimental lattice depth.

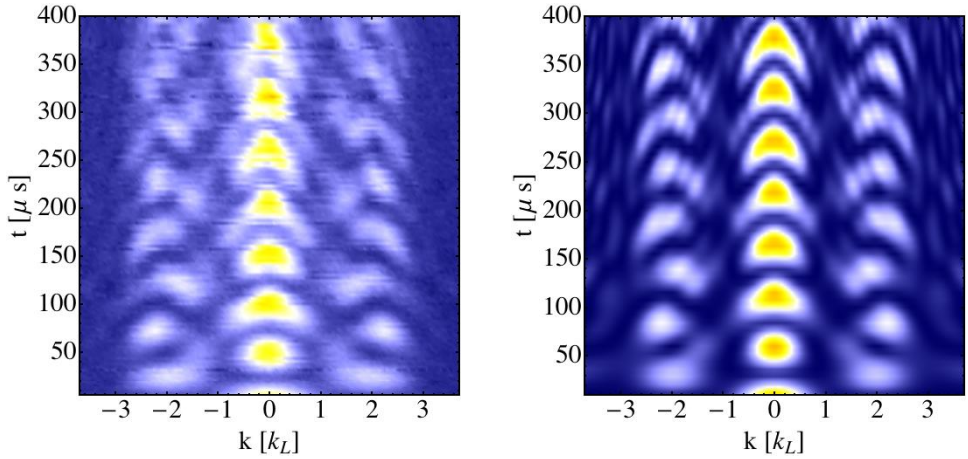

(a) Experiment **(b)** Theory

Figure 1.11: Dynamics of a Fermi sea in a $\lambda_L = 759$ nm optical lattice of depth $s = 16$. The theoretical evolution has been calculated numerically solving Eq. (1.71) approximating the Fermi sea with a Gaussian wave-packet.

1.3 Interactions in ultracold quantum gases

Degenerate quantum gases are usually diluted, namely the De Broglie wavelength λ_{dB} and the interparticle separation $n^{-1/3}$ are much larger than the effective range of interaction r_0, which represents the length-scale beyond which the effect of the interaction potential may be neglected. For this reason most properties of ultracold atoms systems are related to two-body collisions. In particular, since atoms are neutral particles, there is no Coulomb force among them and the interatomic interaction is described by a central potential $V(r)$ generated by the interaction among fluctuating atomic electric dipoles. Thus, at large distances, $V(r)$ can be approximated with a van der Waals potential $-C_6/r^6$ where C_6 is a constant and r is the relative distance between the two particles. At short distances, on the order of a few Bohr radii a_0, the two electron-clouds strongly repel each other, leading to a "hard-core" repulsion. Nevertheless, since these systems are extremely diluted (in ultracold gases the range of interaction is of the order of the Van der Waals length [62] $r_0 \simeq (2\mu C_6/\hbar)^{1/4} \ll n^{-1/3}, \lambda_{dB}$), the fine details of the short-range scattering potential are irrelevant and, therefore,at low-energy, the entire collision process can be parametrized by a single quantity, the scattering length, which is related to the phase shift acquired by the scattered wavefunction in the collision process. Indeed, when the gas is extremely diluted, the scattering among the particles is essentially determined by the asymptotic wave functions, which are directly related to the phase shifts. The Hamiltonian describing

two particles with mass m scattering through a spherically-symmetric potential $V(r)$ is

$$\hat{H} = \frac{\hat{\mathbf{P}}^2}{2M} + \left[\frac{\hat{p}_r^2}{2\mu} + \frac{\hat{\mathbf{L}}^2}{2\mu\hat{r}^2} + V(\hat{r})\right], \tag{1.76}$$

where $\hat{p}_r$ is the relative radial momentum, $\hat{\mathbf{L}}$ is the relative angular momentum, $\hat{P}$ is the center-of-mass momentum, $M = 2m$ the total mass and $\mu = m/2$ is the reduced mass. As usual, the relative motion is separable from the center-of-mass motion, which has a trivial plane wave solution. Considering two particles with relative motion energy $E_k = \hbar^2 k^2/2\mu$, at distances $r \gg r_0$ beyond the effective range of the potential, the asymptotic solution $\psi_{\mathbf{k}}(\mathbf{r})$ is given by the sum of the incident plane wave $e^{i\mathbf{k}\cdot\mathbf{r}}$ and an outgoing scattered wave [63]:

$$\psi_{\mathbf{k}}(\mathbf{r}) \overset{r\to\infty}{\simeq} e^{i\mathbf{k}\cdot\mathbf{r}} + f(\mathbf{k},\mathbf{k}')\frac{e^{ikr}}{r}, \tag{1.77}$$

where $f(\mathbf{k},\mathbf{k}')$ is defined *scattering amplitude* with $\mathbf{k}$ and $\mathbf{k}'$ the incoming and the scattered wavevectors respectively, and with $|\mathbf{k}| = |\mathbf{k}'| = k$ since the collision is elastic. As the potential is assumed to be spherically symmetric, by choosing the axis of quantization along the $\mathbf{k}$ direction, the scattering amplitude can be expanded in spherical partial waves with $m_z = 0$:

$$f(k,\theta) = \sum_{\ell=0}^{\infty}(2\ell+1)\left(\frac{e^{2i\delta_\ell(k)}-1}{2ik}\right)P_\ell(\cos\theta), \tag{1.78}$$

where P_ℓ are the Legendre polynomials of order ℓ and $\delta_\ell(k)$ is the phase shift related to the ℓ-th spherical wave. From this expression the total cross section σ_{tot} is readily obtained through the optical theorem [64]:

$$\sigma_{tot}(k) = \frac{4\pi}{k}Im[f(\theta=0)] = \frac{4\pi}{k^2}\sum_{\ell=0}^{\infty}(2\ell+1)\sin^2\delta_\ell(k). \tag{1.79}$$

It is possible to demonstrate that, for low-energy collisions, $\delta_\ell(k) \sim k^{2\ell+1}$ and that, consequently, for momentum $k \ll r_0^{-1}$ the contributions of partial waves with $\ell \geq 1$ are negligible. Intuitively, at low momentum the particles cannot penetrate the centrifugal barrier $\hbar^2\ell(\ell+1)/2\mu r^2$ present in Eq. (1.76). In this case the scattering amplitude can be approximated just by considering the s-wave ($\ell = 0$) contribution in Eq. (1.78):

$$f(\theta) \simeq f_s = \frac{e^{i2\delta_0(k)}-1}{2ik} = \frac{1}{k\cot\delta_0(k) - ik}. \tag{1.80}$$

Since there is time reversal symmetry [63], $\delta_0(k)$ must be an even function of k and therefore can be expanded for $k \ll r_0^{-1}$ as:

$$k \cot \delta_0 = -\frac{1}{a_s} + \frac{r_{\text{eff}} k^2}{2}, \tag{1.81}$$

where a_s is the s-wave scattering length which can be defined as:

$$a_s = -\lim_{k \to 0} \frac{\tan \delta_0(k)}{k}, \tag{1.82}$$

and r_{eff}, called *effective range*, is of the order of r_0 for Van der Waals potentials and represents the length scale over which the scattering approximation of a momentum-independent scattering length is justified. Then the total cross-section (1.79) can be approximated as:

$$\sigma_{tot} \simeq 4\pi a_s^2. \tag{1.83}$$

It is interesting to see how the scattering is modified if the particles are indistinguishable and quantum statistics plays a role. Indeed the (anti)symmetrization of the two-particle wavefunction $\psi_{\mathbf{k}}(\mathbf{r})$ doubles the contribution of the even partial waves for bosons (the odd partial waves for fermions) and cancels out the contribution of the odd ones (the even ones for fermions), leading to the following total cross-sections:

$$\begin{aligned} \sigma_{tot} &= \frac{8\pi}{k^2} \sum_{\ell \text{ even}}^{\infty} (2\ell + 1) \sin^2 \delta_\ell(k) \qquad \text{Bosons,} \\ \sigma_{tot} &= \frac{8\pi}{k^2} \sum_{\ell \text{ odd}}^{\infty} (2\ell + 1) \sin^2 \delta_\ell(k) \qquad \text{Fermions.} \end{aligned} \tag{1.84}$$

This means that polarized ultracold fermions do not interact because the s-wave channel is forbidden by the Pauli principle and, therefore, the higher ℓ-scattering wave contributions are energetically suppressed. Therefore they represent the ideal test-bench to investigate non-interacting quantum systems.

Since, as stated above, in low temperature diluted quantum gases the details of the interaction potential are irrelevant to the scattering process, it is convenient to replace the complicated full interatomic potential by a much simpler pseudo-potential that nevertheless reproduces the s-wave scattering correctly. In particular, it is possible to consider a hard-sphere potential and substitute the boundary conditions associated to it with an inhomogenous term in the two-body Schrödinger equation. This technique, called Huang's pseudopotential, is an idea successfully borrowed from electrostatics [65]. Usually, in order to calculate the electrostatic potential generated by a charge distribution on a sphere, this

is substituted by an equivalent series of point-like multipoles in the center of the sphere leading to the exact potential outside the sphere. Analogously, if short range details of the real potential are not important, we can substitute the boundary conditions imposed by a hard-sphere potential with a series of point-like scatterers giving rise to s-wave, p-wave and so on. It can be demonstrated [66] that for s-wave scattering, the pseudo-potential that reproduces exactly a hard sphere-potential is

$$U(r) = -\frac{\hbar^2}{m}\frac{4\pi}{k\cot(\delta_0)}\partial_r(r\cdot). \tag{1.85}$$

Using Eq.(1.81) for $k \ll 1/r_{\text{eff}}$, we obtain the pseudo-potential:

$$U(r) = g\,\delta(\mathbf{r})\frac{\partial}{\partial r}(r\cdot), \tag{1.86}$$

with coupling constant $g = 4\pi\hbar^2 a_s/m$. So far we treated the specific case of interactions in three dimensions, where rotational invariance plays a central role in calculating scattering amplitudes. However, in presence of strong transverse confinement, scattering processes generated by a pseudo-potential (1.86) are qualitatively modified leading to counterintuitive consequences. Since interactions in one dimension are one of the main subjects of this work, we will address this topic in the next section.

1.3.1 Interactions in one-dimensional quantum gases

In one dimension binary collisions change qualitatively with respect to their three-dimensional counterpart. Let us consider the transverse harmonic confinement with frequency $\omega_\perp$ in the two-body Hamiltonian:

$$\begin{aligned} \hat{H} &= \frac{\hat{p}_x}{2\mu} + U(r) + \hat{H}_\perp, \\ \hat{H}_\perp &= \frac{\hat{p}_y^2 + \hat{p}_z^2}{2\mu} + \frac{\mu\omega_\perp^2(y^2+z^2)}{2}, \end{aligned} \tag{1.87}$$

where $U(r)$ is the pseudo-potential. As specified in Eq. (1.69), the one-dimensional regime occurs when the atomic motion is frozen below the transverse vibrational energy $\hbar\omega_\perp$. Under these conditions, in the limit of low momentum $k_x \to 0$, it is possible to derive analytically a one-dimensional scattering amplitude [67]:

$$f(k) = -\frac{1}{1 + k_x a_{1D} + \mathcal{O}\left((k_x a_{1D})^3\right)}, \tag{1.88}$$

where a_{1D} is the effective scattering length in one dimension defined as:

$$a_{1D} = -\frac{a_\perp^2}{a_s}\left(1 - C\frac{a_s}{a_\perp}\right), \tag{1.89}$$

where $C = 1.0326...$ is a numerical constant and $a_\perp = \sqrt{\hbar/m\omega_\perp}$ is the transverse harmonic oscillator characteristic length. The scattering amplitude (1.88) can be related to a coupling constant of a δ-like potential $U(x) = g_{1D}\delta(x)$ with:

$$g_{1D} = -\frac{2\hbar^2}{ma_{1D}} = \frac{2\hbar^2 a_{3D}}{ma_\perp^2}\frac{1}{1 - Ca_{3D}/a_\perp}. \tag{1.90}$$

The peculiar expression of g_{1D} highlights how in one dimension confined induced resonances [68, 69] can occur if $a_\perp = Ca_{3D}$, where the coupling strength diverges.

In order to parametrize the interaction in the literature [32, 70] the dimensionless parameter γ is often used:

$$\gamma = \frac{mg_{1D}}{\hbar^2 n_{1D}} = -\frac{2}{n_{1D}a_{1D}}, \tag{1.91}$$

which can be written as the ratio between the interaction energy $g_{1D}n_{1D}$ and the kinetic energy of an ideal homogeneous Fermi gas $\varepsilon = \hbar^2\pi^2 n_{1D}^2/8m$ (see section 3.3). This parameter captures another very peculiar and counterintuitive property of one-dimensional systems: the interaction strength, measured by γ, is inversely proportional to the density n_{1D}. Since ultracold fermions feature low densities even in the quantum degeneracy regime (typically of the order of 10^{13} cm^{-3}, compared to the typical $10^{14} - 10^{15}$ cm^{-3} of Bose-Einstein condensates) because of Fermi pressure, they are the ideal candidates to investigate the physics of strongly interacting phases in one-dimensional systems.

The treatment carried out so far neglects the spin degree of freedom of the atoms, an approximation which simplifies considerably the description of interaction processes in ultracold gases. In general, binary collisions depend significantly on the atomic internal state due to spin-spin interactions and coupling to external fields. Fermionic Ytterbium isotopes, though, feature highly symmetric two-body interactions which have the same strength regardless of the two spin states involved in the scattering process. This is often referred to as $SU(N)$ symmetry [14] and, since it has a central role throughout this work, it will be discussed in detail in the next section.

1.3.2 $SU(N)$-symmetric interactions

$SU(N)$ symmetry is of fundamental importance in many fields of physics, ranging from quantum chromodynamics to many-body systems in condensed matter. In this section

we will illustrate how this symmetry emerges in an ultracold gas of fermionic Ytterbium atoms by describing two-body collisions taking in consideration also the spin degree of freedom. Let us consider two ultracold atoms with total (electronic and nuclear) angular momenta $\hat{\mathbf{F}}_1$ and $\hat{\mathbf{F}}_2$ and relative orbital angular momentum $\hat{\mathbf{L}}$ defined in Eq. (1.76). Rotational invariance of the interaction potential (1.86) leads to the conservation of the overall angular momentum, namely the sum of $\hat{\mathbf{F}} = \hat{\mathbf{F}}_1 + \hat{\mathbf{F}}_2$ and $\hat{\mathbf{L}}$. Moreover, quantum statistics further constrains the value of F and ℓ because the total wavefunction needs to be anti-symmetric for fermions. Since the orbital wavefunction is symmetric, as we are considering s-wave collisions ($\ell = 0$), the spin wavefunction has to be antisymmetric, namely with *even* total spin. Incidentally, this restriction holds also for bosons where the spin wavefunctions are symmetric. Therefore, since the total angular momentum F is conserved because of rotational invariance, it then defines a collisional channel associated to a specific scattering length a_F. By introducing projection operators on the F-subspace:

$$\hat{P}_F = \sum_{M=-F}^{F} |F, M\rangle\langle F, M|, \tag{1.92}$$

with M the total projection along the quantization axis, we can extend the interaction potential (1.86) to the case of two F-spin atoms:

$$U(r) = \sum_{F\,\in\,\text{even}} g_F \hat{P}_F\, \delta(\mathbf{r}) \frac{\partial}{\partial r}(r\cdot). \tag{1.93}$$

In the specific case of ^{173}Yb, the ground state ($^1S_0$) has zero electronic angular momentum $J = 0$ and nuclear spin $I = 5/2 = F_1 = F_2$, and therefore the possible scattering channels are $F = 0, 2, 4$, corresponding to a_0, a_2, a_4 scattering lengths. In this case, to make explicit the different types of interaction processes [71] and their relation with the scattering lengths explicit, we can recast the potential (1.93) in the form:

$$U(r) = c_0(\hat{\mathbb{1}}_1 \otimes \hat{\mathbb{1}}_2) + c_1 \hat{\mathbf{F}}_1 \cdot \hat{\mathbf{F}}_2 + c_2 \hat{P}_0, \tag{1.94}$$

where c_0 takes into account the spin-independent interaction, $\mathbb{1}_i$ is the identity operator acting on the atom $i = 1, 2$, c_1 denotes the spin-spin coupling and c_2 addresses the interaction between the spin-singlets of the type:

$$|0, 0\rangle = \sum_{\alpha=-5/2}^{+5/2} \frac{1}{\sqrt{6}} (-1)^{\alpha+1/2} |\alpha, -\alpha\rangle. \tag{1.95}$$

By comparing Eqs. (1.93) and (1.94), we can find the strength of the three processes as a

function of the scattering lengths:

$$\begin{aligned} c_0 &= \frac{4\pi\hbar^2}{m}\left(\frac{5a_2+23a_4}{28}\right), \\ c_1 &= \frac{4\pi\hbar^2}{m}\left(\frac{a_4-a_2}{7}\right), \\ c_2 &= \frac{4\pi\hbar^2}{m}\left(\frac{7a_0-10a_2+3a_4}{7}\right). \end{aligned} \tag{1.96}$$

As explained in section 1.3, the scattering lengths are determined by the different configurations of the electronic shell of the two colliding atoms. The presence of a non-zero electronic angular momentum J in atomic ground state results in a non-negligible spin-spin coupling (see Eq. (1.94)) that affects the interactions. Indeed, in alkali atoms, as for example bosonic ^{87}Rb [72], [73] and fermionic ^{40}K [74], the hyperfine structure in the ground state leads to a spin-dependent interaction that drives spin-changing oscillations. Oppositely, in ^{173}Yb atoms, the $^1S_0$ ground state has no hyperfine mixing and the electronic wavefunction is the same regardless of the specific nuclear spin state. Therefore all the collisional channels have the same strength. Indeed it has been predicted theoretically [14] that the relative variation among different scattering lengths should be of the order of $\delta a_s/a_s \sim 10^{-9}$, where, for $^1S_0$, $a_s = 199.4\,a_0$ [75] with $a_0 = 0.53\,$Å being the Bohr radius. In the case of the metastable electronic state $^3P_0$, the decoupling between electronic and nuclear spin is broken by the admixture with $^3P_1$ and $^1P_1$ states (see also appendix A), which also causes the optical transition $^1S_0 \rightarrow {}^3P_0$ to have a finite linewidth ($\Gamma \sim 38.5$ mHz). Nevertheless, this admixture is quite small and the resulting nuclear-spin-dependent variation of the scattering lengths has been conservatively estimated [14] to be of the order of $\delta a_s/a_s \sim 10^{-3}$. However, the different electronic configuration of atoms in the $^3P_0$ state with respect to the ground state $^1S_0$ leads to interesting collisional physics, which will be treated in depth in chapter 5.

Differently from alkali, setting all equal scattering lengths reduces c_1 and c_2 to be identically zero and leaves in place only the spin-independent interaction, which leads to the $SU(6)$ symmetry of the total Hamiltonian of the system:

$$\begin{aligned} \hat{H} &= \sum_m \int \hat{\Psi}^\dagger_m(\mathbf{r})\left(-\frac{\hbar^2}{2\mathrm{m}}\nabla^2 + V_{ext}(\mathbf{r})\right)\hat{\Psi}_m(\mathbf{r})d\mathbf{r} \\ &+ g\sum_{m<m'}\int \hat{\Psi}^\dagger_m(\mathbf{r})\hat{\Psi}^\dagger_{m'}(\mathbf{r})\hat{\Psi}_{m'}(\mathbf{r})\hat{\Psi}_m(\mathbf{r})d\mathbf{r}, \end{aligned} \tag{1.97}$$

where $\hat{\Psi}_\alpha(\mathbf{r})$ is the second-quantized annihilation field operator of a particle with spin

component α. More specifically, Hamiltonian (1.97) is invariant under the transformations:

$$\hat{S}_n^m = \int \hat{\Psi}_n^\dagger(\mathbf{r})\hat{\Psi}_m(\mathbf{r})\, d\mathbf{r}, \tag{1.98}$$

which substitutes all particle of spin m with one of spin n. The special case $\hat{S}_m^m = \hat{N}_m$ is the number operator of particles with spin m. These operators are the generators of $SU(6)$ and then satisfy the algebra relations:

$$[\hat{S}_n^m, \hat{S}_p^q] = \delta_{mq}\hat{S}_n^p - \delta_{pn}\hat{S}_q^m. \tag{1.99}$$

On the experimental point of view, a remarkable consequence of the absence of spin-changing collisions is that all the spin mixtures are stable. Therefore, by suitable optical pumping techniques explained in section 2.4, we can reliably initialize our spin distribution in order to realize experimentally $SU(N)$-symmetric Hamiltonians with $2 \leq N \leq 6$. Indeed, it shall be noted that $SU(N)$ is *not* a representation of order N of $SU(2)$, but it is actually a higher symmetry group containing all $SU(M)$ groups with $M < N$. This high degree of tunability with respect to the spin degree of freedom allowed us to investigate the physics of one-dimensional systems as a function of the number of spin components N, realizing experimentally a strongly interacting $SU(N)$-symmetric liquid of fermions. A summary of the many-body theory of fermions in one dimension will be given in chapter 3, starting from the ideal case and introducing interactions in the context of the Luttinger liquid model.

Chapter 2

Experimental setup and procedures

This chapter illustrates the experimental apparatus and the procedures adopted to trap and cool atomic Ytterbium down to quantum degeneracy, to optically manipulate nuclear spin components and to tune the dimensionality of the system by means of optical lattices.

In section 2.1 the vacuum apparatus is outlined in its essential features, with a focus on the setup peculiarities such as the in-vacuum resonator for optical trapping and the high-optical-access glass cell. In section 2.2, the laser systems developed to optically manipulate and address atomic Ytterbium will be briefly described, with reference to their role in the experimental procedure. Section 2.3 is devoted to the detailed description of the overall experimental procedure, which is articulated in six different stages:

- **Zeeman Slower**: an Ytterbium atomic beam coming from an oven is slowed down by radiation pressure of a counter-propagating laser beam on the ${}^1S_0 \rightarrow {}^1P_1$ cycling transition.
- **Magneto-optical trap**: Once the atoms are slowed down, they are trapped in a Magneto-optical trap performed on the narrow intercombination ${}^1S_0 \rightarrow {}^3P_1$ transition.
- **Resonator stage**: The atoms are transferred with efficiency $\eta \sim 80\%$ in a optical dipole trap (ODT) constituted by a standing wave in a in-vacuum optical cavity, where a pre-evaporation is performed.
- **Optical transport**: After pre-evaporation, the atoms are transferred with efficiency $\eta \sim 30\%$ in a tightly-focused beam and they are optically transported into a high-optical-access glass cell with an efficiency of $\eta \sim 66\%$.

- **Crossed dipole trap**: Once in the glass cell, the final optical evaporation is executed in a crossed ODT configuration to achieve quantum degeneracy of both ^{174}Yb and ^{173}Yb isotopes.
- **Optical lattices**: After optical evaporation, the atoms are confined in optical lattice beams along three orthogonal directions. The lattice setup is characterized by studying the visibility decay of the Mott insulator state [7, 76–78].

Finally, in section 2.4, we outline the nuclear spin detection and manipulation techniques used to initialize the atomic spin distribution.

2.1 Vacuum system

The vacuum apparatus is shown in Fig. 2.2. Since Ytterbium is a metal with high melting point (824 °C), it is impossible to use vapor pressure at room temperature to obtain a sufficient flow of atoms to trap. To overcome this difficulty, a 7 g sample of 99.9% pure Ytterbium chunks in natural isotopes composition is heated up in a oven (**1**) at a mean temperature of 500°C[1]. The atomic beam is channeled in a square array of 100 small tubes, 1 cm long and with internal diameter of 0.2 mm. The micro-tubes array is placed right at the exit of the oven (Fig. 2.1) to collimate the atomic beam and to implement a first differential pumping stage performed by the first of the two ion pumps 20 l/s Varian Starcell (**3**) placed after the oven. The temperature of the back of the oven is $T = 475$ °C while the front is heated up at $T = 535$ °C in order to prevent Yb to occlude the micro-tubes. The mean temperature of 500 °C generates an atomic beam with velocity distribution $f(v_z) = m^2 v_z^3/2(k_B T)^2 \exp\left(-m v_z^2/2k_B T\right)$ [79] with most probable velocity $v_{mp} = \sqrt{3k_B T/m} = 332$ m/s.

After the crosses used to monitor the fluorescence of the atomic beam, there is a compressed-air shutter (**4**) to block the atomic beam. Before and after the shutter there are two small tubes (**6**) with lengths 8 and 10 cm, respectively, and with internal diameter 5 mm. Because of their poor conductivity, these tubes define two sequential differential pumping stages: one implemented by the second 20 l/s ion pump (**3**) between the oven and the shutter region, and one between the shutter region and the UHV part of the experiment implemented by the 55 l/s Varian Starcell (**14**). The UHV part of the apparatus, where the experiment takes place, is separated from the rest of the setup by an all-metal VAT-48124 UHV gate valve (**7**). Other three UHV-valves (**2**), (**5**), (**15**) are present in the

[1] The vapor pressure is determined by the relation:

$$\log_{10}(P[\text{Pa}]) = 14.117 - 8111/(T[\text{K}]) - 1.0849 \log_{10}(T[\text{K}]). \tag{2.1}$$

At 500 °C the vapor pressure is about 10^{-2} Torr.

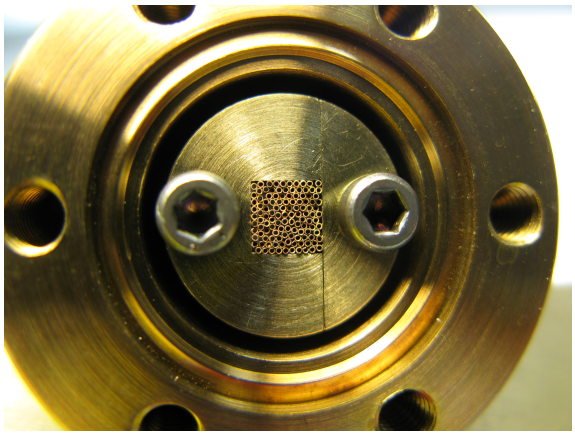

Figure 2.1: Square array of micro-tubes at the front of the oven.

apparatus to allow pre-evacuation with a Turbo pump VARIAN TV-70. After crossing the VAT valve, the atoms travel along the Zeeman Slower (**8**) where they are slowed down from thermal velocity ($\sim$ 300 m/s) to a few tens of m/s (see section 2.3.1) in order to be captured in a magneto-optical trap (MOT, see section 2.3.2). The compensation coil (**10**) balances out the residual magnetic field of the Zeeman slower in the MOT chamber.

The MOT is implemented with two anti-Helmoltz coils (**12**) (for details see Ref. [80]) mounted on a AISI L316 stainless steel octagonal chamber (**9**). On the horizontal plane, the chamber features seven CF40 flanges: one is used to attach the MOT chamber to the Zeeman slower; the four flanges at 45° degrees with respect to the atomic beam axis are used for the horizontal MOT beams; the two flanges orthogonal to the atomic beam axis are used respectively as input window for the optical transport beam and to connect to the glass cell (**11**). All glass windows have broadband AR coating from 400 to 1100 nm. Lastly there is a CF63 flange on the atomic beam axis towards the cross connecting to the 55 l/s Varian Starcell ion pump (**14**). We chose a larger flange diameter in order to maximize the conductance of the connection to the ion pump, which enables pressures of the order of 10^{-11} Torr in the UHV part of the experiment. The pump is connected to the cross using an elbow to minimize spurious magnetic fields and to maximize the access on the main part of the apparatus. Moreover, the MOT chamber has two CF100 flanges on the vertical direction, both with a CF40 window in the center. The upper CF100 flange has two metallic supports to implement an in-vacuum optical cavity (see section 2.1.1) along the axis of two of the four CF16 windows in the horizontal plane of the MOT chamber (see Fig. 2.16).

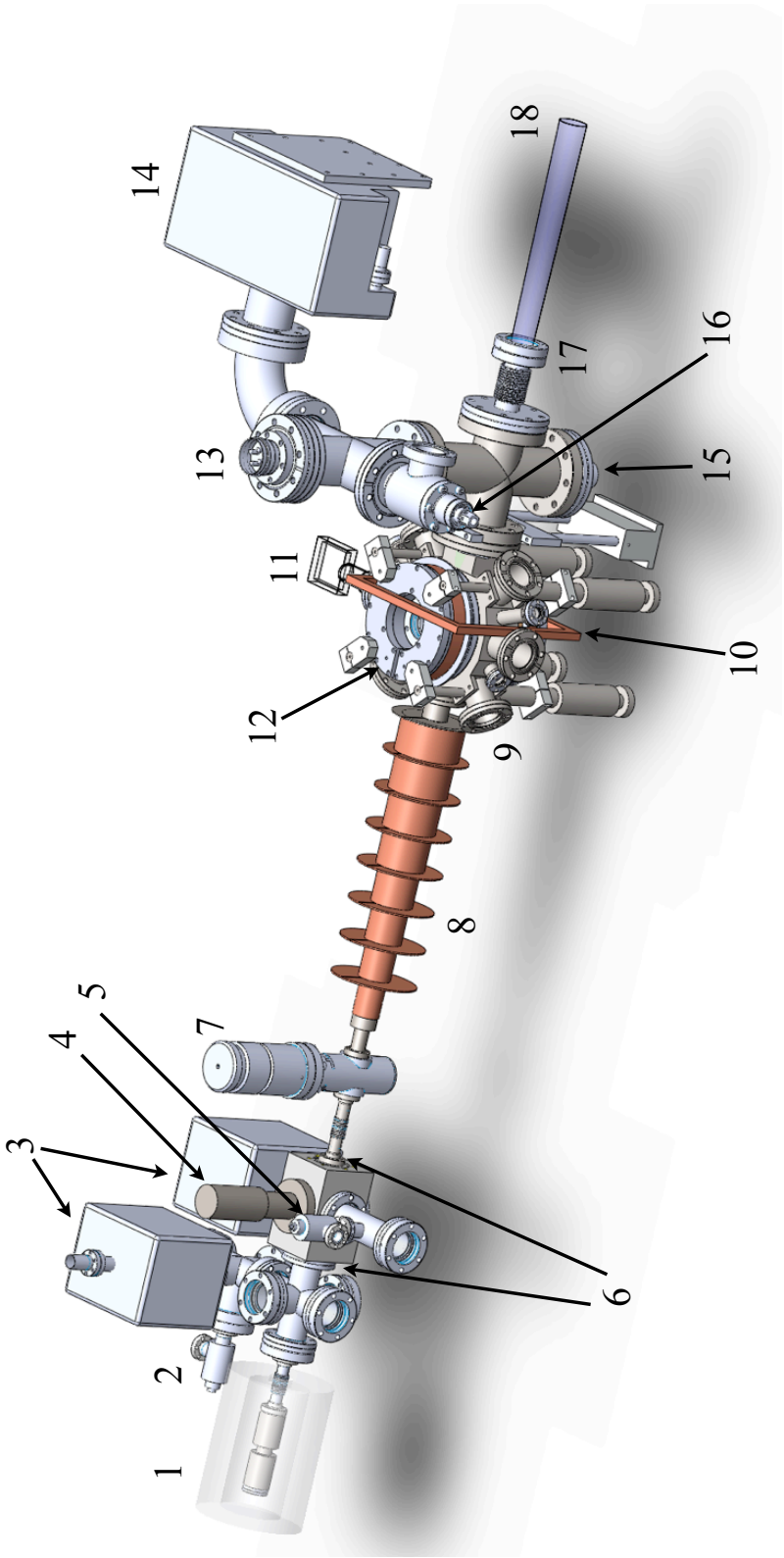

Figure 2.2: 1) Oven. 2) UHV valve. 3) Ion pumps for differential pumping (20 l/s each). 4) Compressed air shutter for atomic beam. 5) UHV valve. 6) Differential pumping tubes (not shown). 7) VAT UHV gate-valve. 8) Zeeman Slower. 9) MOT chamber. 10) Compensation coil. 11) Glass cell. 12) MOT coils. 13) Titanium sublimation pump (TSP). 14) Ion pump for MOT chamber (55 l/s). 15) UHV Gauge, mod. Bayard-Alpert, Varian UHV-24p. 16) UHV Valve. 17) Sapphire window with bellow. 18) Slowing beam at 399 nm.

In order to have a better control on the vacuum, we mounted a titanium sublimation pump (TSP) (**13**) on top of the cross after the MOT chamber. At the bottom of the same cross, there is a Ion Gauge UHV-24P Bayard-Alpert (**15**) to measure the pressure. A bellow separates the MOT chamber and the input window (**17**) of the Zeeman slower beam (**18**). This window is made of sapphire and it is kept at a temperature of about 250 °C to avoid atoms to stick on it and reduce its transmissivity. The bellow compensates for the temperature gradient between the MOT chamber and the sapphire window which is also AR coated for 399 nm to avoid etalon effects.

2.1.1 In-vacuum resonator

One of the peculiarities of this experimental apparatus is the presence of an in-vacuum optical cavity in the MOT chamber [81] to trap and pre-cool the atoms before their optical transport in the glass cell (see section 2.1.2). The Fabry-Perot cavity is made up of two metallic supports screwed down in the CF100 upper flange of the MOT (see Fig. 2.3). The supports hold two spherical mirrors with a radius of curvature $r_c = 2$ m, diameter $d = 6.35$ mm and thickness 2.3 mm. The outer side of the mirrors is AR coated while the inner side has a $R = 99.8\%$ coating, which results in a theoretical finesse of $\mathcal{F} \simeq 1600$. The cavity length is $L = 9$ cm, leading to a free spectral range FSR=1.67 GHz. The cavity

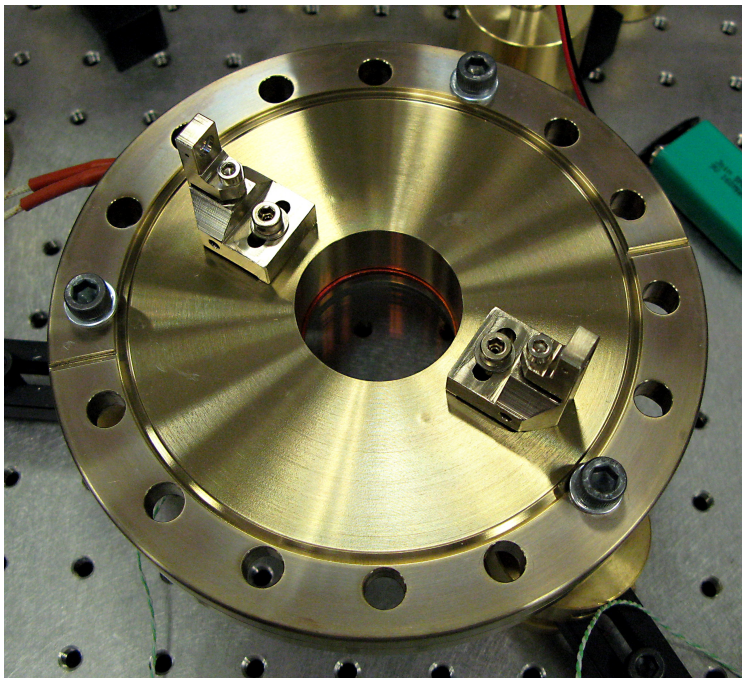

Figure 2.3: In-vacuum resonator mounted on the CF100 flange.

has been pre-aligned before evacuating the setup with the help of the screws present on the metallic supports acting on the vertical degree of freedom and by screwing down the supports themselves with the right tilt for the horizontal alignment (see Fig. 2.3). The CF100 flange features two holes to heat the cavity up in case atomic Ytterbium sticks to the mirrors, which have been used also to test the sensitivity of the cavity alignment to the temperature changes induced by the baking procedure. Once in the vacuum, the cavity got misaligned because of the mechanical stress of the screws holding the CF100 flange to the MOT chamber. Therefore an additional re-alignment has been necessary after the flange had been attached to the MOT chamber.

The cavity geometry has been designed to have the largest possible mode volume in order to match the MOT size, compatibly with the trap depth generated by the intra-cavity power P_{cav}, which has to be higher than the MOT temperature. The geometry described above results in a $w_0 = 300$ μm waist which, along with a measured finesse of $\mathcal{F} \simeq 1850$, leads to a trap depth of $V_0/k_B \simeq 800$ μK $\simeq 8\,T_{MOT}$ with an incident power of $P_{\mathrm{in}} = 1.8$ W. Given the measured cavity finesse, the enhancement factor of the cavity (neglecting the losses) is approximately $4\mathcal{F}/\pi \sim 2350$.

2.1.2 The glass cell

Another crucial feature of this experimental apparatus is the possibility to transport the atoms from the MOT chamber to a high optical access glass cell. In cold atoms experiments, it is becoming more and more common to perform the MOT in a separated vacuum chamber where the atoms are captured and pre-cooled and then optically or magnetically transported in a separated science cell [82, 83]. The possibility to get rid of the constraints imposed by the magneto-optical trap optical setup guarantees high optical access, which is necessary to optical manipulation and high-resolution addressing of the quantum degenerate sample. Another advantage is the possibility to avoid spurious magnetic fields caused by the residual magnetization of the rest of the vacuum apparatus and by the eddy currents induced by metallic vacuum gaskets. Our glass cell is manufactured by HELMA ANALYTICS. Its external faces form a $(60 \times 60 \times 18)$ mm parallelepiped (see Fig. 2.4). Each face is 5 mm thick leading to internal dimensions of $(50 \times 50 \times 8)$ mm. The reduced thickness in the vertical direction (9 mm between the center and the outer face) is thought to have the possibility in the future to implement a high-numerical-aperture objective with a small working distance. The glass cell features a glass-metal junction which leads to a CF40 flange that is attached to the MOT chamber. The geometric centers of the glass cell and of the MOT chamber are separated by 26 cm along which the atoms are optically transported (see section 2.3.4).

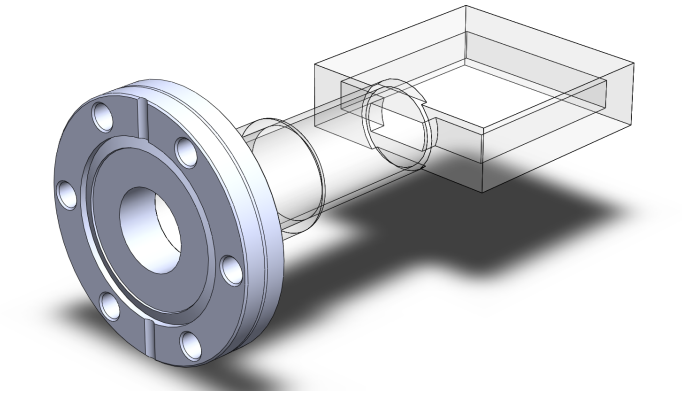

Figure 2.4: 3D model of the glass cell.

2.2 Laser setup

All the lowest atomic transitions of Ytterbium are in the visible range (578 nm, 556 nm, 399 nm). Since high-power, narrow-linewidth lasers in this wavelength range are generally not available on the market, a convenient way to produce such radiations is to use second harmonic generation (SHG) starting from commercial infrared high-power lasers. The scheme we adopted in our lab is to use bow-tie cavities to enhance the efficiency of the frequency-doubling process. In this section, we first outline the laser system built and used during this PhD work to address resonantly atomic Ytterbium transitions at 399 and 556 nm. Then we describe the setup to implement far-off resonant dipole traps with laser light at 1064 nm and optical lattices at 759 nm.

2.2.1 399 nm and 556 nm laser systems

Laser radiation at 399 nm locked on the $^1S_0 \rightarrow {}^1P_1$ Yb transition is used to slow down atoms in the Zeeman slower and to perform absorption imaging (see appendix A). A fiber-coupled tapered-amplifier laser-diode system TOPTICA TA PRO laser delivering 1.1 W at 798 nm is used to inject a Lithium-Triborate (LBO) non-linear crystal 15 mm long, cut for type-I phase matching and stabilized at a temperature of 55 °C (see Fig. 2.5). In order to enhance the 399 nm output power, the LBO is placed in a bow-tie cavity where the frequency-doubling takes place. The cavity consists in two plane mirrors M1 and M2 and two curved mirrors M3 and M4 with radii of curvature of $r_c = 60$ mm and $r_c = 100$ mm respectively. The cavity free spectral range, calculated taking into account the non-linear crystal index of refraction ($n = 1.55$) is FSR = 749 MHz and the finesse is $\mathcal{F} \sim 100$, measured by comparing the full-width-half-maximum (FWHM) of the transmission peak

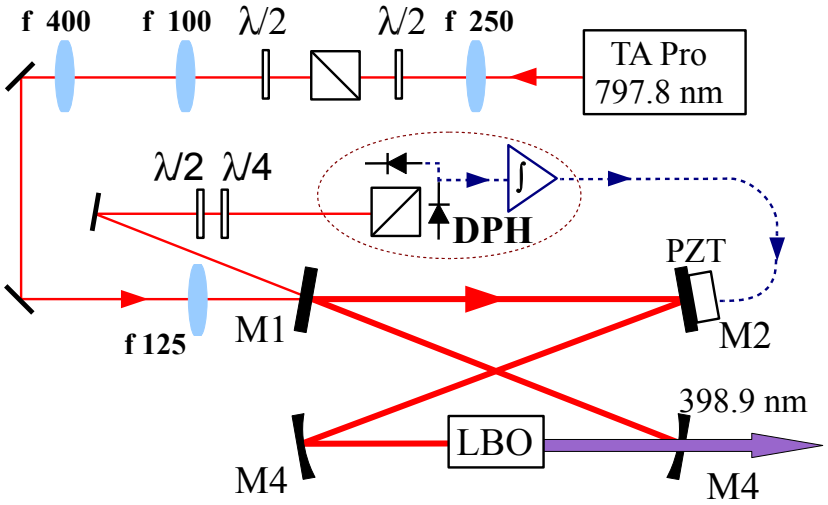

Figure 2.5: Laser setup for SHG from 798 to 399 nm. PZT:piezo controlling the cavity length. DPH: Differential photodiode to generate a Haensch-Couillaud signal. Input coupler (M1) reflectivity $r_1 = 99\%$ at 798 nm. All mirrors (M1, M2, M3) have 99.9% reflectivity at 798 nm. The beam waist inside the crystal is $w_0 = 30$ μm.

with the FSR. The bow-tie cavity has the remarkable advantage to build an inside running wave, instead of the stationary wave built in a standard Fabry-Perot cavity, which could cause spatial hole burning problems. In order to maximize the output power, the input coupler's reflectivity r_1 is tuned in order to match the losses induced by the non-linear crystal, having a transmittivity $t = 1 - \eta$ (where η is the power conversion efficiency), and the losses of the other cavity mirrors[2] taken into account by the reflectivity coefficient r_2.

In order to deliver a stable laser output, the cavity length is tuned with a piezo (PZT) so that the resonance frequency of one longitudinal cavity-mode matches the laser frequency. Since the non-linear crystal is strongly birefringent, as only one polarization induces the SHG, the Haensch-Coulliaud scheme [85] is the most suitable method to lock the cavity to the laser avoiding additional frequency modulations. Indeed this technique is based on a heterodyne detection of the two orthogonal polarizations, which experience a different optical path because of the crystal's birefringence and give rise to a dispersive signal as a function of the length of the cavity. By using this signal as a feedback for the piezo, the

[2]Indeed, when the incoming light is in resonance with the cavity, the reflected power [84] is

$$P_r = \frac{\sqrt{r_1} - \sqrt{r_m}}{(1 - \sqrt{r_1 r_m})^2} P_i \tag{2.2}$$

where $r_m = r_2 t$ and the so-called impedance matching condition is $r_m = r_1$.

cavity is successfully locked to the laser, resulting in a stable output of 550 mW of 399 nm radiation out of 1 W of 798 nm pumping light.

The same techniques described above are used also for the production of laser radiation on the $^1S_0 \rightarrow {}^3P_1$ transition at 556 nm, which is used for magneto-optical trapping beams (section 2.3.2), optical Stern-Gerlach and optical pumping beams (section 2.4) and for Raman beams (section 6.2). In this case a fiber laser at 1112 nm (Menlo Systems mod.

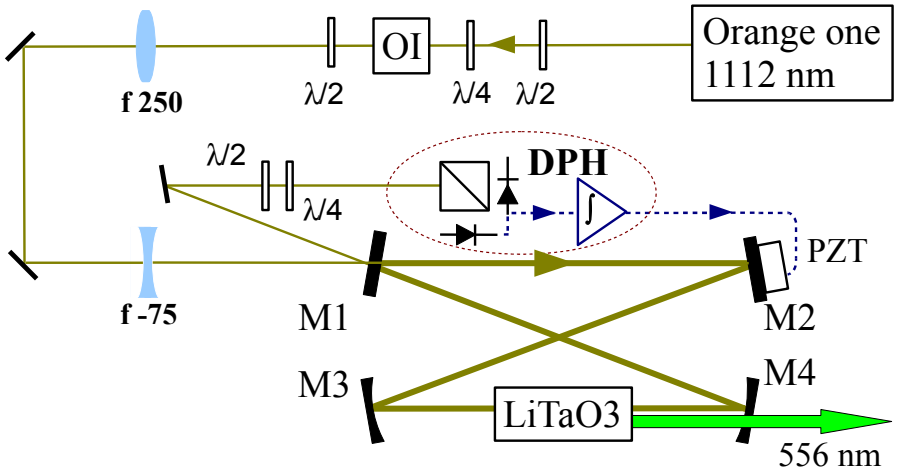

Figure 2.6: Laser setup for SHG from 1112 to 556 nm. OI: Optical isolator. PZT: piezo controlling the cavity length. DPH: Differential photodiode to generate a Haensch-Couillaud signal. Input coupler (M1) reflectivity $r_1 = 95\%$ at 1112 nm. All other mirrors (M1, M2, M3) have 99.9% reflectivity at 1112 nm. Output coupler reflectivity $r_4 = 99.9\%$ for 1112 nm and $r_4 < 1\%$ for 556 nm. The curvature radius of both spherical mirrors is $r_c = 100$ mm. The beam waist inside the crystal is $w_0 = 13$ μm.

ORANGE ONE) injects a 10 mm long Lithium Tantalate ($LiTaO_3$) non-linear crystal placed inside a bow-tie cavity. The crystal is periodically poled with a period of 9.12 μm to ensure quasi phase-matching and is AR-coated for 1112 nm light. The cavity free spectral range is FSR = 567 MHz and the measured finesse is $\mathcal{F} = 67$. When locked using Haensch-Coulliaud method, the cavity produces 1.050 W of 556 nm light out of 2 W of 1112 nm pumping light. Both cavities have been placed in an aluminum box under vacuum in order to increase thermal and acoustic isolation and achieve a better lock stability (Fig. 2.7).

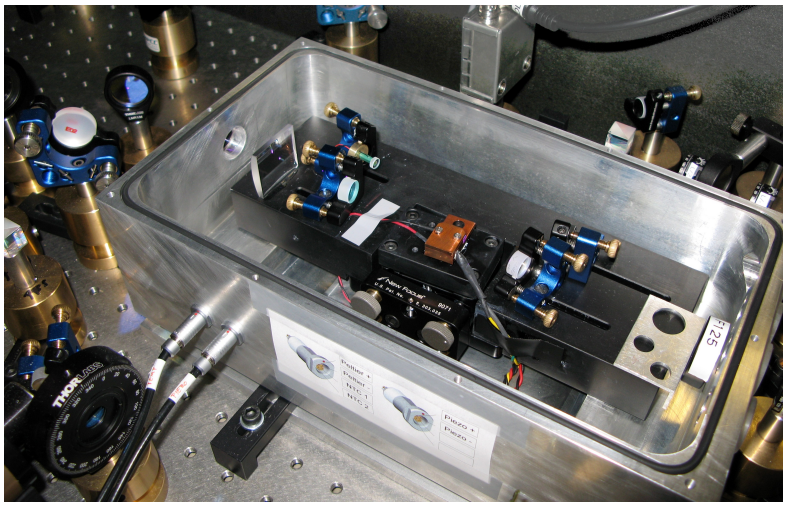

Figure 2.7: Picture of bow-tie cavity for SHG of 399 nm radiation. A vacuum aluminum box has been built to achieve better isolation from thermal noise and acoustic vibrations.

2.2.2 Locking scheme on the intercombination transition

The control of the laser frequency is a crucial ingredient to trap and cool down atomic gases. In order to lock the laser frequency on atomic transitions $^1S_0 \rightarrow {}^1P_1$ and $^1S_0 \rightarrow {}^3P_1$ at 399 nm and 556 nm respectively, we use standard fluorescence spectroscopy techniques and electronic feedback on the lasers. For both spectroscopy setups, we use an atomic beam generated in an additional oven with the same characteristics as the one in the main setup (Fig. 2.2) at average temperature $T = 500$ °C. After the oven there are two crosses used to interrogate the atomic beam with transverse spectroscopy and to detect the atomic fluorescence.

In the case of the spectroscopy on the $^1S_0 \rightarrow {}^1P_1$ at 399 nm there is no need to perform a Doppler-free saturation spectroscopy since the linewidth is $\Gamma = 2\pi \times 29.8$ MHz and the transverse Doppler profile of the collimated atomic beam is of the order of a few MHz. On the other hand, in order to lock the 556 nm laser on the narrow-linewidth $^1S_0 \rightarrow {}^3P_1$ intercombination transition ($\Gamma = 2\pi \times 182$ kHz), it is necessary to perform a Doppler-free saturation spectroscopy. For further details on both spectroscopy setups and on the locking procedures we refer to Ref. [80].

Here we will focus on the new setup for the $^1S_0 \rightarrow {}^3P_1$ saturation spectroscopy on the fermionic ^{173}Yb isotope using the Doppler-free signal coming from the bosonic ^{174}Yb and most abundant isotope. Indeed in the case of ^{174}Yb, the signal-to-noise ratio (SNR) allows a stable lock because bosonic isotopes have no nuclear spin and this results in a

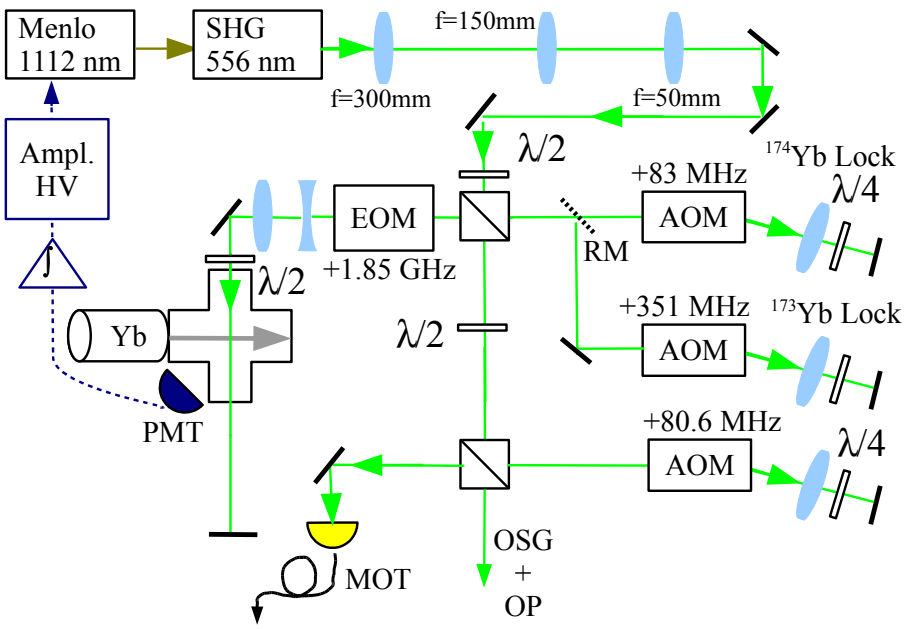

Figure 2.8: 556 nm optical setup for the production of MOT beams and locking on $^1S_0 \rightarrow {}^3P_1$ transition. RM is a removable mirror used to switch between the ^{173}Yb and the ^{174}Yb locking scheme. Fluorescence signal is detected using a photomultiplier (PMT) and is used to drive the laser piezo. A high voltage amplificatore HV is used to increase the dynamical range of frequency corrections.

$J = 0 \rightarrow \ J' = 1$ optical transition in which π-polarized light selects only the magnetic field insensitive $|J = \ 0, m_J = 0\rangle \rightarrow |J' = 1, m'_J = 0\rangle$ transition. In this case, the laser in the spectroscopy branch is detuned by +166 MHz using the acousto-optical modulator (AOM) in double passage, resulting in an effective laser detuning of -166 MHz with respect to the ^{174}Yb atomic resonance (see Fig. 2.8). In the case of the $F = 5/2 \rightarrow F' = 7/2$ transition of ^{173}Yb, atomic fluorescence has a worse SNR because, beyond a smaller natural abundance than ^{174}Yb, the $I = 5/2$ nuclear spin gives rise to six $m_g \rightarrow m_e$ π-transitions, which reduces the signal of a factor six. Moreover all six Doppler-free signals correspond to transitions to excited state sublevels which are sensitive to magnetic field fluctuations. In order to overcome these difficulties, an alternative optical setup has been designed to lock the laser on the ^{174}Yb isotope signal also in case of operation with fermionic ^{173}Yb. In this scheme (see Fig. 2.9), the laser in the spectroscopy branch is detuned by +702 MHz using a double passage AOM and then it passes through a Qubig electro-optical modulator (EOM) EO-T1850M3-VIS resonant at 1.85 GHz. In this way, there is a detuning $\Delta_1 = 702 + 1850$ MHz $= 2552$ MHz between the blue sideband of the EOM-modulated spectroscopy beam and the laser. Since the isotope shift between the

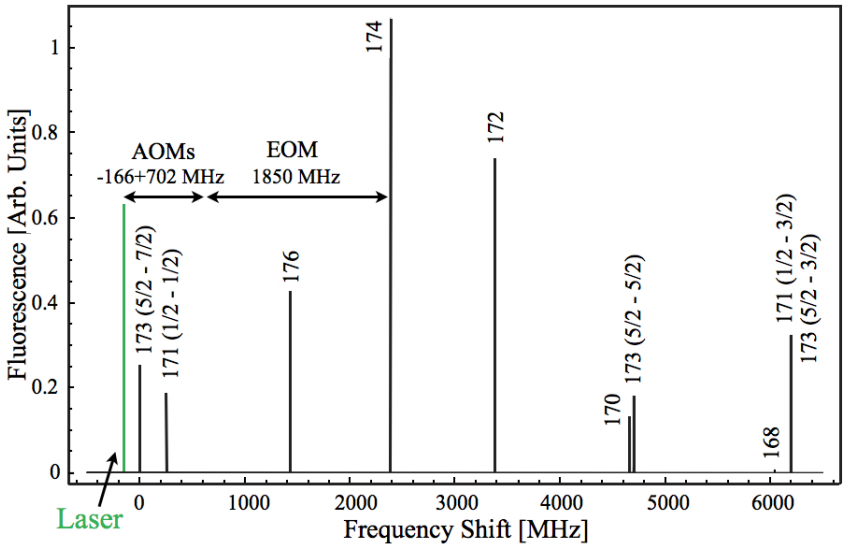

Figure 2.9: Isotope shifts of the intercombination transition ${}^1S_0 \rightarrow {}^3P_1$ [86]. In green is indicated the laser frequency in the locking scheme on the ^{173}Yb isotope with AOM and EOM frequency shifts used to cover the isotope shift $\Delta_{174-173} = 2386$ MHz and to lock on the boson ^{174}Yb.

$F = 5/2 \rightarrow F' = 7/2$ transition of ^{173}Yb and ^{174}Yb is $\Delta_{174-173} = 2386$ MHz, when the spectroscopy beam is resonant with the ^{174}Yb boson, the effective detuning between the laser and ^{173}Yb resonance is $\Delta_1 - \Delta_{174-173} = -166$ MHz, as in the case of the locking scheme on the ^{174}Yb. In this way it is possible to use the same AOMs in the other branches (MOT,OSG,OP) for operation with both ^{174}Yb and ^{173}Yb[3].

It shall be noted that to lock on the ^{174}Yb isotope, we use a power of $P = 600$ μW, whereas we use a higher power with the fermion ($P = 1.2$ mW), since the EOM blue sideband, resonant with the atoms, accounts roughly to only one third of the total spectroscopy beam power. Another significant difference between the two configurations is that the lock-in frequency modulation is executed by the AOM in the case of ^{174}Yb and by EOM in the case of ^{173}Yb, where the +351 MHz AOM is used to stabilize the spectroscopy beam power.

[3]The procedure to switch between the two schemes takes a few minutes because it is just a matter of removing the mirror, change the Lock-in demodulating the fluorescence signal and adjusting the PID gain.

2.2.3 1064 nm Laser system

Laser radiation at 1064 nm is used to trap the atoms in the resonator-enhanced optical dipole trap (section 2.3.3) and to perform optical transport from the MOT chamber to the glass cell (section 2.3.4). For this wavelength the Nd:Yag MEPHISTO MOPA 25 (Innolight/Coherent) laser with linewidth below 100 kHz and maximum output power of 25 W, is used. The frequency of the laser is adjustable using piezo for fast corrections (about 100 kHz bandwidth) and using the laser seed temperature for slow (1 Hz bandwidth) and large range (3 GHz/°C) corrections. In Fig. 2.10a, we show the 1064 nm setup, where two optical paths are used to inject the fibers conveying the laser radiation used for the resonator and the optical transport setup.

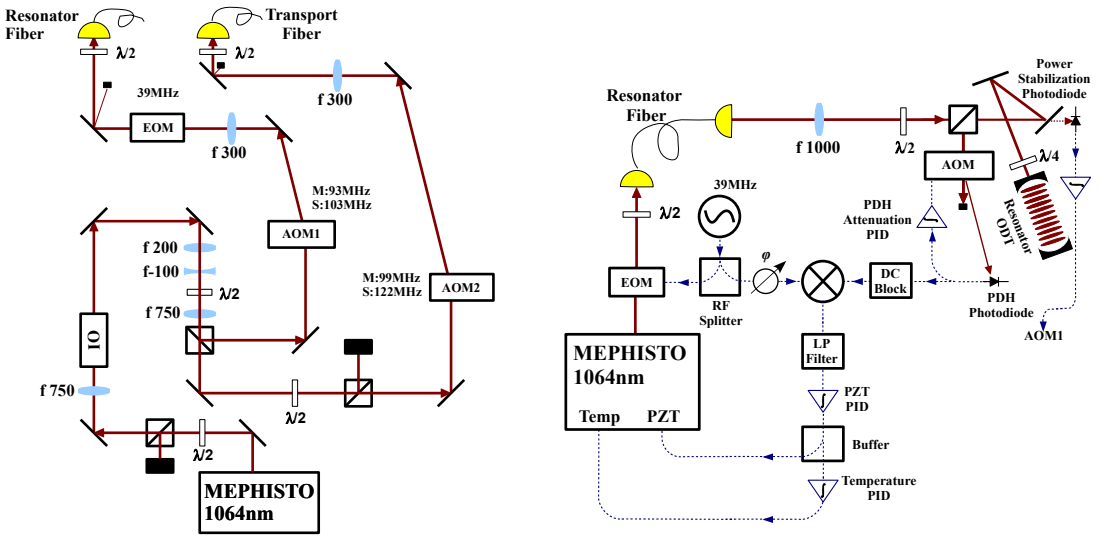

(a) Optical Setup **(b)** PDH lock setup

Figure 2.10: a) Optical setup for the 1064 Mephisto laser. **b)** PDH lock scheme to the resonator. See text for details.

Since high optical powers are involved, in this setup AOMs are driven using a double-frequency driver [87]. Indeed, due to thermal effects inside the AOM crystal, the angular position of the beam can change when the radio-frequency power in the AOM is varied to control the first-order diffracted beam intensity and this misalignment could damage the fibers. To prevent this, in addition to the master radio-frequency f_M driving the AOM, a different slave radio-frequency f_S is used to stabilize the total RF power sent to the crystal. The feedback loop is built using an Analog Devices power detector (AD8361) detecting the total RF power $P_{f_M} + P_{f_S}$ and changing accordingly P_{f_S} by means of a

Voltage control attenuator (VCA). Since f_S deflects the beam at a slightly different angle, after a sufficiently long path, it is possible to block it using a beam damper, to avoid damages to the fibers.

The optical path dedicated to the resonator optical dipole trap has a Qubig EOM driven at 39 MHz used to perform a Pound-Drever-Hall (PDH) [88] lock to the resonator inside the vacuum system (see Fig. 2.10b). The dispersive error signal is processed by a PID acting on the piezo controlling the seed laser of the MEPHISTO. The piezo PID integral gain is limited in DC by a resistance, as the slow frequency corrections are made acting on the temperature through a slow PID with a <3 Hz bandwidth (±200 mV limited output voltage). The input signal of the temperature PID is the output of the piezo PID (which is split with a buffer circuit made of a voltage follower and two op-amps) whose slow variation over time is corrected by tuning the seed temperature. With this locking scheme, the laser stays locked to the in-vacuum resonator all day long. In order to enhance the power range where the laser can stay locked to the resonator, we actively stabilize the power impinging on the PDH photodiode with an additional AOM (see Fig. 2.10b). More specifically, we use the AC part of the error signal for the PDH feedback loop and the DC signal of the PDH photodiode is used to lock the power of the PDH beam itself. In this way we avoid damage to the photodiode at high power and obtain an error signal independent on the in-cavity power. With this scheme we can lock the laser on a broad power range spanning four orders of magnitudes (100 μW, 2 W).

2.2.4 759 nm Laser system

Laser radiation at 759 nm is used to produce three-dimensional optical lattices on the atoms and to perform Bragg spectroscopy on the sample. This specific wavelength (often referred to as "magical"), has been chosen because it induces the same light shift on the ground state $^1S_0$ and on the metastable excited state $^3P_0$ (for details see section 5.1). In order to produce laser radiation at this wavelength, we use a standard setup with a Coherent VERDI 18 laser emitting in single mode at 532 nm which acts as a pump for a Titanium-Sapphire laser (Coherent MBR 110). With this setup we can get routinely 3.5 W of 759 nm light, which is split in three different optical paths each featuring an AOM and an optical fiber to implement the optical lattices along three orthogonal directions. A small portion of the laser light is used to inject a Fabry-Perot cavity to monitor single-mode emission of the MBR.

2.3 Overview of the experimental procedure

2.3.1 Zeeman Slower ($^1S_0 \rightarrow {}^1P_1$)

In order to slow down the atoms coming from the oven and trap them in the magneto-optical trap (MOT), we use the radiation pressure of a laser beam counter-propagating with respect to the atomic beam and resonating with the transition $^1S_0 \rightarrow {}^1P_1$ at 399 nm. Indeed this transition is more suited for this purpose because it has a broader linewidth ($\Gamma_{399} = 2\pi \times$ 28.9 MHz) than the $^1S_0 \rightarrow {}^3P_1$ at 556 nm and therefore the maximum deceleration $a_{max} = \hbar k_L \Gamma / 2m$ it can transmit to the atoms is much larger[4]. As explained in the next section, the intercombination transition at 556 nm is used in order to trap and cool down the atoms in the MOT, as its narrow linewidth ($\Gamma_{556} = 2\pi \times$ 182 kHz) allows a much lower Doppler temperature ($k_B T_D = \hbar\Gamma/2$).

The inhomogeneous Zeeman slower magnetic field $B_{ZS}(z)$ makes the atoms always resonate with the counter-propagating laser beam along the entire path from the oven to the MOT chamber, even if their velocity $v_z(z)$ along the propagation axis z is diminishing, so that the effective detuning from resonance is null in every point in space [90]. Indeed, a laser beam resonating with an atomic transition of linewidth Γ, with wavevector $k_L = 2\pi/\lambda_L$ and detuning δ_L (see Eq. 1.22), exerts the following force on the counter-propagating the atomic beam:

$$F_z(z) = -\frac{\hbar k_L \Gamma}{2} \frac{I/I_s}{1 + I/I_s + 4\left(\delta_L + k_L v_z(z) - \frac{g_{F'}\mu_B m_{F'} B_{ZS}(z)}{\hbar}\right)^2 / \Gamma^2}, \tag{2.3}$$

where $g_{F'}$ is the Landé factor of the excited state, $m_{F'}$ is the projection of the magnetic moment of atoms along the propagation axis and I_s is the saturation intensity. Hence the magnetic field profile $B_{ZS}(z)$ that gives an effective null detuning $\forall z$ is given by the equation:

$$\delta_L + k_L v_z(z) - \frac{g_{F'}\mu_B m_{F'} B_{ZS}(z)}{\hbar} = 0, \tag{2.4}$$

where the polarization of the light $\sigma^{\pm}$ determines the excitation of the Zeeman sublevel $m_{F'} = m_F \pm 1$. Since circular polarization is used, for the Zeeman slower to work is necessary to use an optically closed transition to avoid optical pumping in a dark nuclear spin level. For ^{173}Yb the only choice is the $F = 5/2 \rightarrow F' = 7/2$ transition and in particular we chose a σ^- slowing scheme [91], where the laser beam is red-detuned ($\delta_L/2\pi = -983$ MHz) in order to be resonant with the atoms coming out of the oven at $v_{mp} \sim 330$ m/s where there is zero magnetic field. Conversely, when the atoms are slowed down and the Zeeman

[4] For further details on the Zeeman Slower setup see Ref. [89] and [80].

Slower magnetic field is compensated by a dedicated coil (see Fig. 2.2) in the center of the MOT chamber, the beam is out of resonance and its impact on the atoms trapped in the MOT is minimized. However in our setup the radiation pressure on the fermionic atoms is not negligible since, for the atoms trapped in the MOT, the slowing beam is detuned only -162 MHz with respect to the $F = 5/2 \rightarrow F' = 5/2$ transition (see Fig. 2.11). On the one hand, this gives us the possibility to use the Zeeman slower light to perform a preliminary optical pumping stage inside the MOT chamber and to unbalance the spin population of the atoms towards the $m_F = -5/2$ state in order to produce a large spin-polarized Fermi gas with the techniques illustrated in section 2.4. On the other hand this additional radiation pressure has to be taken into account in the fermionic MOT optimization process, which will be outlined in the next section.

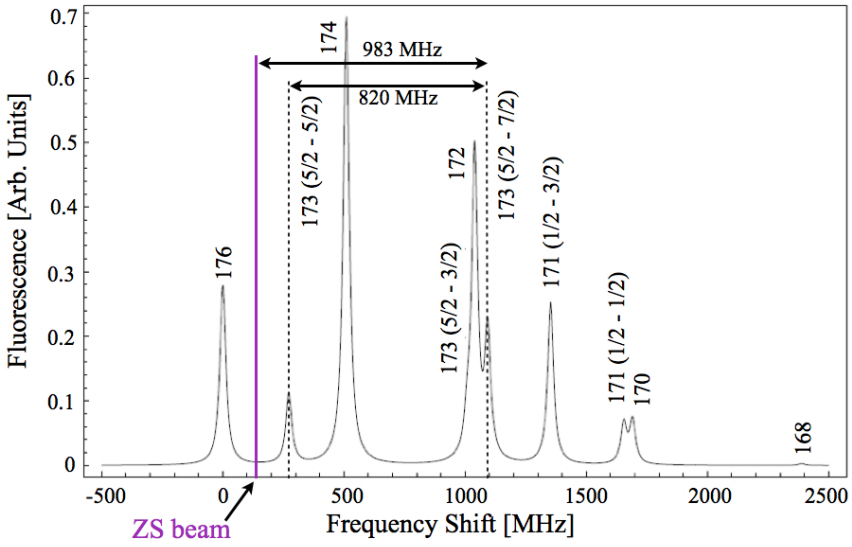

Figure 2.11: Isotope shifts of the dipole allowed transition ${}^1S_0 \rightarrow {}^1P_1$ [86]. In violet is indicated the frequency of the slowing beam with respect the $F = 5/2 \rightarrow F' = 7/2$ of ^{173}Yb. The light is red-detuned only 163 MHz $= 5.46\,\Gamma_{399}$ from the $F = 5/2 \rightarrow F' = 5/2$ transition.

2.3.2 Magneto-optical trap (${}^1S_0 \rightarrow {}^3P_1$)

The magneto-optical trap (MOT) is performed using green light at 556 nm, resonating with the intercombination transition ${}^1S_0 \rightarrow {}^3P_1$. In order to avoid optical pumping in dark states, the ^{173}Yb MOT is performed on the optically closed transition $F = 5/2 \rightarrow F' = 7/2$. The transition is quite narrow ($\Gamma_{556} = 2\pi \times 182$ kHz) and therefore its capture

velocity[5] has a maximum value of 10 m/s for our parameters, namely a beam waist $w_0 \simeq 1.3$ cm, a magnetic field gradient $b \sim 1.6$ Gauss/cm and a saturation parameter of $I/I_s = 80$ for each of the six beams ($P_{tot} = 180$ mW). Since the final velocity of the atoms after the Zeeman slower is about 20 m/s [80, 89], a MOT produced using this transition would be highly inefficient. To overcome this difficulty and reach a higher capture velocity, we perform a frequency modulation of the MOT beams, adding $N_{sb} = 18$ equally-spaced sidebands [93], red-detuned with respect to the atomic transition ("multi-frequency MOT" stage). In order to maximize the number of atoms in the MOT, an optimal sideband spacing $\Delta\omega \simeq \Gamma'$ has been chosen where $\Gamma' = \Gamma\sqrt{1 + I/(I_s N_{sb})} \simeq 2\pi \times 400$ kHz is the effective power-broadened linewidth in our system. In this way, the uniformly "filled" spectral region explored by the sidebands is maximized in order to capture as high as possible velocity classes. With this method, we can routinely trap $N_{at} = 7 \cdot 10^7$ ^{173}Yb atoms and $N_{at} = 1 \cdot 10^9$ ^{174}Yb atoms. Once the number of atoms is optimized in the

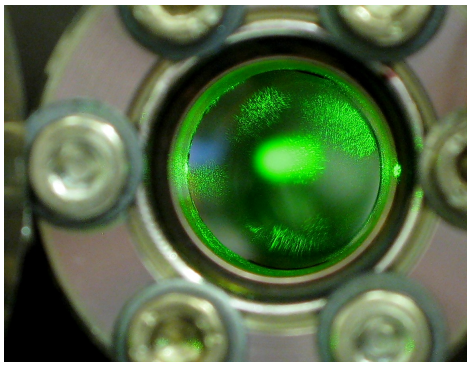

Figure 2.12: MOT of ^{174}Yb bosonic atoms.

multi-frequency MOT, the sidebands are switched off and the single frequency light is tuned in frequency and intensity to minimize the temperature on the basis of the Doppler cooling relation [94]:

$$T = \frac{\hbar\Gamma}{8k_B}\frac{\Gamma}{|\delta_L|}\left[1 + \frac{I_t}{I_s} + \left(\frac{2\delta_L}{\Gamma}\right)^2\right] \tag{2.5}$$

where I_t is the total MOT beam intensity. For the optimal parameters $\delta_L^* \simeq -8\,\Gamma$ and $P_{tot} = 7$ mW, we get $T = 30$ μK for the fermionic isotope and $T = 80$ μK for the bosonic isotope. These temperatures are significantly higher than the Doppler temperature ($T_D = 4.3\,\mu$K) since the MOT density is large enough to let collisional heating mechanisms

[5] The capture velocity is the maximum velocity class that is possible to trap using a MOT and it is defined as [92]:

$$v_c = \left(\frac{\hbar^2 k_L^2}{m\, g_{F'} M_{F'} \mu_B b}\right)\frac{\Gamma}{2}\frac{I/I_s}{1 + I/I_s},$$

where b is the MOT magnetic gradient, k_L is the laser beam wavevector and I_s the saturation intensity.

[95, 96] prevent the Doppler limit to be reached. In any case these temperatures are low enough to yield an efficient transfer inside the resonator optical dipole trap (see section 2.3.3).

It should be noted that in the case of ^{173}Yb, it is necessary to match the sign of the gradient generated by the Zeeman slower and its compensation coils with the radial gradient generated by the anti-Helmoltz MOT coils to take into account the optical pumping of the Zeeman slower beam in the $m_F = -5/2$ state [93]. We found experimentally that the only condition to successfully trap the atoms in the MOT is to have the two gradients with the same sign along the atomic beam axis. Moreover the loading has to be optimized by compensating the radiation pressure caused by the Zeeman Slower beam which has a frequency $-5.46\,\Gamma_{399}$ away from the $^1S_0\,(F = 5/2) \rightarrow {}^1P_1\,(F' = 5/2)$ transition (see section 2.3.1). This force is balanced out by opportunely tilting the MOT beams in the horizontal plane so to have a net force opposite to the Zeeman Slower beam. The MOT optical scheme is shown in Fig. 2.13. For further details on the multi-frequency setup and the MOT optimization, we refer to Ref. [80].

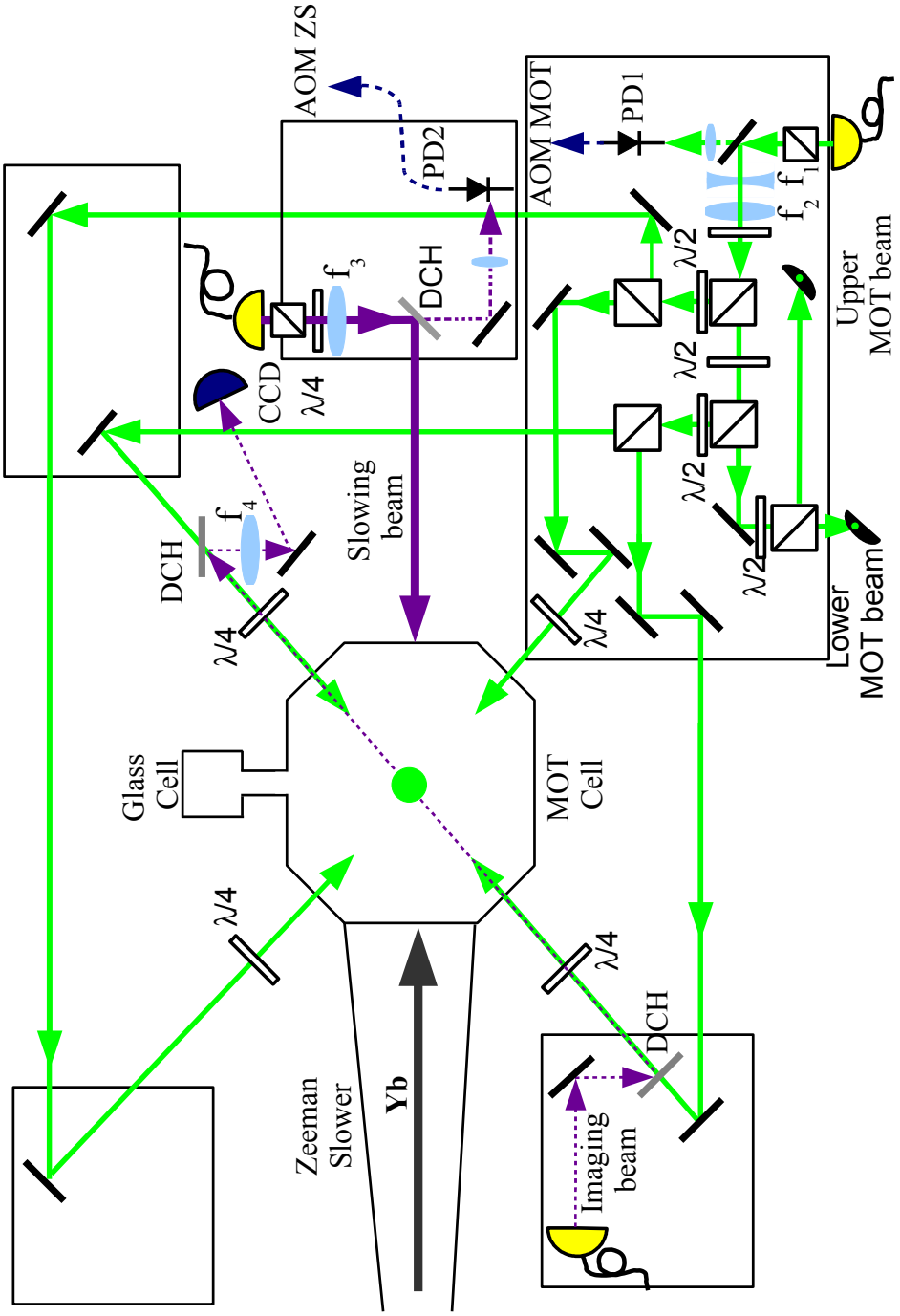

Figure 2.13: Optical scheme top view. f_1=-50 mm, f_2=75 mm, $f_3 = 100$ mm and $f_4 = 250$ mm. DCH stands for dichroic mirror. PD1 and PD2 are the power stabilization photodiodes of the MOT beams and the slowing beam respectively.

2.3.3 Resonator ODT loading and evaporation

As explained in section 2.1.1, the laser at 1064 nm is locked in resonance with the resonator with a Pound-Drever-Hall scheme [88], so that the intensity profile of the off-resonant dipole trap (ODT) is a standing wave forming a 1D optical lattice. Since the trap depth ($V_0/k_B \simeq 800\ \mu$K) is much higher than the MOT temperature we can transfer roughly 80% of the atoms from the fermionic MOT to the resonator trap using the following procedures (see Fig. 2.14):

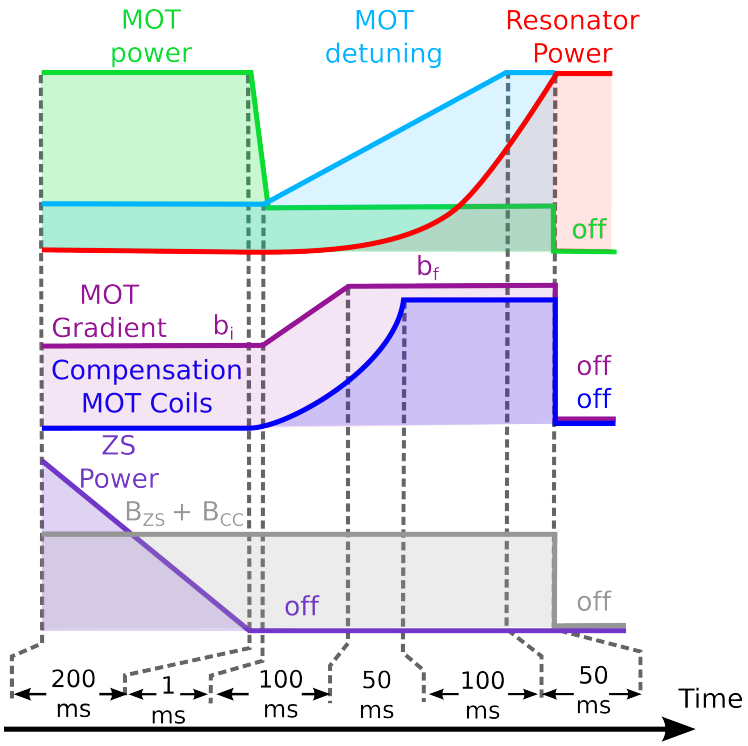

Figure 2.14: Timing of the MOT-resonator ODT transfer procedure (See text for details).

- First of all, the slowing beam power is adiabatically switched off in 200 ms, in order to reduce as gently as possible the residual radiation pressure on atoms trapped in the MOT resonating on the ${}^1S_0$, $(F = 5/2) \rightarrow {}^1P_1\,(F' = 5/2)$ transition (see section 2.3.1). A faster switch off would result in a loss of atoms in the MOT. At the same time the Zeeman slower (B_{ZS}) and the compensation coil (B_{CC}) magnetic fields are kept on, since the resulting gradient is summed up to the MOT coils gradient and it is necessary to hold the atoms in the MOT. Once the atoms are loaded in the resonator ODT, B_{ZS} and B_{CC} can be switched off safely as the atoms in the ground

state are magnetic field insensitive.

- After the slowing beam is switched off, the in-cavity power is ramped up using an exponential ramp of $T = 300$ ms to an input power of $P_{\text{in}} = 1.8$ W (corresponding to $P_{\text{cav}} \sim 4$ kW inside the cavity) with $\tau = 300$ ms[6].

- At the same time, the MOT is compressed raising the magnetic gradient from $b_i = 1.6 \rightarrow b_f = 4.4$ G/cm using a 100 ms linear ramp in order to match the spatial intensity profile of the resonator ODT. Contemporarily, the total MOT power is ramped down in 1 ms from $P_{tot} = 180$ mW $\rightarrow$ 7 mW to cool down the cloud.

- At the same time, the MOT frequency is ramped in 250 ms toward the optimal value which is slightly closer to resonance ($\delta_L \rightarrow -6.5\,\Gamma$) with respect to the optimal MOT value in order to compensate the light shift due to the resonator ODT.

- Three orthogonal compensation coils are used to move in 150 ms the zero of the MOT quadrupole magnetic field and superimpose the center-of-mass of the atomic cloud in the resonator beam waist.

In Fig. 2.15 we show a time-of-flight image of the single-frequency MOT and of the atoms trapped in the resonator ODT before evaporation. To evaluate the temperature inside the resonator ODT, we use the relation $T \simeq m\sigma_z^2/k_B t_{TOF}^2$ (where m is the atomic mass) using only the cloud width σ_z along the vertical direction. This is caused by the extremely high trapping frequency ($\omega_\perp \sim 2\pi \times 300$ kHz) along the orthogonal direction, namely the resonator axis. Since we cannot completely switch off the in-cavity power to keep the laser locked to the resonator, our switch time is limited by the power stabilization PID time-constant, namely a few ms. As a consequence, we are effectively performing a band mapping measurement (see section 1.2.2) along the resonator axis, which causes the asymmetric momentum distribution.

After the loading stage, we evaporatively cool the atoms in the resonator, by lowering the trap optical depth to $P_{\text{in}} \sim 250$ mW ($P_{\text{cav}} = 540$ W) using two exponential ramps, with $T_1 = 1$ s, $\tau_1 = 500$ ms and $T_2 = 500$ ms, $\tau_2 = 250$ ms. After the cooling stage, we obtain $N_{at} \sim 1 \cdot 10^7$ atoms at approximately $T \simeq 5$ μK.

[6] In general, in our lab, an exponential ramp between initial and final value P_0 and P_f is defined as:

$$P(t) = P_0 - \frac{P_{\text{f}} - P_0}{e^{-T/\tau} - 1}\left(1 - e^{-t/\tau}\right)$$

where T is the total duration of the ramp, τ is the exponential time constant.

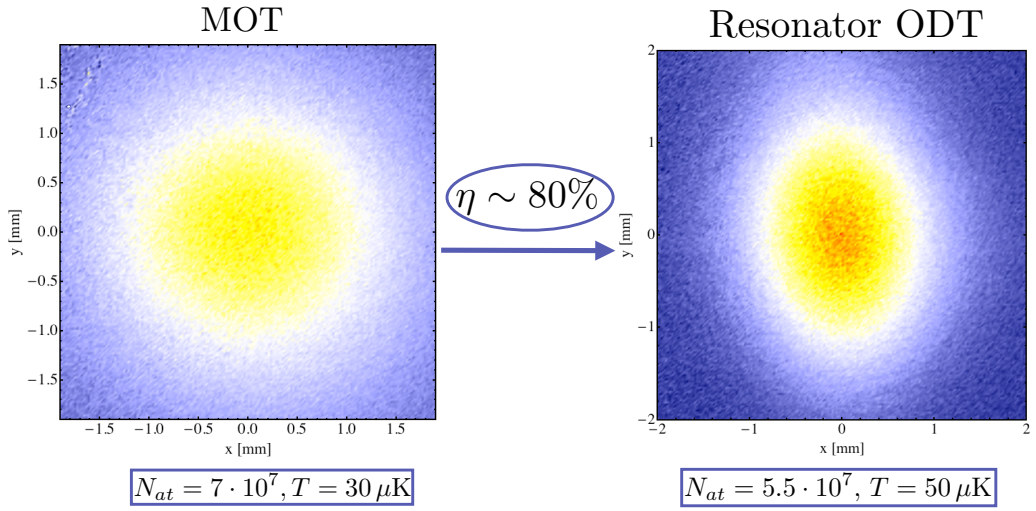

Figure 2.15: False color absorption images of the atoms after release from the MOT (left) and from the resonator ODT loading (right) after a holding time of 30 ms. The times-of-flight are 28 ms and 13 ms respectively.

2.3.4 Optical Transport and Crossed Dipole Trap

In order to transport the atoms in the high optical access glass cell, we load the atoms in a tightly-focused transport beam at 1064 nm whose focus is mechanically moved by a lens. Once the atoms are cooled down in the resonator ODT, the transport beam is switched on using a 200 ms exponential ramp ($\tau = 100$ ms). Right afterwards, the power incident on the cavity is ramped down to $P_{\text{in}} = 100$ μW by means of an exponential ramp of 200 ms ($\tau = 100$ ms). The corresponding in-cavity power ($P_{\text{cav}} \sim 230$ mW) is large enough to keep the laser locked to the resonator but it is too low to hold the atoms, which can be transferred to the transport beam ODT. An adiabatic switch-off of the resonator ODT is essential to maximize the efficiency of the transfer process. The transport ODT consists in a tightly-focused beam ($w_0 = 30$ μm and $P = 3.4$ W) at 1064 nm with depth $V_0/k_B \simeq 90$ μK. The 30 μm waist is a good compromise to obtain on the one hand a reasonably high axial frequency $\omega_z \simeq 2\pi \times 5$ Hz (crucial to speed up the transport) and a sufficient trap depth ($V_0/k_B \sim 80$ μK) and, on the other hand, to have a trap volume large enough for an efficient mode matching with the resonator ODT. In order to optimize the mode matching, the angle between the resonator ODT and the transport beam is 17.26° degrees (see Fig. 2.16) [81]. The efficiency of the transfer is $\eta \sim 30\%$, that is $N_{at} = 3 \cdot 10^6$ pre-transport. The 30 μm beam waist is produced by focusing a collimated beam with a waist about $w_0 \sim 1$ cm using a lens of focal length $f = 1$ m mounted on an air-bearing translation stage AEROTECH ABL 1500b (see Fig. 2.17) which mechanically moves the

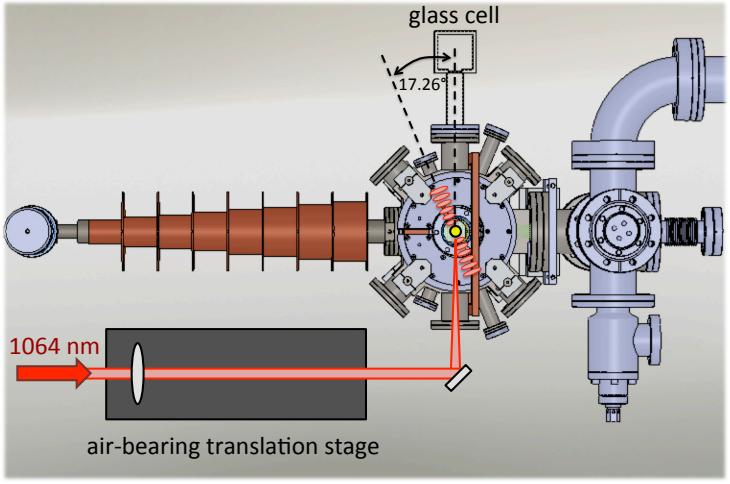

Figure 2.16: Sketch of the experimental configuration of the transfer from resonator to transport ODT. The angle between the resonator axis and the transport beam is highlighted.

beam focus and performs optical transport [82, 83]. In order to avoid spherical aberrations which would lead to a larger effective waist in the focus, it is crucial to use a 3 inches aspherical $f = 150$ mm lens to collimate the beam. Since the longitudinal frequency of the

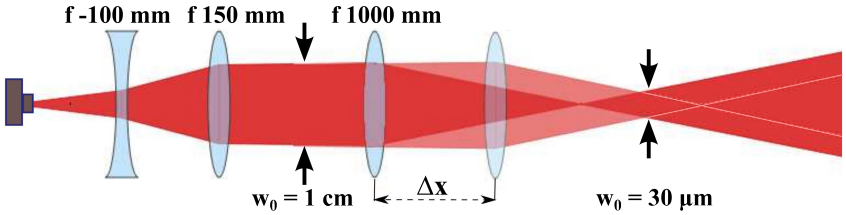

Figure 2.17: Optical scheme for the production of the $w_0 \sim 1$ cm collimated beam used for optical transport. The 1064 nm radiation is coming out from a fiber without a collimator after which the waist is enlarged by a diverging $f = -100$ mm lens and collimated by a 3 inches $f = 150$ mm aspherical lens.

transport is $\omega_z \simeq 2\pi \times 5$ Hz, we should choose a transport duration $T > 1$ s to be on the safe side and transport the atoms adiabatically in order to avoid heating. On the other hand, given the lifetime $\tau = (13.4 \pm 1.2)$ s [97] of the cloud in the transport beam, a much longer ramp is less efficient because, even if more adiabatic, the atoms suffer losses due to background gas collisions. For this reasons we chose $T = 2.5$ s to cover a distance of $\Delta x = 26.4$ cm (see Fig. 2.16). The ramp profile is a polynomial spline of fifth degree with

zero initial jerk[7] which leads to an efficiency of $\eta \sim 66\%$ with a final temperature 30% higher than the initial one (see Fig. 2.18). To evaluate correctly the transport efficiency we compare the number of atoms transported in the glass cell with the atoms hold in the MOT chamber for an equivalent amount of time. In this way we can rule out the losses due to background gas collisions. Once the atoms have been transported in the glass cell,

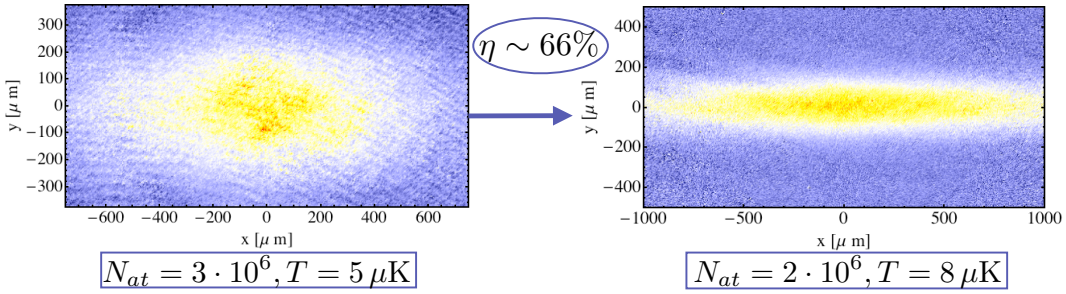

Figure 2.18: False color absorption images of the atoms in the transport beam after 2.7 s holding time in the MOT chamber (left) and right after the optical transport in the glass cell (right). The time-of-flight is 13 ms and 5 ms respectively.

an additional beam of $w_0 = 60$ μm and $P = 3$ W is focused onto the atoms. This beam is generated by an IPG FIBERTECH multimode laser at 1070 nm and it is orthogonal to the transport beam in order to create a crossed dipole trap configuration (see Fig. 2.19). This is the ODT configuration where the final evaporation is executed to reach quantum degeneracy.

2.3.5 ^{173}Yb Degenerate Fermi Gas

In order to achieve Fermi degeneracy of the atomic cloud trapped in the crossed ODT, we perform optical evaporative cooling using a two-stage ramp. The evaporative cooling is effective only for samples with more than one spin component, otherwise at low temperature the s-wave scattering is inhibited by Pauli principle. During the first stage (4 seconds) both beams are ramped down ($\tau_{transport} = 3.5$ s, $\tau_{cross} = 3$ s) and the gas reaches a reduced temperature of about $T/T_F \simeq 0.5$. The second ramp affects only the crossed beam of the trap and is much flatter ($T = 2.6$ s$, \tau = 2.5$ s) with respect to the first one because the more the gas enters the degenerate regime, the more the s-wave collisions are inefficient because only the atoms on the Fermi surface participate to the thermalization. Indeed the evaporation efficiency sharply drops down as T/T_F approaches unity value (see Fig. 2.20).

[7] The jerk is defined as $da(t)/dt$, namely the derivative of the acceleration over time.

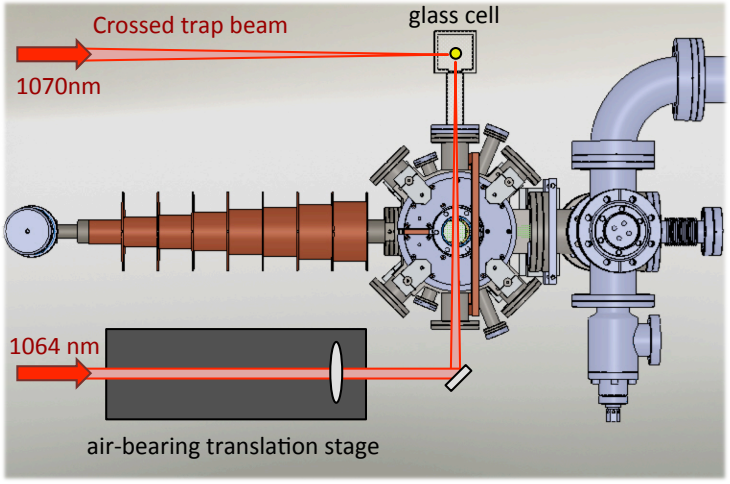

Figure 2.19: Sketch of the experimental configuration used to implement the crossed ODT after transport in the glass cell.

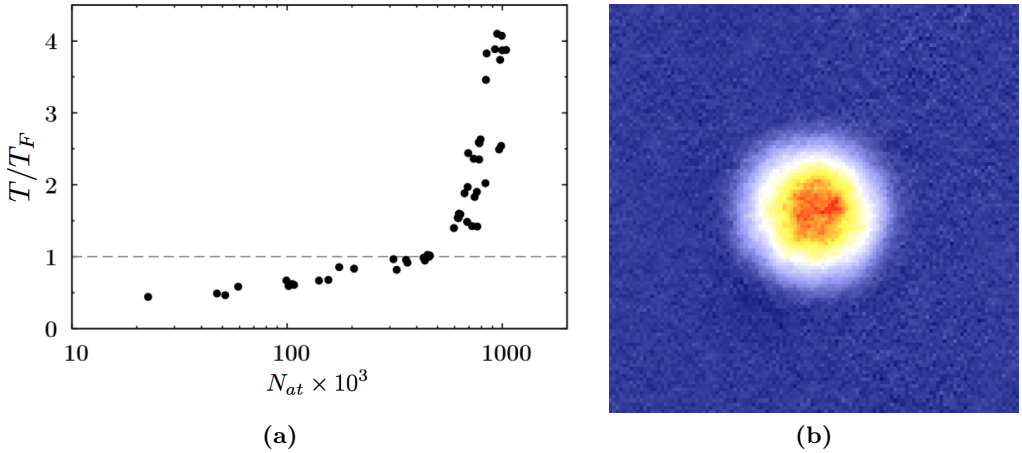

Figure 2.20: (a) T/T_F as a function of the number of atoms during the evaporation process. As T/T_F approaches unity, cooling efficiency drops down, as a signature of the Fermi degeneracy regime. (b) Six-component Fermi gas with $T/T_F = 0.1$ and $N_{at} = 1 \cdot 10^4$ per spin component.

In order to fully characterize the trap frequencies along the three orthogonal directions we used three different methods. The vertical frequency ω_z is measured by switching the trap off for 1 ms and then on again to let the gravity start the vertical oscillation. The horizontal frequencies ω_x is measured by inducing a displacement orthogonal to the transport beam by applying a voltage to a piezo-mounted mirror on the optical transport

path. The other horizontal frequency ω_y is measured by studying the ^{174}Yb BEC aspect-ratio evolution in time-of flight. Indeed, in a classical approximation, the BEC cloud dimensions after the sudden release of the dipole trap are subjected to a dilation $R_\alpha(t) = R_\alpha(0)\lambda_\alpha(t)$ [98], where the scaling factors $\lambda_\alpha(t)$ along the three directions $\alpha = x, y, z$ evolve according to the following equation:

$$\ddot{\lambda}_\alpha(t) = \frac{\omega_\alpha^2}{\lambda_\alpha \lambda_x \lambda_y \lambda_z}. \tag{2.6}$$

By knowing the other two frequencies, we can extract the third one by fitting the experimental data with the theoretical evolution letting ω_y as a free parameter. For $P_{\mathrm{Tr}} = 40$ mW and $P_{\mathrm{cr}} = 1.025$ W of the transport and crossed beam respectively, the final trap frequencies are:

Table 2.1: ODT trap frequencies after evaporation

ν_x [Hz]	ν_y [Hz]	ν_z [Hz]	ν_{geom} [Hz]
(53.8 ± 0.5)	(99.5 ± 0.5)	(90.3 ± 0.6)	(78.4 ± 0.4)

2.3.6 Optical Lattices

The optical lattices (OL) setup consists in three retroreflected beams, one along the vertical direction and two orthogonal beams in the horizontal plane, one of which forms an angle of 35° with respect to the transport axis. The geometrical configuration is shown in Fig. 2.21. The power of all three lattice beams is actively stabilized by controlling the voltage of three photodiodes (V_{PD}) picking up a small part of the beams right before the glass cell. The power stabilization is then performed using standard PIDs acting on the AOMs before the fibers (see section 2.2.4). The three AOMs are driven by means of three different radiofrequencies, separated by tens of MHz to avoid cross interference terms.

In order to calibrate the lattice depth $s = V_0/E_R$ in unit of recoil energy (see section 1.2.2), we used two independent methods with ^{174}Yb BEC: the Raman-Nath (RN) diffraction (see Fig. 2.22) [60, 99, 100] and the amplitude modulation (AM). In the RN method, we measure the lattice depth s by fitting the evolution of the diffraction pattern using Bessel functions (see section 1.2.2). In the AM method, we induce a transition from the lowest to the second excited lattice band, directly measuring the band gap. The results of the lattice depth calibration s as a function of the photodiode voltage V_{PD} are shown in table 2.2. Moreover, by comparing the results of the lattice depth calibrations with the

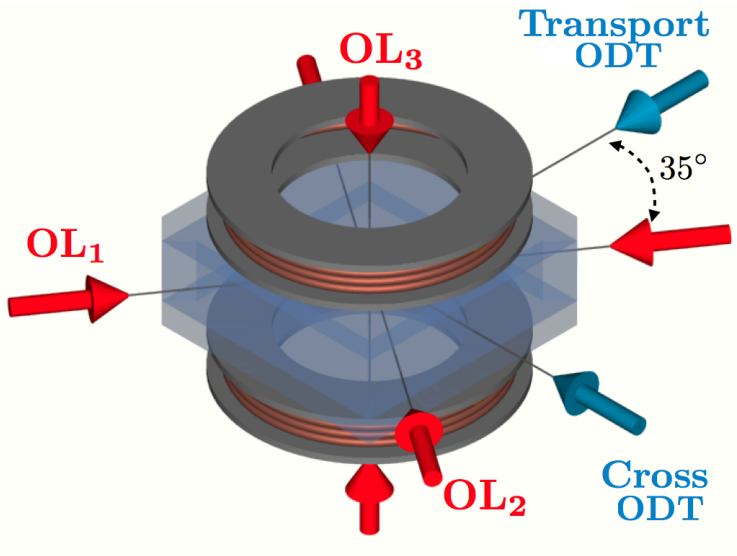

Figure 2.21: Optical lattice geometry. The beams 1 and 2 are respectively 55° and 35° tilted with respect to the transport ODT.

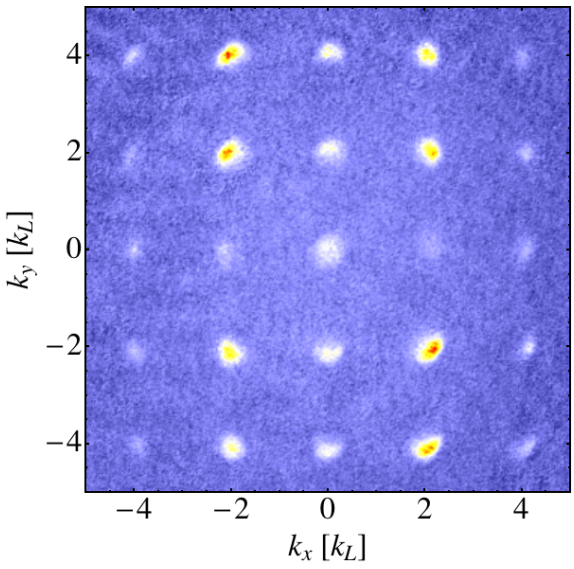

Figure 2.22: Time-of-flight image (t_{TOF} = 28 ms) of the in-plane Raman-Nath diffraction of a ^{174}Yb BEC. Diffraction peaks up to the third order can be observed.

theoretical lattice depth (see Appendix A for $^1S_0$ optical transitions), we can extract the waist of the three beams and, taking into account the 10% loss of the retroreflected beam, the radial frequency $\omega_r(s)$ induced by the residual harmonic confinement (see table 2.2).

Table 2.2: Lattice beam waist, lattice depth and trap frequencies calibration

	w_0 [μm]	$s(V_{PD})$	$\omega_r(s)/2\pi$ [Hz]
beam 1	96.1	$s_1 = 11.1\,V_1 - 0.18$	$7.104\sqrt{s}$
beam 2	111.3	$s_2 = 8.45\,V_2 - 1.09$	$6.160\sqrt{s}$
beam 3	102.3	$s_3 = 8.78\,V_3 + 0.10$	$6.777\sqrt{s}$

In order to load the lowest band of the lattice and maximize the adiabaticity, we increase the intensity of the three optical lattice beams using an exponential ramp ($T = 150$ ms, $\tau = 20$ ms). To test the adiabaticity of the ramp, we perform visibility measurements on the ^{174}Yb bosonic Mott insulator (MI) state [7, 76–78]. The procedure consists in adiabatically ramping up the intensity of the 3D lattice at $s = 20$ so that the atoms, initially in a superfluid phase-coherent state, are pinned on lattice sites by the on-site interaction U (see also section 5.2), which becomes the dominant energy scale with respect to the tunneling energy J (see Eq. 1.66). We wait a variable time in the MI state and then we ramp down the lattice depth to $s = 4$ with a 15 ms linear ramp. If no three-body losses or other dissipative mechanisms such as heating have occurred during the holding time, then the characteristic phase coherence of the superfluid can be restored within the tunneling time $h/J \sim 6$ ms. We then wait 10 ms to restore coherence and measure the visibility of the interference pattern of the momentum distribution, which is a direct measurement of the first order correlation function in the system. In particular, the visibility [76] is defined as:

$$\mathcal{V} = \frac{n_{\max} - n_{\min}}{n_{\max} + n_{\min}}. \tag{2.7}$$

The maximum density $n_{\max}$ is measured at the first lateral peaks of the interference pattern at $(k_x, k_y) = (0, \pm 2k_L)$ and $(k_x, k_y) = (\pm 2k_L, 0)$ (see Fig. 2.22). The minimum density $n_{\min}$ is measured along two diagonals $k_y = \pm k_x$ at the distance $2k_L$ from the central peak. The decay of the visibility is caused by heating [78] due to a non-adiabatic loading process and by three-body losses due to large density in the center of the cloud. In order to minimize the three-body losses, we decreased the BEC density by diminishing the number of atoms from typical $N_{BEC} = 3 \cdot 10^5$ to $N_{BEC} = 1.4 \cdot 10^5$. To further decrease the density, we also changed the ODT trap configuration by adiabatically moving backward the lens on the transport translation stage by $\Delta f = 4$ mm. In this way we lower the geometric frequency from $\nu_{\text{geom}} = (78.4 \pm 0.4)$ Hz to $\nu_{\text{geom}} = (56.4 \pm 0.6)$ Hz (see table

2.3). By loading the atoms in the optical lattice using the same ramp starting from the

Table 2.3: ODT trap frequencies calibration with and without defocusing.

	ν_x [Hz]	ν_y [Hz]	ν_z [Hz]	ν_{geom} [Hz]	P_{Tr} [mW]	P_{cr} [W]
$\Delta f = 0$ mm	(53.8 ± 0.5)	(99.5 ± 0.5)	(90.3 ± 0.6)	(78.4 ± 0.4)	40	1.025
$\Delta f = 4$ mm	(26.3 ± 0.7)	(97.5 ± 0.6)	(70.0 ± 0.5)	(56.4 ± 0.6)	50	1.110

two different ODT configurations, we can isolate the contribution of the three-body losses on the decoherence of the MI state and assess the adiabaticity of the loading procedure. The results are shown in Fig. 2.23, where the visibility after a variable holding time in the Mott insulator phase is shown to have a longer lifetime $\tau_{\mathcal{V}} = (503 \pm 27)$ ms in the $\nu_{\mathrm{geom}} = (56.4 \pm 0.6)$ Hz configuration compared to the lifetime $\tau_{\mathcal{V}} = (252 \pm 37)$ ms in the $\nu_{\mathrm{geom}} = (78.4 \pm 0.4)$ Hz configuration. For longer ramps the visibility lifetime is limited by inelastic light scattering caused by lattice beams [78].

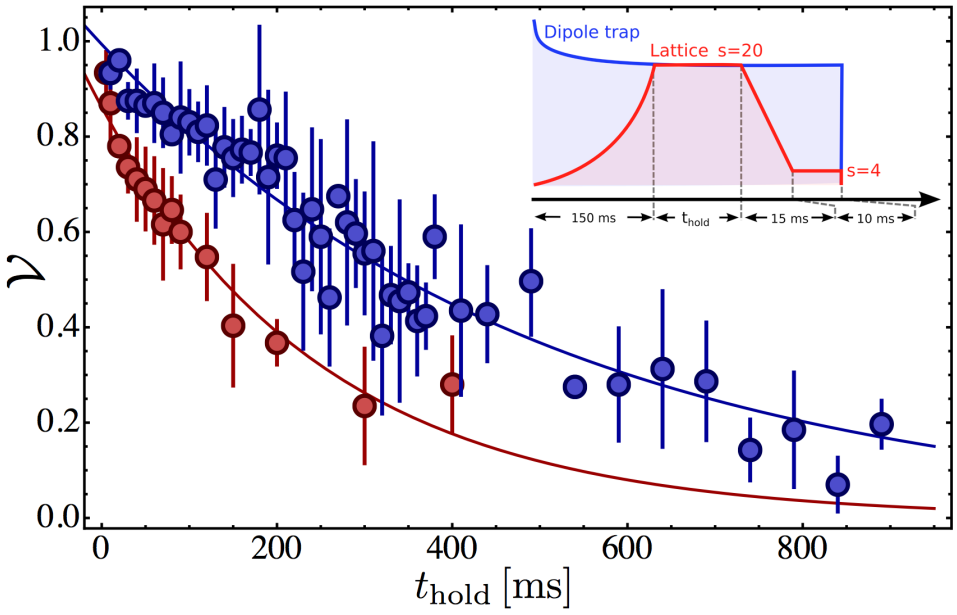

Figure 2.23: Visibility as a function of the holding time in the Mott insulator phase for two different trapping frequencies (see text). Blue (red) data points refer to $\nu_{\mathrm{geom}} = 78.4$ Hz ($\nu_{\mathrm{geom}} = 56.4$). Inset: experimental procedure.

2.3.7 Imaging

In order to measure the atom number we use absorption imaging on the cycling ${}^1S_0 \rightarrow {}^1P_1$ transition. The column density of the cloud $n_c(x,y) = \int n(x,y,z)dz$ integrated along the imaging direction z is extracted from the transmitted intensity profile $I_t(x,y)$ of the imaging resonant beam:

$$I_t(x,y) = I_0(x,y)e^{-\sigma n_c(x,y)} \longrightarrow n_c(x,y) = -\frac{1}{\sigma}\log\left(\frac{I_t(x,y)}{I_0(x,y)}\right), \tag{2.8}$$

where $I_0(x,y)$ is the intensity profile without the atoms and $\sigma = 3\lambda^2/2\pi$ is the resonant scattering cross section of the atoms with λ being the wavelength of the imaging laser. The discretized density on the CCD pixels is measured as:

$$n_c(i,j) = -\frac{S}{\sigma}\log\left(\frac{P_{ij} - B_{ij}}{F_{ij} - B_{ij}}\right), \tag{2.9}$$

where S is the pixel area including the magnification and P_{ij}, F_{ij}, B_{ij} are the signal intensities on the pixel (i,j) corresponding respectively to the imaging beam with atoms, without the atoms and with the imaging laser off to remove the background. For a thermal cloud we use a standard two-dimensional Gaussian fit:

$$n_c(x,y) = A \cdot \exp\left[-\left(\frac{(x-x_0)^2}{2\sigma_x^2} + \frac{(y-y_0)^2}{2\sigma_y^2}\right)\right] + b, \tag{2.10}$$

where the fitting parameters are the widths σ_x, σ_y, the center of the cloud $(x_0,\ y_0)$, the amplitude A and the offset b.

When the atoms enter the quantum degeneracy regime, we have to use different fitting functions depending on whether we deal with a degenerate Bose or Fermi gas. In the case of a pure BEC, we use a two dimensional Thomas-Fermi profile:

$$n_c(x,y) = A \cdot \left[1 - \left(\frac{x-x_0}{r_x}\right)^2 - \left(\frac{y-y_0}{r_y}\right)^2\right]^{3/2} + b, \tag{2.11}$$

where r_x, r_y are the Thomas-Fermi radii.

In the case of a degenerate Fermi gas, the temperature enters both as a pre-factor and as an argument of the Polylogarithmic function (see Eq. 1.16). Thus an accurate thermometry requires also knowledge of the trap frequencies and a precise calibration of $n_c(x,y)$ in terms of optical density, which are both parameters subjected to experimental uncertainties. The most common approach to overcome this difficulty is to use the relation (1.8) between temperature and fugacity and use $\mathcal{F}$ as a fitting parameter. Thus the fit

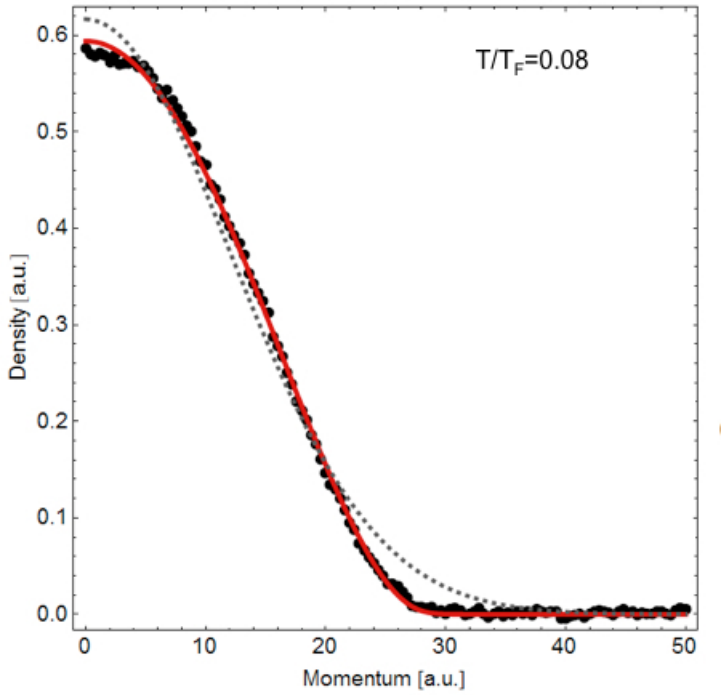

Figure 2.24: One-dimensional cut of the density fit (red solid line) performed using Eq. (1.16). The points are the measured density profile of a six components trapped Fermi gas with $N_{at} = 1 \cdot 10^4$ per component at $T/T_F = 0.08$ after a time-of-flight of 23 ms. The Gaussian fit (dotted line) clearly is an inadequate description of the momentum distribution.

expression becomes:

$$n_c(x,y) = A \cdot \frac{\mathrm{Li}_2\left(-\mathcal{F}\exp\left[-\frac{x^2}{2\sigma_x^2} - \frac{y^2}{2\sigma_y^2}\right],\right)}{\mathrm{Li}_2\left(-\mathcal{F}\right)} + b, \tag{2.12}$$

where the fitting parameters are A, b, $\mathcal{F}$, and $\sigma_i^2 = \frac{k_B T}{m} t^2$, where t is the time-of-flight. An example of fit is shown in Fig. 2.24 where we highlight the difference between a Gaussian fit profile (dotted line) and the experimental data fitted with Eq. (2.12).

We built several imaging setups to measure the atom number in all the different stages of the experimental cycle. In the MOT chamber we image the atoms on CCD BlueFox 220AG (640×480 with pixel size 7.4×7.4 μm) along the direction at 45° with respect to the transport beam (see Fig. 2.13). The imaging is performed using a single lens in two possible configurations: one consisting in a $f = 200$ mm lens at 75 cm from the center of the MOT chamber, which provides a 0.330x magnification used to image the MOT and the

atoms in the resonator; the other configuration, consisting in a $f = 250$ mm lens placed at 38 cm from the atoms providing a 1.912x magnification, is used to image the atoms in the resonator at the end of evaporation and in the transport beam.

In the glass cell we built two imaging setups: one along the vertical direction consisting in a single $f = 150$ mm lens providing a 3.193x magnification. In this case we chose an achromatic doublet to have the possibility to perform absorption imaging on both ${}^1S_0 \rightarrow {}^1P_1$ and ${}^1S_0 \rightarrow {}^3P_1$ cycling transitions. The CCD is an Andor iXon$^{\mathrm{EM}}$+DU885KCSO with 1002×1004 pixels of size 8×8 μm and 14 bit resolution. The other imaging system is superimposed on the crossed ODT beam and is performed on a CCD BlueFox 220AG using a single $f = 100$ mm lens providing a 1.856x magnification.

2.4 Nuclear spins detection and manipulation

In order to initialize the spin distribution of the ^{173}Yb Fermi gas with a high degree of precision, nuclear spin detection and manipulation techniques have been developed. The simplicity of these protocols relies on the peculiar features of the ${}^3P_1$ manifold. Indeed, on the one hand the transition linewidth is narrow ($\Gamma = 2\pi \times 182$ kHz), but on the other hand the coupling to an external magnetic field is as large as in the alkali atoms ($g_{F'} = 0.425$ for the ${}^3P_1$ ($F' = 7/2$) state) leading to a magnetic field sensitivity $g_{F'}\mu_B = 2\pi \times 595$ kHz/G $\sim 3\,\Gamma$/G. This means that a modest magnetic field of tens of Gauss is enough to produce a Zeeman splitting that allows us to selectively address optical transitions of a particular nuclear spin component without affecting the others. This feature lies at heart of the procedures, outlined in the following sections, used to detect and initialize the nuclear spin distribution of the atomic cloud.

2.4.1 Spin distribution detection

Since ^{173}Yb is a diamagnetic atom that has a purely nuclear spin, it is not possible to detect the populations of the six nuclear spin components using a standard magnetic Stern-Gerlach experiment. Hence, in order to overcome this difficulty, it is necessary to use optical techniques, in particular using light that exerts a spin-dependent dipole force on atoms, thus performing an "optical Stern-Gerlach" (OSG) experiment [101, 102]. As explained in section 1.2, in the specific case of the transition ${}^1S_0 \rightarrow {}^3P_1$, the optical dipole force exerted on atoms with spin component m_g is given by the contribution of the three

excited states $F_e = 7/2, 5/2, 3/2$ of the $^3P_1$ manifold:

$$V_{m_g}^{(q)}(\mathbf{r}) = \frac{3\pi c^2}{2\omega_0^3}\Gamma\left(\frac{|\mathcal{S}_{m_g}^{(q)}(7/2)|^2}{\Delta_{7/2}} + \frac{|\mathcal{S}_{m_g}^{(q)}(5/2)|^2}{\Delta_{5/2}} + \frac{|\mathcal{S}_{m_g}^{(q)}(3/2)|^2}{\Delta_{3/2}}\right) I(\mathbf{r}), \tag{2.13}$$

where q refers to light polarization and $\Delta_{7/2}, \Delta_{5/2}, \Delta_{3/2}$ are the detunings from the $F' = 7/2, 5/2, 3/2$ states. In particular a σ-polarized light with a detuning $\Delta_{7/2} = -566$ MHz $\simeq -3100\,\Gamma$ and waist $w_0 = 60\,\mu$m is used to exert a spin dependent potential on the atoms displayed in Fig. 2.25. The beam is aligned (see Fig. 2.26) in order to let the atomic cloud sample the region of maximum gradient of the Gaussian beam profile, which generates the optical dipole force (1.24). Depending on whether the OSG polarization is σ^- or σ^+, the greatest attractive dipole force acts respectively on the $m_g = -5/2$ or $m_g = +5/2$ Zeeman component. To perform the nuclear spin population detection, we

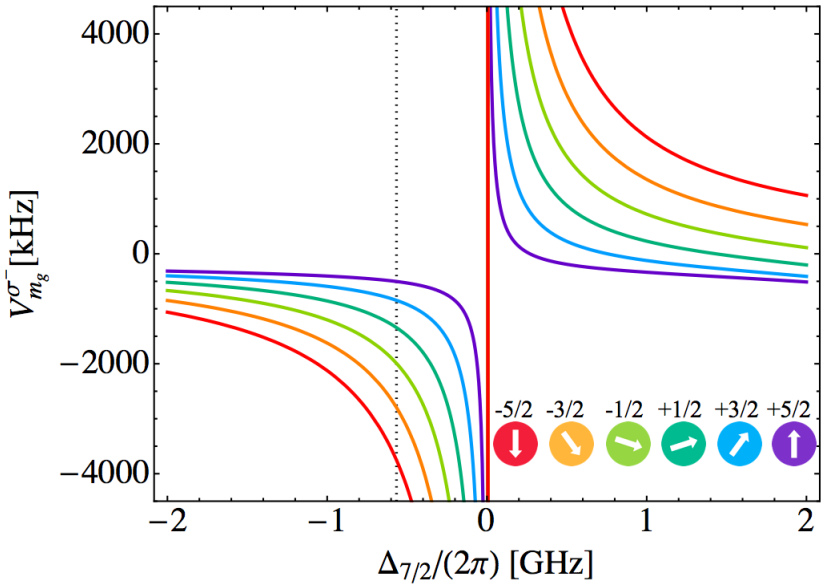

Figure 2.25: Spin-dependent OSG potential as a function of the detuning with respect to the $F = 5/2 \rightarrow F' = 7/2$ resonance for σ^- polarization. The dotted line is the frequency of the OSG beam. The different colors indicate different nuclear spin components. The beam waist is $w_0 = 60$ μm and the power is $P = 10$ mW.

use a 1.25 ms square pulse with power $P = 10$ mW and, after suddenly switching off the ODT, we let the cloud expand for a $t_{TOF} = 4.5$ ms. To define the quantization axis, a bias magnetic field $B_{OSG} = 2.5$ Gauss is applied along the light propagation axis. A typical absorption image of the OSG experiment is shown in Fig. 2.26.

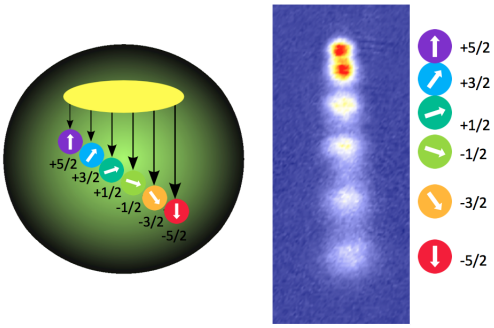

Figure 2.26: Left: the beam is misaligned on the atomic cloud in order to exploit the gradient of the Gaussian beam profile. Right: Absorption image of the Fermi gas subjected to the σ^- OSG pulse. The different density of the nuclear spin components is due to the spin-dependent compression exerted on the atoms. Despite the different densities might suggest population imbalance, the spins are equally populated within a 5% tolerance.

2.4.2 Spin distribution initialization

In order to actively manipulate the nuclear spin components, we developed a spin-selective optical pumping (OP) method based on laser pulses resonant with the ${}^1S_0\,(F = 5/2) \rightarrow {}^3P_1\,(F' = 7/2)$ transition. Since this is a narrow transition ($\Gamma = 2\pi \times 182$ kHz), it is possible to selectively address only one single Zeeman component of the excited state manifold, as displayed in Fig. 2.27. The ${}^3P_1\,(F' = 7/2)$ Zeeman sublevels are separated by a homogeneous magnetic field of $B = 22.7$ Gauss, resulting in a relative Zeeman shift $\Delta_Z = 2\pi \times 13.6$ MHz $\simeq 75\ \Gamma$ (see Fig. 2.27). The magnetic field is produced with two coils in Helmoltz configuration with inner and outer radius of 6 and 10 cm, respectively. The total measured inductance is $L_{Coils} = 8.69$ mH and the total measured resistance $R_{Coils} = 4.88\ \Omega$. The distance between the two coils is 4.9 cm (see Fig. 2.28).

The selective optical pumping procedure is then carried out by two independent beams OP^{σ^+} and OP^{σ^-} (see Fig. 2.28) circularly and orthogonally polarized so that only the transitions $m_g \rightarrow m_g \pm 1$ are resonantly excited. By shining on the atomic cloud two series of light pulses of 5 ms each with the right laser frequencies (green arrows in Fig. 2.27), it is possible to selectively pump the atoms out of a specific nuclear spin state.

The pumping procedure is executed right after the transport in the glass cell, before the evaporation, when the atomic cloud temperature is $T \simeq 8\ \mu$K, and therefore the heating due to photon scattering is negligible. The initial atomic spin distribution coming from the

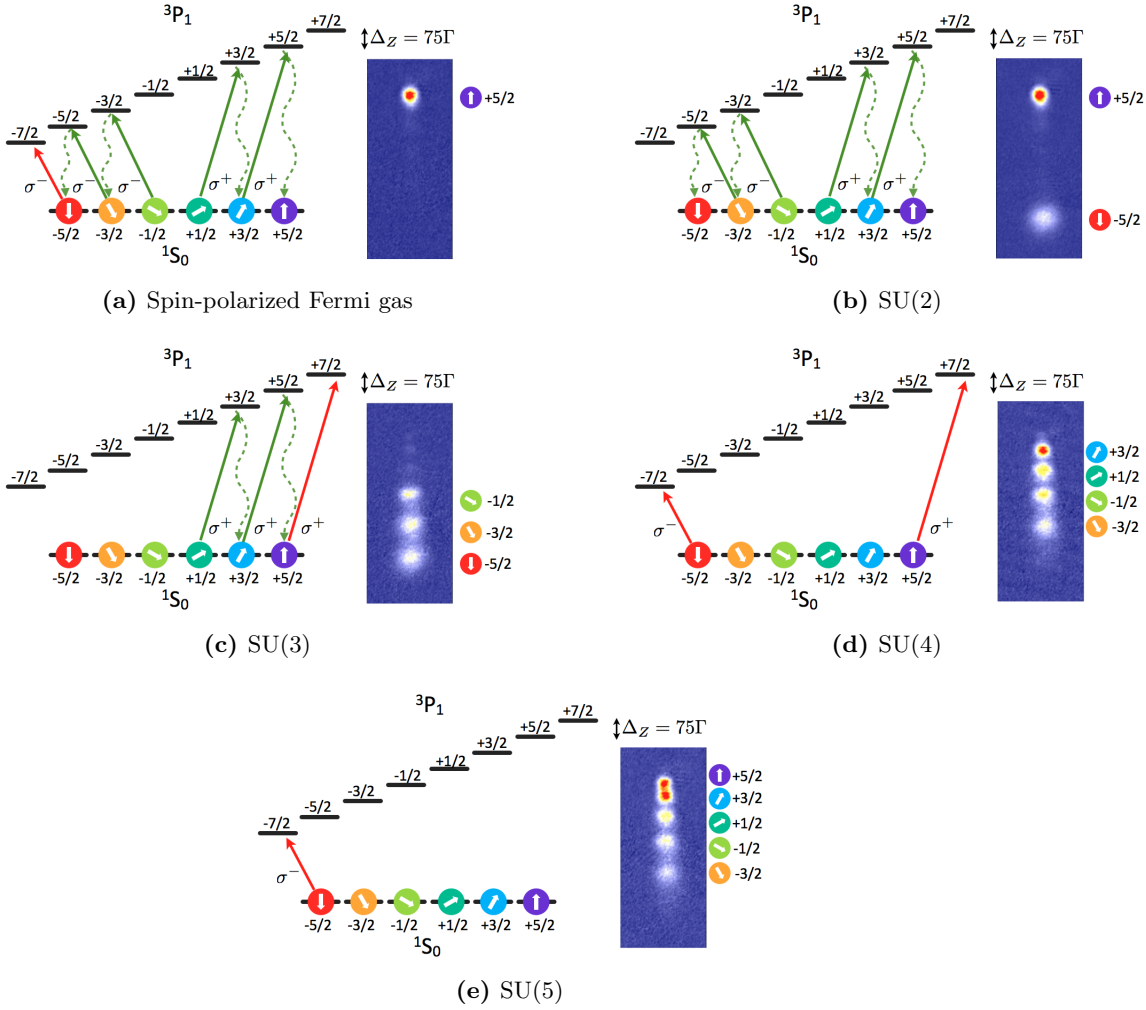

(a) Spin-polarized Fermi gas

(b) SU(2)

(c) SU(3)

(d) SU(4)

(e) SU(5)

Figure 2.27: Protocols for spin initialization with optical pumping performed through σ^+ and σ^--polarized beams resonant on specific Zeeman components of the $^1S_0 \rightarrow {}^3P_1$. Green arrows indicate transitions used in the optical pumping procedure. Red arrows indicate optically-closed transitions that are used to blast away the unwanted populations at the end of the evaporation. For clarity sake, not all the possible spontaneous emission processes are shown.

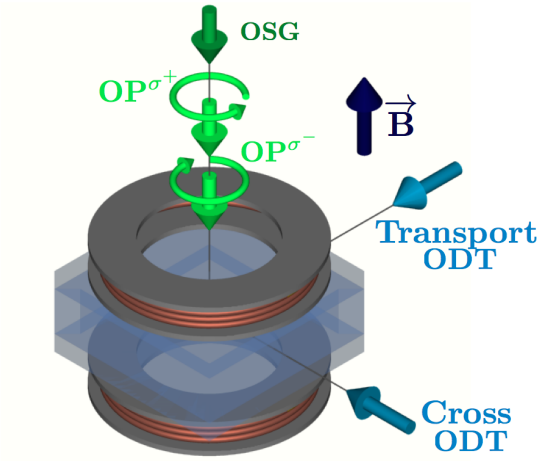

Figure 2.28: Optical scheme for OSG and OP beams. The OSG beam has σ polarization, the sign of which depends on the particular experimental configuration.

MOT is approximately thermal with six equally populated spin components. Typically the complete pumping procedure with four pulses produces a two-component Fermi gas in the stretched states $m_g = \pm 5/2$ (see 2.27b). In order to produce a spin-polarized Fermi gas an additional blast step is needed at the end of the evaporation (red arrows in Fig. 2.27) in order to eliminate the unwanted populations from the trap (Fig. 2.27a). The blast pulse is performed at $B = 14.6$ Gauss, which correspond to a Zeeman shift $\Delta_Z = 2\pi \times 8.75$ MHz $\sim 48\ \Gamma$. The magnetic field has been chosen in order to minimize the residual heating on the other spin components compatibly with the dynamic frequency range of the AOMs used for the OP pulses. Since the transition to the stretched states is closed and the trap is shallower, a 150 μs pulse is enough to blast away the unwanted spin population. By opportunely combining pumping and blast pulses, it is possible to produce balanced mixtures with one up to six components with unwanted population below 5% (Fig. 2.27). With these protocols, we can reliably produce degenerate Fermi gases interacting within different $SU(N)$ symmetry classes, where N ranges from 1 to 6.

We evaluated the final T/T_F in the ODT at the end of the evaporation for all the six spin mixtures (see Fig. 2.29) by fitting the degenerate Fermi gas profile as described in section 2.3.7. If on the one hand the heating due to the pumping stage is negligible, on the other hand, the blast stage heats up the cloud since it is performed at the end of the evaporation. This is the reason of the higher temperatures of the spin-polarized Fermi gas ($N = 1$) and of all the mixtures where a blast stage is needed ($N = 3, 4, 5$) with respect to the spin mixtures ($N = 2, 6$) where only optical pumping is sufficient. Moreover, since with more spin components the evaporation is more efficient, we get a lower T/T_F for

$N = 3, 4, 5$ with respect to the spin-polarized case, obtained by evaporating a two-spin mixture. For the same reason, the higher temperature of the $SU(2)$ gas ($T/T_F = 0.19(2)$) compared to the $SU(6)$ gas can be explained in terms of lower evaporation efficiency. Therefore, the $SU(2)$ routine contemplates a longer evaporation ramp (4 seconds) while in the case of the $SU(6)$ gas, a 2.6 seconds ramp is enough to reach $T/T_F = 0.12(1)$.

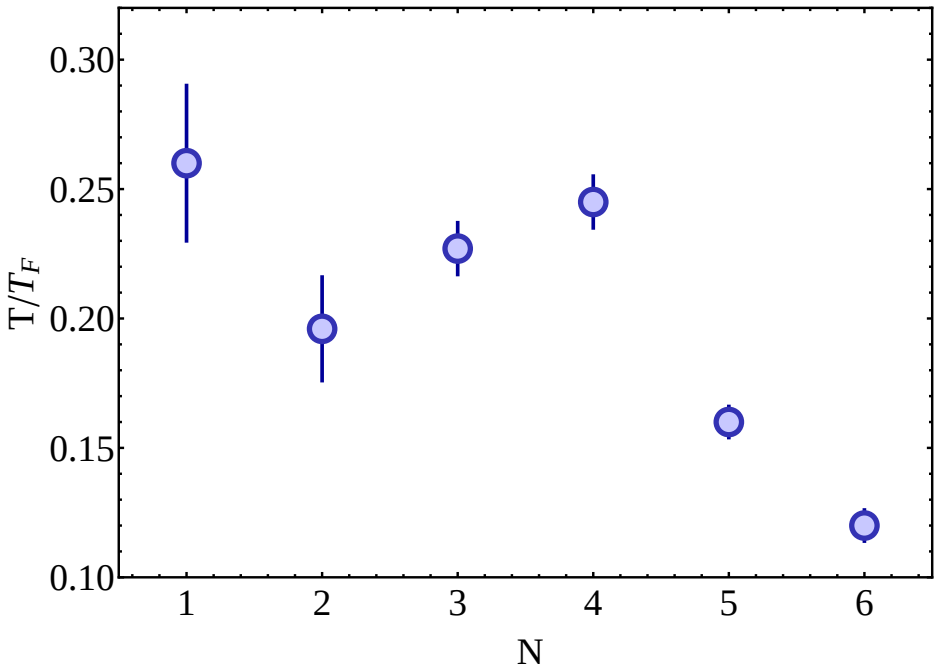

Figure 2.29: Final temperature in the ODT as a function of the number of spin components N. See text for details.

2.4.3 Optical pumping and OSG setup

The two optical pumping beams (OP^{σ^+} and OP^{σ^-} in Fig. 2.28) are delivered by two different fibers both mounted on a vertical breadboard. The OP^{σ^+} beam is generated using the MOT AOM and injected in the same fiber of OSG with orthogonal polarization with respect to the OSG light (see Fig. 2.8). The OSG and OP^{σ^+} beams are then separated by a polarizing beam splitter (PBS) placed right after the fiber. The same PBS is also used to combine the two optical pumping beams having linear and orthogonal polarization. Two wave-plates turn the horizontal and vertical polarization into σ^+ and σ^- respectively (see Fig. 2.30). On the other hand, in the OSG beam optical path there is a $f = 400$ mm lens mounted on a translation stage used to adjust the waist in order to maximize the optical gradient on the atoms, and a $\lambda/4$ waveplate to determine the polarization of the

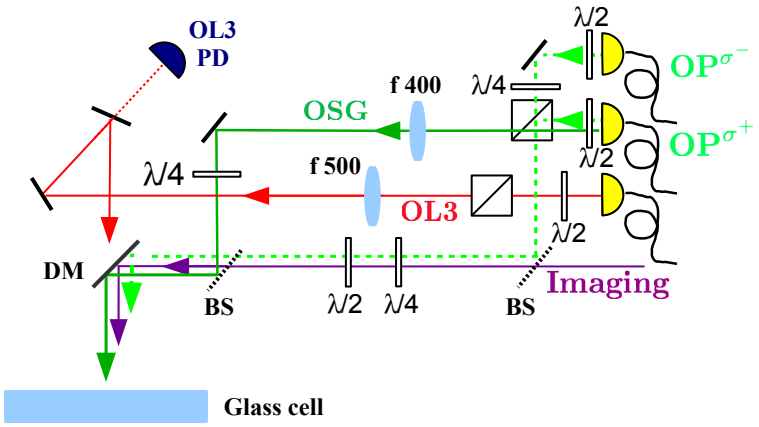

Figure 2.30: Optical scheme for vertical imaging, optical stern gerlach (OSG), the two optical pumping beams (OP$^{\sigma^{\pm}}$) and vertical optical lattice (OL3). DM: long-pass dichroic mirror. BS: beam splitter. PD: OL3 power stabilization photodiode.

OSG light. The two optical pumping and OSG beams are then further recombined by a 70:30 beam splitter and reflected by a long-pass dichroic mirror Thorlabs-DMLP567 onto the atoms. The vertical lattice beam (OL3) passes through the same dichroic mirror and the vertical imaging beam is superimposed on the OP path using another beam splitter (see Fig. 2.30).

Chapter 3

Theory of one-dimensional liquid of fermions

One-dimensional many-body fermionic systems exhibit fascinating and peculiar properties which are very different from their higher-dimensions counterparts. Indeed, in three and two-dimensional Fermi liquids, low-energy excitations of the interacting system are efficiently described by well-defined nearly free quasi-particles. Differently, in one-dimensional systems all low-energy excitations display collective nature. This deep difference is originated by the one-dimensional Fermi surface consisting in two discrete points, while being continuous in higher dimensions. In order to deal with this distinctive feature, in 1963 Luttinger proposed a model [103], which was then solved exactly by Lieb and Mattis [104] in 1965. The exact diagonalization relies on a Bogolioubov transformation which defines low-energy excitations as free bosonic collective modes.

In this chapter we start from the Fermi liquid theory failure (section 3.1) and review[1] in section 3.2 the formalism and the theoretical concepts that lead to the exact solution of the paradigmatic Luttinger liquid model [33] for both spinless and spinful fermions in one dimension. In particular, applying this formalism to the case of spinful fermions leads to the striking prediction that spin and charge low-energy collective excitations propagate with different velocities, a.k.a. the spin-charge separation. In section 3.3, we apply the Luttinger formalism to the case of ultracold atomic gases following Refs. [108, 109] and discuss the Luttinger parameters in our experimental system. In section 3.4 we briefly review the Bethe-Ansatz technique that enables the exact solution of the many-body problem of an interacting one-dimensional liquid of fermions. We also show the insights given by this powerful tool on the momentum distribution of a two-component Fermi

[1] The references of this short review are mainly [105],[106] and [107].

gas in the strong coupling regime, both a $T = 0$ [110] and $T > 0$ [111]. Finally, in section 3.5, we address the generalization of the Luttinger liquid theory to the case of a multi-component fermionic liquid, focusing in particular on the case of $SU(N)$-symmetric interactions (see also section 1.3.2) where counterintuitive effects are predicted, such as the "high-spin bosonization" [34].

3.1 Fermi liquid failure in one dimension

When particles motion is confined along one direction, the individual motion of a particle is not allowed anymore. Indeed, if a particle tries to move in one dimension, necessarily it interacts with the others, giving rise to a collective excitation (see Fig. 3.1). Hence the reduced dimensionality hinders single-particle motion to the point that the particles must be regarded as strongly correlated even when their interactions are weak.

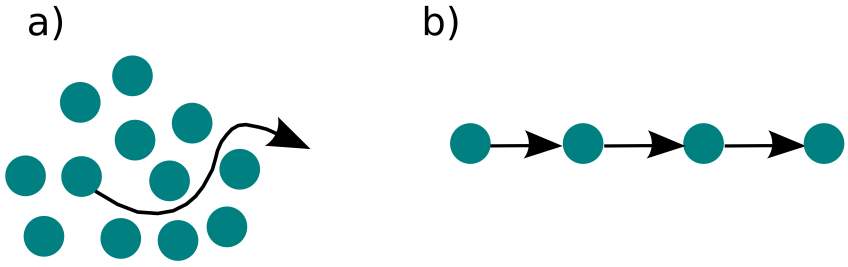

Figure 3.1: (a) In high dimensions Fermi liquid description is based on nearly free quasi-particles excitations that behave as single particles. (b) In one dimension only low-energy collective excitations are allowed.

A more formal argument on the failure of the Fermi liquid picture is based on the analysis of the density-density linear response function of a non-interacting homogeneous electron gas, a.k.a. Lindhard function:

$$\chi_0(\mathbf{q},\omega) = \frac{1}{L^D}\sum_{\mathbf{k}\sigma}\frac{n_{\mathbf{k}\sigma} - n_{\mathbf{k}+\mathbf{q}\sigma}}{\hbar\omega + \xi_{\mathbf{k}\sigma} - \xi_{\mathbf{k}+\mathbf{q}\sigma} + i\hbar\eta}, \tag{3.1}$$

where $\xi_{\mathbf{k}\sigma} = \varepsilon_{\mathbf{k}\sigma} - \mu$, $\varepsilon_{k\sigma} = \hbar^2 k^2/2m$ with k the momentum of the single particle, μ is the chemical potential, $\eta = 0^+$ and L^D is the total volume of the system with dimensionality D and linear size L. The first difference between one and higher dimensions regards the electron-hole continuum, namely the region on the $(\mathbf{q},\omega)$ plane (with $\mathbf{q}$ and ω being the momentum and frequency excitation, respectively) where it is possible to create a number-conserving particle-hole excitation. In high dimensions, for $|\mathbf{q}| < 2k_F$ it is possible to

create an excitation of arbitrarily low-energy by annihilating a particle just below the Fermi energy and recreating it just above the Fermi energy (Fig. 3.2a). In one dimension instead, the structure of the electron–hole continuum is different because the "Fermi surface" in this case consists of only two points ($\pm k_F$) and therefore excitations of vanishing energy are impossible except at wave vectors 0 and $2k_F$ (Fig. 3.2b). Another striking difference

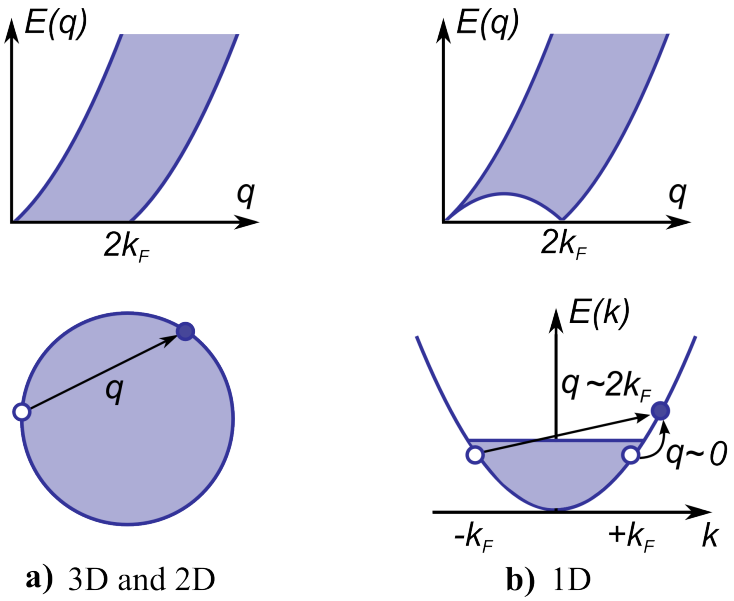

Figure 3.2: Particle-hole excitation spectrum in high dimensions (a) and one dimension (b). The gap between $q = 0$ and $q = 2k_F$ is due to the peculiar one-dimensional Fermi surface, composed by only two points ($\pm k_F$). In high dimensions the gap is absent.

concerns the static density-density response function $\chi_0(\mathbf{q}, \omega \to 0)$, which is proportional to the density of states at the Fermi level $N(0)$. It is easy to see that, for $\mathbf{q}$ such that $\xi_{\mathbf{k}+\mathbf{q}} = -\xi_{\mathbf{k}}$ (a.k.a nesting condition), singularities can appear in $\chi_0(\mathbf{q}, \omega \to 0)$. In three and two dimensions there is only a limited set of points (for $|\mathbf{q}| = 2k_F$) at which this occurs and integration over $\mathbf{k}$ (see Eq. 3.1) leads to singularities just in the derivatives of $\chi_0(\mathbf{q}, 0)$. In one dimension instead, it is reasonable to linearize the dispersion relation around the Fermi energy and to individuate two dispersion branches, namely:

$$\begin{aligned} \xi_k^R &\sim \hbar v_F(k - k_F), \\ \xi_k^L &\sim -\hbar v_F(k + k_F), \end{aligned} \tag{3.2}$$

where R and L stand for right and left-moving electrons. Hence the nesting condition for $q = 2k_F$ is valid for every momentum k around the Fermi wavevector and $\chi_0(\mathbf{q}, 0)$ itself

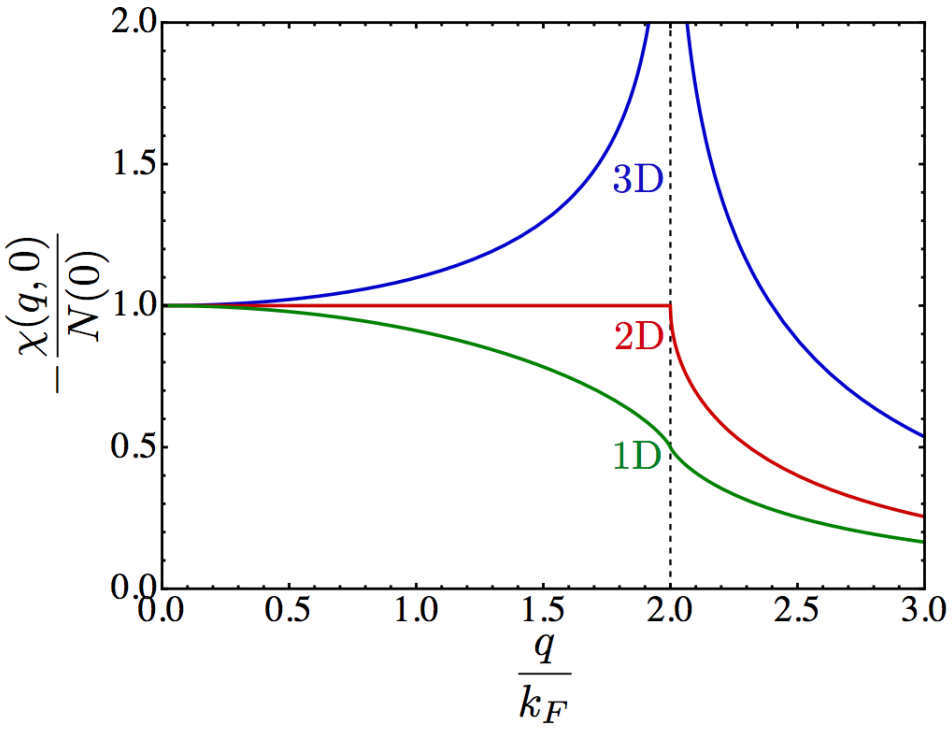

Figure 3.3: The behavior of the static density-density response function $\chi_0(q,0)$ normalized by the density of state at the Fermi energy $N(0)$ [106]. At $q = 2k_F$ it is possible to note singularities in the second and first derivative of $\chi_0(q,0)$ respectively in three and two dimension. In one dimension the function itself displays a logarithmic singularity at $q = 2k_F$.

has a logarithmic divergence, as shown in Fig. 3.3. A divergent non-interacting linear response function is a strong indication that a perturbation theory, no matters how weak is the interaction, is likely to fail. Hence, to find the ground state and the low-energy excitations of the interacting system, it is necessary to abandon the Landau-Fermi liquid theory and to start out with a completely new approach called *bosonization*, that lies at heart of the Tomonaga-Luttinger liquid model.

3.2 The Luttinger liquid model

One-dimensional quantum fluids, either fermionic or bosonic, constitute a universality class named by Haldane [33] in 1981 Luttinger liquids. The basis of this class of systems is the Tomonaga-Luttinger model that was introduced in 1963 [103] by Luttinger to describe the behavior of one-dimensional interacting Fermi gases at *zero temperature*. The starting

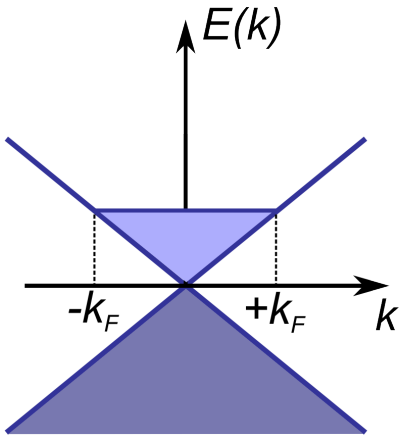

Figure 3.4: Single–particle energy spectrum of the Luttinger model. Occupied states are shown in light-blue while the grey-blue area represents the states which lead to infinite negative energy.

point of the model is the spinless Hamiltonian:

$$\begin{aligned} \hat{H} &= \hat{H}_0 + \hat{H}_{int} \\ &= \sum \varepsilon_k \hat{a}_k^\dagger \hat{a}_k + \frac{1}{2L} \sum_{kk'q} V(q)\, \hat{a}_{k+q}^\dagger \hat{a}_{k'-q}^\dagger \hat{a}_{k'} \hat{a}_k, \end{aligned} \tag{3.3}$$

where $\hat{a}_k^\dagger$ and $\hat{a}_k$ are creation and annihilation fermionic operators, $\varepsilon_k = \hbar^2 k^2/2m$ and $V(q)$ is the Fourier transform of the two-body interaction potential.

3.2.1 Bosonization

Since in one dimension the Fermi surface is constituted by two points $\pm k_F$, in order to describe low-energy excitations of the system the non-interacting Hamiltonian can be safely linearized around these two points. Hence two different dispersion branches are obtained for right and left-moving particles and the Hamiltonian can be written as:

$$H_0 = \sum_{k,r} \hbar v_F (rk - k_F) \hat{a}_{k,r}^\dagger \hat{a}_{k,r} \tag{3.4}$$

where $v_F = \hbar k_F/m$ is the Fermi velocity and $r = +1(-1)$ for right-(left-) moving particles. In the following the letter r is also used as an index $r = R(L)$ to indicate right-(left-) movers. By linearizing the Hamiltonian, an infinite number of occupied states at arbitrarily large negative energies have been introduced (Fig. 3.4). To avoid infinities in the theory, these infinite occupied states can be interpreted as a *vacuum* state $|0\rangle$ with respect

to which low-energy excitations around the Fermi surface are well defined. Hence this interpretation enforces a definition of normal ordering of operators with respect to the *vacuum* state[2]. The main point of the bosonization method is to assume that, because of the peculiar feature of one-dimensional systems, the low-energy excitations are long-wavelength ($q \ll k_F$) collective modes, which are likely to be represented by the density fluctuation operators:

$$\begin{aligned} \hat{\rho}_q^\dagger &= \sum_k \hat{a}_{k+q}^\dagger \hat{a}_k, \\ \hat{\rho}_q &= \sum_k \hat{a}_{k-q}^\dagger \hat{a}_k. \end{aligned} \tag{3.6}$$

It is worth noting that these operators display bosonic nature as they are product of two fermionic operators and that the interaction term in Hamiltonian (3.3) can be expressed in terms of $\hat{\rho}_q^\dagger$ and $\hat{\rho}_q$ as:

$$\hat{H}_{int} = \frac{1}{2L} \sum_q V(q) \hat{\rho}_{-q} \hat{\rho}_q, \tag{3.7}$$

Therefore, these operators have the considerable advantage to make the interaction Hamiltonian quadratic, while the same Hamiltonian, written in the fermionic representation, is an inconvenient product of four operators. Then the main objective of bosonization is to define rigorously some bosonic operators $\hat{b}_q^\dagger$ and $\hat{b}_q$ and to express also the linearized non-interacting Hamiltonian (3.4) in terms of these operators. By analyzing the commutation relations of left and right-moving density fluctuations, it is evident that for different species:

$$[\hat{\rho}_{qR}^\dagger, \hat{\rho}_{-q'L}^\dagger] = 0. \tag{3.8}$$

For the same species, instead, it is needed to take care of normal ordering to avoid infinities in the sum $\sum_k$ on occupied states (for a detailed derivation, we refer to Appendix C). Considering the quantization of momentum $q = 2\pi n/L$, with integer $n > 0\,(n < 0)$ for $r = R(L)$, the commutator can be recast as:

$$\left[\hat{\rho}_{qr}^\dagger, \hat{\rho}_{-q'r}^\dagger\right] = -\delta_{qq'} \frac{qrL}{2\pi}, \tag{3.9}$$

where $r = +1(-1)$ for right and left-movers respectively. Then, up to a normalization factor, this is a bosonic commutation relation and it is possible to define the following

[2]The definition of normal ordering for two generic creation and annihilation operators $\hat{A}$ and $\hat{B}$ is:

$$: \hat{A}\hat{B} := \hat{A}\hat{B} - \langle 0|\hat{A}\hat{B}|0\rangle. \tag{3.5}$$

bosonic operators:

$$\begin{aligned}\hat{b}_q^\dagger &= \left(\frac{2\pi}{L|q|}\right)^{1/2}\left[\Theta(q)\hat{\rho}_{qR}^\dagger + \Theta(-q)\hat{\rho}_{qL}^\dagger\right], \\ \hat{b}_q &= \left(\frac{2\pi}{L|q|}\right)^{1/2}\left[\Theta(q)\hat{\rho}_{qR} + \Theta(-q)\hat{\rho}_{qL}\right].\end{aligned} \tag{3.10}$$

where Θ is the step function and

$$\begin{aligned}\left[\hat{b}_q, \hat{b}_{q'}^\dagger\right] &= \delta_{qq'}, \\ \left[\hat{b}_q^\dagger, \hat{b}_{q'}^\dagger\right] &= \left[\hat{b}_q, \hat{b}_{q'}\right] = 0.\end{aligned} \tag{3.11}$$

Then the commutator between the non-interacting Hamiltonian (3.4) and the bosonic operators is

$$\begin{aligned}\left[\hat{H}_0, \hat{b}_q^\dagger\right] &= \hbar v_F |q| \hat{b}_q^\dagger, \\ \left[\hat{H}_0, \hat{b}_q\right] &= -\hbar v_F |q| \hat{b}_q.\end{aligned} \tag{3.12}$$

Hence $\hat{b}_q^\dagger$ and $\hat{b}_q$ are acting respectively as rising and lowering operators for $\hat{H}_0$, defining a boson algebra. For the proof that the boson representation is a complete basis of the Hilbert space we refer to Ref. [33] and [105]. In conclusion, Hamiltonian (3.4) can be represented in terms of bosonic operators as:

$$\hat{H}_0 = \sum_{q\neq 0} \hbar v_F |q| \hat{b}_q^\dagger \hat{b}_q. \tag{3.13}$$

3.2.2 Interactions

As stated above, the interaction term (3.7) is straightforwardly written in terms of fluctuation density operators and can be easily introduced into the model. Since low-energy excitations are restricted in the vicinity of the two-points constituting the Fermi surface ($\pm k_F$), there are only two types of scattering processes in the spinless case:

(a) Forward-scattering ($|q| \sim 0$): Interaction does not change the original directions of the two fermions.

(b) Back-scattering ($|q| \sim 2k_F$): Interaction makes two fermions exchange direction of motion.

More formally, this can be viewed by writing $\hat{a}_k$ in terms of right- and left-moving operators:

$$\hat{a}_k = \Theta(k)\hat{a}_{kR} + \Theta(-k)\hat{a}_{kL}. \tag{3.14}$$

Then, by the sign of the step functions, it can be individuated at which wavevector q the different contributions in the density fluctuation operators are different from zero:

$$\begin{aligned}\hat{\rho}_q &= \sum_{k,r} \hat{a}^\dagger_{k-q,r}\hat{a}_{k,r} \\ &= \underbrace{\Theta(k-q)\Theta(k)\,\hat{\rho}_{q,R} + \Theta(-k+q)\Theta(-k)\,\hat{\rho}_{q,L}}_{|q|\sim 0} \\ &\quad + \underbrace{\Theta(k-q)\Theta(-k)\hat{a}^\dagger_{k-q,R}\hat{a}_{k,L}}_{q\sim 2k_F} + \underbrace{\Theta(-k+q)\Theta(k)\hat{a}^\dagger_{k-q,L}\hat{a}_{k,R}}_{q\sim -2k_F}.\end{aligned} \tag{3.15}$$

Substituting (3.15) in (3.7), three possible low-energy processes can be distinguished and are graphically displayed in Fig. 3.5. Their scattering amplitudes are called respectively g_4, g_2 and g_1 for historical reasons. Two contributions to the interaction term can be individuated. The first one is responsible for the forward-scattering processes:

$$\hat{H}^{(1)}_{int} = \frac{1}{2L}\sum_{|q|<\Lambda} V(q)\left[\underbrace{(\hat{\rho}_{-q,R}\hat{\rho}_{q,R} + \hat{\rho}_{-q,L}\hat{\rho}_{q,L})}_{g_4} + \underbrace{(\hat{\rho}_{-q,R}\hat{\rho}_{q,L} + \hat{\rho}_{-q,L}\hat{\rho}_{q,R})}_{g_2}\right], \tag{3.16}$$

where Λ is a cutoff to select only the vicinity of the Fermi surface. The second one is responsible for the back-scattering processes and accounts for the g_1 processes:

$$\hat{H}^{(2)}_{int} = \frac{1}{2L}\sum_{||q|-2k_F|<\Lambda} V(q)\sum_{k,k'}\left(\underbrace{\hat{a}^\dagger_{k+q,R}\hat{a}_{k,L}\hat{a}^\dagger_{k'-q,L}\hat{a}_{k',R} + L\leftrightarrow R}_{g_1}\right). \tag{3.17}$$

For spinless fermions the processes g_1 can be recast as a g_2 process up to a minus sign (for details see Appendix C). With this simplification, we can send the cutoffs to infinity and combining eqs. (3.4), (3.16) and (3.17), eventually the total Luttinger model Hamiltonian is obtained:

$$\hat{H}_{LM} = \sum_{k,r}\hbar v_F(rk - k_F)\hat{a}^\dagger_{kr}\hat{a}_{kr} + \frac{1}{2L}\sum_{q,r} g_4\hat{\rho}_{-q,r}\hat{\rho}_{q,r} + g_2\hat{\rho}_{-q,r}\hat{\rho}_{q,-r}, \tag{3.18}$$

where $g_4 = V(q\sim 0)$ and $g_2 = V(q\sim 0) - V(2k_F)$. By bosonizing the kinetic part $\hat{H}_0$ of the Hamiltonian, we can now express the Luttinger Hamiltonian in terms of bosonic

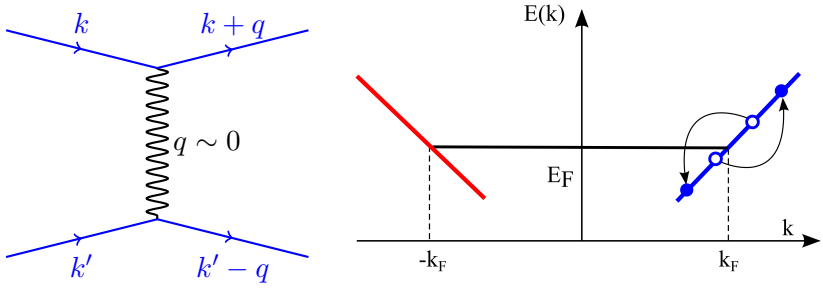

(a) $g_4\hat{\rho}_{-q,R}\hat{\rho}_{q,R}$

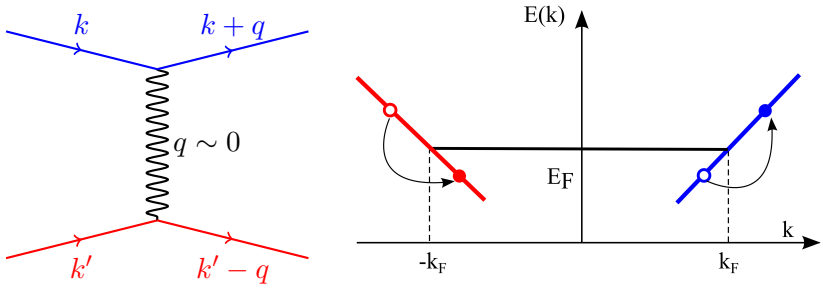

(b) $g_2\hat{\rho}_{-q,R}\hat{\rho}_{q,L}$

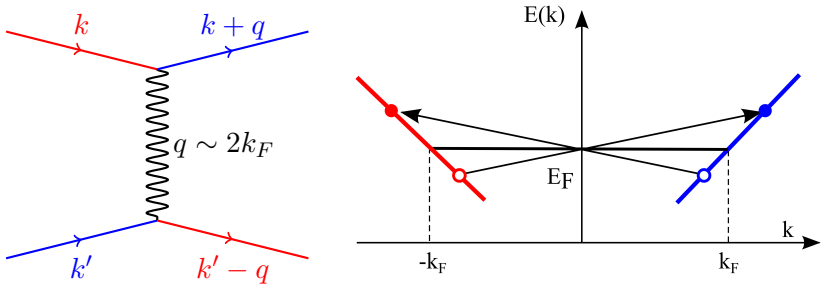

(c) $g_1\hat{a}^\dagger_{k+q,R}\hat{a}^\dagger_{k'-q,L}\hat{a}_{k',R}\hat{a}_{k,L}$

Figure 3.5: Graphical representation of the three different interaction processes in a one-dimensional Fermi liquid. Blue (red) lines represent right (left) moving particles. The notation g_4, g_2 and g_1 for the different scattering processes is called "g-ology" and it has historical reasons.

operators and diagonalize it by means of a Bogolioubov transformation.

3.2.3 Exact diagonalization

The Hamiltonian (3.18) is readily expressible in terms of the bosonic operators (3.10):

$$\hat{H}_{LM} = \sum_{q\neq 0} \left[\left(\hbar v_F + \frac{g_4}{2\pi} \right) |q| \hat{b}_q^\dagger \hat{b}_q + \frac{g_2}{4\pi} \left(\hat{b}_q^\dagger \hat{b}_{-q}^\dagger + \hat{b}_q \hat{b}_{-q} \right) \right]. \tag{3.19}$$

Since this Hamiltonian is quadratic in the bosonic operators also in the presence of interaction, it can be easily diagonalized by a Bogolioubov transformation:

$$\begin{aligned} \hat{b}_q^\dagger &= \cosh(\varphi)\hat{\beta}_q - \sinh(\varphi)\hat{\beta}_{-q}, \\ \hat{b}_q &= \cosh(\varphi)\hat{\beta}_{-q} - \sinh(\varphi)\hat{\beta}_q^\dagger, \end{aligned} \tag{3.20}$$

where φ is a rotation angle chosen to eliminate off-diagonal terms. By choosing $\varphi = g_2/(2\pi\hbar v_F + g_4)$, the Hamiltonian (3.19) can be written as:

$$\hat{H}_{LM} = \sum_q \hbar c_q |q| \beta_q^\dagger \beta_q, \tag{3.21}$$

where the new "sound velocity" is given by:

$$c_q = \sqrt{\left(v_F + \frac{g_4}{2\pi\hbar} \right)^2 - \left(\frac{g_2}{2\pi\hbar} \right)^2}. \tag{3.22}$$

Hence in a one-dimensional system arbitrarily large interactions (no perturbation theory is needed) just renormalize the sound velocity associated to a density fluctuations of fermions. Thus if $g_4, g_2 > 0$, the interacting system is somehow "stiffer", having a higher sound velocity than the non-interacting velocity v_F.

3.2.4 Spin-charge separation

Considering also the spin degree of freedom in one-dimensional liquid of fermions leads to a very counter-intuitive and fascinating phenomenon, namely *spin-charge separation*. Indeed, because of the collective nature of the low-energy excitations, a complete separation of the dynamics of the spin and charge degrees of freedom occurs. In this case, the density fluctuation operators can be redefined[3] as:

$$\hat{\rho}_r(q) \equiv \hat{\rho}_{r\uparrow}(q) + \hat{\rho}_{r\downarrow}(q), \tag{3.23}$$

[3] In order to make the notation clearer, from now on $\hat{\rho}_{q,r,\sigma} = \hat{\rho}_{r,\sigma}(q)$.

where $\hat{\rho}_{r,\uparrow}(q)$ and $\hat{\rho}_{r,\downarrow}(q)$ are the q-density fluctuation operators referred to r-moving particles with spin $\uparrow$ and $\downarrow$. Hence the linearized kinetic term becomes obviously:

$$H_0 = H_{0\uparrow} + H_{0\downarrow} = \sum_{k,r,\sigma} \hbar v_F (rk - k_F) \hat{a}^\dagger_{k,r,\sigma} \hat{a}_{k,r,\sigma}, \tag{3.24}$$

where the index $\sigma = \uparrow, \downarrow$. It shall be noted that, since we are considering a balanced spin-mixture, the Fermi wavevector k_F is the same for both spin species. As spin is introduced in the model, the more general case of spin-dependent interaction potentials has to be considered and therefore parallel spin ($g_{4||}$ and $g_{2||}$) and opposite spin ($g_{4\perp}$ and $g_{2\perp}$) interaction processes have to be distinguished. By introducing the definition (3.23) in the forward-scattering term ($q \sim 0$), Eq. (3.16) can be recast by summing over the spin degree of freedom:

$$\begin{aligned} \hat{H}^{(1)}_{int} \quad = \quad & -\frac{1}{2L} \sum_{\sigma,r} \sum_{q \neq 0} \left[g_{4||} \hat{\rho}_{r,\sigma}(-q) \hat{\rho}_{r,\sigma}(q) + g_{4\perp} \hat{\rho}_{r,\sigma}(-q) \hat{\rho}_{r,-\sigma}(q) \right] \\ & + \left[g_{2||} \hat{\rho}_{r,\sigma}(-q) \hat{\rho}_{-r,\sigma}(q) + g_{2\perp} \hat{\rho}_{r,\sigma}(-q) \hat{\rho}_{-r,-\sigma}(q) \right]. \end{aligned} \tag{3.25}$$

On the other hand, adding the spin degree of freedom in the back-scattering contribution at $q \sim 2k_F$ gives rise to two different terms:

- a $g_{1||}$ process (see Fig. 3.5c) that, by rearranging the fermion operators can be recast as $-g_{2||}$ process (forward-scattering with different spins) following exactly the same argument of section 3.2.2 (for details see Appendix C).
- a $g_{1\perp}$ process that involves a spin-flip term cannot be expressed in form of density fluctuations operators, represented in Fig. 3.6.

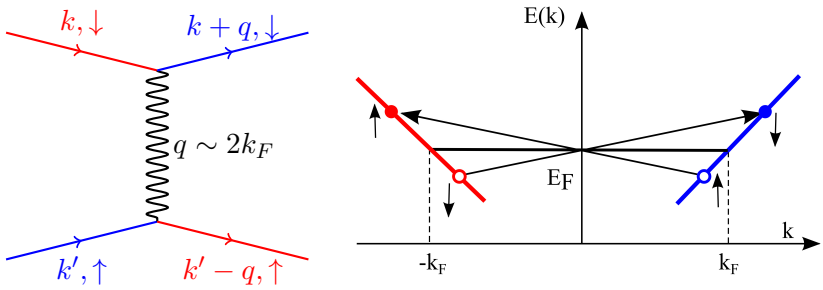

Figure 3.6: Graphical representation of the interaction process $g_{1\perp} \hat{a}^\dagger_{k+q,R\downarrow} \hat{a}_{k,L\uparrow} \hat{a}^\dagger_{k'-q,L\downarrow} \hat{a}_{k',R\uparrow}$ that involves a spin-flip of particles and therefore cannot be reconducted to a $g_{2\perp}$ process. Blue (red) lines represent right (left) moving particles.

$$\begin{aligned}\hat{H}^{(2)}_{int} &= -\frac{1}{2L}\sum_{q\neq 0}\sum_{\sigma,r} g_{1||}\,\hat{\rho}_{r,\sigma}(-q)\hat{\rho}_{-r,\sigma}(q) \\ &\quad +\frac{1}{2L}\sum_{q\neq 0}\sum_{\sigma,r} g_{1\perp}\,\hat{a}^{\dagger}_{k+q,r,\sigma}\hat{a}_{k,-r,-\sigma}\hat{a}^{\dagger}_{k'-q,-r,\sigma}\hat{a}_{k',r,-\sigma}. \end{aligned} \tag{3.26}$$

Thus, by substituting $g_{2||} \to g_{2||} - g_{1||}$, the total Luttinger Hamiltonian with spin degrees of freedom can be written in more compact form as:

$$\begin{aligned}\hat{H}_{LM} &= \sum_{k,r,\sigma} \hbar v_F(rk - k_F)\hat{a}^{\dagger}_{k,r,\sigma}\hat{a}_{k,r,\sigma} \\ &\quad +\frac{1}{2L}\sum_{q,r,\sigma} g_{4||}\hat{\rho}_{r,\sigma}(-q)\hat{\rho}_{r,\sigma}(q) + g_{4\perp}\hat{\rho}_{r,\sigma}(-q)\hat{\rho}_{r,-\sigma}(q) \\ &\quad +\frac{1}{2L}\sum_{q,r,\sigma} (g_{2||} - g_{1||})\hat{\rho}_{r,\sigma}(-q)\hat{\rho}_{-r,\sigma}(q) + g_{2\perp}(q)\hat{\rho}_{r,\sigma}(-q)\hat{\rho}_{-r,-\sigma}(q) \\ &\quad +\frac{1}{2L}\sum_{q,r,\sigma} g_{1\perp}\left(\hat{a}^{\dagger}_{k+q,-r,\sigma}\hat{a}_{k,r,-\sigma}\hat{a}^{\dagger}_{k'-q,r,\sigma}\hat{a}_{k',-r,\sigma'}\right). \end{aligned} \tag{3.27}$$

If $g_{1\perp} > 0$, it is possible to demonstrate [107] that the back-scattering term is *irrelevant* in the sense of renormalization group theory. In other words, $g_{1\perp}$ is renormalized to zero in the long-wavelength limit and its only effect is to renormalize the g_2 coupling constant, which remains a free parameter of the theory. Therefore, since ^{173}Yb has repulsive interactions, the spin-flip term can be neglected.

Remarkably, bosonization of Hamiltonian (3.27) can be fulfilled by introducing two spin-symmetric (charge) and spin-antisymmetric (spin) bosonic operators:

$$\begin{aligned}\hat{c}_q &= \frac{1}{\sqrt{2}}\left(\hat{b}_{q\uparrow} + \hat{b}_{q\downarrow}\right), \\ \hat{s}_q &= \frac{1}{\sqrt{2}}\left(\hat{b}_{q\uparrow} - \hat{b}_{q\downarrow}\right), \end{aligned} \tag{3.28}$$

where $\hat{b}^{\dagger}_{q\sigma}$ and $\hat{b}_{q\sigma}$ are based on definitions (3.10) with indexes σ added on both sides of the equations. It shall be noted that charge and the spin operators commute with each other $[\hat{c}^{\dagger}_q, \hat{s}_q] = 0$. This means that $\hat{c}^{\dagger}_q(\hat{s}^{\dagger}_q)$ creates charge (spin) fluctuations but no spin (charge) fluctuations. Thus, these excitations live in completely decoupled Hilbert spaces and, therefore, the bosonized Luttinger Hamiltonian (3.27) is separable into two mutually commuting parts:

$$\hat{H}_{LM} = \hat{H}_c + \hat{H}_s, \tag{3.29}$$

where:

$$\hat{H}_c = \sum_{q\neq 0}\left[\left(\hbar v_F + \frac{g_{4||}+g_{4\perp}}{\pi}\right)|q|\hat{c}_q^\dagger\hat{c}_q + \left(\frac{g_{1||}-g_{2||}-g_{2\perp}}{4\pi}\right)|q|\left(\hat{c}_q^\dagger\hat{c}_{-q}^\dagger + \hat{c}_{-q}\hat{c}_q\right)\right], \quad (3.30)$$

and:

$$\hat{H}_s = \sum_{q\neq 0}\left[\left(\hbar v_F + \frac{g_{4||}-g_{4\perp}}{\pi}\right)|q|\hat{s}_q^\dagger\hat{s}_q + \left(\frac{g_{1||}-g_{2||}+g_{2\perp}}{4\pi}\right)|q|\left(\hat{s}_q^\dagger\hat{s}_{-q}^\dagger + \hat{s}_{-q}\hat{s}_q\right)\right]. \quad (3.31)$$

By applying the same Bogolioubov transformation of sec. 3.2.3, it is possible to exactly diagonalize the Hamiltonian obtaining, in the low-q limit, two different velocities for spin and for charge excitations:

$$\begin{aligned} v_c &= \sqrt{\left[v_F + \left(\frac{g_{4||}+g_{4\perp}}{2\pi\hbar}\right)\right]^2 - \left[\frac{(g_{1||}-g_{2||})-g_{2\perp}}{2\pi\hbar}\right]^2} \\ v_s &= \sqrt{\left[v_F + \left(\frac{g_{4||}-g_{4\perp}}{2\pi\hbar}\right)\right]^2 - \left[\frac{(g_{1||}-g_{2||})+g_{2\perp}}{2\pi\hbar}\right]^2} \end{aligned} \quad (3.32)$$

In conclusion, as spin and charge excitations evolve in time according to two different and independent Luttinger Hamiltonians $\hat{H}_c$ and $\hat{H}_s$, charge and spin velocities are different.

3.2.5 Current and density field approach

From now on, the interactions couplings g_1, g_2 and g_4 are assumed to be q-independent. In ultracold atoms experiments, as explained in section 1.3, this condition is well satisfied. Hence, with this assumption, in this section we introduce a new formalism that will be used in section 3.3 to apply Luttinger theory to ultracold gases. Coming back to the spinless case we can conveniently rewrite the Hamiltonian (3.19) in terms of the two following bosonic fields:

$$\begin{aligned} \phi(x) &= -N\frac{\pi x}{L} + \frac{-i\pi}{L}\sum_{q\neq 0}\frac{1}{q}e^{-\alpha|q|/2-iqx}\left(\hat{\rho}_{qR}+\hat{\rho}_{qL}\right), \\ \Pi(x) &= \frac{J}{L} + \frac{1}{L}\sum_{q\neq 0}e^{-\alpha|q|/2-iqx}\left(\hat{\rho}_{qR}-\hat{\rho}_{qL}\right), \end{aligned} \quad (3.33)$$

where α is a cutoff parameter to be sent to 0 at the end of any calculation, $N = N_R + N_L$ and $J = N_R - N_L$ where $N_r = \sum_k :\hat{a}_{kr}^\dagger\hat{a}_{kr}:$ is the number of particles added to ground state on the $r = R, L$ moving branch. These two fields are related to the density and the

current operators in the thermodynamic limit ($L \to \infty$):

$$\begin{aligned} -\frac{1}{\pi}\partial_x\phi(x) &= \hat{\rho}_R(x) + \hat{\rho}_L(x), \\ \Pi(x) &= \hat{\rho}_R(x) - \hat{\rho}_L(x). \end{aligned} \tag{3.34}$$

The spinless Luttinger Hamiltonian (3.19) can be written in terms of these operators[4]:

$$\hat{H}_{LM} = \frac{u}{2}\int dx\, \left[\pi K\, \Pi(x)^2 + \frac{1}{\pi K}(\partial_x\phi)^2\right], \tag{3.35}$$

where:

$$u = \sqrt{\left(v_F + \frac{g_4}{2\pi\hbar}\right)^2 - \left(\frac{g_2}{2\pi\hbar}\right)^2}, \qquad K = \sqrt{\frac{2\pi\hbar v_F + g_4 - g_2}{2\pi\hbar v_F + g_4 + g_2}}. \tag{3.36}$$

The convenience of this approach relies on the fact that the Hamiltonian can be rewritten elegantly as a harmonic oscillator where u is the sound velocity and K, also known as Luttinger parameter, is a dimensionless quantity that determines the behavior of key physical observables such as as the momentum distribution, the correlation function and the density of states.

In the "spinful" case, the charge and spin fields can be defined as:

$$\phi_{c,s}(x) = \frac{1}{\sqrt{2}}\left[\phi_\uparrow(x) \pm \phi_\downarrow(x)\right], \tag{3.37}$$

$$\Pi_{c,s}(x) = \frac{1}{\sqrt{2}}\left[\Pi_\uparrow(x) \pm \Pi_\downarrow(x)\right], \tag{3.38}$$

where the $+(-)$ sign stands for charge (spin) operators. Then the total Luttinger Hamiltonian can be written as:

$$\hat{H}_{LM} = \sum_{\nu=c,s}\frac{u_\nu}{2}\int dx\, \left[\pi K_\nu\, \Pi_\nu(x)^2 + \frac{1}{\pi K_\nu}(\partial_x\phi_\nu)^2\right], \tag{3.39}$$

where:

$$u_\nu = v_F\sqrt{\left(1 + \frac{\xi_{4\nu}}{2}\right)^2 - \left(\frac{\xi_\nu}{2}\right)^2}, \qquad K_\nu = \sqrt{\frac{1 + \xi_{4\nu}/2 + \xi_\nu/2}{1 + \xi_{4\nu}/2 - \xi_\nu/2}} \tag{3.40}$$

[4]The non-interacting Hamiltonian (3.24) written in terms of the bosonic fields $\phi(x)$ and $\Pi(x)$ is

$$\hat{H}_0 = \frac{1}{2}\int dx\, v_F\, \left[\pi\Pi(x)^2 + \frac{1}{\pi}(\partial_x\phi(x))^2\right]$$

where $\xi_\nu = g/\pi\hbar v_F$ is a dimensionless parameter specified by the following definitions:

$$\begin{aligned} \xi_{4c} &= \frac{g_{4||}+g_{4\perp}}{\pi\hbar v_F}, \qquad \xi_{4s} = \frac{g_{4||}-g_{4\perp}}{\pi\hbar v_F}, \\ \xi_c &= \frac{g_{1||}-g_{2||}-g_{2\perp}}{\pi\hbar v_F}, \qquad \xi_s = \frac{g_{1||}-g_{2||}+g_{2\perp}}{\pi\hbar v_F}. \end{aligned} \tag{3.41}$$

These relations will be applied in section 3.3 to the case of a 1D ultracold Fermi gas. As explained in chapter 4, in this work only charge (density) excitations have been addressed through the experimental comparison between non-interacting harmonically trapped 1D Fermi gases and their interacting counterparts with two up to six spin components.

3.3 Luttinger liquid model for ultracold Fermi gases

In this section we will apply the general Luttinger formalism to ultracold fermionic gases confined in one dimension following Refs. [108, 109]. A harmonically trapped one-dimensional Fermi gas can be efficiently described by the following Hamiltonian:

$$\hat{H} = \sum_\sigma \int dx\, \hat{\Psi}^\dagger_\sigma(x) \left[\frac{-\hbar^2}{2m}\partial_x^2 + V_{ext}(x)\right] \hat{\Psi}_\sigma(x) + g_{1D} \int dx\, \hat{\Psi}^\dagger_\uparrow(x)\hat{\Psi}^\dagger_\downarrow(x)\hat{\Psi}_\downarrow(x)\hat{\Psi}_\uparrow(x) \tag{3.42}$$

where $V_{ext}(x)$ is the external harmonic potential, and $\hat{\Psi}^\dagger_\sigma(x)$ and $\hat{\Psi}_\sigma(x)$ are fermion creation and destruction operators in real space. In the homogeneous case ($V_{ext} = 0$), the Hamiltonian can be written in momentum space as:

$$\hat{H} = \sum \varepsilon_k \hat{a}^\dagger_k \hat{a}_k + \frac{g_{1D}}{L} \sum_{kk'q} \hat{a}^\dagger_{k+q,\uparrow}\hat{a}^\dagger_{k'-q\downarrow}\hat{a}_{k'\downarrow}\hat{a}_{k\uparrow} \tag{3.43}$$

It shall be noted that this Hamiltonian is the same as Eq. (3.3), from which the Luttinger liquid model has been derived, except for the fact that only atoms in different spin states interact. Indeed, as explained in sec. 1.3, in an ultracold Fermi gas, atoms of the same spin species do not interact because s-wave collisions are suppressed by the Pauli principle and higher partial wave collisions are energetically forbidden. As a consequence, when applying the Luttinger model to ultracold fermions, it can be safely assumed $g_{1||} = g_{2||} = g_{4||} = 0$, retaining only the $g_\perp$ processes. Moreover, all the different scattering processes have the same strength given by the 1D coupling constant g_{1D} shown in Eq. (1.90). Hence, a unique dimensionless interaction parameter can be defined

$$\xi = \frac{g_{1D}}{\pi\hbar v_F},$$

which in the homogeneous case, neglecting numerical pre-factors of order unity, can be interpreted as the ratio between the kinetic energy of an ideal Fermi gas with $v_F = \hbar\pi n/2m$ and the interaction strength $g_{1D}n$. Indeed, ξ is proportional to γ (1.91) with the relation $\xi = \pi^2\gamma/2$. By applying these considerations to Eqs. (3.41), the Luttinger spin and charge

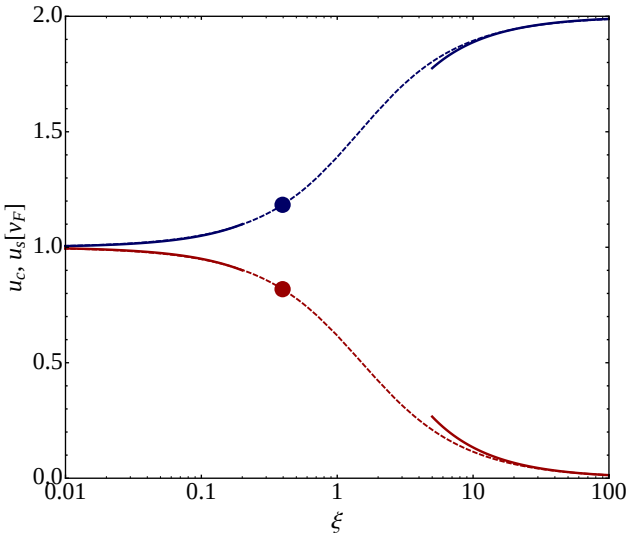

Figure 3.7: Charge (blue) and spin (red) velocities in unit of the Fermi velocity v_F as a function of the interaction parameter ξ. The solid lines are $u_{c,s}$ in the strong and weak coupling regime. The dashed lines are an interpolation between the two regimes. The points correspond to the value of ξ obtained for the 1D parameters of the systems specified in section 4.1.

velocities for a homogeneous ultracold quantum gas become:

$$\begin{aligned} u_c &= v_F\sqrt{1+\xi}, \\ u_s &= v_F\sqrt{1-\xi}. \end{aligned} \tag{3.44}$$

It shall be noted that in the non-interacting case $\xi = 0$, the trivial result $u_c = v_F = u_s$ is obtained. In the weak coupling limit ($\xi \ll 1$), it is possible to approximate the charge and spin velocities as:

$$\begin{aligned} u_c &= v_F\left(1+\frac{\xi}{2}\right), \\ u_s &= v_F\left(1-\frac{\xi}{2}\right). \end{aligned} \tag{3.45}$$

On the other hand, it is possible to investigate the strong-coupling regime starting from the Bethe-Ansatz exact solution (see also section 3.4) [32] of the Hamiltonian with a perturbation series around $\xi \to \infty$. To the first order, the Luttinger velocities are:

$$\begin{aligned} u_s &= \frac{2\pi\hbar n}{3m\xi}, \\ u_c &= \frac{\pi\hbar n}{m}(1 - 8\ln(2)/\pi^2\xi), \end{aligned} \tag{3.46}$$

where $n = N/L$ is the density of the 1D Fermi gas. The expansion around $\xi \to \infty$ confirms the intuition that when the repulsion between the atoms of the two different species is very strong, some properties of the gas are similar to those of an ideal single-component gas of indistinguishable particles. Intuitively, the infinite repulsion mimics the effects of a Pauli repulsion between distinguishable particles, i.e. atoms in a different internal state (see also section 3.4). The same phenomenon occurs, for instance, for strongly interacting bosons in 1D, where there is a mapping between hard-core bosons and free fermions [112–114]. In this limit the asymptotic values of the charge and spin velocity are:

$$u_c = \frac{\hbar\pi n}{m} = 2v_F, \qquad u_s = 0, \tag{3.47}$$

where $v_F = \hbar\pi n/2m$ is the Fermi velocity of a 1D homogeneous Fermi gas. Then, for

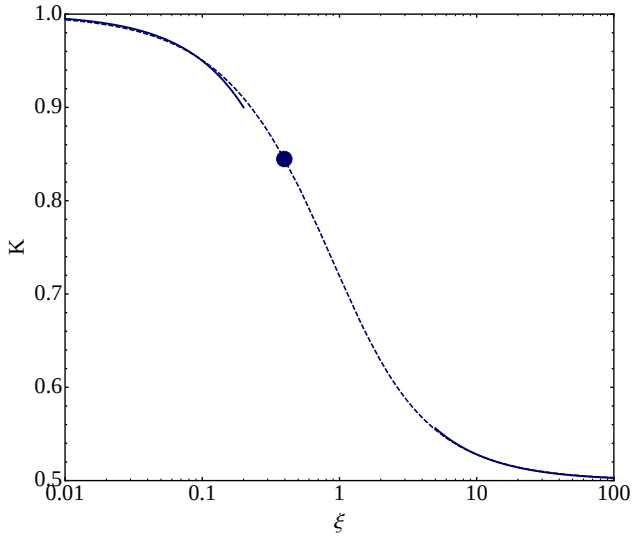

Figure 3.8: The solid lines show the Luttinger parameter K as function of ξ in the strong and weak coupling regime. The dashed lines are an interpolation between the two regimes. The point corresponds to the value of $K \simeq 0.8$ obtained for the 1D parameters of the systems specified in section 4.1.

infinite repulsions, the interacting 1D Fermi gas can be mapped on a non-interacting Fermi gas with a doubled Fermi wavevector $2k_F$ and with spin dynamics completely frozen.

The regime explored in this work is an intermediate coupling with $\xi \simeq 0.4$ as shown by the points in Fig. 3.7. Analogously, the Luttinger parameter in our system is $K \simeq 0.8$, an intermediate value between the non-interacting case $K = 1$ and the strongly interacting regime $K = 0.5$ (see Fig. 3.8). In order to estimate the Luttinger parameters of the experimental system, the inhomogeneity due to the harmonic trapping potential has been taken into account by performing a local density approximation (LDA), as explained in section 4.1.

3.4 Beyond Luttinger Liquid

The Luttinger Liquid paradigm is defined by assuming $T = 0$ and linearizing the single particle dispersion around the two Fermi points. Hence it constitutes an approximation of the original Hamiltonian, which nevertheless gives fundamental insights on the physics of one-dimensional many-body systems. However, there is an analytical method, originally proposed by H. Bethe in 1931 [115], that allows to exactly solve the problem of N_{at} particles interacting with a δ-like potential in one dimension. This powerful method, usually referred to as Bethe-Ansatz technique, relies on the hypothesis that the wavefunction ψ of such many-body systems is a superposition of plane waves [116], namely:

$$\psi = \sum_P C_{P,Q} \exp\left[i\left(k_{P1}x_{Q1} + \cdots + k_{PN_{at}}x_{QN_{at}}\right)\right], \tag{3.48}$$

where $0 < x_{Q1} < x_{Q2} < \cdots < x_{QN_{at}} < L$, with L the linear size of the homogeneous system, and P, Q are permutations of N_{at} integers[5]. This technique was successfully applied to one-dimensional systems of interacting bosons [117] and fermions [32] allowing the exact computation of the ground-state energy and the corresponding wavefunction.

Moreover the Bethe-ansatz technique gives access to the momentum distribution of the interacting system, by Fourier transforming the exact one-particle density matrix $\rho(x)$:

$$n(k) = \int dx\, e^{-ikx}\rho(x). \tag{3.49}$$

This turns out to be extremely useful in the comparison between theory and experiments as the momentum distribution $n(k)$ is one of the main observables in ultracold gases experiments.

[5]The coefficients $C_{P,Q}$ can be then arranged in a $N_{at}! \times N_{at}!$ matrix.

In Ref. [110], Ogata et al. used Bethe-Ansatz for a two-component fermionic 1D Hubbard chain with quarter-filling $N_{at}/L = 1/2$ at $T = 0$, in the limit of strong interactions ($\gamma \to \infty$). In this case, the momentum distribution features a power-law singularity (see Fig. 3.9) around k_F, contrary to the sharp jump of $n(k)$ at $k = k_F$, characteristic of the non-interacting Fermi gas:

$$n(k) \propto \frac{1}{2} - C|k - k_F|^{\alpha} \,\mathrm{Sign}(k - k_F), \tag{3.50}$$

where C is a numerical constant and $\alpha = 1/8$ [111].

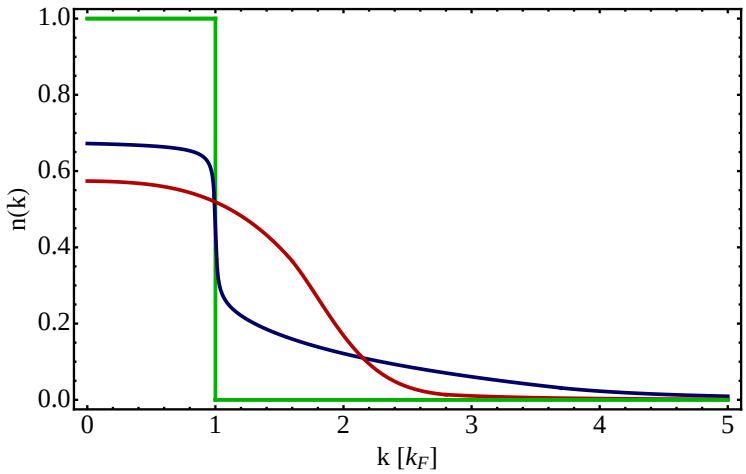

Figure 3.9: Momentum distributions for an ideal Fermi gas (green) and for a two-component Fermi gas in the strong-coupling limit in the $T = 0$ case (from Ref. [110], blue) and in the $T_S < T \ll T_F$[111] (red). See text for details.

Bethe-Ansatz offers also the possibility to include thermal fluctuation and compute the observables at $T > 0$. In Ref. [111], Cheianov at al. studied a two-component one-dimensional Fermi gas at $T > 0$ in the strong-coupling regime and, contrary to the non-interacting case, they find out that T_F is not anymore the only relevant energy scale in the system. Indeed, considering the spin degree of freedom, they individuate another characteristic temperature scale T_S, related to spin excitations. Intuitively, these are related to an imbalance between $N_\uparrow$ and $N_\downarrow$ with respect to the absolute energy minimum, which corresponds to the balanced mixture ($N_\uparrow = N_\downarrow = N_{at}/2$). The typical energy scale of these spin excitations is estimated in the $\gamma \to \infty$ limit as:

$$T_S \simeq \frac{8 \ln 2}{3} \frac{T_F}{\gamma}. \tag{3.51}$$

Hence we can individuate two different quantum ($T \ll T_F$) regimes:

$T \ll T_S$: a low temperature regime, which reduces to the Luttinger Liquid model. In this regime low-energy excitations are successfully described in terms of collective, coherent spin and charge modes. The momentum distribution in this regime is shown by the blue curve in Fig. 3.9.

$T > T_S$: an intermediate temperature regime, where the spin degree of freedom is strongly disordered but nevertheless density fluctuations are still well described by the Luttinger liquid theory. This has been recently referred as "spin-incoherent Luttinger liquid" [118–120]. The resulting $n(k)$ is shown by the red curve Fig. 3.9.

As shown Fig. 3.9, the crossover between the two regimes leads to a significant change in the momentum distribution. In the spin-incoherent regime, the singularity at $k = k_F$ vanishes and the large momentum tail gets suppressed. Nevertheless, in both cases there is an overall broadening of the momentum distribution compared to the non-interacting regime. This broadening can be understood intuitively (see Fig. 3.10) by considering a two-component balanced spin-mixture with $N_\uparrow + N_\downarrow$ atoms in a box in two extreme cases: the non-interacting regime ($\gamma = 0$) and the strong-coupling limit ($\gamma = \infty$). Interestingly

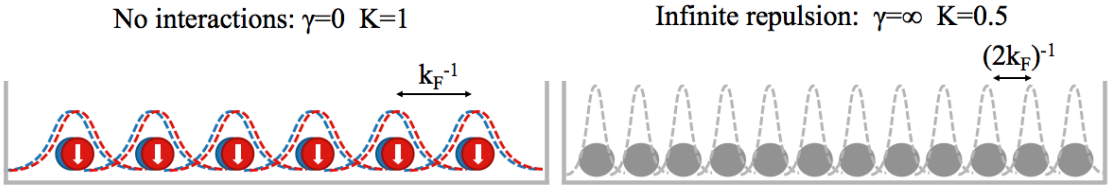

Figure 3.10: Intuitive picture of fermionization between distinguishable fermions. The interaction parameters γ and K are defined in Eqs. (1.91) and (3.40), respectively.

there is a mapping between these two cases, since in the strong-coupling regime, repulsive interactions act as an additional Pauli principle, as particles tent to avoid each other to minimize their mutual overlap. In this regime, the strongly-interacting Fermi gas exhibits a wavefunction whose absolute square value is the same as the one of an ideal Fermi gas, but with twice the number of particles or, equivalently, with twice the Fermi wavevector. This mapping has been verified for a one-dimensional gas of strongly interacting bosons [113, 114] and for two fermions in one-dimensional tubes [121]. This means that some physical observables, such as the spatial density profile and the density-density correlation function, are efficiently described by the non-interacting theory. This mapping is often referred as "fermionization" of distinguishable fermions and explains intuitively the broadening of $n(k)$ towards large momenta at strong and intermediate coupling. As we will see, fermionization plays a central role in explaining the physics of strongly-interacting fermions

in reduced dimensions, namely in one-dimensional wires created by 2D optical lattices (chapter 4) and in "zero-dimensional" wells realized in a 3D optical lattice (chapter 5).

3.5 Multi-component one-dimensional systems

Ultracold gases offer the possibility to engineer and investigate experimentally new quantum systems, which could be studied only on a theoretical point of view. This is the case of the multi-component one-dimensional systems, which were studied in the past [122] and still trigger renewed interest nowadays [116, 123–125]. In principle, the generalized Hamiltonian for a one dimensional system with N fermionic spin components features a real-symmetric interaction couplings matrix $g_{\sigma,\sigma'}$:

$$\hat{H} = \sum_{\sigma=1}^{N} \int dx\, \hat{\Psi}^{\dagger}_{\sigma}(x) \left(\frac{-\hbar^2}{2m} \partial_x^2 \right) \hat{\Psi}_{\sigma}(x) + \sum_{1 \leq \sigma < \sigma' \leq N} g_{\sigma,\sigma'} \int dx\, \hat{\Psi}^{\dagger}_{\sigma}(x) \hat{\Psi}^{\dagger}_{\sigma'}(x) \hat{\Psi}_{\sigma'}(x) \hat{\Psi}_{\sigma}(x), \tag{3.52}$$

where $\sigma = 1, \ldots, N$ denotes the spin component. The bosonization of Hamiltonian (3.52) individuates N different bosonic fields, which generalize the charge and spin modes of the two-component Luttinger liquid. All these bosonic modes have in principle different velocities. However, since the interaction is spin-independent, $g_{\sigma,\sigma'} = g_{1D}$, with g_{1D} defined in Eq. (1.90), and the Hamiltonian displays a $SU(N)$ symmetry (see section 1.3.2). In this highly symmetric case, the bosonization is significantly simplified and the normal modes operators generalizing the charge and spin operators defined in Eq. (3.37) can be built with the help of the traceless Cartan sub-algebra generators of $SU(N)$ [126]:

$$\phi_0 = \frac{1}{\sqrt{N}} \sum_{\sigma=1}^{N} \phi_{\sigma} \tag{3.53}$$

$$\phi_l = \frac{1}{\sqrt{l(l+1)}} \sum_{\sigma=1}^{N} C_{\sigma}^{(l)} \phi_{\sigma}, \;\; l = 1, \ldots, N-1, \tag{3.54}$$

where:

$$C_{\sigma}^{(l)} = \begin{cases} 1 & \text{if } \sigma \leq l \\ -l & \text{if } \sigma = l+1 \\ 0 & \text{otherwise} \end{cases}, \tag{3.55}$$

and ϕ_σ is the bosonic operator defined in Eqs. (3.33) for particles with spin σ. Note that ϕ_0 defined in Eq. (3.53) is the analogous of the charge mode ϕ_c, namely a totally symmetric linear combination of the N operators ϕ_σ. All the other $N-1$ modes, defined in Eq. (3.54), are a generalization of the two-component spin mode ϕ_s and display all the

same velocity.

Beyond bosonization, also Bethe-Ansatz (see section 3.4) can give valuable insights on the physics of multi-component one-dimensional fermions. Indeed, by using this technique, it is possible to prove a counterintuitive mapping to a 1D spinless bosonic liquid, a phenomenon called by the authors of Ref. [127] "high-spin bosonization". In this case, the term bosonization does not refer to the analytical technique to solve the Luttinger model. Instead, it recalls that, in one dimension, increasing the number of spin-component N keeping fixed and balanced the number of particles per spin component ($N \to \infty$, with $N_{at}/N > 0$), interacting fermions exhibit properties of a spinless bosonic liquid. We can give an intuitive explanation of this result: by raising the number of spin components in the system, the degree of distinguishability in the system is increased as well, causing the system to lose its fermionic character. In the extreme limit where the number of spin components is the same as the number of particles, the Pauli principle is ineffective since the fermions are all distinguishable. This result has been rigorously proven by C. N. Yang and Y. Y. Zhuang in 2011 [34] assuming a balanced spin mixture and $SU(N)$ symmetry. Therefore, exploiting the precise control on spin population of ^{173}Yb and its highly symmetric interactions, we can verify this prediction experimentally, as shown in the following chapter.

Chapter 4

Multi-component one-dimensional liquid of fermions

Ultracold atoms are the ideal test-bench to study many-body quantum physics in reduced dimensions owing to the possibility to use optical lattices to tune the dimensionality of the system. In the last years much effort has been devoted to the experimental study of ultracold bosonic atoms in one dimension, with the observation e.g. of Tonks gases [113, 114], non-equilibrium dynamics [128] and quantum phase transitions [129]. On the other hand, one-dimensional fermions have been long investigated theoretically over the last fifty years, e.g. with the application of the Bethe-Ansatz technique [32] (see section 3.4 above) for N particles with contact interaction and with the definition of the Luttinger Liquid theoretical paradigm [33]. Nevertheless, apart from experiments on molecular bound states in one dimension [130], spin imbalance [131] and fermionization in few-fermions systems [121], a comprehensive experimental investigation of one-dimensional Fermi gases was still lacking. In this chapter we report the experiments performed during my PhD thesis to characterize a multi-component one dimensional liquid of fermions realized by loading ^{173}Yb atoms in a two-dimensional optical lattice.

In the first place (section 4.1), we characterized the role of correlations in the one-dimensional fermionic wires by showing how increasing the numbers of spin components leads to a broadening of the momentum distribution width driven by interactions. On the other hand it is shown how the momentum distribution in three dimensions does not exhibit any dependence on the number of spin components, demonstrating the crucial role of reduced dimensionality in enhancing correlations in the system. In section 4.2, Bragg spectroscopy has been used to investigate density excitations of the system both at high momentum ($q > k_F$) and low momentum ($q \ll k_F$). In particular it is shown

how the response to long-wavelength excitations changes by varying the number of spin components compared to the response in three dimensions. In section 4.3 we characterized the system by studying the lowest collective excitation (breathing mode) as a function of the number of spin components. In particular, we validated for the first time the large-spin bosonization first predicted in Ref. [34], according to which a high-spin one-dimensional liquid of fermions exhibits properties of a bosonic spinless liquid.

4.1 Momentum distribution

The starting point of these measurements is a ^{173}Yb degenerate trapped Fermi gas at $T \leq 0.3\,T_F$ and with $N_{at} \simeq 6500$ atoms per spin component. The momentum distributions $n(k)$ (where k is the atomic momentum divided by the reduced Planck's constant $\hbar$) are analyzed varying the number of spin components by means of the all-optical techniques illustrated in section 2.4. After loading the Fermi gas in a two-dimensional $\lambda_L = 759$ nm optical lattice of depth $s = 40$ using an exponential ramp of 150 ms, we wait 10 ms and then suddenly switch off the trap in less than 10 μs. A time-of-flight (TOF) measurement is performed by detecting the atomic density by means of absorption imaging after a ballistic expansion of $t_{TOF} = 23$ ms, as done in previous works to measure the $n(k)$ of a Tonks-Girardeu gas [114]. The expansion is in the far-field regime, which maps the initial momentum distribution $n(k)$ onto the expanded density in coordinate space. A typical image of the atomic cloud is reported in Fig. 4.1, where x denotes the axis of the wires. The cloud is elongated along y since this is the direction of tighter in-trap confinement, which corresponds to higher momentum in the far-field regime. Integration over y and normalization to the same unity area results in the $n(k)$ curves plotted in Fig. 4.2 and 4.4 for a different number of spin components N.

4.1.1 Ideal 1D Fermi gas momentum distribution

In the noninteracting case $N = 1$ the measured curve is very well accounted for by the theory of a trapped ideal Fermi gas (Fig. 4.2). In order to calculate the theoretical non-interacting momentum distribution we had to take into account the presence of a trapping potential along the tube axis x, with (angular) frequency $\omega_x = 2\pi \times (102.9 \pm 0.2)$ Hz. This inhomogeneity causes the 1D fermionic wires to have a nonuniform density profile, which translates, according to section 1.1, in the following one-dimensional momentum distribution:

$$n_{1D}(k) = -\sqrt{\frac{k_B T}{2\pi m \hbar^2 \omega_x^2}}\,\mathrm{Li}_{1/2}\left(-\mathcal{F} e^{-\frac{\hbar^2 k^2}{2 m k_B T}}\right), \tag{4.1}$$

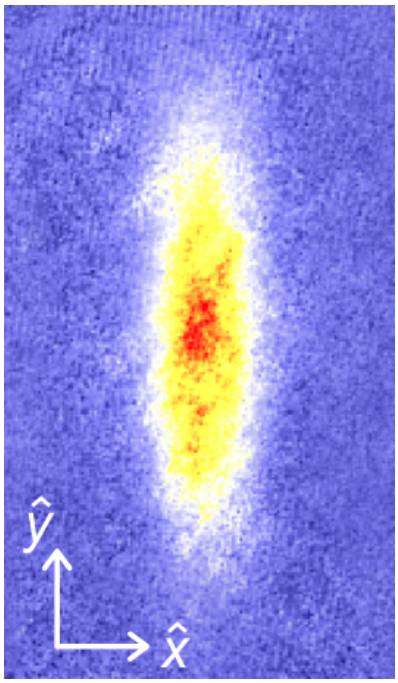

Figure 4.1: False color time-of-flight absorption image of a six spin component 1D Fermi gas. The x-axis is the direction of the wires and the density is integrated along the vertical y-axis. Here the number of atoms per spin component is $N_{at} = 6500$.

where $\mathcal{F}$ is the fugacity and $\mathrm{Li}_{1/2}$ is the Polylogarithmic function of order 1/2. Additionally, moving out of the trap center, the number of atoms per wire is decreasing from a maximum of 20 (per spin component) in the central wire, to a vanishing occupation of the more peripheral wires (see Fig. 4.3).

In order to consider these two effects, the following procedure was adopted: the number of fermions N_{ij} in the wire ij has been calculated in the noninteracting case by determining the lowest-energy configuration of N_{ij} which satisfies both Fermi statistics (assuming $T = 0$) and the constraint on the total atom number $N_{at} = \sum_{ij} N_{ij}$. The calculation has been performed by taking into account a wire-dependent energy potential offset:

$$\epsilon_{ij} = \frac{1}{2} m\omega_y^2 d^2 i^2 + \frac{1}{2} m\omega_z^2 d^2 j^2, \tag{4.2}$$

where $d = \lambda_L/2$ is the lattice spacing and $\omega_y = 2\pi \times 93$ Hz and $\omega_z = 2\pi \times 96$ Hz are the angular frequencies of the slowly-varying harmonic trapping potentials in the orthogonal

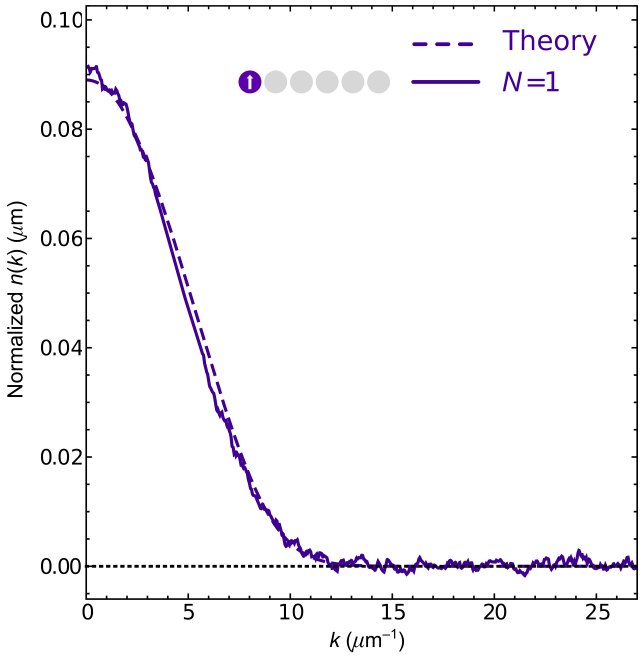

Figure 4.2: Solid line: Momentum distribution $n(k)$ measured after time-of-flight absorption imaging for polarized fermions loaded in the 1D wires. Dashed line: theoretical curve calculated taking $\omega_x = 2\pi \times 103$ Hz, $T/T_F = 0.3$, $V_0 = 40E_R$. The experimental curve is obtained averaging over 35 images.

directions to the wires. Hence the total energy to be minimized in order to find N_{ij} is

$$E[\{N_{ij}\}] = \sum_{ij} N_{ij} \left(\frac{1}{2} m\omega_y^2 d^2 i^2 + \frac{1}{2} m\omega_z^2 d^2 j^2 \right) + \sum_{n_x=0}^{N_{ij}} \hbar\omega_x \left(n_x + \frac{1}{2} \right). \tag{4.3}$$

The resulting atom distribution N_{ij} at $T = 0$ (see Fig. 4.3) is used to determine the local Fermi temperature $T_F(i,j) = N_{ij}\hbar\omega_x/k_B$ of the wire ij, which in turn determines the fugacity $\mathcal{F}_{ij}$ through the relation:

$$\mathrm{Li}_{1/2}\left(-\mathcal{F}_{ij}\right) = -\frac{T_F(ij)}{T}. \tag{4.4}$$

In this way it is possible to determine the momentum distribution $n_{ij}(k)$ in each wire using Eq. (4.1), and then calculate the weighted average $n(k)$ over all the wires, taking the number of atoms per wire N_{ij} as weight:

$$n(k) = \frac{1}{N_{at}} \sum_{ij} N_{ij} n_{ij}(k). \tag{4.5}$$

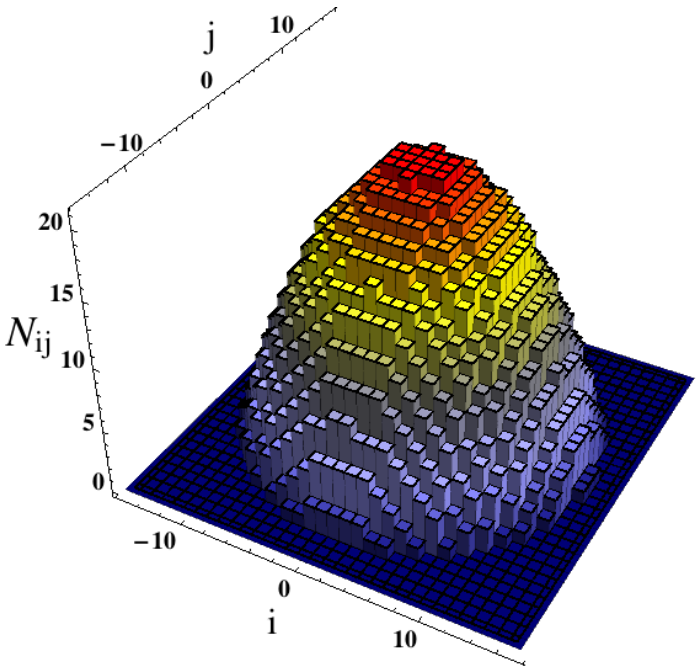

Figure 4.3: Distribution of atoms N_{ij} in the tubes at $T = 0$. In our experimental configuration, the central tubes feature about 20 atoms.

This procedure yields a very good description of the experimental system, as we can verify by looking at the agreement between the experimental data and the theoretical curve for $N = 1$ in Fig. 4.2, where the only adjusted parameter is the ratio T/T_F. The temperature assumed for the calculation is $T = 0.3\,T_F$, which well agrees with the T/T_F ratio measured in the 3D Fermi gas after ramping down the lattices and fitting the time-of-flight density distribution with Eq. (2.12).

4.1.2 Multi-component Fermi gas momentum distribution

Increasing the number of components N, a clear monotonic broadening of the momentum distribution is observed, which manifests in a reduction of the weight at low k and in a slower decay of the tails at large k (see Fig. 4.4). The observed broadening of $n(k)$ arises from a pure many-body effect. Indeed, an opposite behavior would be predicted on the basis of a simple mean-field argument: repulsive interactions between trapped fermions determine an effectively weaker confinement along the wire axis x and hence a broader in-situ density profile. This in turn would lead to a narrower time-of-flight momentum distribution $n(k)$ with respect to that of the ideal gas (see Fig. 4.7). The increased width is rather caused by the strong correlations induced in the system by the

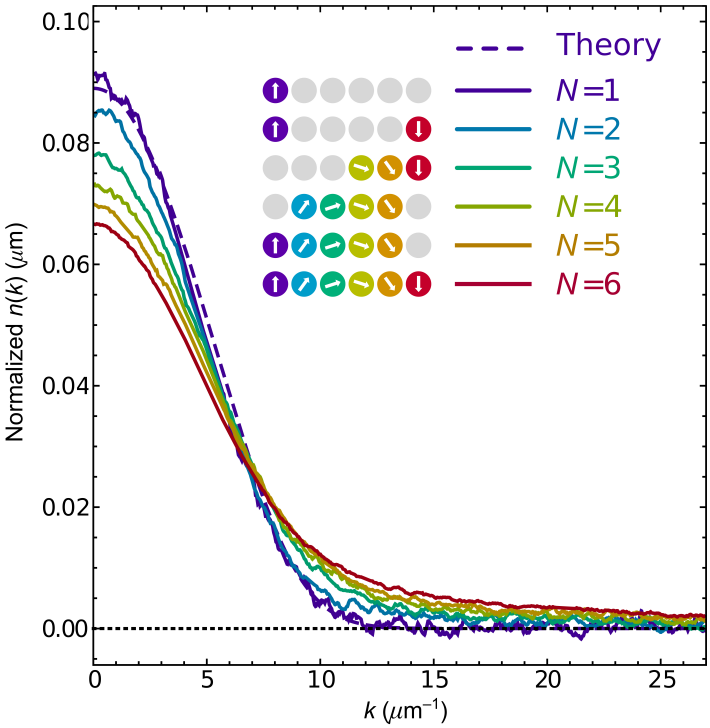

Figure 4.4: Momentum distribution $n(k)$ of 1D Fermi gases measured after time-of-flight absorption imaging for a different number N of spin components in the system. Each curve results from the average of 30-50 experimental images, after integration along the y-axis and normalization to unity area. Dashed line: theoretical curve calculated for the $N = 1$ case.

inter-particle repulsion. In order to give a qualitative understanding of this effect we recall the "fermionization" argument, explained in section 3.4. Considering the case of infinite repulsion for a spin-1/2 system, we can define the opposite-spin density-density correlation function as

$$G_{\uparrow\downarrow}(d) = \langle \hat{n}_\uparrow(x+d)\hat{n}_\downarrow(x)\rangle, \tag{4.6}$$

where $\hat{n}_\uparrow(x)$ and $\hat{n}_\downarrow(x)$ are the density operators for the two spin components at position x. Because of strong repulsion among atoms, $G_{\uparrow\downarrow}(d)$ falls to zero for $d \to 0$ as $G_{\uparrow\uparrow}(d)$ does in the case of a spin-polarized gas, thus mimicking the effects of a Pauli repulsion between distinguishable particles. As explained in section 3.4, this "fermionization" effect, restricting the effective space which is available to the particles, causes them to populate states with larger momentum [110, 111].

Moreover, as shown in section 3.4, the details of $n(k)$ depend nontrivially on the temperature, owing to the thermal population of spin excitations whose typical energy

scale $k_B T_S$ defines the crossover between the spin-ordered regime ($T \ll T_S$) and the spin-incoherent Luttinger liquid regime ($T \gg T_S$) [111]. This energy scale corresponds to the maximum energy difference between different spin configurations and, in the limit of large γ, can be estimated as:

$$\epsilon(\gamma) = \frac{8 \ln 2}{3} \frac{E_F}{\gamma}, \tag{4.7}$$

which, for our experimental parameters, corresponds to a spin temperature $T_S = \epsilon/k_B \simeq 0.4\, T_F$. The temperature regime for our experiments is $T \simeq 0.3\, T_F$, which is then slightly below the temperature scale for spin excitations (for further details see the following section).

A possible explanation of the observed changes in $n(k)$ in terms of different temperatures for different N has been ruled out. Indeed, it has been verified that, after slowly ramping down the lattices in $t = 150$ ms to recover a 3D Fermi gas, the temperature measured for the different spin mixtures has the same value $T = 0.3\, T_F$ for all N within the experimental uncertainties. In this 3D regime the effects of interactions are very weak. As a matter of fact, for 3D Fermi gases we have not detected any significative change in $n(k)$ as a function of N (Fig. 4.5). This observation makes the temperature measurement in 3D reliable and suggests that the observed broadening in the interacting 1D system comes from the increased correlations.

In particular, the difference between the two cases is highlighted in Fig. 4.6 where 1D and 3D momentum distribution are compared on a log-log scale. The one-dimensional momentum distribution is expected to exhibit a power law singularity at k_F (see Fig. 3.9). However, in our experimental configuration, this feature is washed out by the inhomogeneity induced by the trap and by the averaging over different tubes. It is interesting to note that, in the 1D case, the large-momentum tails display a behaviour consistent with a power-law, where the slopes differ depending on the number of spin components N. Conversely, in the 3D case, no large-momentum tail is observed and no significant dependence on N can be detected within our signal-to-noise ratio (SNR). It shall be noted, though, that our SNR is insufficient also to observe the well-known large-momentum tail of the form $n(k) \to C/k^4$, where C is usually defined as contact [132–134]. It could be interesting to further investigate the large-momentum behaviour as a function of N by improving our SNR, and compare the data with theoretical predictions for multi-component fermions that, to our knowledge, are still missing, as discussed in the following subsection.

Comparison with theoretical models

So far, no theoretical predictions on the momentum distributions are available for an interacting one-dimensional liquid in the intermediate coupling regime and at finite temper-

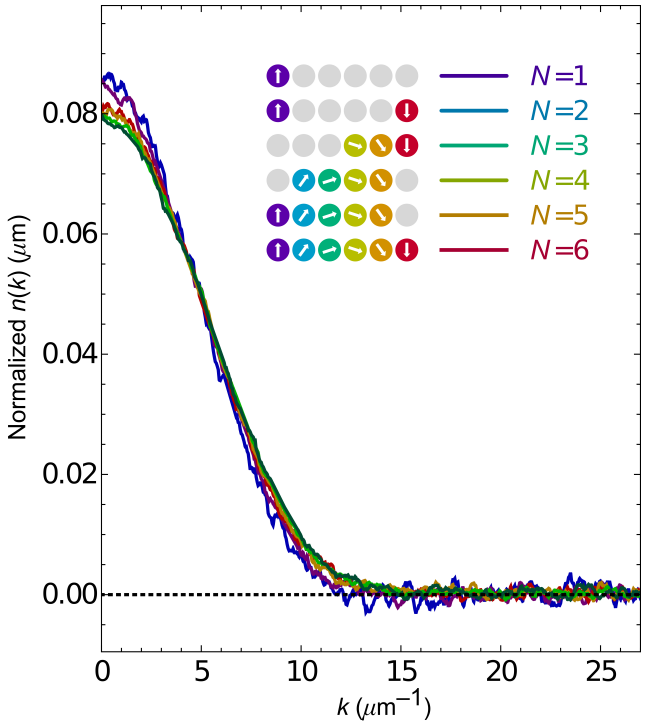

Figure 4.5: Momentum distribution $n(k)$ of 3D Fermi gases measured after time-of-flight absorption imaging for a different number N of spin components in the system. Each curve results from the average of 20-30 experimental images, after integration along the y-axis and normalization to unity area. Varying the number of spin components do not introduce any significant difference in the 3D momentum distributions.

ature, nor for the two-component neither for the multi-component case. As mentioned in section 3.4, the theoretical predictions on the momentum distribution are restricted to the limit of strong coupling ($\gamma \to \infty$) and to the two-component Fermi gases, therefore we limit our analysis to these very special cases. In particular, for $N = 2$, the interaction regime of our 1D samples is described by the dimensionless parameters $\gamma = 4.8$ and $K_c = 0.8$ (see sections 1.3.1 and 3.3), both evaluated by averaging over the different tubes. These values lie in the strongly-interacting regime between the ideal Fermi gas ($\gamma = 0, K_c = 1$) and a fully fermionized gas ($\gamma = \infty, K_c = 0.5$). Figure 4.7 shows the comparison between the momentum distribution calculated using mean-field theory arguments and the theoretical $n(k)$ for $N = 2$ and infinite interactions ($\gamma \to \infty$) in the two limiting regimes $T = 0$ [110] and $T_S < T \ll T_F$ [111]. These curves are based on a Bethe-Ansatz calculation of the homogeneous momentum distributions $n_{theor}(k)$, both shown in Fig. 3.9. In order to take into account the harmonic confinement, a LDA approach is applied to $n_{theor}(k)$, which is

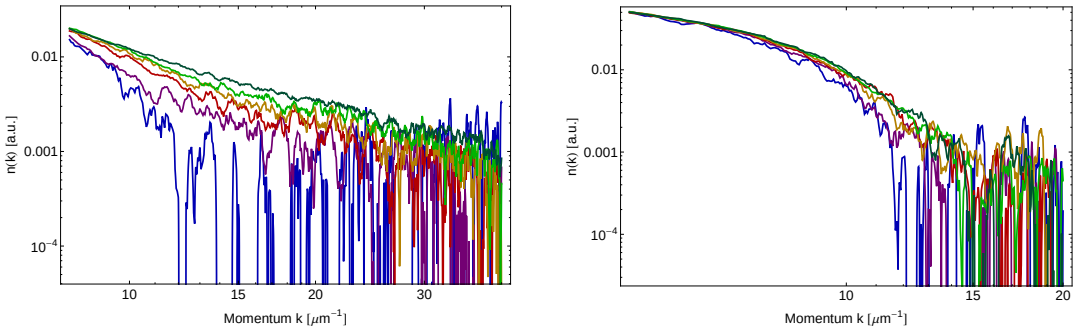

(a) $n(k)$ tail in 1D **(b)** $n(k)$ tail in 3D

Figure 4.6: Momentum distribution tail on a log-log scale to highlight the difference between interacting multi-component fermions in one and three dimensions. Note that in one dimensional case the tails have different slopes depending on the number of spin components.

then averaged over the density distribution of the-harmonically confined single wire:

$$n_{1D}(x) = -\sqrt{\frac{mk_BT}{2\pi\hbar^2}}\mathrm{Li}_{1/2}\left(-\mathcal{F}e^{-\frac{m\omega_x^2}{2k_BT}x^2}\right), \tag{4.8}$$

which defines a local Fermi wavevector $k_F(x) = \pi n_{1D}(x)$. To take into account infinite interaction, we followed the fermionization argument and compute the density distribution for the two-component Fermi gas with infinite interactions as its non-interacting counterpart with $N_{at} \to 2N_{at}$. The density $n_{1D}(x)$ is used to compute a local $n_{theor}\left[k; k_F(x)\right]$ which is averaged over the $n_{ij}(x)$ of the single wire ij. This procedure is repeated for all the wires computing a weighted average over the whole sample. The average momentum distributions $n(k)$ is then:

$$n_{LDA}(k) = \frac{1}{N_{at}}\sum_{ij} N_{ij}\left[\frac{1}{A_{ij}}\int dx\, n_{ij}(x)\, n_{theor}\left[k; k_F(x)\right]\right], \tag{4.9}$$

where $A_{ij} = \int dk \int dx\, n_{ij}(x)\, n_{theor}\left[k, k_F(x)\right]$ is the normalization constant for the wire ij.

On the other hand, the mean-field profile (dotted line in Fig. 4.7) is computed by estimating the effective weaker confinement induced by strong interaction considering a Thomas-Fermi radius $R_{TF} = \sqrt{2\mu/m\omega_x^2}$ of a fermionized gas, by scaling the Fermi energy $\mu = N_{at}\hbar\omega_x \to 2N_{at}\hbar\omega_x$. Then the Thomas-Fermi radius scales as $R_{TF} \to \sqrt{2}R_{TF}$. A qualitative comparison between the two many-body momentum distributions and the mean-field prediction shows that our interaction regime is not explainable in terms of

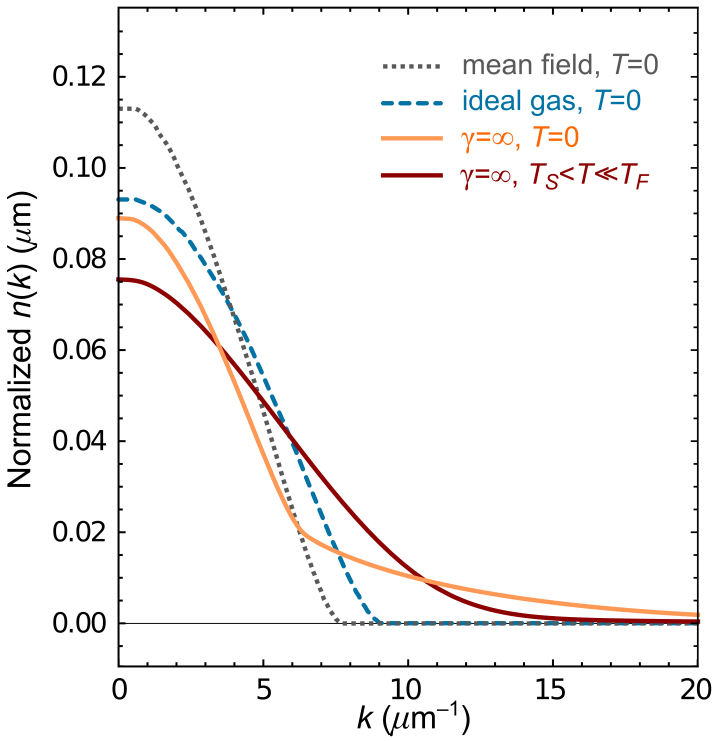

Figure 4.7: Theoretical momentum distributions for $N = 2$ calculated using a LDA approach in different cases. Ideal Fermi gas at $T = 0$ (dashed), mean- field treatment of infinite interactions at $T = 0$ (dotted), full many-body problem for infinite interactions both for $T = 0$ (light solid, from [110]) and $T_S < T \ll T_F$ (dark solid, from [111]).

mean-field theory and that $n(k)$ is determined by many-body correlations.

4.2 Bragg spectroscopy

Bragg spectroscopy is a powerful technique that gives access to the density excitations of an atomic system [135–137]. It relies on stimulated inelastic light scattering and is performed by exciting the atomic cloud with two off-resonant laser beams (see Appendix D). This technique allows the selective excitation of density waves with energy $\hbar\omega = \hbar(\omega_1 - \omega_2)$ and momentum $\hbar\mathbf{q} = \hbar(\mathbf{k_1} - \mathbf{k_2})$, where ω_i and $\mathbf{k}_i$ are the (angular) frequencies and the wavevectors of the two Bragg beams, respectively (Fig. 4.8). In atomic physics experiments typically $\omega/2\pi$ is up to few MHz and consequently we can approximate $|\mathbf{k_1} - \mathbf{k_2}| \sim 2|k_L|\sin(\theta/2)$, where θ is the angle between the beams. The density response function $\chi(\mathbf{q}, \omega)$ of the physical system is directly related to the dynamic form

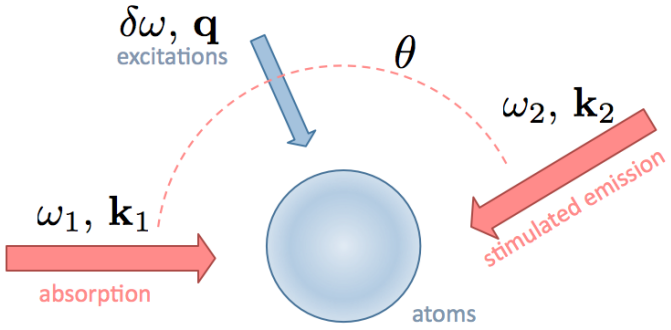

Figure 4.8: Schematic of a typical Bragg experiment in ultracold atoms. The atomic cloud is excited by absorption and stimulated emission cycles of far-off resonance light.

factor $S(\mathbf{q},\omega)$ through the fluctuation-dissipation theorem by the relation [106, 138]:

$$\mathrm{Im}\left[\chi(\mathbf{q},\omega)\right] = -\frac{\pi}{\hbar}\left[S(\mathbf{q},\omega) - S(-\mathbf{q},-\omega)\right], \tag{4.10}$$

where $S(\mathbf{q},\omega)$ is defined as:

$$S(\mathbf{q},\omega) = \frac{1}{Z}\sum_{mn} e^{-\beta E_m} |\langle n|\hat{\rho}^\dagger_{\mathbf{q}}|m\rangle|^2 \delta\left(\hbar\omega - E_n - E_m\right), \tag{4.11}$$

where $\hat{\rho}^\dagger_{\mathbf{q}}$ is defined in section 3.2.1 in Eq. (3.6). In the case of an ideal homogeneous Fermi gas at finite temperature [138], it is possible to calculate analytically the dynamical form factor $S_{hom}(q,\omega)$ following the definitions (3.6):

$$\begin{aligned} S_{hom}(\mathbf{q},\omega) &= \frac{1}{Z}\sum_{mnkk'} e^{-\beta E_m} \langle m|\hat{a}^\dagger_{\mathbf{k'}-\mathbf{q}}\hat{a}_{\mathbf{k'}}|n\rangle\langle n|\hat{a}^\dagger_{\mathbf{k}+\mathbf{q}}\hat{a}_{\mathbf{k}}|m\rangle\, \delta\left(\varepsilon_{k+q} - \varepsilon_k - \hbar\omega\right) \\ &= \frac{1}{Z}\sum_{mk} e^{-\beta E_m} \langle m|\hat{a}^\dagger_{\mathbf{k}}\hat{a}_{\mathbf{k}}(1 - \hat{a}^\dagger_{\mathbf{k}+\mathbf{q}}\hat{a}_{\mathbf{k}+\mathbf{q}})|m\rangle\, \delta\left(\varepsilon_{k+q} - \varepsilon_k - \hbar\omega\right) \\ &= \sum_{\mathbf{k}} g_{\mathbf{k}}(1 - g_{\mathbf{k}+\mathbf{q}})\, \delta\left(\varepsilon_{k+q} - \varepsilon_k - \hbar\omega\right), \end{aligned} \tag{4.12}$$

where the occupation number is defined as:

$$g_{\mathbf{k}} = \frac{1}{Z}\sum_m e^{-\beta E_m}\langle m|\hat{a}^\dagger_{\mathbf{k}}\hat{a}_{\mathbf{k}}|m\rangle = \frac{1}{\mathcal{F}^{-1}e^{\beta\varepsilon_k} + 1}. \tag{4.13}$$

4.2.1 Dynamical Structure Factor of a 1D ideal Fermi gas

In one dimension the energy conservation condition enforced by the delta function is

$$\frac{\hbar^2(k+q)^2}{2m} - \frac{\hbar^2 k^2}{2m} = \frac{\hbar^2 q^2}{2m} + \frac{\hbar^2\, kq}{m} = \hbar\omega \longrightarrow k = \frac{\omega m}{\hbar q} - \frac{q}{2}, \tag{4.14}$$

and the expression of the dynamical form factor of a homogenous 1D fermi gas becomes:

$$S_{hom}(q,\omega) = g\left(\frac{m\omega}{\hbar q} - q/2\right)\left[1 - g\left(\frac{m\omega}{\hbar q} + q/2\right)\right]. \tag{4.15}$$

In Fig. 4.9a, $S_{hom}(q,\omega)$ is shown for an extended range of momenta and frequencies. In order to take into account the effect of harmonic trapping we can use LDA following the approach presented in [139]. Similarly to the procedure used to derive Eq. (4.9), we define a position-dependent dynamical form factor $S\left[q,\omega;k_F(x)\right]$ which is then averaged over the density distribution $n_{1D}(x)$ in (Eq. 4.8):

$$S_{1D}(q,\omega) = \int dx\, n_{1D}(x)\, S_{hom}\left[q,\omega;k_F(x)\right]. \tag{4.16}$$

To match our experimental configuration, we need to take into account the harmonic confinement of every single wire ij and then compute a weighted average over the different wires. Following the same LDA approach of section 4.1.1, the dynamical structure factor is computed as:

$$S_{LDA}(q,\omega) = \frac{1}{N_{at}}\sum_{ij} N_{ij}\left[\frac{1}{A_{ij}}\int dx\, n_{ij}(x)\, S_{hom}\left[q,\omega;k_F(x)\right]\right], \tag{4.17}$$

In Figs. 4.9 and 4.10, it is evident how the gap between $q = 0$ and $q = 2k_F$ present in the homogeneous case (see also section 3.1) is smeared out in the case of harmonic trapped gas , as shown in Fig. 4.9b. Averaging over several tubes, this effect is even enhanced (Fig. 4.9c). As shown in the next section, we first performed Bragg spectroscopy at $q > 2k_F$, where density excitations are well described by particle-hole excitation scheme. Successively we measured excitations at low momentum $q < k_F$ to compare the non-interacting Fermi gas response with collective long-wavelength excitations in a N-component Luttinger Liquid regime, with $N = 2$ and $N = 6$.

4.2.2 Bragg spectroscopy at high momentum

In order to probe density excitations at $q > 2k_F$, we used as Bragg beams the incoming and the retroreflected lattice beam 2 (see section 2.3.6) at $\lambda_L = 759$ nm longitudinal to

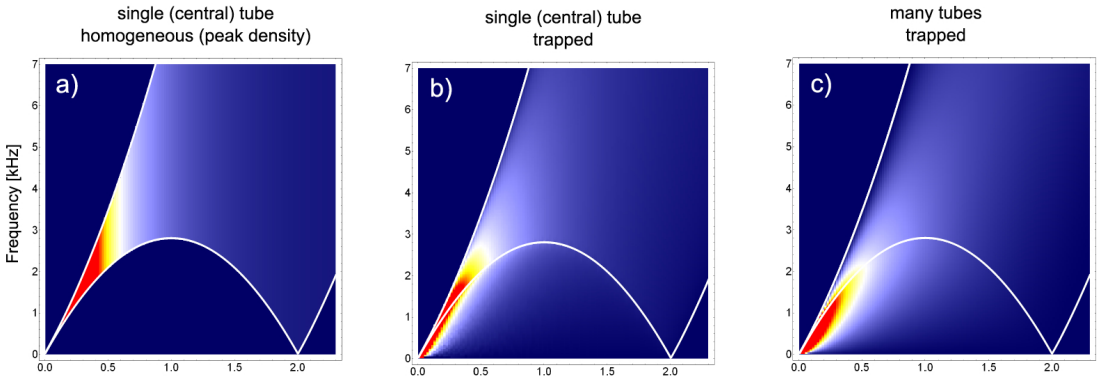

(a) $S_{hom}(q,\omega)$ **(b)** $S_{1D}(q,\omega)$ **(c)** $S_{LDA}(q,\omega)$

Figure 4.9: Dynamic Structure factor of a one-dimensional Fermi gas. The white solid lines delimit the region where the particle-hole excitation fulfill energy conservation in the homogeneous case **(a)**. The gap due to peculiar Fermi surface in one dimension is smeared out in the harmonically confined **(b)** and in the **(c)** LDA dynamic form factor.

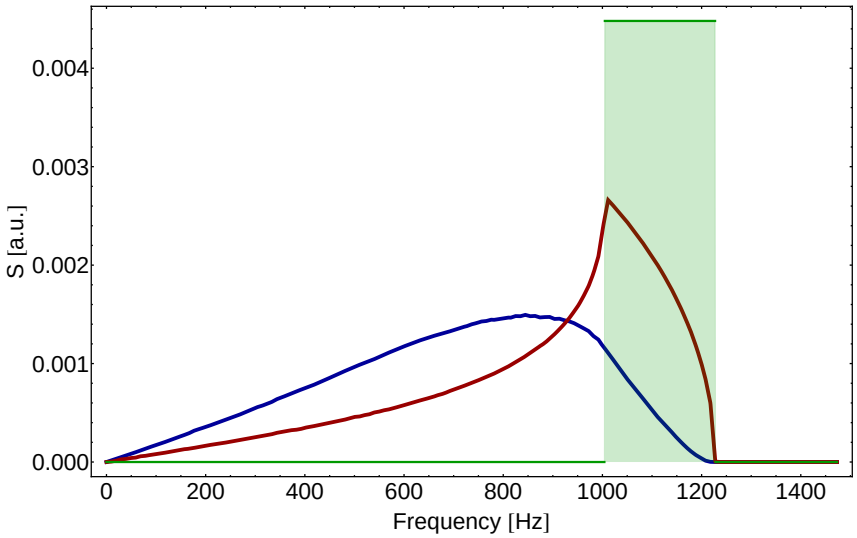

Figure 4.10: A $q = 0.2k_F$ cut of $S_{hom}(q,\omega)$ (green), $S_{1D}(q,\omega)$ (red) and $S_{LDA}(q,\omega)$ (blue). The gap of the homogeneous system is washed out by harmonic confined and averaging over different tubes.

the direction of the wires. We drive the OL2 AOM (see section 2.2.4) using two radio-frequencies, so that the spectrum of both the incoming and retroreflected beam has both the frequencies ω_1 and ω_2, resulting in both a left-moving and a right-moving density excitation[1]. In this way we can use a single fiber to deliver the Bragg pulse in order to minimize the effect of laser phase fluctuations. The momentum transfer is determined by the angle between the incoming and the retroreflected beam ($\theta = 180°$) and hence is $q = |\mathbf{k}_1 - \mathbf{k_2}| = 2k_L$, where $k_L = 2\pi/\lambda_L$ is the lattice wavevector. Since the one-dimensional Fermi gas has $N_{at} \simeq 6500$ per spin component and a Fermi energy of $E_F \simeq 2$ kHz, we have $q/2k_F^{av} = 1.66$ where k_F^{av} is the average Fermi wavevector considering harmonic confinement and the weighted average over different wires. At wavevectors $q > 2k_F$, the number-conserving density excitations can be described as particle-hole excitations fulfilling the energy conservation condition in Eq. (4.14), that for $q = 2k_L$ becomes:

$$\frac{\omega(k)}{\omega_R} = 4\left(1 \pm \frac{k}{k_L}\right), \tag{4.18}$$

where we defined $\omega_R = E_R/\hbar = 2\pi \times 1.997$ kHz.

The experimental procedure is the following: after loading the Fermi gas in a $s = 40$ two-dimensional optical lattice using an exponential ramp of 150 ms, we wait 10 ms and then apply a 500 μs Bragg pulse and suddenly switch off the trap in less than 10 μs. A time-of-flight (TOF) measurement is performed by detecting the atomic density by means of absorption imaging after a ballistic expansion of $t_{TOF} = 28$ ms. To be safely in the Bragg regime we chose a pulse height of $s = 1.6$ and an interaction time of $t = 500$ μs (see section 1.2.2). In this way the particle-hole excitation is resonant only with the classes of momentum of the Fermi sea fulfilling the energy conservation condition in Eq. (4.18). To visualize how the excitation varies with frequency, we integrate over y and normalize every image to the same unity area and then plot the sequence of one-dimensional profiles as a function of atomic momentum k and frequency ω (Fig. 4.11). In order to quantify the particle-hole excitation and evaluate the dynamical form factor at $q = 2k_L$, we counted the atoms excited out of the Fermi sea as a function of frequency (Fig. 4.12). Note that, for frequencies of the order of $4\omega_R$, there is a strong overlap between the excitations and the central peaks, which makes the excitation measurement difficult. Therefore, in order to consistently evaluate the response of the system, we decided to subtract to every image a reference image with zero excitations. Unluckily, since this procedure does not take into account the atom number fluctuations, the data are a bit noisy. Anyway, by comparing the $q = 2k_L$ excitations of a SU(6) one-dimensional Fermi gas with theoretical predictions

[1] The two-frequency spectrum is obtained by mixing the $\nu_0 = 105$ MHz AOM carrier radio-frequency with the desired frequency difference $\Delta\nu = (\nu_1 - \nu_2)/2$ obtaining $\nu_0 \pm \Delta\nu$ driving the AOM. In this way $(\omega_1 - \omega_2)/2\pi = 2\Delta\nu$.

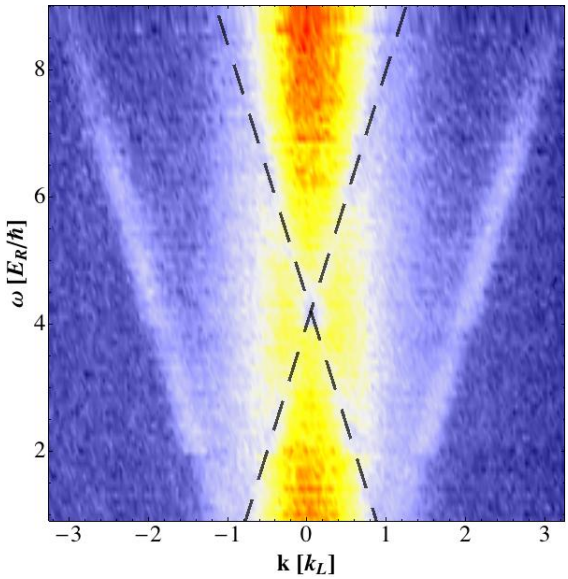

Figure 4.11: Density plot of one-dimensional momentum distributions versus atomic momentum k and frequency ω of a SU(6) one-dimensional Fermi gas after a $q = 2k_L$ Bragg pulse. Here $N_{at} = 6000$ atoms per spin component which leads to $E_F/h \simeq 2$ kHz. Dashed lines, defined by Eqs. (4.18), individuate the portion of the Fermi sea that is resonant with the Bragg pulse.

obtained using Eq. (4.17), we can conclude that there is a reasonable agreement between the non-interacting theory and the dynamic form factor at $q > 2k_F$ (solid line in Fig. 4.12). Indeed, as expected, the density excitations at high momentum are well described as particle-hole excitations and interactions play a minor role in this case. As we will see in the next section, in the Luttinger Liquid regime for $q < k_F$, the interactions modify the density excitations spectrum through the onset of a collective mode.

4.2.3 Bragg spectroscopy at low momentum

In order to access the low-momentum part of the spectrum, we chose a geometric configuration with two $\lambda_L = 759$ nm Bragg beams aligned at a small angle $\theta = 16^o$, resulting in a momentum transfer $\hbar q \simeq 0.2k_F^0$ along the wire axis (being k_F^0 the Fermi wavevector corresponding to the peak density of the central wire). Bragg pulse length (30 ms) and intensity (18 mW) are chosen in such a way to result in a combined interaction-time and power broadening < 100 Hz, much less than the width of the measured spectra. As in the measurement at $q = 2k_L$, the spectrum of each of the two Bragg beams contains both the frequencies ω_1 and ω_2, resulting in both a left-moving and a right-moving charge excitation. The Bragg excitation is quantified by measuring the momentum transferred

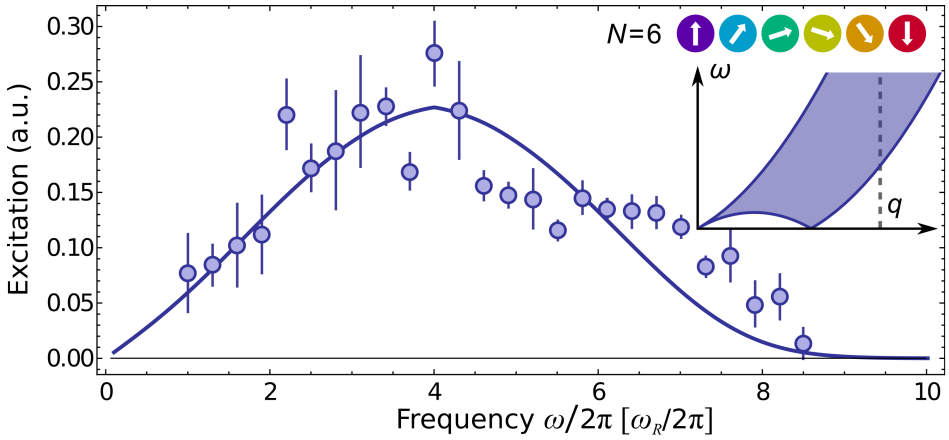

Figure 4.12: The points show the measured amount of excitations transferred after a Bragg pulse with energy $\hbar\omega$ and momentum $q = 2k_L$. The solid line is the calculated response function for the ideal Fermi gas using a LDA approximation (Eq. 4.11) with no free parameter. The error bars are the standard deviation from the mean over 3 measurements. Both the experimental and theoretical spectra have been normalized to unity area. Inset: a sketch of the excitation spectrum for the ideal 1D Fermi gas. The dashed line indicates the section of the excitation spectrum probed in this measurement.

to the cloud by time-of-flight imaging ($t_{TOF} = 23$ ms). Differently with respect to the $q \gg k_F$ case, where it is possible to detect the number of atoms ejected from the atomic cloud, at $q \ll k_F$ the amount of excitations can be detected as an increase in the width of the momentum distribution measured in time-of-flight. Note that, since the Bragg light is far-detuned with respect to any atomic resonance, the Bragg perturbation acts equally on the different nuclear spin states, i.e. we are only exciting *charge* modes (density waves) and not *spin* modes (spin waves), which would propagate with a different velocity.

At small excitation momenta ($q \ll k_F$) 1D fermions feature a well-resolved excitation spectrum. Number-conserving excitations in the ideal 1D Fermi gas correspond to particle-hole pairs with energy $\hbar\omega = v_F q$. As described in chapter 3, this physical picture changes profoundly in the case of an interacting spin mixture. According to the Luttinger theory, excitations acquire a collective nature and their spectrum is described by a linear dispersion relation $\omega = c|q|$, where c is the renormalized sound velocity. In a two-component Luttinger liquid with repulsive contact interactions the Luttinger parameter K, defined in Eq. (3.40), can assume values in the interval $0.5 < K < 1$ and this yields to a sound velocity $c = v_F/K$ which is larger than v_F. In other words, repulsive interactions increase the stiffness of the many-body state, shifting the spectrum towards higher energies (see inset of Fig. 4.14). Figure 4.13 shows the measured excitation spectrum for the spin-polarized case $N = 1$ at

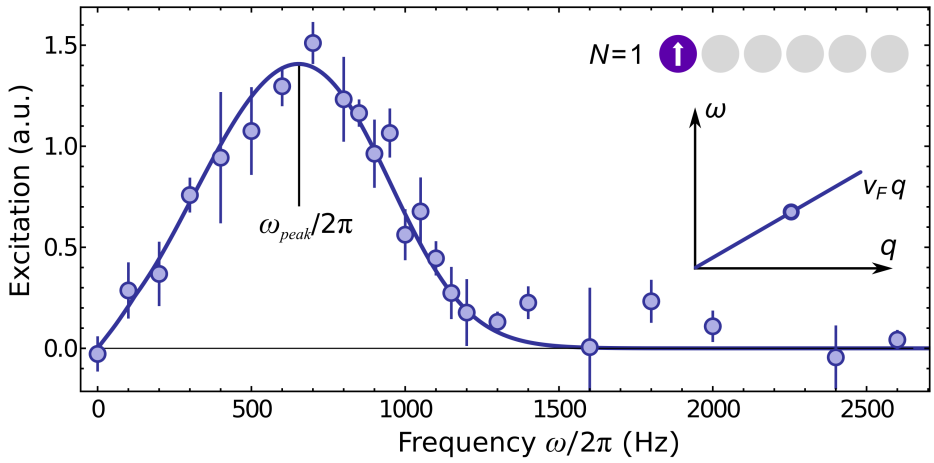

Figure 4.13: The points show the measured momentum transfer after a Bragg excitation with energy $\hbar\omega$ and momentum $q \simeq 0.2k_F^0$ (see text) for $N = 1$. The solid line is the calculated response function for the ideal Fermi gas using a LDA approximation. The error bars are standard deviations over up to 5 repeated measurements per frequency. Both the experimental and theoretical spectra have been normalized to unity area. Inset: a sketch of the excitation spectrum at low-q for the ideal one-dimensional Fermi gas.

low momentum transfer $\hbar q \sim 0.2k_F^0$ (being k_F^0 the peak Fermi wavevector in the central wire). A clear resonance is observed, in very good agreement with the calculated response for the ideal 1D Fermi gas (solid line, with no free parameters). In the low momentum regime, the homogeneous system displays a δ-like response as a function of frequency (see Fig. 4.10). However, in our experimental configuration, the width of the resonance plotted in Fig. 4.13 is mainly due to the inhomogeneity induced by the trap and to the averaging over different tubes. Also in this case though, by considering the full dynamic form factor in the noninteracting case, we can verify theoretically that the peak of the resonance ω_{peak} depends linearly on the excitation momentum $\hbar q$ up to the value used in our measurements. This means that, despite the average over different inhomogeneous systems and the finiteness of our momentum transfer, we are effectively probing the low-q regime of linear dispersion in the excitation spectrum.

In the interacting system with more than one component, the response displays a shift towards higher energy which reflects a higher sound velocity. Experimentally, the shift in the sound velocity is characterized by determining the frequency ω_{peak} corresponding to the excitation peak. This quantity is obtained by performing a Gaussian fit (blue dashed lines in Fig. 4.14) of the experimental data. For $N = 2$ (Fig. 4.14a), the measured shift with respect to the non-interacting case is $(+15 \pm 4)\%$, in agreement with the expected

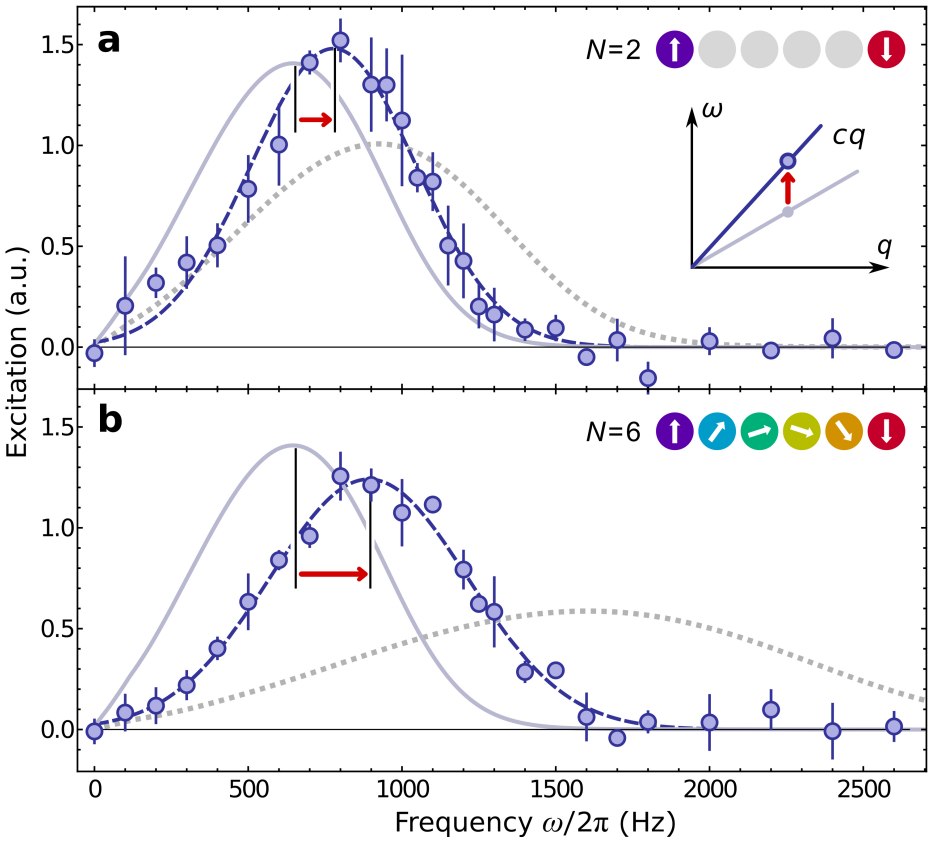

Figure 4.14: The points show the measured momentum transfer after a Bragg excitation with energy $\hbar\omega$ and momentum $q \simeq 0.2k_F^0$(see text) for **(a)** $N = 2$ and **(b)** $N = 6$. The light solid line recalls the theoretical response for the ideal Fermi gas. The dashed lines are Gaussian fits to the experimental data, in order to guide the eye and to extract the peak excitation frequency. The dotted lines are the theoretical response of the fully fermionized system which is equivalent to an ideal gas with **(a)** $2 \times N_{at}$ and **(b)** $6 \times N_{at}$ particles. The error bars are standard deviations over up to 5 repeated measurements per frequency. Both the experimental and theoretical spectra have been normalized to unity area. The red arrows indicate the shift in the excitation resonance with respect to the non-interacting case. Inset: a sketch of the excitation spectrum at low q for the ideal Fermi gas (light solid line) and for the two-component Luttinger liquid (dark solid line) with repulsive interactions.

$(+10 \pm 2)\%$ shift in the sound velocity predicted on the basis of the Luttinger theory for a trapped gas. The theoretical shift in the sound velocity expected for the low-q excitation spectrum in this case has been evaluated following the results of references [70, 109] for the harmonically trapped systems by performing the same LDA and averaging over wires procedure described in section 4.1.2.

For $N = 6$, the spectrum shows a much larger shift $(+33 \pm 4)\%$ (Fig. 4.14b), which disagrees with the predictions for a spin-1/2 system, signaling an increased effect of interactions, in qualitative accordance with the change in the momentum distributions $n(k)$ of Fig. 4.4. The calculated spectra for trapped fermions with infinite interactions (dotted lines in Fig. 4.14) are also plotted, which evidence how the measured spectra lie between the response of the ideal Fermi gas and that of a fully fermionized system. The curves for infinite repulsion in Fig. 4.14 have been derived following the fermionization picture, i.e. by calculating the quantity in Eq. (4.10) for the dynamic form factor $S_{LDA}(q, \omega)$ of an ideal Fermi gas with $N \times N_{at}$ particles.

In order to confirm that the resonance shift to higher energies is due to strong interactions present in the one-dimensional system, we compared the density excitations of a three-dimensional Fermi gas with one and two components. In this case, as shown in Fig. 4.15, there is no significant difference between the two datasets, meaning that in three dimensions interactions change negligibly the response of the system. Indeed both datasets are in good agreement with the theoretical prediction of the dynamical structure factor (Eq. 4.12) with no fit parameter.

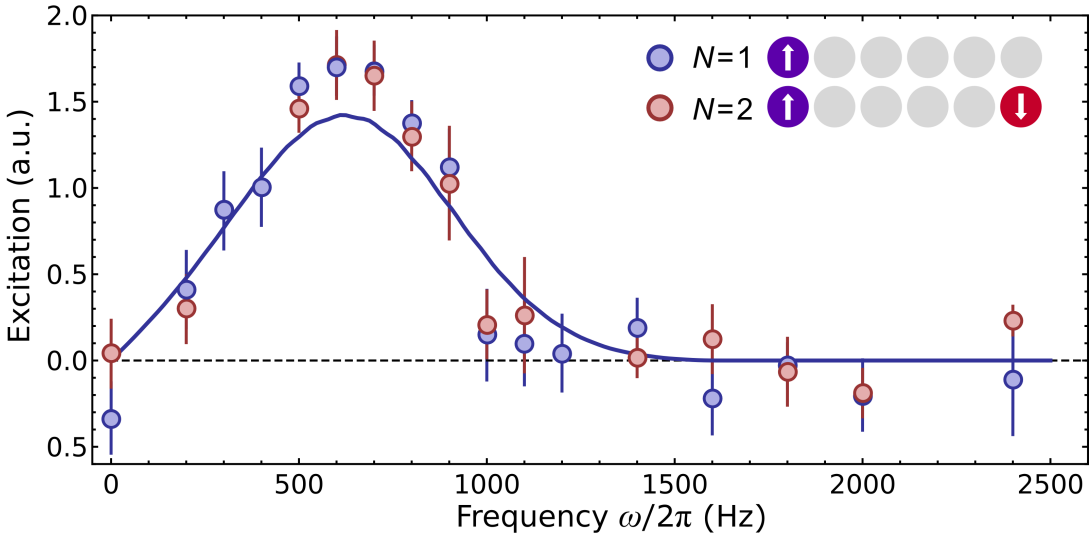

Figure 4.15: Bragg excitation of a 3D Fermi gas with $N = 1$ and $N = 2$ components at $q = 0.27\, k_F$ as a function of frequency $\hbar\omega$. The blue solid line is the theoretical response for the ideal Fermi gas calculated evaluating numerically Eq. (4.12) at $T/T_F = 0.35$. The error bars are standard deviations over up to 3 repeated measurements per frequency.

4.3 High-spin bosonization: breathing measurements

Collective modes represent a powerful probe of the state of trapped quantum gases and a sensitive observable to correlations present in the system. In the case of a trapped 1D gas, the lowest-energy collective mode is the breathing oscillation in which the axial radius of the cloud oscillates in time. In order to study collective modes, we measured the ratio $\beta = (\omega_B/\omega_x)^2$, where $\omega_B/2\pi$ is the breathing mode frequency, which is compared with the center-of-mass oscillation frequency $\omega_x/2\pi$ (dipole mode). Moreover, in the case of one-dimensional systems, there is a well established theory to compute the collective modes frequencies based on the exact Bethe-ansatz equilibrium density distribution and the hydrodynamic equations. As shown in the next sections, these techniques allow an accurate comparison between theory and experimental results.

4.3.1 Theoretical prediction

For a non-interacting ($N = 1$) 1D Fermi gas $\beta = 4$, as in a classical gas. This can be understood intuitively by considering, in a single-particle picture, two classical particles starting from the center of the trap with opposite velocities. While they perform a complete oscillation along the wires with angular frequency ω_x, their relative distance has completed two periods with angular frequency $\omega_B = 2\omega_x$.

However if we consider an interacting 1D system, the physical picture changes completely. To give a theoretical prediction about the normal mode of the interacting system it is necessary in the first place to compute the ground-state energy of a homogeneous interacting 1D Fermi gas exactly using a Bethe-Ansatz technique (see section 3.4) which consists in the following self-consistent set of equations [127]:

$$\frac{E_{hom}}{L} = \frac{\hbar^2}{m}\left(\frac{n\gamma}{\lambda}\right)^3 \int_0^1 x^2 g(x)dx, \tag{4.19}$$

$$\lambda = 2\gamma \int_0^1 g(x)dx, \tag{4.20}$$

$$g(x) = \frac{N}{2\pi} - \frac{1}{\pi}\sum_{\ell=1}^{N-1} \int_1^\infty g(x')dx' \left[\frac{\ell\lambda}{(\ell\lambda)^2 + (x-x')^2} + \frac{\ell\lambda}{(\ell\lambda)^2 + (x+x')^2}\right], \tag{4.21}$$

where N is the number of spin components and n is the linear density. From the ground-state energy, it is possible to compute the expressions for the chemical potential $\mu_{hom} = \partial E_{hom}/\partial N_{at}$ and the sound velocity $c_{hom}^2 = n(\partial\mu_{hom}/\partial n)/m$. With the chemical potential of an homogeneous system, it is possible to apply a LDA over the harmonic trap with

frequency ω_x to find the inhomogeneous density distribution $n(x)$:

$$\mu_{hom}[n(x)] + \frac{1}{2}m\omega_x^2 x^2 = \mu, \tag{4.22}$$

where μ is the global chemical potential of the system, which is determined by the normalization condition

$$N_{1D} = \int_{-R_x^{TF}}^{R_x^{TF}} n(x),$$

where $R_x^{TF} = \sqrt{2\mu/m\omega_x^2}$ is the Thomas-Fermi radius (see section 1.1). The equilibrium density $n(x)$ calculated numerically from Bethe-ansatz + LDA equations can be used to compute the frequencies of the collective density oscillations of the one-dimensional interacting system [127, 140, 141]. In order to compute the normal modes of a two-component Fermi gas, a sum rule approach borrowed from nuclear physics [142, 143] has been used in the literature. Indeed, it is possible to give a rigorous upper bound to the collective mode frequency by evaluating weighted energy moments of the dynamical structure factor related to a one-body excitation operator $\hat{F}$.

$$m_p = \int_0^\infty \omega^p S_{F^\dagger F}(\omega) = \sum_n |\langle n|\hat{F}|0\rangle|^2 \omega_n^p. \tag{4.23}$$

In the case of breathing frequencies, the operator is $\hat{F} = \sum_i \hat{x}^2$ and the sum-rule used is [70]:

$$\omega_B^2 = \frac{1}{\hbar}\frac{m_1}{m_{-1}} = 2\frac{\langle x^2\rangle}{d\langle x^2\rangle/d\omega_x^2}, \tag{4.24}$$

where $m_1 = \left[\sum_i \hat{x}^2, \left[H, \sum_i \hat{x}^2\right]\right] = (2N_{at}\hbar/m)\langle x^2\rangle$ and $m_{-1} = \alpha/2$, where α is the static polarizability of the system [140]. In this approach, the Bethe-ansatz solution is used to evaluate the mean value $\langle x^2\rangle = \int x^2 n(x)dx/N_{1D}$. The numerical evaluation of the ratio $\beta = \omega_B/\omega_x$ through Eq. (4.24) is shown in Fig. 4.16. The interaction is quantified by the parameter $\eta = N_{1D}a_{1D}^2/a_x^2$, where $a_x = \sqrt{\hbar/m\omega_x}$ is the harmonic oscillator length along the tubes. Note that in both the limiting cases of an ideal gas ($\gamma = 0$, $\eta \gg 1$) and a fully fermionized ($\gamma = \infty$, $\eta \ll 1$) gas, the breathing frequency is the same as that of a gas of noninteracting fermions ($N = 1$). Indeed, in the infinitely interacting regime the strong repulsion plays the role of an additional Pauli principle between distinguishable fermions and makes possible a mapping with an ideal Fermi gas with twice the number of atoms (see section 3.4). Moreover the ratio β has an absolute minimum at $\beta_2^{th,min} \simeq 3.62$ at finite interactions $N_{at}a_{1D}^2/a_x^2 \sim 1$.

Another approach to compute the collective modes of the system is based on the superfluid hydrodynamic description of the dynamics of the 1D Fermi gas. This approach

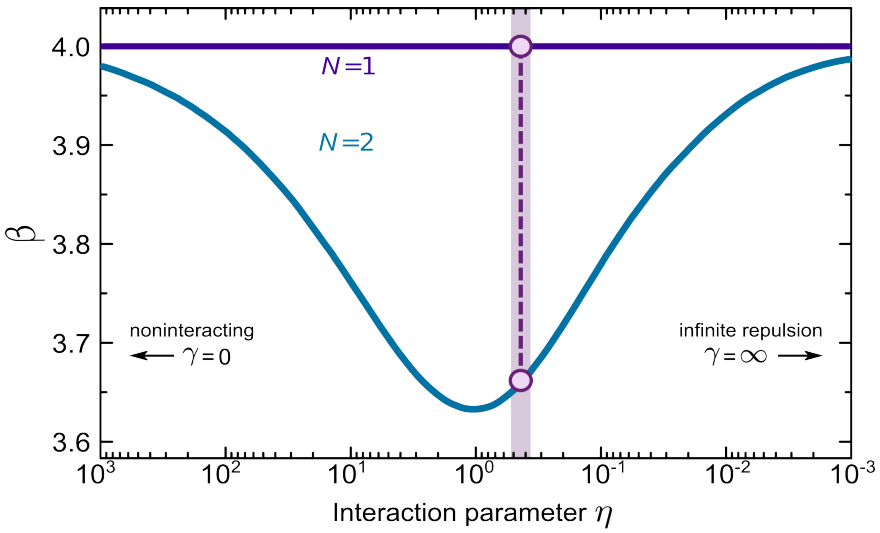

Figure 4.16: Squared ratio $\beta = (\omega_B/\omega_x)^2$ of the breathing mode frequency ω_B to the trap frequency ω_x, as a function of the coupling strength $\eta = N_{1D}\, a_{1D}^2/a_x^2$ for an inhomogeneous two-component 1D Fermi gas with repulsive interactions. The solid lines have been determined numerically from Eq. (4.24) [70]. The violet points correspond to the theoretical predictions for our experimental parameter, namely $\eta = 0.44 \pm 0.08$, where the error is given by the experimental uncertainty on the system parameters.

is valid only under the collisional regime where $N_{1D}(1-\mathcal{T}) \gg 1$ namely the probability of transmission after a scattering event is extremely low. Considering our parameters $k_F \sim 8\ \mu\text{m}^{-1}$, $a_\perp \sim 950\, a_0$ according to [67] we can estimate $\mathcal{T} \sim 0.2$. Taking $N_{1D} \sim 20$ as the number of atoms in the central tube we got $N_{1D}(1-\mathcal{T}) \sim 16$ so the approximation is reasonably justified. The hydrodynamics of a Fermi gas is ruled by the following equations:

$$\frac{\partial}{\partial t} n(x,t) + \frac{\partial}{\partial x}\left[n(x,t)v(x,t)\right] = 0, \quad \text{(continuity equation)} \tag{4.25}$$

$$m\frac{\partial}{\partial t} v(x,t) + \frac{\partial}{\partial x}\left[\mu_{hom}(n) + \frac{1}{2}m\omega_x^2 x^2 + \frac{1}{2}mv^2\right] = 0, \quad \text{(Euler equation)} \tag{4.26}$$

Considering small density fluctuations $\delta n(x,t) = n(x,t) - n(x)$ around the equilibrium distribution $n(x)$ and small velocities $v(x,t)$ with respect to the equilibrium value $v(x) \equiv 0$, it is possible to linearize Eqs. (4.25) and (4.26). Using the ansatz $\delta n(x,t) = e^{i\omega_j t} n(x)$ we can formulate the following eigenvalue problem:

$$\frac{1}{m}\frac{\partial}{\partial x}\left[n\frac{\partial}{\partial x}\left(\frac{\partial \mu_{hom}(n)}{\partial n}\delta n(x,t)\right)\right] + \omega_j^2 \delta n(x) = 0. \tag{4.27}$$

These equations can be written in terms of bosonic field of the Luttinger liquid model $\phi(x,t)$ and $\Pi(x,t)$ defined in Eqs. (3.33):

$$\begin{aligned} \delta n(x,t) &= -\frac{\partial}{\partial x}\phi(x,t), \\ j(x,t) &= n(x,t)v(x,t) = u_c(x)K(x)\Pi(x,t), \end{aligned} \tag{4.28}$$

where $u_c(x) \equiv u_c(n(x)) = \sqrt{[\partial\mu/\partial n]n(x)/m}$ and $K_c(x) \equiv K_c(n(x)) = [\partial n/\partial\mu]u_c(x)$ are the LDA position-dependent parameters of the Luttinger Hamiltonian, defined in Eq.(3.18). In this notation Eq. (4.27) can be recast as:

$$\frac{\partial}{\partial x}\left[u_c(x)K(x)\frac{\partial}{\partial x}\left(\frac{u_c(x)}{K(x)}\delta n(x,t)\right)\right] + \omega_j^2\delta n(x) = 0. \tag{4.29}$$

The numerical solution of Eq. (4.29) for different number of spin components, keeping fixed the number of particle per spin component, has been derived in Ref. [127] and the results are shown in Fig. 4.17. It is interesting to note that increasing the number of spin components N, β asymptotically approaches the value predicted for a spinless one-dimensional boson gas. This is a phenomenon that the authors of Ref. [127] called "high-spin bosonization" and that has been predicted by C. N. Yang and Y. Y. Zhuang [34] by demonstrating rigorously that, given a N-component 1D Fermi gas, the energy per particle in the limit $N \to \infty$ is the same as that of a 1D spinless boson gas. To prove this result, it is necessary to assume that all fermions interact with the same strength. In the next section it will be shown how the SU(N) symmetry of Ytterbium atoms has allowed the first experimental demonstration of high-spin bosonization.

4.3.2 Experimental procedures and results

The breathing mode frequency is measured using the following experimental procedure (see Fig. 4.18a): after evaporation in the dipole trap, the Fermi gas is loaded in the 2D optical lattice at $s = 40$ and, after 10 ms, we switch off the dipole trap in 10 μs changing the frequency from $\omega_x/2\pi \sim 100$ Hz to $\omega_x/2\pi \sim 65$ Hz. We wait a variable holding time t_{hold} in which the atoms oscillate along the wires and then we switch off the lattice in 5 μs. After a $t_{TOF} = 23$ ms expansion, we measure the cloud radius r by absorption imaging as a function of the holding time t_{hold} in the lattice. The cloud radius r is measured by integrating the images along the y-axis and then performing a 1D Gaussian fit of the integrated density.

In order to measure the dipole mode frequency, the center-of-mass oscillation of the cloud is studied as a function of the holding time t_{hold}. The experimental procedure to

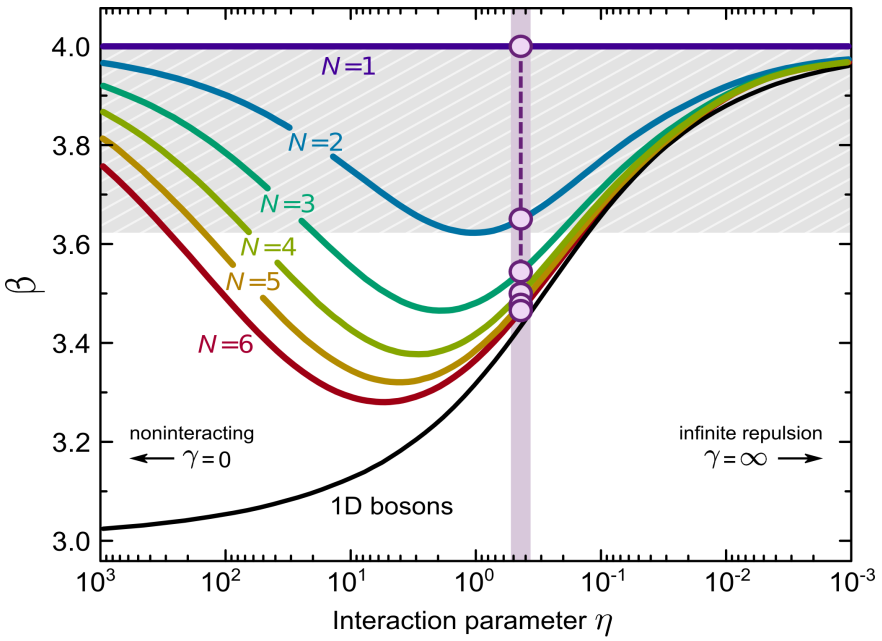

Figure 4.17: Squared ratio $\beta = (\omega_B/\omega_x)^2$ of the breathing mode frequency ω_B to the trap frequency ω_x, as a function of the coupling strength $\eta = N_{1D}\, a_{1D}^2/a_x^2$ for an inhomogeneous 1D Fermi gas with repulsive interactions. The solid lines have been determined numerically from Eq. (4.29) [127]. The points correspond to the theoretical predictions for our experimental parameter, namely $\eta = 0.44 \pm 0.08$, where the error is given by the experimental uncertainty on the system parameters. Increasing the number of spin components leads to high spin-bosonization.

measure the dipole mode is the following (see Fig. 4.18b): after evaporation in the dipole trap, the Fermi gas is loaded in the 2D optical lattice at $s = 40$ and the dipole trap is switched off using a 50 ms long linear ramp; then we set the lattice beams power to $s_z \sim 35$ and $s_y \sim 30$ for 3 ms, bring the lattice again at $s = 40$ and then wait a variable holding time t_{hold} before switching off the lattice. At $s_z \sim 35$ and $s_y \sim 30$ the trap minimum does not coincide with the one at $s_y = s_z = 40$. This, combined with a non-perfect overlap of the two beams, leads to the excitation of the dipole mode. The dipole frequency measurement has been performed using a one-dimensional BEC of ^{174}Yb, whose center-of-mass position was detectable with much higher precision with respect to the 1D Fermi gas. To extract the dipole frequency for the fermionic isotope ^{173}Yb, we correct for a factor $\sqrt{174/173}$. It has been verified that the 50 ms linear ramp to switch off the dipole trap does not excite any center-of-mass oscillation. Moreover, at $s = 30$, the system is still purely one-dimensional because the transverse confinement frequency $\omega_\perp = 2\pi \times 19$ kHz leads to a negligible tunneling among the tubes ($h/J \sim 1$ s, see Eq. 1.66) on the timescales

of the experiment.

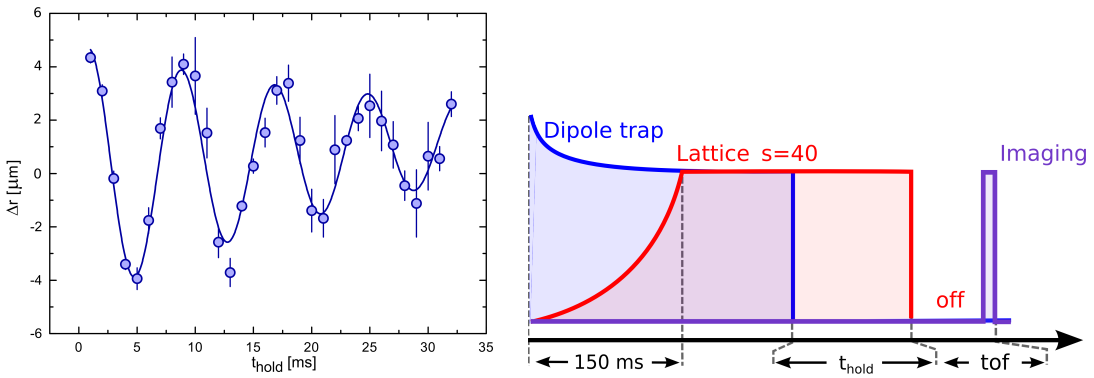

(a) Breathing oscillations of a $N = 6$ 1D Fermi gas with $N_{at} = 6000$ per component. A fit to the experimental data gives $\omega_B/2\pi = (125 \pm 1)$ Hz.

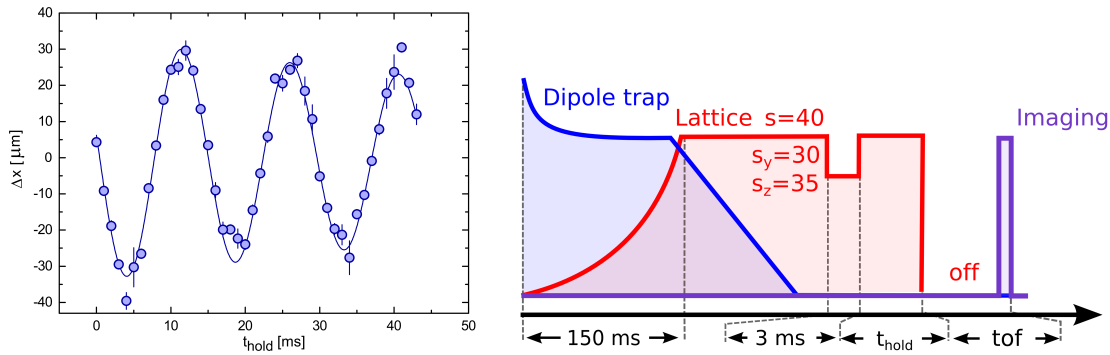

(b) Dipole oscillations of a one-dimensional ^{174}Yb BEC. A fit to the experimental data gives $\omega_x/2\pi = (67.1 \pm 0.8)$ Hz.

Figure 4.18: Typical breathing **(a)** and dipole **(b)** mode measurements using the corresponding experimental procedure (right). The error bars are the standard deviation from the mean. The blue solid lines are fits with a damped sinusoidal fit. In this case ($N = 6$) $\beta = 3.46 \pm 0.01$.

It shall be noted that a damping of the breathing oscillations is observed both for the interacting and for the spin-polarized Fermi gas. In order to explain this observation we performed a Montecarlo simulation by studying the dynamics of a classical sample of non-interacting atoms randomly extracted by a Gaussian spatial distribution with variance σ in a Gaussian optical dipole trap. We find out that there is a significant damping already for a distribution width of the order of 10% of the beam waist (see Fig. 4.19), which roughly corresponds to our Thomas-Fermi radius $R_{TF} \sim 7$ μm. The damping has been thus attributed to the dipole trap anharmonicity.

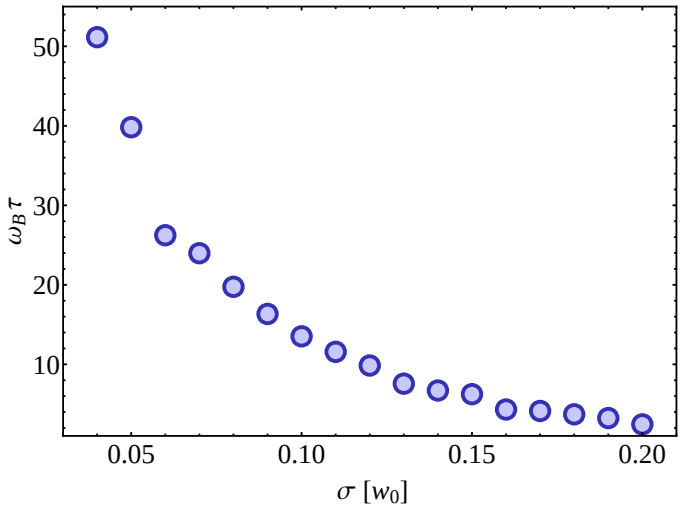

Figure 4.19: Number of coherent breathing oscillation performed in a damping time τ as a function of the width σ (in waist units) of the initial atomic spatial Gaussian distribution. The points are the results of a classical simulation to estimate the damping due to trap anharmonicity. The damping coefficient τ is estimated using a fit with a damped sinusoidal function.

In Fig. 4.20 the measured squared ratio $\beta = (\omega_B/\omega_x)^2$ as a function of N is shown. For $N = 1$ the measured value $\beta_1^{exp} = 3.93 \pm 0.10$ is in good agreement with the expected value $\beta_1^{th} = 4$ for the ideal Fermi gas (upper horizontal line).

For $N = 2$, our experimental parameter ($N_{at} a_{1D}^2/a_x^2 = 0.44 \pm 0.08$, evaluated averaging over the tubes) leads to a theoretical prediction $\beta_2^{th} = 3.650 \pm 0.015$ (red line) which is again in excellent agreement with the measured value $\beta_2^{exp} = 3.69 \pm 0.10$. The grey region in Fig. 4.20 shows the range of frequency ratios derived from Ref. [70] for $N = 2$ and for any possible value of the repulsion strength.

The experimental data clearly show that changing N causes markedly different effects from those induced by simply changing the interaction strength in an $N = 2$ mixture. In fact, by increasing N, the constraints of the Pauli principle become less stringent and the number of binary-collisional partners increases, causing the system to "lose" its fermionic behaviour. Our experimental observation are in excellent agreement with the theoretical predictions formulated in Ref. [127]. Moreover, our experimental value at $N = 6$ ($\beta_6^{exp} = 3.46 \pm 0.08$) clearly falls out of the range expected for a $N = 2$ liquid (Fig. 4.20, grey regions), and already approaches the value expected for 1D spinless bosons, validating for the first time "high-spin bosonization" of a one-dimensional Fermi gas.

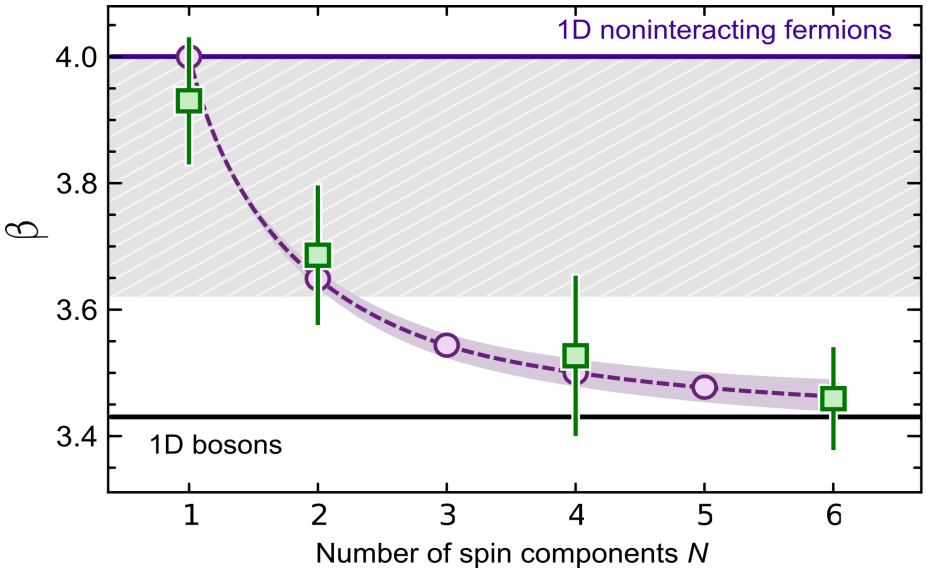

Figure 4.20: Squared ratio $\beta = (\omega_B/\omega_x)^2$ of the breathing mode frequency ω_B to the trap frequency ω_x, as a function of the number of spin components N. The points show the experimental data, obtained as the weighted average over sets of up to 9 repeated measurements (the error bars are standard deviations of the mean). The blue solid line shows the theoretical value (4, exact) for the ideal 1D Fermi gas. The grey area shows the range of frequency ratios derived from Ref. [70] for $N = 2$ and any possible value of the repulsion strength. The circles show the theoretical predictions for the average interaction parameter $\eta = 0.44$ for our experiment based on Eq. (4.29). The dashed line is a guide to the eye, while the height of the violet shaded region indicates the uncertainty on the theoretical values resulting from the experimental uncertainty $\Delta\eta = 0.08$ (coming from the measured atom number and trapping frequencies). The black solid indicates the theoretical prediction for 1D spinless bosons.

4.4 Conclusions and Outlook

In this set of experiments we provided the first experimental characterization of a multi-component Luttinger liquids with tunable $SU(N)$ symmetry. The possibility of tuning the number of spin components allows us to study different regimes of interplay between Fermi statistics and degree of distinguishability in this novel 1D tunable system. In a quantum simulation perspective, the controlled realization of 1D multi-component fermions represents a powerful test bench for large-spin models and opens to the investigation of fundamental effects, such as spin-charge separation (section 3.2.4), first predicted for a $N = 2$ fermionic system. Indeed, the work carried out so far concerns exclusively charge (density) collective modes, since the excitations studied are all spin-independent. In par-

ticular we observed a blue shift in the resonance of the charge dynamical structure factor in the case of two-component Fermi gas. Differently, given two spin species $|\uparrow\rangle$ and $|\downarrow\rangle$, a spin-selective Bragg excitation [144, 145] should allow in principle the comparison between the charge and spin velocity through the measurement of the charge and spin dynamical structure factors (see Appendix D), defined as:

$$S_{c,s}(\mathbf{q},\omega) = 2\left[S_{\uparrow\uparrow}(\mathbf{q},\omega) \pm S_{\uparrow\downarrow}(\mathbf{q},\omega)\right], \tag{4.30}$$

where plus and minus sign refer respectively to charge and spin subscripts. Alternatively, a redshift of the spin dipole frequency is predicted to be observed [108] as a consequence of a spin-selective excitation. In Chapter 6 it is explained in detail how to generate the spin-dependent light shifts necessary to access collective spin excitations.

In addition, exploiting the metastable state $^3P_0$ and its collisional properties (see Chapter 5) it will be possible to investigate two-orbital physics of $SU(N)$ fermionic atoms confined in a one-dimensional chain [126]. In this more complex case, the presence of the exchange energy induces a mixing of the charge and spin collective modes associated to different electronic states and the onset of four separated collective modes is predicted.

Chapter 5

Orbital magnetization oscillations

In this chapter we report experiments performed exploiting the $^3P_0$ electronic state of Ytterbium atoms. The lifetime of this state is of the order of tens of seconds, which is much longer than the typical timescale of an atomic physics experiment. As a consequence, Ytterbium atoms can be considered to have two alternative ground states, analogously to alkali atoms having two hyperfine ground states. The crucial difference is that $^1S_0$ and $^3P_0$ states are separated by an optical energy and this leads to several interesting consequences. First of all, differently from alkalis, it is possible to implement state-dependent optical potentials, which are far-detuned with respect to the main allowed transitions of both electronic states and therefore lead to negligible heating rates. Two prominent examples are the "magic" [146] and "anti-magic" [29] wavelengths which give rise respectively to the same and to the opposite light shift between ground and excited state. In particular the magic-wavelength enables the implementation of optical potentials that do not perturb the frequency of the $^1S_0 \rightarrow {}^3P_0$ transition, which is used in optical atomic clocks based on alkaline-earth-like atoms as Ytterbium [25] or Strontium [27]. Secondly, the different electronic structure, together with Fermi statistics, significantly affects collisions between two atoms in the ground and excited state. Indeed, the main focus of this chapter is to study binary interactions between atoms in two different electronic orbitals in a three-dimensional optical lattice. We observed for the first time fast, coherent orbital magnetization oscillations driven by spin-exchange processes and exploited this new observable to determine the inter-orbital scattering properties.

In section 5.1 we will briefly outline the laser system and the experimental setup built to address the ultra-narrow optical transition to the metastable state and we will focus on the spectroscopy of a spin-polarized Fermi gas in a three-dimensional optical lattice. In section 5.2 we will illustrate how Fermi statistics constrains the states available for doubly occupied lattice sites, affecting inter-orbital binary collisions as well as the coupling with

laser excitation and external magnetic field. We show spectroscopic measurements and interpret them with the help of a simple model. Section 5.3 concerns the mechanism underlying spin-exchange oscillations and the experimental procedure to observe them. Finally, in section 5.4, we show how measuring the spin-exchange frequency as a function of the lattice depth and the magnetic field allowed us to determine the scattering properties of the system.

5.1 The $^1S_0 \rightarrow {}^3P_0$ ultra-narrow clock transition

In the last years ultra-narrow optical transitions in alkaline-earth-like atoms such as Yb [24, 25] or Sr [26–28] have been intensively investigated as candidates to improve the current frequency standard with a new generation of atomic clocks. Indeed, these two-electron atoms exhibit narrow intercombination transitions ($\Delta S \neq 0$) to the triplet ^3P_J as a result of a small violation of the LS-coupling approximation (see also Appendix A). In particular, the $^3P_0$ state is connected to the ground state by a $J = 0 \rightarrow J' = 0$ transition, which is forbidden to all orders. However in fermionic isotopes, the hyperfine interaction between the nuclear magnetic moment and the electrons admixes this state with the atomic levels with total angular momentum $J = 1$, thus opening an electric-dipole decay to the ground state. On the other hand, for all alkaline-earth-like bosonic isotopes the transition is observable only by inducing the mixing with the $J = 1$ electronic states through an external magnetic field. In the specific case of ^{173}Yb, the calculated linewidth of the clock transition is $\Gamma = 2\pi \times 38.5$ mHz [147] or equivalently a $\tau = 26$ s lifetime. The exact transition frequency $518\,294\,576\,847.6 \pm 4.4$ kHz, corresponding to $\lambda_C = 578.4$ nm, has been measured in Ref. [24].

In order to coherently control such a narrow transition, we developed an ultra-stable laser source starting from the 1156 nm light emitted by a quantum dot laser in a 15-cm long external-cavity configuration with an intra-cavity electro-optical modulator (Qubig GmbH, DC-coupled, broadband, Brewster-cut facets) for high-bandwidth frequency stabilization. The laser radiation at 578 nm is then produced by second-harmonic generation in a bow-tie cavity to enhance the efficiency of the frequency-doubling process, similarly to the laser systems for 399 and 556 nm wavelengths, described in section 2.2.1. We obtain up to 50 mW of 578 nm light, a small part of which is coupled to a 10 cm long ULE (Ultra-Low Expansion) glass cavity to which the laser frequency is locked. The feedback is performed by both the piezo moving the grating of the external cavity and the EOM inside the external cavity. The former is used to correct in the low-frequency range up to 200 Hz, whereas the latter is used in the high-frequency domain obtaining an overall bandwidth of 500 kHz. The ULE cavity, surrounded by a thermally-stabilized copper shield, is located

in a 10^{-7} mbar vacuum chamber to greatly reduce its mechanical and thermal sensitivity. The whole system is placed on an anti-vibration platform to further reduce seismic noise, and is enclosed in an isolation box to decouple the system from the lab environment. The long-term drift of the cavity has been characterized to be 3.5 Hz/s and is corrected using a digital feed-forward loop. However, erratic fluctuations of some Hz/s, that we ascribe to an imperfect thermal stabilization of the ULE cavity, limit the mid-term stability of our laser. More details about the laser system and the characterization of the ULE drift can be found in Ref. [148] and in the PhD thesis of my coworker Giacomo Cappellini [36].

Another crucial ingredient to coherently excite atoms in the metastable state is the possibility to realize an optical trapping potential generating the same light shift, defined in Eq. (1.45)[1] for both ground and excited states. In this way differential light shifts undermining the stability of the resonance can be avoided, as well as broadening due to inhomogeneity of the harmonic confinement. There are several optical magic-wavelengths [149] (see Fig. 5.1), but the most convenient experimentally is $\lambda_M = 759.35$ nm [146], which is used in this experiment.

Beside being subjected to the same light shift in the ground and excited states, to observe narrow lines, the atoms need to be tightly confined in the direction of interrogation in order to avoid atomic motion to cause Doppler broadening of the clock transition. This condition is fulfilled by the use of a deep optical lattice along the same direction of the laser clock interrogation. Intuitively, this means that the atomic wave-packet needs to have a much smaller spatial extension than the wavelength $\lambda_C = 2\pi/k_C$ of the incident electric field $E(\mathbf{r}) = \boldsymbol{\varepsilon} E_0 e^{i(k_C R - \omega_C t)} + c.c.$ where R is the position of the atom in the optical lattice. Indeed, under this condition, called *Lamb-Dicke* regime, it is possible to resolve transitions between well defined vibrational states $|g, n\rangle$ and $|e, n'\rangle$ where we defined $|^1S_0\rangle = |g\rangle$ and $|^3P_0\rangle = |e\rangle$. The probability of the transition is proportional to the product of the squared electric dipole matrix element $|\langle e|\hat{d}|g\rangle|^2$ and the squared spatial overlap of the two vibrational states $P_{n\rightarrow n'} = |\langle n'|e^{ik_C \hat{R}}|n\rangle|^2$. In the harmonic approximation, we can write $\hat{R} = a_{ho}(\hat{a}^\dagger + \hat{a})/\sqrt{2}$, with $a_{ho} = \sqrt{\hbar/m\omega_{ho}}$ being the harmonic oscillator length. Therefore, in this approximation we can expand the exponential obtaining:

$$\begin{aligned} P_{n\rightarrow n'} &\propto |\langle n'|1 + \eta(\hat{a}^\dagger + \hat{a})|n\rangle|^2 + \mathcal{O}(\eta^2) \\ &= \delta_{n,n'} + \underbrace{\eta\sqrt{n+1}\delta_{n',n+1}}_{\text{red sideband}} + \underbrace{\eta\sqrt{n}\delta_{n'+1,n}}_{\text{blue sideband}} + \mathcal{O}(\eta^2), \end{aligned} \tag{5.1}$$

[1] The light shift in Eq. (1.45) can be recast as $V_m(\mathbf{r}) = -\alpha_m(\omega_L)E_0^2(\mathbf{r})$, where $E_0(\mathbf{r})$ is the electric field amplitude and

$$\alpha_m(\omega_L) = -\frac{2}{\hbar}\sum_{n\neq 0}\frac{\omega_n - \omega_m}{(\omega_n - \omega_m)^2 - \omega_L^2}|\langle n|\hat{d}|m\rangle|^2,$$

is called AC-stark polarizability.

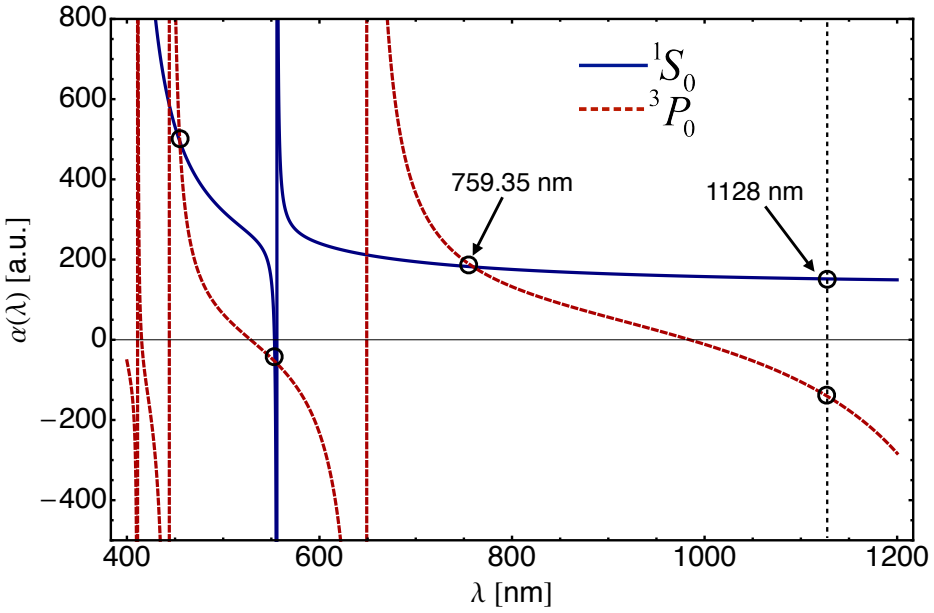

Figure 5.1: AC Polarizability in atomic units for $^1S_0$ and $^3P_0$ states. The circles indicate the magic (759 nm) and anti-magic (1128 nm) wavelengths. Other calculated magic-wavelengths at 551.5 and 465.4 nm [149] are also indicated. The atomic resonances and their respective linewidths used to calculate the AC stark shifts are reported in Appendix A.

where, with Eq. (1.59), we defined the Lamb-Dicke parameter as:

$$\eta = \frac{k a_{ho}}{\sqrt{2}} = \left(\frac{\lambda_M}{\lambda_C}\right) \frac{1}{\sqrt{2} s^{1/4}}, \tag{5.2}$$

which is predictably proportional to the ratio between the optical lattice magic-wavelength λ_M and the clock wavelength λ_C and inversely proportional to the lattice depth s defined in section 1.2.2. The Lamb-Dicke regime is defined for $\eta \ll 1$, namely when transitions with $n \neq n'$ are suppressed. In this work we used a Lamb-Dicke parameter η ranging from $0.44\,(s = 20)$ to $0.37\,(s = 38)$. The $\delta_{nn'}$ contribution in Eq. (5.1) refers to the carrier, namely to the transition between two identical vibrational levels, whereas the $\delta_{n',n+1}\,(\delta_{n'+1,n})$ term takes into account processes in which the final state has a higher (lower)vibrational energy. Therefore the latter transition occurs at higher (lower) frequency $\omega_0 \pm \omega_{ho}$ with respect to the carrier ω_0, as shown in Fig. 5.2 (in our notation the lattice vibrational spacing is $\hbar\omega_\perp \equiv \hbar\omega_{ho}$). The experimental procedure to observe the transition in a spin-polarized Fermi gas is made up by the following steps: after forced evaporation of a two spin mixture, we blast away the unwanted spin component using a resonant pulse (see section 2.4) and load the cloud adiabatically into the magic-wavelength

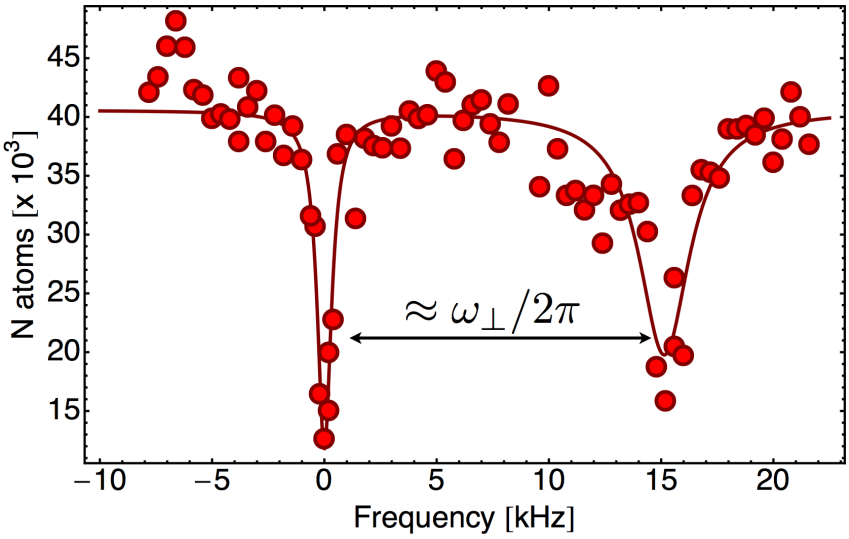

Figure 5.2: Laser spectroscopy on a $m = -5/2$ spin-polarized Fermi gas in a three-dimensional optical lattice with $s = 20.5$ (the band gap is $\hbar\omega_\perp = 2\pi \times 15.3$ kHz) with intensity $I_0 \sim 2$ mW/cm^2. On the vertical axis we report the number of atoms still in the ground state after the 100 ms excitation pulse. The two peaks are associated to the carrier and the blue sideband, separated by an energy difference $\hbar\omega_\perp$ corresponding to the band gap between the lowest and the first excited band.

$\lambda_M = 759$ nm lattice by means of a 150 ms exponential ramp. During lattice loading, the dipole trap is adiabatically switched off using a 50 ms ramp in order not to cause any differential light shift between $|g\rangle$ and $|e\rangle$ that would strongly affect the resonance frequency. Then, after 10 ms, we perform a 100 ms 578 nm laser pulse and we switch off the lattice beams. After ballistic expansion, we image the atoms remained in the ground state by absorption imaging on the $^1S_0 \rightarrow {}^1P_1$ transition. This detection method is reliable as the lifetime of the excited state is much longer than the typical time-of-flight.

Since the degenerate Fermi gas is loaded mainly in the lowest lattice band, or equivalently in the lowest vibrational level, the red sideband is strongly suppressed. On the other hand, the peak corresponding to the blue sideband is broader, as the first excited band has a wider energy dispersion with respect to the lowest lattice band. As we can see from Fig. 5.2, the width of the resonance corresponding to the carrier is of the order of 500 Hz for an intensity of $I \sim 2$ mW/cm^2. Indeed, since the saturation intensity is extremely low ($I_s = 0.26$ nW/cm^2), the transition is always saturated by the laser light and by tuning the intensity we can decide at will the resonance width. The narrowest resonance we managed to observe, compatibly with the mid-term drift of the ULE cavity, has a linewidth of 46 Hz, as shown in Fig. 5.3.

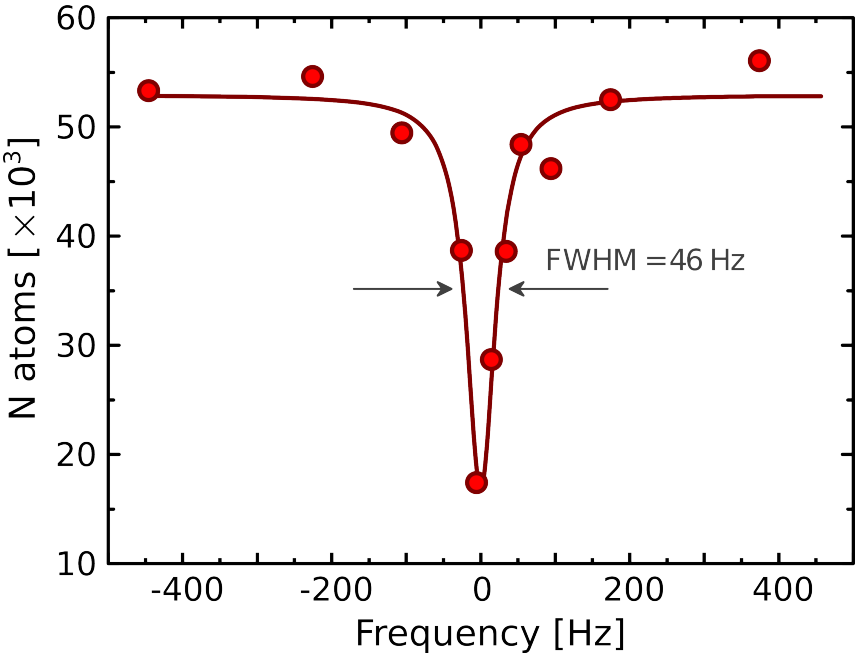

Figure 5.3: Narrow resonance showing the linewidth of our laser on the time scale of 5 minutes. The main limitation is the mid-term drift of the ULE cavity.

5.2 Clock spectroscopy of a two-component Fermi gas

In this section we investigate the spectroscopy of a two-component Fermi gas in a three-dimensional optical lattice, showing how the interplay between Fermi statistics and collisional shifts determine the shape of the spectrum [40]. We first outline a simple model taking into account collisional channels associated to different electronic states, the interaction with the spectroscopy laser and the effect of magnetic fields on the atomic system. Secondly we focus on the experimental spectrum at finite magnetic field, identifying the different peaks with the help of the model.

5.2.1 Direct and exchange interaction

Let us consider two interacting atoms in the same lattice site and in two different nuclear spin states $|\uparrow\rangle$ and $|\downarrow\rangle$, where the arrows are placeholders for two arbitrary nuclear spin states. For the time being we assume that the atoms share the same spatial Wannier wavefunction [11], but later on we will remove this assumption to take into account the case of strong interaction. Let us assume that the laser light is π-polarized so that the optical excitation conserves the nuclear spin. Since the electronic state and the nuclear

spin are completely decoupled, the whole Hilbert space consists in the following states allowed by global anti-symmetrization:

$$\Big\{ |gg\rangle \otimes |s\rangle,\ \frac{|eg\rangle + |ge\rangle}{\sqrt{2}} \otimes |s\rangle,\ \frac{|eg\rangle - |ge\rangle}{\sqrt{2}} \otimes |t\rangle,\ |ee\rangle \otimes |s\rangle \Big\}, \tag{5.3}$$

where $|t\rangle$ and $|s\rangle$ stands for the symmetric (triplet) and antisymmetric (singlet) two-particle nuclear spin states:

$$\begin{aligned} |s\rangle &= \frac{|\uparrow\downarrow\rangle - |\downarrow\uparrow\rangle}{\sqrt{2}}, \\ |t\rangle &= \frac{|\uparrow\downarrow\rangle + |\downarrow\uparrow\rangle}{\sqrt{2}}. \end{aligned} \tag{5.4}$$

The orbital part of the wavefunction determines the collisional channel through which the two atoms interact in the lattice sites. In particular let us focus on binary collisions between two atoms in different electronic states namely:

$$\begin{aligned} |eg^+\rangle &\equiv |s\rangle\frac{|eg\rangle + |ge\rangle}{\sqrt{2}} = \frac{1}{2}\big[|e\uparrow\rangle|g\downarrow\rangle - |g\downarrow\rangle|e\uparrow\rangle + |g\uparrow\rangle|e\downarrow\rangle - |e\downarrow\rangle|g\uparrow\rangle\big], \\ |eg^-\rangle &\equiv |t\rangle\frac{|eg\rangle - |ge\rangle}{\sqrt{2}} = \frac{1}{2}\big[|e\uparrow\rangle|g\downarrow\rangle - |g\downarrow\rangle|e\uparrow\rangle - |g\uparrow\rangle|e\downarrow\rangle + |e\downarrow\rangle|g\uparrow\rangle\big]. \end{aligned} \tag{5.5}$$

By writing down explicitly these two states we can define a more compact notation that individuates the anti-symmetrized two-particle states $|g\uparrow, e\downarrow\rangle$ and $|e\uparrow, g\downarrow\rangle$

$$|eg^\pm\rangle = \frac{1}{\sqrt{2}}\left[\underbrace{\left(\frac{|e\uparrow\rangle|g\downarrow\rangle - |g\downarrow\rangle|e\uparrow\rangle}{\sqrt{2}}\right)}_{|e\uparrow,g\downarrow\rangle} \pm \underbrace{\left(\frac{|g\uparrow\rangle|e\downarrow\rangle - |e\downarrow\rangle|g\uparrow\rangle}{\sqrt{2}}\right)}_{|g\uparrow,e\downarrow\rangle}\right], \tag{5.6}$$

which are characterized by a defined nuclear spin associated to an electronic state. This formulation is useful to derive the formal expression of the two-body interaction potential (see Eq. (1.86)) characterized by the collisional channels associated to the states outlined in Eq. (5.3) and their respective projection operators $\hat{P}_{gg} = |gg\rangle\langle gg|$, $\hat{P}_{eg^\pm} = |eg^\pm\rangle\langle eg^\pm|$ and $\hat{P}_{ee} = |ee\rangle\langle ee|$:

$$U(\mathbf{r} - \mathbf{r}') = \left(g_{gg}\hat{P}_{gg} + g^+_{eg}\hat{P}_{eg^+} + g^-_{eg}\hat{P}_{eg^-} + g_{ee}\hat{P}_{ee}\right)\delta(\mathbf{r} - \mathbf{r}') \tag{5.7}$$

with $(g_{gg}, g_{eg}^{\pm}, g_{ee}) = 4\pi\hbar^2(a_{gg}, a_{eg}^{\pm}, a_{ee})/m$. In particular, by decomposing the projection operators $\hat{P}_{eg^{\pm}}$ on the states defined in Eq. (5.6), we obtain:

$$\hat{P}_{eg^{\pm}} = \frac{1}{2}\left(\underbrace{|e\uparrow, g\downarrow\rangle\langle e\uparrow, g\downarrow| + |g\uparrow, e\downarrow\rangle\langle g\uparrow, e\downarrow|}_{\text{direct}} \pm \underbrace{|e\uparrow, g\downarrow\rangle\langle g\uparrow, e\downarrow| \pm |g\uparrow, e\downarrow\rangle\langle e\uparrow, g\downarrow|}_{\text{exchange}} \right) \tag{5.8}$$

where the *direct* interaction takes into account those processes that preserve the nuclear spin of the single particles while the *exchange* contribution denotes the collisions involving a nuclear spin-flip.

As anticipated in section 1.3.2, also the metastable state $|e\rangle$ is decoupled from the nuclear spin in first approximation and therefore the collisional channel properties are determined exclusively by the electronic state. For this reason, the two-component formulation used so far can be easily generalized to the multi-component case $-5/2 \leq m \leq +5/2$ [14]. In particular, this formalism can be used to write down the second quantization many-body Hamiltonian of two-orbital ^{173}Yb atoms in an optical lattice interacting within the $SU(N)$ symmetry class. Since in this notation the anti-symmetrization is already taken into account, the passage to the second quantization formulation of the two-body interaction is easily obtained by the substitution $|g\uparrow, e\downarrow\rangle \rightarrow \hat{\Psi}^{\dagger}_{g\uparrow}(\mathbf{r})\hat{\Psi}^{\dagger}_{e\downarrow}(\mathbf{r}')$. In this way we obtain the total Hamiltonian of the system:

$$\begin{aligned}
\hat{H} &= \sum_{\alpha m} \int d\mathbf{r}\, \hat{\Psi}^{\dagger}_{\alpha m}(\mathbf{r}) \left(-\frac{\hbar^2}{2\mathrm{m}}\nabla^2 + V_{ext}(\mathbf{r}) \right) \hat{\Psi}_{\alpha m}(\mathbf{r}) \\
&+ \sum_{\alpha} g_{\alpha\alpha} \sum_{m<m'} \int \hat{\Psi}^{\dagger}_{\alpha m}(\mathbf{r})\hat{\Psi}^{\dagger}_{\alpha m'}(\mathbf{r})\hat{\Psi}_{\alpha m'}(\mathbf{r})\hat{\Psi}_{\alpha m}(\mathbf{r}) d\mathbf{r} \\
&+ \frac{g^{+}_{eg} + g^{-}_{eg}}{2} \int d\mathbf{r}\, \hat{\rho}_e(\mathbf{r})\hat{\rho}_g(\mathbf{r}) \\
&+ \frac{g^{+}_{eg} - g^{-}_{eg}}{2} \sum_{m,m'} \int d\mathbf{r}\, \hat{\Psi}^{\dagger}_{gm}(\mathbf{r})\hat{\Psi}^{\dagger}_{em'}(\mathbf{r})\hat{\Psi}_{gm'}(\mathbf{r})\hat{\Psi}_{em}(\mathbf{r})
\end{aligned} \tag{5.9}$$

where $\hat{\Psi}^{\dagger}_{\alpha m}(\mathbf{r})$ is the creation operator of a fermion with orbital state $\alpha = g, e$ and $\hat{\rho}_{\alpha} = \sum_m \hat{\Psi}^{\dagger}_{\alpha m}(\mathbf{r})\hat{\Psi}_{\alpha m}(\mathbf{r})$ is the density of atoms in the orbital state α. If we neglect the external trapping potential and consider only the deep magic-wavelength lattice, the natural basis to expand the field operator are Wannier functions:

$$\hat{\Psi}^{\dagger}_{\alpha m}(\mathbf{r}) = \sum_i w(\mathbf{r} - \mathbf{r}_i)\hat{c}^{\dagger}_{i\alpha m} \tag{5.10}$$

where $\hat{c}^{\dagger}_{i\alpha m}$ and $w(\mathbf{r} - \mathbf{r}_i)$ are respectively the creation operator and the Wannier function

[11] centered on site i of the optical lattice. The Hamiltonian (5.9) can be then reduced to:

$$\begin{aligned}\hat{H} &= J\sum_{\alpha m\langle ij\rangle}(\hat{c}^{\dagger}_{i\alpha m}\hat{c}_{j\alpha m}+\text{h.c.})+\sum_{\alpha,i}\frac{U_{\alpha\alpha}}{2}\hat{n}_{i\alpha}(\hat{n}_{i\alpha}-1)\\ &+ V\sum_{i}\hat{n}_{ig}\hat{n}_{ie}+V_{\text{ex}}\sum_{m,m'}\hat{c}^{\dagger}_{igm}\hat{c}^{\dagger}_{iem'}\hat{c}_{igm'}\hat{c}_{iem}\end{aligned} \tag{5.11}$$

where $J = \int d\mathbf{r}\, w^*(\mathbf{r})(-\hbar^2\nabla^2/2\text{m})\, w(\mathbf{r}+\mathbf{R})$ is the tunneling energy[2] between nearest neighbors (also defined in Eq. 1.66) and $U_{\alpha\alpha} = g_{\alpha\alpha}\int d\mathbf{r}|w(\mathbf{r})|^4$ and $U^{\pm}_{eg} = g^{\pm}_{eg}\int d\mathbf{r}|w(\mathbf{r})|^4$ denote the on-site interaction energies. The quantities

$$\begin{aligned}V &= \frac{U^{+}_{eg}+U^{-}_{eg}}{2}\\ V_{\text{ex}} &= \frac{U^{+}_{eg}-U^{-}_{eg}}{2}\end{aligned} \tag{5.12}$$

describe the direct and exchange interactions respectively and constitute the main observables of this work.

As stated above, the decoupling between nuclear and electronic states preserves the $SU(N)$ invariance of the more general Hamiltonian (5.11) with respect to the Hamiltonian (1.97) reported in section 1.3.2, which includes only $|g\rangle$ atoms. Differently from operators (1.98), in this case the generators of the $SU(N)$ symmetry group are defined summing also over the two electronic states:

$$\hat{S}^m_n = \sum_j \hat{S}^m_n(j) = \sum_{j,\alpha}\hat{S}^m_n(j,\alpha) = \sum_{j,\alpha}\hat{c}^{\dagger}_{jm\alpha}\hat{c}_{j\alpha m}. \tag{5.13}$$

Actually, since there are two electronic states, the symmetry group of the Hamiltonian (5.11) can be related to the $SU(2)$ pseudo-spin algebra in the $\{|g\rangle, |e\rangle\}$ Hilbert space generated by the operators:

$$\hat{T}^{\mu} = \sum_j \hat{T}^{\mu}_j = \sum_{j\alpha\beta m}\hat{c}^{\dagger}_{jm\alpha}\hat{\sigma}^{\mu}_{\alpha\beta}\hat{c}_{j\beta m}, \tag{5.14}$$

where σ^{μ} (with $\mu = x, y, z$) are the Pauli matrices in the $\{|g\rangle, |e\rangle\}$ basis. If the collisions between different electronic states are elastic, the Hamiltonian (5.9) shows also a $U(1)$ symmetry $[\hat{T}^z, \hat{H}] = 0$, in addition to the $SU(N)$ symmetry which is associated with the independence of scattering and of the trapping potential from the nuclear spin ($[\hat{S}^n_m, \hat{H}] = 0$

[2] Since we use an optical lattice at the magic-wavelength the trapping potential, and hence the tunneling energy, is identical both for $|g\rangle$ and $|e\rangle$.

for all n, m). This highly symmetric system opens interesting opportunities for quantum simulation of orbital magnetism as discussed further in section 5.5. In the next section we will introduce a simple model explaining the properties of the optical transitions between the states introduced in Eq. (5.3) showing the constraints imposed by Fermi statistics.

5.2.2 Laser excitation on two-particle states

Following Ref. [150], the interaction Hamiltonian of a pair of atoms with coherent laser light can be written as the sum of two operators acting individually on the two atoms:

$$\hat{H}_L = \hat{H}_1 + \hat{H}_2, \tag{5.15}$$

where each Hamiltonian describe the interaction between the atom $i = 1, 2$ and the laser light. Using the formalism defined in section 1.2 and assuming only π-polarized light ($q = 0$):

$$\hat{H}_i = \frac{\hbar}{2}(\Omega\hat{\Sigma}_i^\dagger + \Omega^*\hat{\Sigma}_i) \tag{5.16}$$

where Ω does not depend on the atomic index i because the phase of the electromagnetic field is the same for both atoms, as we assume that they sit in the same lattice site. Since both the ground and excited state have no hyperfine structure and we are considering only two nuclear spin states, the raising operator defined in Eq. (1.37) can be simplified to $\hat{\Sigma}_i = \sum_{m=\uparrow\downarrow} \mathcal{S}^{(0)}_{mm}|e_i, m\rangle\langle g_i, m|$, with $\mathcal{S}^{(q)}_{m_g,m_e}(F_e)$ being the coefficients taking into account the angular part of the matrix element. It shall be noted that the coefficients $\mathcal{S}^{(0)}_{mm}$ correspond to those of a $F_g = 5/2 \to F_e = 5/2$ transition as they are inherited from the higher $J = 1$ electronic states responsible for the hyperfine mixing with the $^3P_0$ state leading to a finite electric dipole moment. In order to make the notation more compact, it is convenient to absorb the Clebsch-Gordan coefficient in the Ω definition:

$$\Omega_\uparrow = \Omega\mathcal{S}^{(0)}_{\uparrow\uparrow}, \qquad \Omega_\downarrow = \Omega\mathcal{S}^{(0)}_{\downarrow\downarrow}. \tag{5.17}$$

In this way we can write the Hamiltonian (5.16) as:

$$\hat{H}_i = |e_i\rangle\langle g_i| \otimes \frac{\hbar}{2}(\Omega_\uparrow P_{i\uparrow} + \Omega_\downarrow P_{i\downarrow}) + h.c.\,, \tag{5.18}$$

where $\hat{P}_{im} = |m\rangle_i\langle m|_i$ are the projection operators defined in Eq. (1.30) for $F_e = 5/2 = F_g$, referred to the atom $i = 1, 2$ with spin $m = \uparrow, \downarrow$. This formulation highlights how the laser excitation is also related to the nuclear spin sector of the Hilbert space through the Clebsch-Gordan dependence. By defining the operators $\hat{\mathbb{1}}_i = P_{i\uparrow} + P_{i\downarrow}$ and $\hat{\sigma}_{iz} = P_{i\uparrow} - P_{i\downarrow}$,

the Hamiltonian (5.18) can be recast as:

$$\hat{H}_i = |e_i\rangle\langle g_i| \otimes \frac{\hbar}{2}(\Omega^+ \mathbb{1}_i + \Omega^- \hat{\sigma}_{zi}) + h.c.\,, \tag{5.19}$$

with $\Omega^{\pm} = (\Omega_\uparrow \pm \Omega_\downarrow)/2$. This formulation of the laser excitation Hamiltonian is convenient to highlight the optical transitions between the states defined in Eq. (5.3). In particular, starting from the lowest energy state $|gg\rangle|s\rangle$ we have:

$$H_L|gg\rangle|s\rangle = \frac{\hbar}{2}\left[\sqrt{2}\Omega^+|eg^+\rangle + \sqrt{2}\Omega^-|eg^-\rangle\right] \tag{5.20}$$

In the special case $\Omega_\uparrow = -\Omega_\downarrow$, which only occurs in the spin-symmetric mixtures $m = \pm 5/2, \pm 3/2, \pm 1/2$ (see appendix B), only the transition to the $|eg^-\rangle$ state is allowed and, counterintuitively, the symmetry of the nuclear spin wavefunction is changed from a singlet to a triplet by an optical excitation. In all the remaining spin mixtures there is a finite probability of exciting both the $|eg^+\rangle$ and the $|eg^-\rangle$ states. Moreover, starting from the states $|eg^{\pm}\rangle$, there is a finite probability to populate the state $|ee\rangle|s\rangle$, proportional to the following matrix elements:

$$\begin{aligned} \langle s|\langle ee|H_L|eg^+\rangle &= \frac{\hbar}{2}\sqrt{2}\Omega^+, \\ \langle s|\langle ee|H_L|eg^-\rangle &= \frac{\hbar}{2}\sqrt{2}\Omega^-. \end{aligned} \tag{5.21}$$

It shall be noted that the Hilbert space basis (5.3) is made of eigenstates of the two-body interaction Hamiltonian, as they are all defined by the collisional channels. We will see in the next section how a magnetic field mixes these states defining a new eigenstate basis.

5.2.3 Magnetic field mixing

Similarly to the interaction with an optical field, we can model the effect of a magnetic field with the Hamiltonian:

$$\hat{H}_Z = \hat{H}_1 + \hat{H}_2 \tag{5.22}$$

with:

$$\hat{H}_i = g_\alpha \mu_B \frac{\hat{I}_{zi}}{\hbar} B_z \tag{5.23}$$

where g_α is the g-factor of the state $\alpha = g, e$, μ_B is the Bohr magneton and $\hat{I}_{zi}$ denotes the projection along the quantization axis of the angular momentum of atom $i = 1, 2$. It shall be noted that, without hyperfine mixing, the coupling to an external magnetic field of $^3P_0$ and $^1S_0$ states would be equal and caused entirely by the nuclear magnetic moment with

coupling strength $g_g\mu_B/h = 207$ Hz/G [147]. Because of the mixing with higher P_1 states, however, the $^3P_0$ state features an additional Zeeman splitting of $\delta g\mu_B/\hbar = 113$ Hz/G. As for the case of optical fields, the Hamiltonian $\hat{H}_i$ acts only on the state of the atom i with orbital state α and magnetic momentum projection m as $\hat{H}_i|\alpha, m\rangle_i = g_\alpha \mu_B m B_z$. By using the former simple relation, we can calculate the matrix elements of $\hat{H}_Z$ on the interaction eigenstates introduced in Eq. (5.3):

$$\begin{aligned} \langle gg|\hat{H}_Z|gg\rangle &= g_g(m+m')\mu_B B, \qquad (5.24) \\ \langle ee|\hat{H}_Z|ee\rangle &= g_e(m+m')\mu_B B, \\ \langle eg^{\pm}|\hat{H}_Z|eg^{\mp}\rangle &= \frac{1}{2}(m-m')\delta g\,\mu_B B, \\ \langle eg^{\pm}|\hat{H}_Z|eg^{\pm}\rangle &= \frac{1}{2}(m+m')(g_e+g_g)\,\mu_B B. \end{aligned} \qquad (5.25)$$

Interestingly, the magnetic field mixes the two interaction eigenstates $|eg^{\pm}\rangle$. Therefore, considering only the sub-space $\{|eg^-\rangle, |eg^+\rangle\}$ and combining the Zeeman Hamiltonian $\hat{H}_Z$ and the onsite interaction Hamiltonian:

$$\hat{H}_0 = \begin{pmatrix} U_{eg}^+ & 0 \\ 0 & U_{eg}^- \end{pmatrix}, \qquad (5.26)$$

we can write the global Hamiltonian of the two-particle system $\hat{H}_{eg} = \hat{H}_0 + \hat{H}_Z$ as:

$$\hat{H}_{eg} = \begin{pmatrix} (U_{eg}^+ - U_{gg}) + \frac{1}{2}\delta g\,(m+m')\mu_B B & \frac{1}{2}(m-m')\delta g\,\mu_B B \\ \frac{1}{2}(m-m')\delta g\,\mu_B B & (U_{eg}^- - U_{gg}) + \frac{1}{2}\delta g\,(m+m')\mu_B B \end{pmatrix}, \qquad (5.27)$$

where on the diagonal we considered the energy difference $\langle eg^{\pm}|\hat{H}_{eg}|eg^{\pm}\rangle - \langle gg|\hat{H}_{eg}|gg\rangle$ which is more closely related to the spectroscopic observable. Therefore, the presence of the external magnetic field generates two eigenenergy branches:

$$U_{eg}^{H,L}(B) = \frac{1}{2}(m+m')\delta g\,\mu_B B + (V - U_{gg}) \pm \sqrt{V_{ex}^2 + \left(\frac{1}{2}(m-m')\delta g\,\mu_B B\right)^2} \qquad (5.28)$$

where H, L correspond to the high and low-energy branches (see Fig. 5.4). As shown by spectroscopic studies (see section 5.2.4), the exchange energy V_{ex} is measured to be positive and therefore the high- (low-) energy branches are adiabatically connected to the $a_{eg}^+(a_{eg}^-)$ collisional channels. In general, the two eigenstates as a function of magnetic field

are:

$$\begin{aligned} |eg^L\rangle &= \gamma(B)|eg^-\rangle + \delta(B)|eg^+\rangle \\ |eg^H\rangle &= -\delta(B)|eg^-\rangle + \gamma(B)|eg^+\rangle \end{aligned} \tag{5.29}$$

where the coefficients $\gamma(B)$ and $\delta(B)$ depend on the magnetic field and satisfy $\gamma^2(B) + \delta^2(B) = 1$ and $\gamma(0) = 1$, $\delta(0) = 0$. The qualitative dependence of the energy on the magnetic field is shown in Fig. 5.4 in the particular case of a symmetric mixture where the single-particle Zeeman splitting (the first term in Eq. 5.28) is zero. In the next section,

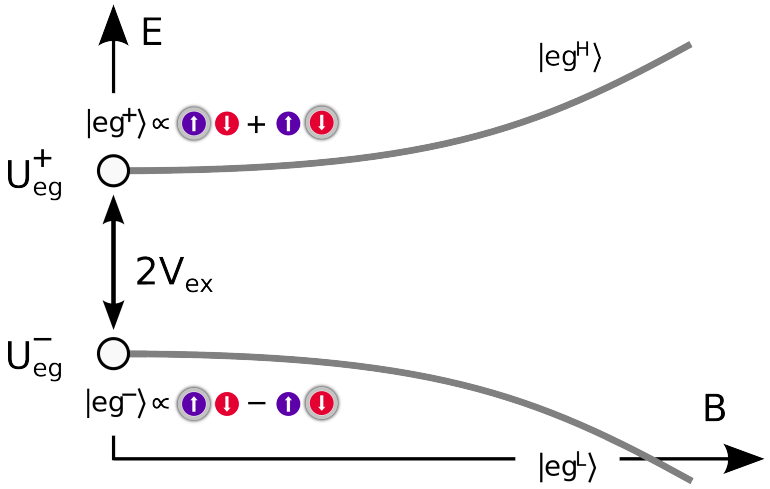

Figure 5.4: Eigenenergies of $\hat{H}_{eg}$ as a function of the magnetic field B in the case of a symmetric mixture $m = -m'$.

with the help of this simple model we will investigate the spectrum of such a system in order to identify the different peaks and quantify the interaction shifts.

5.2.4 Spectroscopy

In this section we will focus on the particular case of the spin-symmetric mixture $m = -5/2$, $m' = +5/2$, where the effect of the magnetic mixing is maximum and the single-particle Zeeman shift is canceled. The experimental procedure is the same as the one described in section 5.1, except for the spin distribution initialization. In particular the number of atom is such that the sample displays both singly and doubly occupied sites. By optically addressing atoms in the doubly-occupied sites, we can study the effect of interactions. The typical spectrum at finite magnetic field is shown in Fig. 5.5. The extremal peaks correspond to singly occupied lattice sites and are indeed separated by the Zeeman energy. The identification is easily done by performing spectroscopy with a

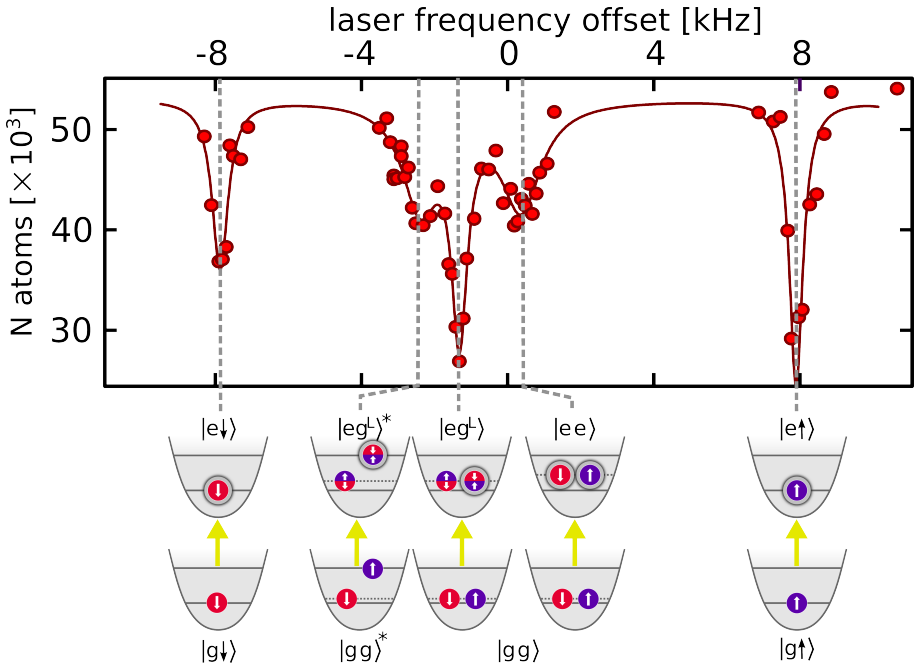

Figure 5.5: Spectrum of the $\lambda_C = 578$ nm clock transition for the excitation of a two-spin mixture ($m = \pm 5/2$)of ^{173}Yb atoms trapped in a $s = 30$ 3D lattice at $B = 28$ G. The vertical axis shows the number of residual $|g\rangle$ atoms after the excitation, while the horizontal axis shows the offset with respect to the clock transition frequency. The labels below the plot identify the different features of the spectrum. The dependence of the peak centers on the magnetic field B allows us to attribute them to the excitation of one atom in either singly-occupied sites ($|e\downarrow\rangle$ and $|e\uparrow\rangle$) or in doubly-occupied sites ($|eg^L\rangle, |ee\rangle$, and $|eg^L\rangle^*$) [40].

spin-polarized Fermi gas in $m = -5/2$ and $m' = +5/2$ respectively. Since the differential magnetic factor is positive $\delta g = 113.4$ Hz/G, we can assign the lowest energy peak to $m = -5/2$.

The three additional peaks refer to the doubly occupied lattice sites and their identification can be carried out by analyzing their dependence on the magnetic field which has been done in Ref. [40] for several spin mixtures. We briefly review the peak assignments:

- The central peak, as depicted in the cartoon at the bottom of Fig. 5.5, can be identified from the dependence on the magnetic field as the transition from a $|gg\rangle$ singlet to the state $|eg^L\rangle$ defined in the previous section. As shown in Fig. 5.6, the position of this peak depends on the square root of the magnetic field as predicted by Eq. (5.28). Since we know, because of Clebsch-Gordan coefficients, that in the symmetric spin mixtures $m = -m'$ the transition to $|eg^+\rangle$ is forbidden by anti-symmetrization of

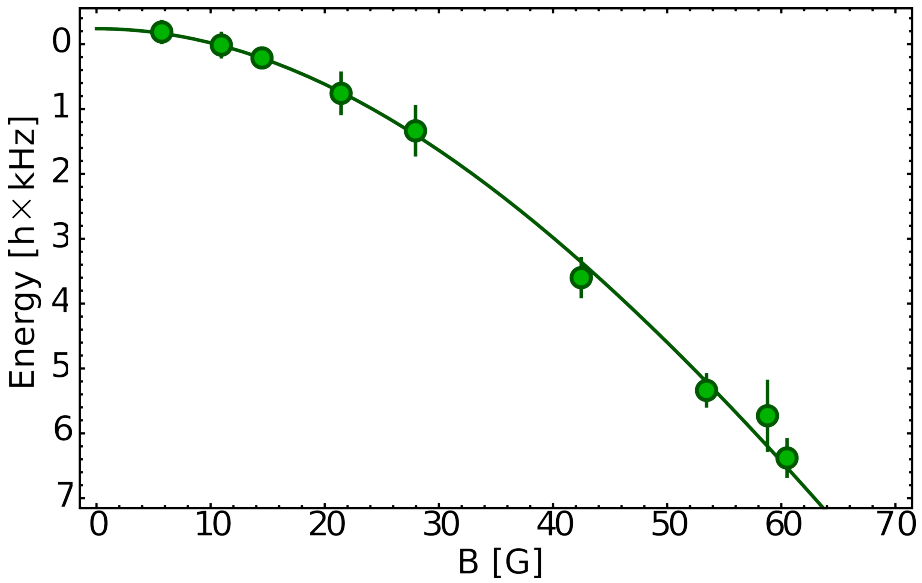

Figure 5.6: Resonance frequency of the $|gg\rangle \rightarrow |eg^-\rangle$ process in a $m = \pm 5/2$ spin-mixture as a function of the bias magnetic field. The experimental points are fitted with the function (5.28) with $V - U_{gg}$ and $V_{\rm ex}$ as free parameters. The zero energy is the defined by the Zeeman splitting between the single particle peaks (see Fig. 5.5).

the total wavefunction, we can identify the peak as the one adiabatically connected to the $|eg^-\rangle$ state at $B = 0$. Moreover, since the peak position decreases as the magnetic field increases, we can infer that the $|eg^-\rangle$ state has lower energy than the $|eg^+\rangle$ state and therefore the sign of $V_{ex} = (U^+_{eg} - U^-_{eg})/2$ is positive. By fitting the data with Eq. (5.28), we have an experimental access to the quantities $V - U_{gg}$ and $V_{\rm ex}$ defined in Eqs. (5.12). If we assume that the interaction energy is given by:

$$U^{\pm}_{eg} = \frac{4\pi\hbar^2 a^{\pm}_{eg}}{m} \int |w_0(\mathbf{r})|^2 \, d\mathbf{r}, \tag{5.30}$$

with $w_0(\mathbf{r})$ the Wannier function in the lowest band, we can estimate the two scattering lengths to be $a^-_{eg} = (215 \pm 40)\, a_0$ and $a^+_{eg} = (2600 \pm 500)\, a_0$. The estimate of a^-_{eg} is reliable and in accordance with Ref. [40]. As shown in the next section, more insightful experimental observation and a more refined theoretical model are needed for the determination of the scattering length a^+_{eg}, as Eq. (5.30) is no longer valid.

- The peak at frequencies higher than the $|eg^L\rangle$ is the two-photon transition $|gg\rangle \rightarrow |ee\rangle$ to the spin singlet with two excited atoms, passing through the virtual state $|eg^L\rangle$. This identification is based on the experimental observation that in the spin-

symmetric mixture $m = -m'$ this peaks is insensitive to the magnetic field. In all the other spin mixtures this peak has a linear dependence on the magnetic field, namely:

$$\langle ee|H_Z|ee\rangle - \langle gg|H_Z|gg\rangle = (m + m')\delta g\, \mu_B B. \tag{5.31}$$

Moreover, the peak is less evident than the central one, which is explainable with its two-photon nature.

- The peak at lower frequencies than the central one is assigned to a $|gg\rangle^* \rightarrow |eg^L\rangle^*$ transition where both states have an atom in an excited band. This identification is based on the evidence that the peak dependence on the magnetic field is the same as the $|eg^L\rangle$ state, but with a systematic redshift with respect to the central peak. Moreover, the peak is more pronounced when there are more atoms in the sample confirming the relation with the excited bands.

These measurements demonstrate the possibility to spectrally resolve doubly occupied sites in a deep 3D lattice owing to the narrow line of the clock transition. Moreover, the magnetic field mixing enables the identification of the different spectral features. However, when $\delta g \mu_B B \gg V_{\text{ex}}$, the Zeeman splitting determines the dominant energy scale of the system and the eigenstates of the Hamiltonian tend to an equal superposition of $|eg^+\rangle$ and $|eg^-\rangle$ states:

$$\begin{aligned} |eg^L\rangle &\rightarrow \left(\frac{|eg^+\rangle - |eg^-\rangle}{\sqrt{2}}\right) = |g\uparrow, e\downarrow\rangle \\ |eg^H\rangle &\rightarrow \left(\frac{|eg^+\rangle + |eg^-\rangle}{\sqrt{2}}\right) = |e\uparrow, g\downarrow\rangle \end{aligned} \tag{5.32}$$

Since these two limiting states are eigenstates of $\hat{H}_Z$, the global Hamiltonian $\hat{H}_{eg}$ defined in Eq. (5.33) can be written on the basis $\{|g\uparrow, e\downarrow\rangle, |e\uparrow, g\downarrow\rangle\}$ as:

$$\hat{H}_{eg} = \begin{pmatrix} V + \delta g\, m\mu_B B & V_{\text{ex}} \\ V_{\text{ex}} & V + \delta g\, m'\mu_B B \end{pmatrix}. \tag{5.33}$$

We will see in the next section how exploiting the magnetic field mixing, it is possible to observe coherent spin-exchange dynamics.

5.3 Spin-exchange oscillations

As shown in the previous section, through spectroscopy it is possible to get information about the different inter-orbital collisional channels. However, spectroscopic measurements

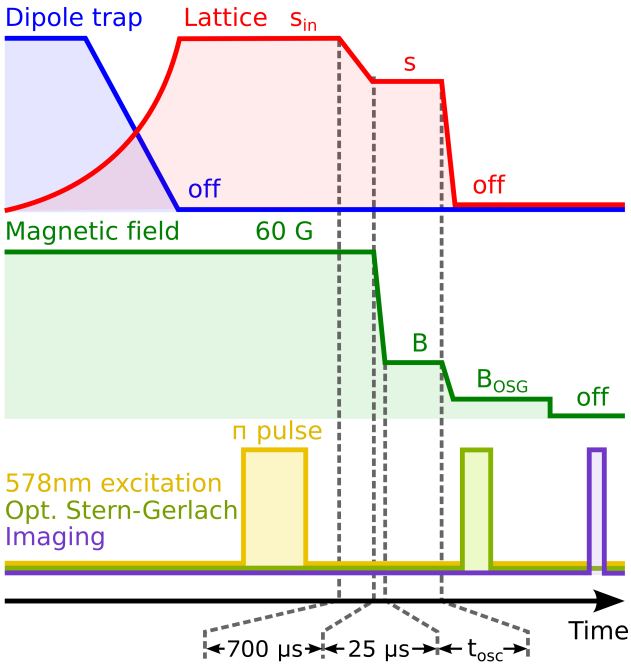

Figure 5.7: Typical experimental sequence to trigger spin-exchange dynamics (see text for details).

do not highlight the coherent nature of the binary collision between atoms in different electronic states. In the last years, coherent spin-changing dynamics (see section 1.3.2) has been observed with both bosonic [72, 73] and fermionic [74] alkali atoms in their ground state. In the case of ^{173}Yb, spin-exchange interactions arise from the difference in the spin-singlet and spin-triplet inter-atomic potential curves in the scattering of one $|g\rangle$ and one $|e\rangle$ atom. In order to understand the mechanism behind such interactions, let us consider two atoms prepared in the initial state $|\psi_0\rangle = |g\uparrow, e\downarrow\rangle = \frac{1}{\sqrt{2}}[|eg^+\rangle - |eg^-\rangle]$. The energy difference in the collisional channels results in a spin-exchange dynamics in which the spins of the $|g\rangle$ and $|e\rangle$ atoms are periodically flipped at a frequency $2V_{\mathrm{ex}}/h$, with probability of finding a ground-state atom in the $|g\uparrow\rangle$ state being given by

$$P(|g\uparrow\rangle)(t) = \frac{1}{2}\left[1 + \cos\left(\frac{2V_{\mathrm{ex}}}{\hbar}t\right)\right]. \tag{5.34}$$

The procedure to observe spin-exchange oscillations is displayed in Fig. 5.7. The experiment is performed on quantum degenerate Fermi gases of ^{173}Yb in the symmetric spin mixture $m = \pm 5/2$, which is produced by evaporative cooling in the crossed ODT until approximately 4×10^4 atoms are left at a temperature $T \simeq 0.15\, T_F \simeq 25$ nK. The atomic cloud is then adiabatically loaded in a 3D optical lattice operating at the magic-wavelength

$\lambda_L = 759.35$ nm and, at the same time, the optical dipole trap intensity is ramped to zero in order to avoid unwanted light shifts on the clock transition. Before the lattice loading, we slightly compress the dipole trap in order to load more doubly occupied sites in the central region of the cloud. Moreover, the atom number is chosen in order to minimize the first excited band occupation in order to avoid $|gg\rangle^* \rightarrow |eg\rangle^*$ processes. With this procedure the average filling is $0.5 \leq \overline{n} \leq 1$ atoms per lattice site and per spin component.

The atoms are then excited by a 578 nm π-pulse, resonant with the $|gg\rangle \rightarrow |eg^L\rangle$ transition. The excitation is performed at a large lattice depth $s_{in} \geq 30$, in order to avoid tunneling of atoms during the excitation time, and at large magnetic field (60 G), in order to have a sizeable admixture of the spin-singlet state $|eg^+\rangle$ into the $|eg^L\rangle$ state ($|\gamma|^2 \simeq 0.75$, $|\delta|^2 \simeq 0.25$). After the excitation, pulse the lattice depth is quickly ramped to s in 700 μs and then the magnetic field is quenched to a very low bias field (3.5 G) in a time $t_{\rm ramp} = 25$ μs, which is fast enough to have a significant population of the $|eg^H\rangle \simeq |eg^+\rangle$ state by nonadiabatic Landau-Zener excitation. The creation of a superposition of $|eg^-\rangle$ and $|eg^+\rangle$ states allows us to start the spin dynamics, which is observed by detecting the fraction of ground-state atoms in the different spin states by performing optical Stern-Gerlach (OSG) detection after different evolution times [151]. Figure 5.8 shows clear oscillations of the ground-state magnetization $[N(g\uparrow) - N(g\downarrow)] / [N(g\uparrow) + N(g\downarrow)]$, which are driven by the spin-exchange process. These oscillations provide a clear demonstration of the coherent nature of this spin-exchange interaction. The measurement of their frequency provides a direct, model-independent determination of the interaction strength, which is $2V_{\rm ex} = h \times (13.87 \pm 0.17)$ kHz for the data in Fig. 5.8. The finite bias magnetic field $B \simeq 3.5$ G used for the measurement yields a slightly faster oscillation frequency than $2V_{\rm ex}/h$ (by ~ 100 Hz). In order to show the zero-field oscillation frequency the datapoints in Fig. 5.8 have been corrected by using the finite-B model described later in section 5.4. The experimental points have been offset by a constant value ($\simeq 5\%$) to take into account a slight unbalance of the spin mixture resulting from an imperfect preparation of the initial state which also leads to the asymmetry of the $|e\downarrow\rangle$, $|e\uparrow\rangle$ peaks in the spectrum in Fig. 5.5. The relatively small amplitude of the oscillation in Fig. 5.8 can be ascribed to three different causes:

- the small initial admixture of the $|eg^+\rangle$ state in the $|eg^L\rangle = \gamma|eg^-\rangle + \delta|eg^+\rangle$ state due to the excitation at a finite B, which leads to the more general time-dependent probability amplitude:

$$P(|g\uparrow\rangle)(t) = \frac{1}{2}\left[1 + 2\gamma\sqrt{1-|\gamma|^2}\cos\left(\frac{2V_{\rm ex}}{\hbar}t\right)\right]; \tag{5.35}$$

- the finite switching time of the magnetic field, which makes the projection onto the

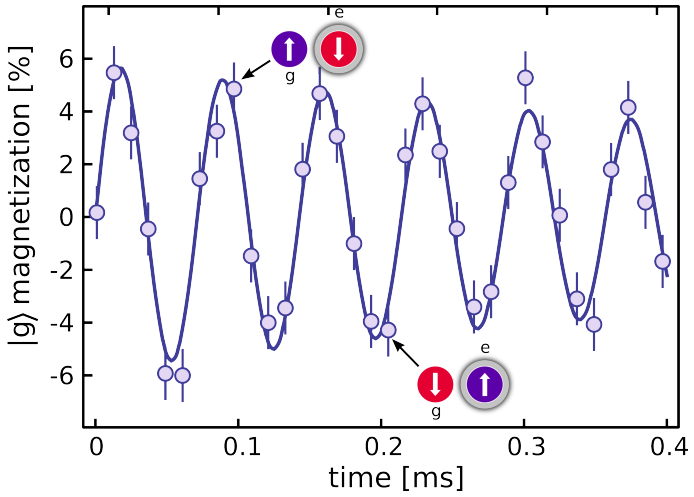

Figure 5.8: Time-resolved detection of two-orbital spin-exchange oscillations at a lattice depth $s = 30.8$ after quenching the magnetic field from 60 G to a bias field of 3.5 G. The points show the difference in fractional population between $|g\uparrow\rangle$ and $|g\downarrow\rangle$ atoms. The points are averages over 5 repeated measurements and the line is the result of a fit using a damped sinusoidal function (a global error bar based on the fit residuals has been assigned to the points).

new eigenstates at low B only partially diabatic;

- the presence of singly-occupied lattice sites not participating to the spin oscillation, yet contributing to the background signal;

We also have checked that these spin oscillations disappear if no laser excitation pulse is performed: collisions among $|g\rangle$ atoms can only take place in the spin-singlet channel, and the $SU(N)$ interaction symmetry grants the absence of spin-changing collisions. We have checked that no other nuclear spin states, different from $|\uparrow\rangle$ and $|\downarrow\rangle$, are populated during the spin-exchange dynamics. Moreover, the 3D lattice setting allows us to study the dynamics of an isolated two-atom system in which only one atom is in the excited state, therefore significantly reducing the effects of inelastic $|e\rangle - |e\rangle$ collisions. Nevertheless, we measure a finite lifetime of the spin-exchange oscillations, on the order of ~ 2 ms, after which the oscillation amplitude becomes comparable with the scattering of the points, as shown in Fig. 5.9. In order to investigate the origin of this damping, we have performed additional experiments in which we introduce a variable waiting time t_{wait} between the laser excitation to the $|eg^L\rangle$ state and the magnetic field quench. For t_{wait} as large as 30 ms (more than one order of magnitude larger than the observed damping time) we still detect high-contrast spin-exchange oscillations. This rules out the explanation of the

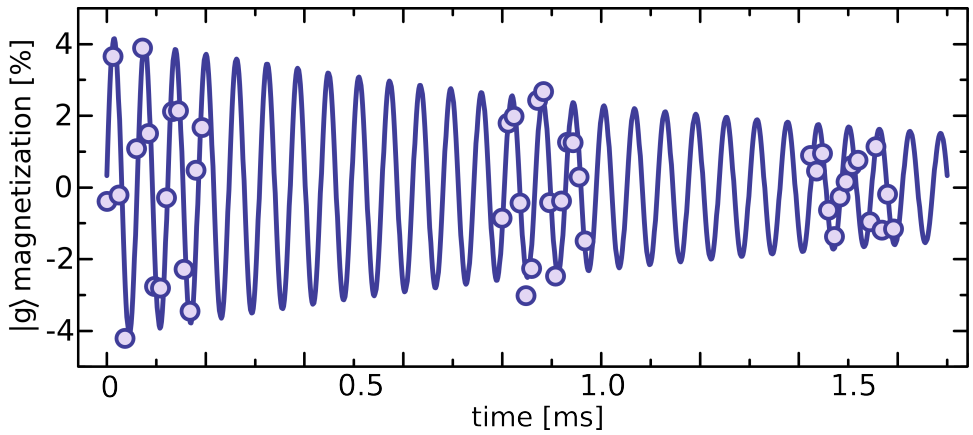

Figure 5.9: Spin exchange oscillations taken at $s = 35$ with longer hold times to evaluate the damping (see text for details).

damping shown in Fig. 5.9 in terms of either a detrimental effect of inelastic $|g\rangle - |e\rangle$ collisions in doubly-occupied sites, or a possible collisional dephasing introduced by the tunneling of highly mobile atoms in excited lattice bands. After the exclusion of these fundamental mechanisms of decoherence, it seems highly plausible that the decay of the spin-exchange oscillations arises from technical imperfections (associated e.g. to the fast switching of the magnetic field).

5.4 Characterization of inter-orbital collisions

In this section, we will show how the spin-exchange dynamics not only proves the coherent nature of the exchange interaction, but it can also be a valuable tool to investigate the strength and the properties of the $|eg^+\rangle$ spin-singlet collisional channel, measuring the frequency of spin-exchange oscillations as a function of the lattice depth s and of the magnetic field B. This characterization has been carried out with the symmetric spin mixture $m = \pm 5/2$, where a direct spectroscopic excitation of the $|gg\rangle \rightarrow |eg^+\rangle$ process is forbidden by angular momentum conservation, as explained in section 5.2. On the other hand, the spin mixture $m = \pm 5/2$ maximizes the magnetic field mixing between $|eg^+\rangle$ and $|eg^-\rangle$ states (see Fig. 5.10), leading to more easily observable spin-exchange oscillations.

Lattice depth dependence

In these measurements the optical excitation is performed at a lattice depth $s_{in} \geq 30$, then the optical lattice is ramped to s in ~ 700 μs, immediately before the quench which

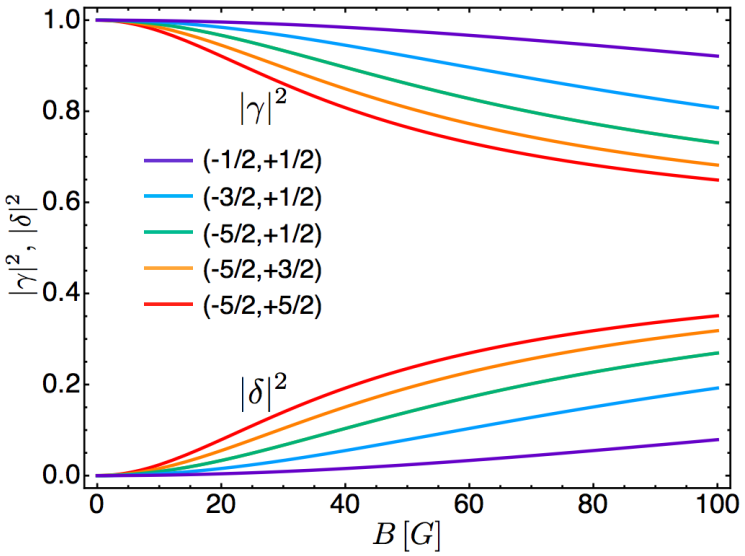

Figure 5.10: Absolute square values of the mixing coefficients $\gamma(B)$ and $\delta(B)$ ($|eg^L\rangle = \gamma(B)|eg^-\rangle + \delta(B)|eg^+\rangle$) as a function of magnetic field. The mixing depends on the difference $(m - m')$, as shown in Eq. (5.24).

initiates the spin dynamics (see Fig. 5.7). The points in Fig. 5.11 show the dependence of the spin oscillation frequency $2V_{\rm ex}/h$ on the lattice depth, clearly exhibiting a monotonic increase with s. The measured values of $2V_{\rm ex}$ are significantly large, ≈ 5 times larger than the Hubbard interaction energy of two ground-state atoms trapped in the lattice sites, and approaches from below the energy separation between the ground and first excited band of the three-dimensional lattice. In this regime the usual treatment of interactions, based on the evaluation of the Hubbard onsite interaction energy displayed in Eq. (5.30), is expected to fail. At large interaction strength, the two-particle wavefunction cannot be expressed in terms of lowest-band Wannier functions since, in the limit of infinite repulsion, the two atoms tend to spatially separate in each lattice site [121] and the probability of finding them at the same position drops to zero. For a system of two particles in a harmonic potential it has been shown that, for a scattering length a_s significantly larger than the harmonic oscillator length a_{ho}, the interaction energy saturates at the energy of the first excited harmonic oscillator state [152, 153]. In order to relate our measurements to the values of the scattering lengths $a_{eg}^{\pm}$, we follow a similar treatment to that adopted in Refs. [154, 155]. The Hamiltonian describing two atoms interacting in a lattice potential well is

$$H = \frac{p_1^2}{2m} + \frac{p_2^2}{2m} + V_{lat}(\mathbf{r}_1) + V_{lat}(\mathbf{r}_2) + V_{int}(\mathbf{r}_1 - \mathbf{r}_2), \tag{5.36}$$

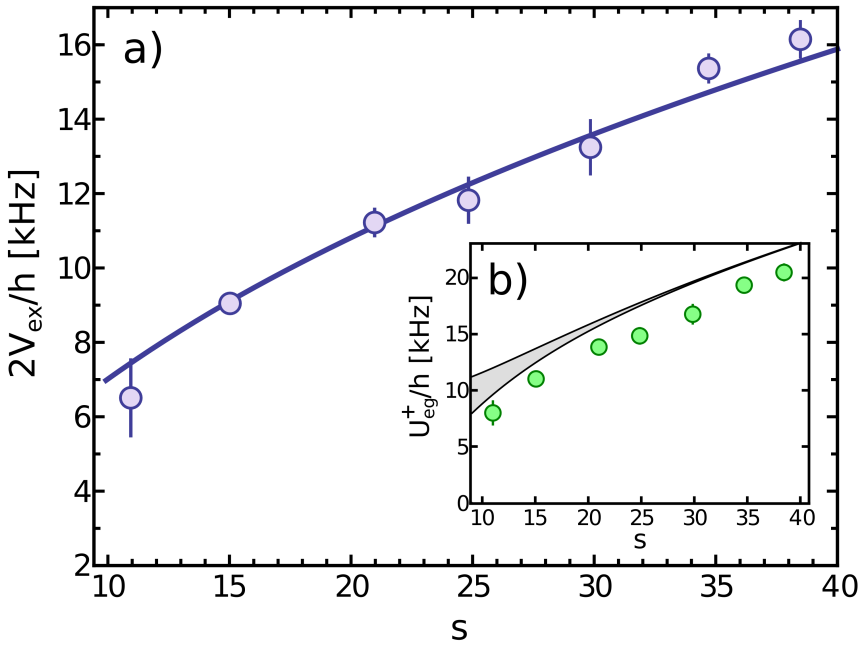

Figure 5.11: a) The points show the measured spin-exchange frequency as a function of the lattice depth s. The data have been corrected for the small bias magnetic field $B = 3.5$ G in order to show the zero-field spin-exchange frequency. Each point is the average of at least 3 different measurements and the error bar shows the statistical error. The line is a fit based on the model described in the main text. b) The points show the interaction energy of the $|eg^+\rangle$ state, calculated as the sum of the experimentally measured $2V_{\rm ex}$ and the U^-_{eg} calculated by using $a^-_{eg} = 219.5\, a_0$ [40]. The shaded area shows the energy difference between ground and first excited lattice band.

where $V_{lat}(\mathbf{r}) = V_0 \sum_{i=x,y,z} \sin^2(kr_i)$ is the lattice potential experienced by each atom and $V_{int}(\mathbf{r}) = \frac{4\pi\hbar^2}{m} a_s\, \delta(\mathbf{r}) \frac{\partial}{\partial r} r$ is the interaction potential, expressed in the form of the regularized pseudopotential introduced in section 1.3. The interaction energy for the two particles was derived by evaluating the anharmonic corrections to the lowest-order parabolic approximation of the potential. In order to separate the anharmonic contribution due to the lattice potential (which is essentially important for a quantitative comparison with the experimental data), we expand $V_{lat}(\mathbf{r})$ around the origin up to the $10^{\rm th}$ order:

$$V_{lat}(\mathbf{r}) = V_0 \sum_{i=x,y,z} (k^2 r_i^2 - \frac{1}{3} k^4 r_i^4 + \frac{2}{45} k^6 r_i^6 + ...). \tag{5.37}$$

This order of expansion is high enough to describe properly the shape of an individual lattice well. In order to consider the effects of tunneling, which are important only at low lattice depth, the potential should be expanded to a higher order, at least to the 20^{th}, making the problem computationally much longer to solve. Recalling that $\omega_\perp = 2\sqrt{s}E_R/\hbar = \sqrt{2V_0k_L^2/m}$ (Eq. 1.59) we can rewrite the Hamiltonian as:

$$H = \frac{p_1^2}{2m} + \frac{p_2^2}{2m} + \frac{1}{2}m\omega_\perp^2 r_1^2 + \frac{1}{2}m\omega_\perp^2 r_2^2 + V_{int}(\mathbf{r}_1 - \mathbf{r}_2) + V_{anh}(\mathbf{r}_1, \mathbf{r}_2), \tag{5.38}$$

where $V_{anh}(\mathbf{r}_1, \mathbf{r}_2)$ contains the anharmonic terms coming from the expansion of the lattice potential. By making the substitution[3] $\mathbf{R} = \frac{\mathbf{r}_1+\mathbf{r}_2}{\sqrt{2}}$ and $\mathbf{r} = \frac{\mathbf{r}_1-\mathbf{r}_2}{\sqrt{2}}$, we can write the Hamiltonian in terms of "center-of-mass" $\{\mathbf{R}, \mathbf{P}\}$ and "relative" $\{\mathbf{r}, \mathbf{p}\}$ coordinates:

$$H = \underbrace{\frac{P^2}{2m} + \frac{1}{2}m\omega_\perp^2 R^2}_{H_{CM}} + \underbrace{\frac{p^2}{2m} + \frac{1}{2}m\omega_\perp^2 r^2 + V_{int}(\mathbf{r})}_{H_{\text{Busch}}} + V_{anh}(\mathbf{R}, \mathbf{r}). \tag{5.39}$$

where the first part refers to the center-of-mass motion, while the second part refers to the relative motion + interaction part of the Hamiltonian, which was solved analytically by T. Busch et al. in Ref. [152] finding the following eigenfunctions:

$$\psi_{\text{B}}(\mathbf{r}) = A \exp\left(-\frac{r^2}{2a_\perp^2}\right) \Gamma\left(-\frac{E}{2\hbar\omega_\perp} + \frac{3}{4}\right) \mathcal{U}\left(-\frac{E}{2\hbar\omega_\perp} + \frac{3}{4}, \frac{3}{2}, \frac{r^2}{a_\perp^2}\right), \tag{5.40}$$

where Γ is the Euler function, $\mathcal{U}$ are the confluent hypergeometric functions, A is a normalization factor, $a_\perp = \sqrt{\hbar/m\omega_\perp}$ is the harmonic oscillator length and E is the total energy, given by the solution of the equation:

$$\sqrt{2}\frac{\Gamma\left(-\frac{E}{2\hbar\omega_\perp} + \frac{3}{4}\right)}{\Gamma\left(-\frac{E}{2\hbar\omega_\perp} + \frac{1}{4}\right)} = \frac{a_\perp}{a_s}. \tag{5.41}$$

However, for a true lattice potential, the anharmonic terms $V_{anh}(\mathbf{R}, \mathbf{r})$ couple the relative and center-of-mass motion, making the problem impossible to be solved analytically. In order to extend the exact results for the parabolic well to the case of a lattice potential well, we diagonalize numerically the full Hamiltonian in Eq. (5.39) written on the basis of the eigenfunctions of $\hat{H}_{CM} + \hat{H}_{\text{Busch}}$, namely

$$\Phi_{\alpha,\beta}(\mathbf{r}, \mathbf{R}) = \Psi_\alpha(\mathbf{R})\, \psi_\beta(\mathbf{r}), \tag{5.42}$$

[3] This unusual change of variables is used to write the center-of-mass and the relative motion contribution with the atomic mass instead of the total and reduced mass, respectively.

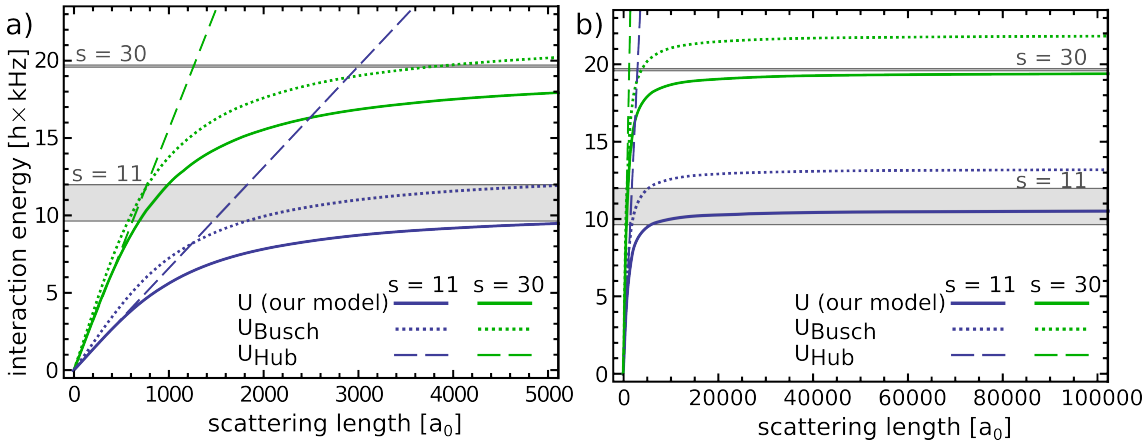

Figure 5.12: a) Interaction energies for two particles in a lattice site, calculated for two lattice depths $s = 11$ and $s = 30$ according to three different models (see text). The interaction energy U calculated using our model is well approximated by the usual Hubbard relation U_{Hub} at small scattering length. **b)** The same results are plotted up to larger values of a_s. For large a_s the interaction energy U saturates at the energy difference between the ground and the first-excited lattice band, here represented by the grey regions (the width of these regions reflects the finite width of the energy bands caused by tunnelling).

where $\alpha = \{N, L, M\}$ and $\beta = \{n, \ell, m\}$ are the set of quantum numbers of the 3D isotropic harmonic oscillator in spherical coordinates for the center-of-mass and the relative motion respectively. $\Psi_\alpha(\mathbf{R})$ are the 3D harmonic oscillator eigenfunctions, while $\psi_\beta(\mathbf{r})$ differ depending on the value of the angular momentum quantum number ℓ: for $\ell \neq 0$, we use the harmonic oscillator eigenfunctions $\phi_{n,\ell,m}(\mathbf{r})$, which are still solutions of the Hamiltonian H_{Busch}, since they are not affected by the δ-like interaction term being null in the origin. Differently, in the case of $\ell = 0$, we use the eigenfunctions defined in Eq. (5.40), which are linear combinations of harmonic oscillators wavefunctions with $\ell = 0$.

By evaluating the anharmonic terms (up to 10^{th} order) on this complete basis and by numerical diagonalization of the total Hamiltonian, we derive the dependence of the interaction energy in the motional ground state $U(s, a_s) = E(s, a_s) - E(s, 0)$ as a function of the scattering length a_s and of the lattice depth s. The results are shown in Fig. 5.12, where the curves related to three different models are displayed: 1) our model, containing anharmonic terms and the coupling between relative and center-of-mass motion (U, solid lines); 2) the solution for a parabolic potential [152], containing only the harmonic part of the potential (U_{Busch}, dotted lines); 3) the usual expression for the interaction energy in the Hubbard model [10], which takes into account the full lattice potential and depends linearly on a_s (U_{Hub}, dashed lines). In addition, the energy gaps between lowest and first excited

band for $s = 11$ and for $s = 30$ are shown. The interaction energy derived from our model saturates at the first excited band of the lattice for large values of the scattering length, as expected, and, for low a_s, it is well approximated by the usual Hubbard expression U_{Hub}. Instead, the U_{Busch} curves saturate at a higher energy, coincident with $\hbar\omega_\perp = 2\sqrt{s}E_R$.

In Fig. 5.11 we fit the experimental data of the spin oscillation frequency vs. s with the function $\left[U(a_{eg}^+, s) - U(a_{eg}^-, s)\right]/h$ (solid line), assuming the value $a_{eg}^- = 219.5\, a_0$ for the spin-triplet scattering length measured in Ref. [40]. The result of the fit is a spin-singlet scattering length $a_{eg}^+ = (3300 \pm 300)\, a_0$. This scattering length is remarkably large and, as shown in the inset of Fig. 5.11, causes the energy of the $|eg^+\rangle$ state to almost saturate to the energy gap between the first two lattice bands (grey zones).

Magnetic field dependence

A useful way to characterize the exchange interaction is to measure the spin-exchange oscillations as a function of the magnetic field. At a finite B the spin-exchange oscillation shows a faster frequency, as the Zeeman energy increasingly contributes to the energy difference between $|eg^L\rangle$ and $|eg^H\rangle$ (see Fig. 5.4). In the particular case of the spin-symmetric mixture $m = \pm 5/2$, we have from Eq. (5.28):

$$U_{eg}^H(B) - U_{eg}^L(B) = 2\sqrt{V_{ex}^2 + \Delta B^2}. \tag{5.43}$$

where we have defined $\Delta B = \frac{5}{2}\delta g\, \mu_B B$. However the simple model outlined in section 5.2 is not taking into account that strong interactions modify significantly also the two-particle spatial wavefunctions. In order to get the intuition, we can consider analytical wavefunctions $\psi_B(\mathbf{r})$ defined in (5.40) without anharmonic corrections for several scattering lengths. It is evident that when the scattering length a_s becomes comparable or larger than the harmonic oscillator length $a_\perp$, a node appears in the radial probability profile (see Fig. 5.13) as the two particles tend to spatially separate in each lattice site [121]. The magnetic field dependence of the spin-exchange oscillations gives the opportunity to appreciate the contribution of the motional degree of freedom. Indeed, the Franck-Condon factor between the two-particle spatial wavefunctions of the $|eg^+\rangle$ and $|eg^-\rangle$ collisional channels mitigates the mixing induced by an external field. By considering also the spatial overlap between the two states $|eg^\pm\rangle$, the external magnetic field coupling between the two collisional channels becomes:

$$\langle\Phi^\mp|\langle eg^\mp|\hat{H}_Z|eg^\pm\rangle|\Phi^\pm\rangle = F\,\Delta B, \tag{5.44}$$

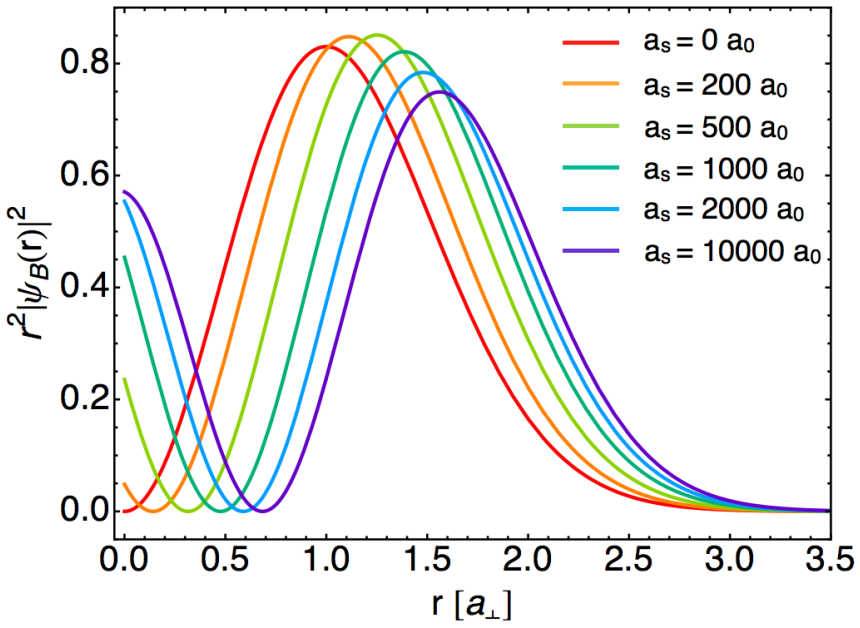

Figure 5.13: Radial probability profiles of the wavefunctions $\psi_B(r)$ for increasing scattering lengths. We consider the harmonic approximation of a lattice well with $s = 30$, corresponding to $a_\perp = 977\, a_0$.

where we have defined the Franck-Condon factor as:

$$F = \langle \Phi^{\mp} | \Phi^{\pm} \rangle = \iint \mathrm{d}\mathbf{r}\, \mathrm{d}\mathbf{R}\, \Phi_{eg}^{\mp *}(\mathbf{r}, \mathbf{R}) \Phi_{eg}^{\pm}(\mathbf{r}, \mathbf{R}), \tag{5.45}$$

namely the overlap integral between the spin-triplet and spin-singlet wavefunctions $\Phi_{eg}^{\pm}$, computed by evaluating the eigenstates of the interacting system including anharmonic corrections. In Fig. 5.14, we show the Franck-Condon factors $F = \langle \Phi(a_1) | \Phi(a_2) \rangle$ for several pairs of scattering lengths. As expected, $F = 1$ along the diagonal (where $a_1 = a_2$), since the two states coincide, while it drops down to ~ 0.6 for the maximal difference in scattering lengths. Taking into account the motional degree of freedom, the data can to be compared with a simple two states model in which the Hamiltonian of the two-atom system, including interaction energy and Zeeman shift, is written on the $\{|eg^+\rangle, |eg^-\rangle\}$ basis as

$$H = \begin{pmatrix} U_{eg}^{-} & F\Delta B \\ F\Delta B & U_{eg}^{+} \end{pmatrix}. \tag{5.46}$$

It shall be noted that this is the same Hamiltonian shown in Eq. (5.33) with the addition of the Franck-Condon factor F. By diagonalizing Hamiltonian (5.46), we find the fit model

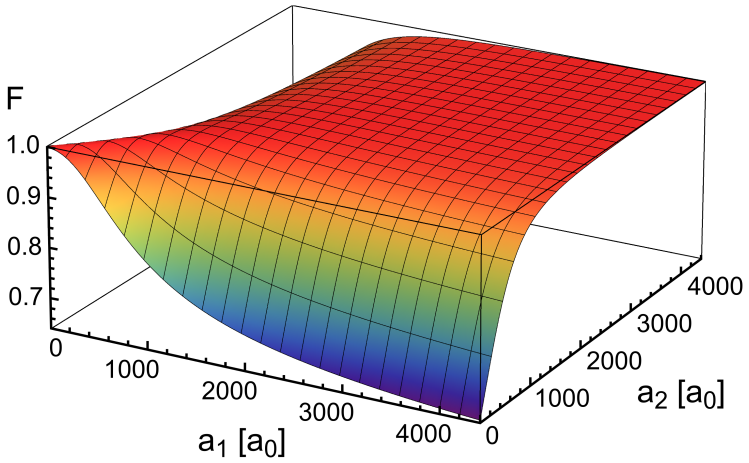

Figure 5.14: Franck-Condon factor $F(a_1, a_2) = \langle \Phi(a_1) | \Phi(a_2) \rangle$ describing the overlap of the two wavefunctions for two different scattering lengths a_1 and a_2 in units of the Bohr radius a_0.

to extract the scattering lengths of the two different collisional channels namely:

$$U_{eg}^{H}(B) - U_{eg}^{L}(B) = 2\sqrt{\left[V_{ex}\left(a_{eg}^{+}, a_{eg}^{-}\right)\right]^2 + \left[F\left(a_{eg}^{+}, a_{eg}^{-}\right)\Delta B\right]^2}. \tag{5.47}$$

The circles in Fig. 5.15 show the measured spin-oscillation frequency $(U_{eg}^{H} - U_{eg}^{L})/h$ at lattice depth $s = 30$ as a function of B, while the squares indicate the energy of the $|eg^{L}\rangle$ state determined by fitting the position of the peaks in the spectroscopic measurements (Fig. 5.6). The solid lines in Fig. 5.15 show the predictions of this model by using $a_{eg}^{-} = 219.5\, a_0$, $a_{eg}^{+} = 3300\, a_0$ (from the fit in Fig. 5.11) and the Franck-Condon factor $F = 0.77$ calculated by using the interacting wavefunctions obtained previously. The agreement with the experimental data is quite good, showing the substantial validity of the model in Eq. (5.46) as long as the overlap factor F between the interacting wavefunctions is considered. Alternatively, we have performed a simultaneous fit of the two datasets in Fig. 5.15 using the fitting function (5.47) letting U_{eg}^{+} and F as functions of the free parameter a_{eg}^{+} while considering $a_{eg}^{-} = 219.5\, a_0$. The result (dashed lines) is $a_{eg}^{+} = (4400 \pm 600)\, a_0$, which is $\sim 2\sigma$ away from the more precise determination coming from the fit of the data shown in Fig. 5.11. We note that a precise determination of a_{eg}^{+} is complicated by the fact that, in this regime of strong interactions, the dependence of U_{eg}^{+} on a_{eg}^{+} is extremely weak and small effects coming e.g. from calibration uncertainties or from higher-order contributions in the theory could yield significant changes. We also note that, in the presence of a tight trapping, the interpretation of the results in terms of an effective scattering length should be considered [156]. However, we stress that, differently from

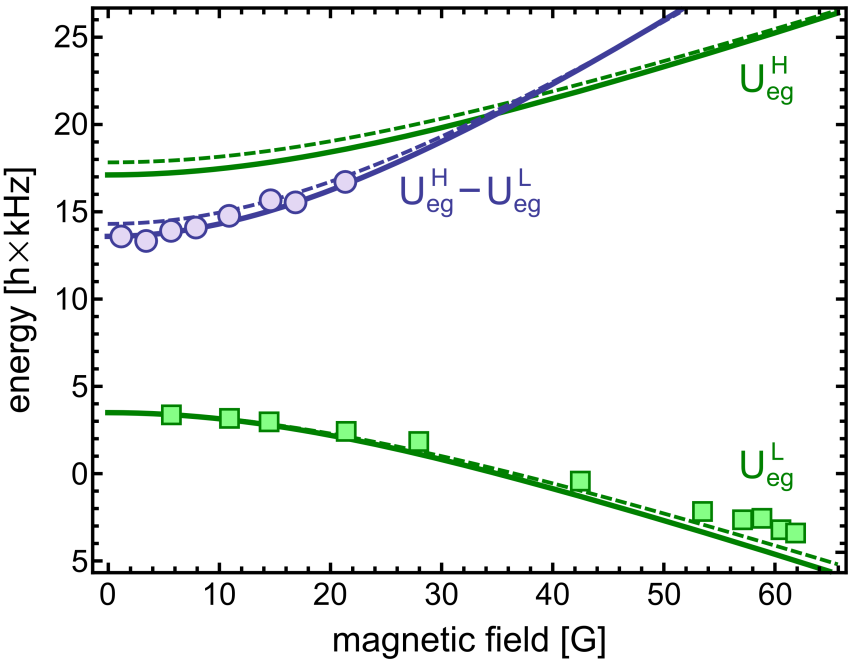

Figure 5.15: Circles: measured spin-exchange frequency $(U^H_{eg} - U^L_{eg})/h$ at $s = 30$ as a function of the magnetic field. Squares: measured energy of the $|eg^L\rangle$ state derived from the spectroscopic measurements (Fig. 5.6). The solid lines show the predictions of the model in Eq. (5.46) by using the a^-_{eg} value derived in Fig. 5.11. The dashed lines show a fit of the points to the same model leaving a^-_{eg} as free parameter (see main text for more details).

a^+_{eg}, our determination of $V_{\rm ex}$ is free from any assumption or modeling and represents an accurate measurement of the spin-exchange coherent coupling in an actual experimental configuration.

5.5 Conclusions and outlook

In conclusion, in this work we have observed for the first time fast, long-lived inter-orbital spin-exchange oscillations by exploiting a system of ultracold alkaline-earth-like fermions trapped in a 3D optical lattice. The direct observation of several periods of these oscillations has allowed us to demonstrate the coherence of the process and to measure the exchange interaction strength in an accurate, model-independent way. We note that, if compared with the spin dynamics observed in other atomic systems, arising from either small differences in the scattering lengths [72, 74, 157] or from second-order tunnelling between adjacent sites of an optical lattice [158], the oscillation that we have measured is

significantly fast. In particular, the exchange energy V_{ex}, on the order of $\sim h \times 10$ kHz, is much larger than both the Fermi ($k_B T_{\mathrm{F}}$) and the thermal ($k_{\mathrm{B}} T$) energies. As explained in the previous section, the only energy scale that actually constrains V_{ex} is the lattice band gap, which provides an additional degree of tunability to the system. The direct measurement of V_{ex} has also allowed us to provide a determination of the inter-orbital spin-singlet scattering length a_{eg}^{+}, which exceeds the spin-triplet a_{eg}^{-} one by ~ 10 times.

In the immediate future, the possibility to measure the spin-exchange frequency with an accuracy of the order of 10^{-3} paves the way to $SU(N)$ symmetry testing in the $a_{eg}^{\pm}$ collisional channels. Indeed, as stated in section 5.1, the relative variations of the scattering lengths involving the $^3P_0$ state is predicted to be $\delta a/a \sim 10^{-3}$ for Strontium atoms. However for Ytterbium atoms, the relative variation is arguably expected to be higher given the larger hyperfine mixing compared to Strontium. Therefore, during this thesis, we also observed and optimized spin-exchange oscillations in different spin mixtures (see Fig. 5.16).

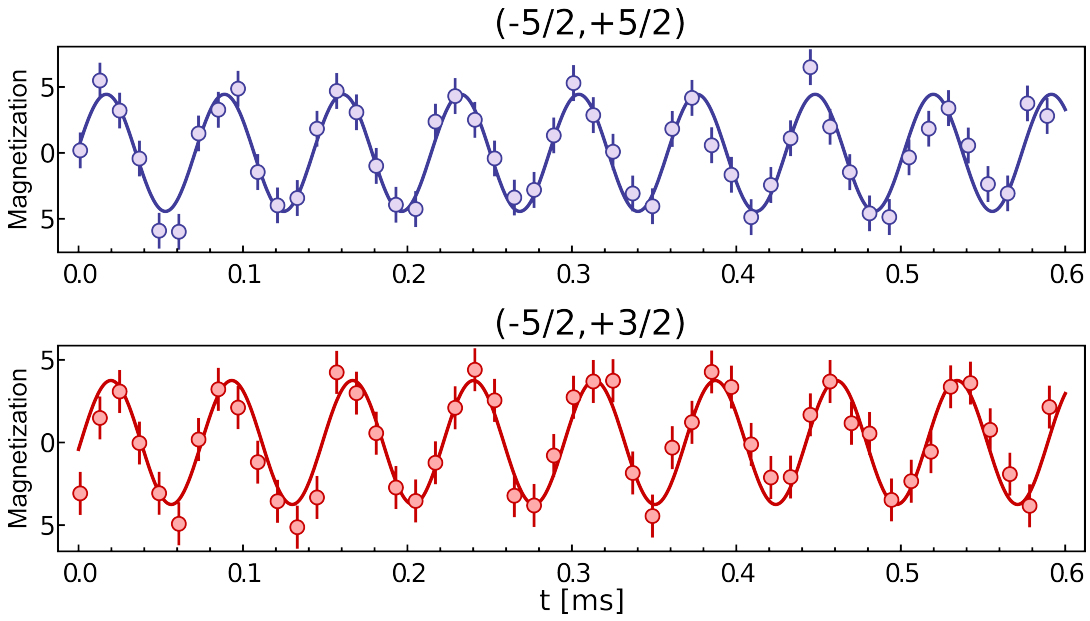

Figure 5.16: Spin exchange oscillations for the spin mixtures $m = \pm 5/2$ (blue) and $m = -5/2, m' = +3/2$ (red).

On a broader point of view, these findings make ^{173}Yb remarkably interesting for the observation of quantum magnetism in a two-orbital system with $SU(N)$ interaction symmetry [14], which would provide valuable insights into the physics of strongly correlated transition-metal oxides and heavy-fermion materials. In particular, the presence of such a strong exchange interaction, together with the possibility to implement state-dependent

lattices with negligible heating rates, makes ^{173}Yb a unique playground to engineer quantum many-body Hamiltonians beyond the celebrated Hubbard model. A remarkable example is the paradigmatic Kondo lattice model (KLM) used to study strong correlations induced by magnetic fluctuations in electron systems. The Kondo effect is essentially based on the exchange interaction between a local magnetic moment of an ionic impurity and the spin of conduction electrons [159]. As the temperature is lowered, a resonance develops in the interaction, and below a critical, Kondo temperature T_K, the spin of the local magnetic moment of the impurity is screened by the Fermi sea. Similarly, the KLM is based on an array of localized neutral magnetic impurities "melting" at low temperature into the conduction sea, where they become mobile excitations. Once mobile, these free spins acquire charge and give rise to a Fermi liquid with strongly enhanced effective mass, the so-called *heavy fermion liquid*. Ultracold atomic Ytterbium allows the possibility to study KLM physics by using a state-dependent optical lattice that pins $|e\rangle$ atoms[4], mimicking the magnetic impurities lattice. The same optical potential needs to loosely confine the $|g\rangle$ atoms, which are in a metallic state playing the role of conduction electrons. For example, using $\lambda \sim 655$ nm light would lead to $\alpha_e(\lambda)/\alpha_g(\lambda) \sim 10$, as shown in Fig. 5.1. In such a system, for $V_{\rm ex} \gg J_g$, a strong effective mass enhancement of the $|g\rangle$ atoms is predicted [14], which can be observed by dipolar center-of-mass oscillations [160] or measuring the lattice momentum distribution with standard time-of-flight techniques. Moreover, on a further perspective, this strong spin-exchange interaction entangles two stable internal degrees of freedom of the atom [161], which can be independently and coherently manipulated, opening new realistic possibilities for quantum information purposes.

[4]The reason why it is convenient to suppress the tunneling J_e of $|e\rangle$ atoms is to limit the losses due to inelastic $e-e$ collisions.

Chapter 6

Raman processes in Ytterbium Fermi gases

In the recent years, ultracold atoms have been proven to be an ideal platform to investigate the physics of condensed-matter models in a clean and well-controlled environment. One of the most remarkable achievement is the realization of synthetic background gauge fields [30, 43–45], akin to magnetic fields in electronic systems. In this line of research, most experimental setups and theoretical proposals are characterized by the use of coherent Raman transitions giving rise to position or velocity-dependent couplings in the ultracold gas, whose physical effect is captured by the minimal substitution $\hat{\mathbf{p}} \to \hat{\mathbf{p}} - \mathbf{A}(\hat{\mathbf{r}})$ in the effective Hamiltonian, with $\mathbf{A}(\hat{\mathbf{r}})$ being the gauge potential. In this context, the simplest possible system is provided by a Raman coupling with a momentum transfer ($k_R \neq 0$) in a Λ-configuration, described in section 1.2.1 by the effective Hamiltonian (1.53), which can be written in terms of Pauli matrices as:

$$\hat{H}_R = \frac{\hbar^2}{2m}(k\hat{\mathbb{1}} + k_R\hat{\sigma}_z)^2 + \frac{\delta}{2}\hat{\sigma}_z + \frac{\Omega_R}{2}\hat{\sigma}_x. \tag{6.1}$$

This simple Hamiltonian features a uniform time-constant vector potential [44] along one direction $q\,A = \hbar k_R \hat{\sigma}_z$. Nevertheless, Hamiltonian (6.1) provides the same non-trivial dispersion of particle subjected to equal Rashba-Dresselhaus spin-orbit coupling and an external magnetic field [41] and has been implemented for both Bose-Einstein condensates [42] and degenerate Fermi gases [162, 163]. In other theoretical schemes and experimental setups, optical lattices are suitably combined with Raman couplings inducing laser-assisted tunneling in real space. The different periodicities of optical lattices and Raman beams imprint a non trivial Peierls phase onto the atomic wavefunction, which is analogous to the Aharanov-Bohm phase experienced by a charged particle in a magnetic field enabling

the realization of the Harper-Hofstadter Hamiltonian in 2D lattices [164–167].

So far all experiments on synthetic gauge fields have been carried out with alkali atoms and mostly with bosons. In this chapter we will show how fermionic ^{173}Yb provides an extremely rich and flexible system offering a wide range of Raman configurations, as the number of states resonantly coupled can be opportunely tuned. In particular, coupling more than two spin states yields the possibility to interpret Raman transitions as a tunneling matrix element between neighboring sites of a synthetic dimension [47, 48] defined by the atomic internal state.

This chapter reports the technical characterization of the ^{173}Yb Raman system, which was propaedeutic to the implementation of spin-orbit coupling and synthetic dimensions, developed in the PhD thesis of my coworker Marco Mancini [49]. In section 6.1 we illustrate how the specific features of ^{173}Yb determine Raman couplings and their symmetries. In section 6.2 we give a brief description of two different experimental schemes, while in sections 6.3 and 6.4 specific configurations are characterized.

6.1 Raman processes in ^{173}Yb

In this section we generalize the Raman process in a Λ-configuration, illustrated in section 1.2.1, to the more complex case of a multi-level atom, focusing on the particular case of ^{173}Yb. Since this fermionic isotope has purely nuclear spin in the $^1S_0$ ground state, the Raman coupling goes to zero if the laser detuning Δ is large compared to the characteristic hyperfine separation of the excited state manifold Δ_{hfs}. Indeed, in the case of ^{173}Yb, the Raman process has to flip the nuclear spin I by addressing the electronic degree of freedom. Intuitively, the only way this can happen is by a two-photon process that virtually brings the electron in the excited state manifold, where the hyperfine interaction $\mathbf{I}\cdot\mathbf{J}$ makes the nuclear spin precess, and then de-excites the electron in a different $^1S_0$ nuclear spin component. Therefore, analogously to the light shift for a multi-level atom evaluated in Eq. (1.39), we will consider two-photon processes relying on the hyperfine structure of a single fine-structure excited state (in this specific case $^3P_1$). Hence, considering many sublevels $-F_g \leq m_g \leq F_g$ in the ground state, the Raman amplitude resonantly coupling m_g and m_g' can be calculated by summing over the different states F_e of the excited state

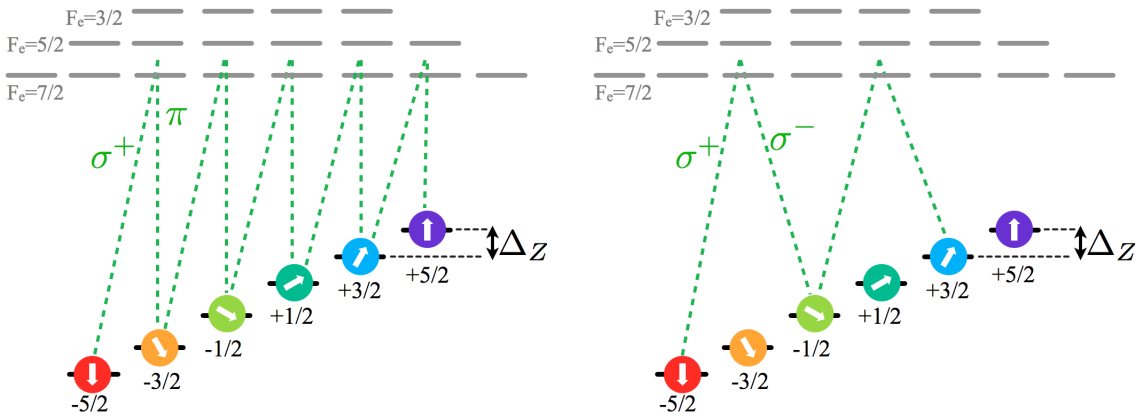

(a) $\Delta m_g = \pm 1$ **(b)** $\Delta m_g = \pm 2$

Figure 6.1: Scheme of Raman transitions in the case of $\boldsymbol{\sigma^+\pi}$ (a) and $\boldsymbol{\sigma^+\sigma^-}$ (b) polarizations. Typically, the Zeeman splitting is $\Delta_Z \sim 2\pi \times 10$ kHz. The excited state hyperfine separations (several GHz) are not to scale.

manifold, weighted for their respective detunings:

$$\begin{aligned}\Omega^{(qq')}_{m_g m'_g} &= \frac{\Omega_q \Omega^*_{q'}}{4}\left(\sum_{F_e}\frac{\mathcal{S}^{(q)}_{m_g}(F_e)\mathcal{S}^{(q')}_{m'_g}(F_e)}{\Delta_{F_e}}\right)\\ &= \frac{3\pi c^2}{2\omega_0^3}\Gamma_{J_e J_g}\left(\sum_{F_e}\frac{\mathcal{S}^{(q)}_{m_g}(F_e)\mathcal{S}^{(q')}_{m'_g}(F_e)}{\Delta_{F_e}}\right)\sqrt{I_q I_{q'}},\end{aligned} \tag{6.2}$$

with $m_g - m'_g = q' - q$. These amplitudes are calculated assuming a bias magnetic field inducing a Zeeman splitting Δ_Z between the ground-state nuclear spin components playing the role of the frequency difference $\omega_{20} - \omega_{10}$ introduced in section 1.2.1. By evaluating Eqs. (6.2), it turns out that beyond the $\Delta m_g = \pm 1$ processes (Fig. 6.1a), also $\Delta m_g = \pm 2$ couplings (Fig. 6.1b) are non zero since, for $\Delta \simeq \Delta_{hfs}$, the excited states $F_e = 3/2, 5/2, 7/2$ have different weights in determining the Raman amplitude[1]. This feature opens the possibility to induce a coherent dynamics in a subset of the $^1S_0$ manifold through $\boldsymbol{\sigma^+\sigma^-}$ processes just by tuning the polarization of the Raman beams. Moreover, similarly to the light shifts and the scattering rates, also the Raman couplings

[1] By evaluating Eq. (6.2), we can prove that far-detuned light ($\Delta \gg \Delta_{hfs}$), on the one hand, induces on ^{173}Yb a spin-independent light shift (see Eq. (1.44)) and, on the other hand, gives rise to a zero Raman coupling because of the relation:

$$\sum_{F_e}\mathcal{S}^{(q)}_{m_g}(F_e)\mathcal{S}^{(q')}_{m'_g}(F_e) = 0, \tag{6.3}$$

that holds for both $\Delta m_g = \pm 1$ and $\Delta m_g = \pm 2$ processes.

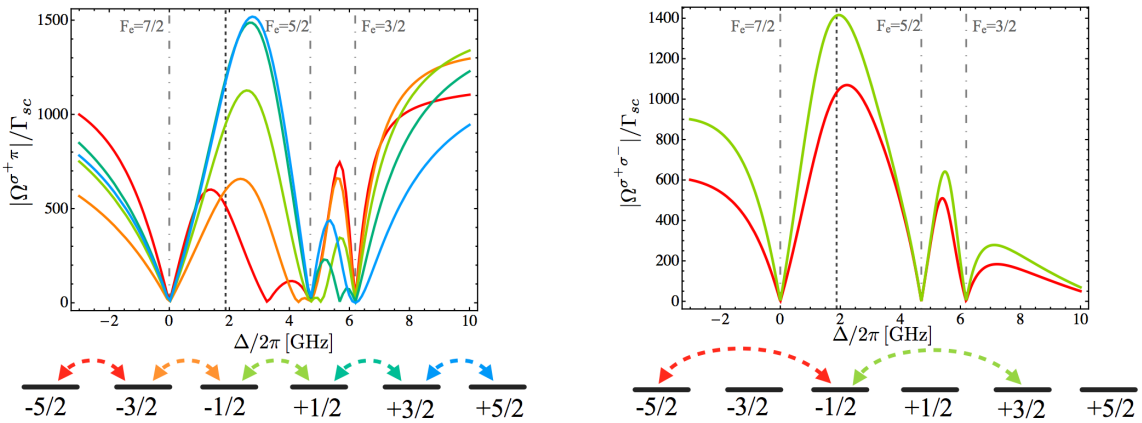

(a) $\Delta m_g = \pm 1$ **(b)** $\Delta m_g = \pm 2$

Figure 6.2: Ratio of the Raman coupling Ω (in absolute value) over the inelastic scattering rate Γ_{sc} for the $\sigma^+\pi$ **(a)** and $\sigma^-\sigma^+$ **(b)** processes as a function of detuning Δ with respect to the $F_e = 7/2$ resonance. The grey dashed-dotted lines indicate the hyperfine resonances $F_e = 7/2, 5/2, 3/2$ and the black dashed line marks the detuning $\Delta_{7/2} = 1.876$ GHz chosen in the current setup. In **(b)**, $\Omega^{\sigma^+\sigma^-}_{m_g,m_g+2} = \Omega^{\sigma^+\sigma^-}_{-m_g-2,-m_g}$.

inherit symmetry relations from Clebsch-Gordan coefficients, namely:

$$\Omega^{\sigma^\pm\pi}_{m_g,m_g+1} = \Omega^{\sigma^\mp\pi}_{-m_g,-m_g-1} \tag{6.4}$$

$$\Omega^{\sigma^+\sigma^-}_{m_g,m_g+2} = \Omega^{\sigma^+\sigma^-}_{-m_g-2,-m_g}. \tag{6.5}$$

Analogously to relations (1.42), these symmetries are broken by the presence of an external magnetic field.

The narrow-line intercombination transition $^1S_0 \to {}^3P_1$ at 556 nm ($\Gamma = 2\pi \times 182$ kHz) was preferred over the dipole allowed $^1S_0 \to {}^1P_1$ transition at 399 nm ($\Gamma' = 2\pi \times 28.9$ MHz) in order to maximize the ratio between the coherent Raman coupling Ω and the inelastic scattering rate Γ_{sc}. Indeed, for $\Delta \gtrsim \Delta_{hfs}$, the scaling relations $\Gamma_{sc} \sim \Gamma/\Delta^2$ and $\Omega \sim \Delta_{hfs}/\Delta^2$ yield the proportionality $\Omega/\Gamma_{sc} \sim \Delta_{hfs}/\Gamma$ [168], namely the ratio between the hyperfine separation and the decay rate of the excited state used to generate the Raman couplings. Since the $^3P_1$ excited state has smaller decay rate and a larger hyperfine splitting than $^1P_1$, this choice allowed us to reach a large ratio $\Omega/\Gamma_{sc} \sim 10^3$ at $\Delta_{7/2} = 1.876$ GHz. Indeed this value has been chosen in order to maximize the ratio of the Raman Rabi frequency over the inelastic scattering rate (see Fig. 6.2).

Another important consequence of a purely nuclear spin is that the ground-state Zee-

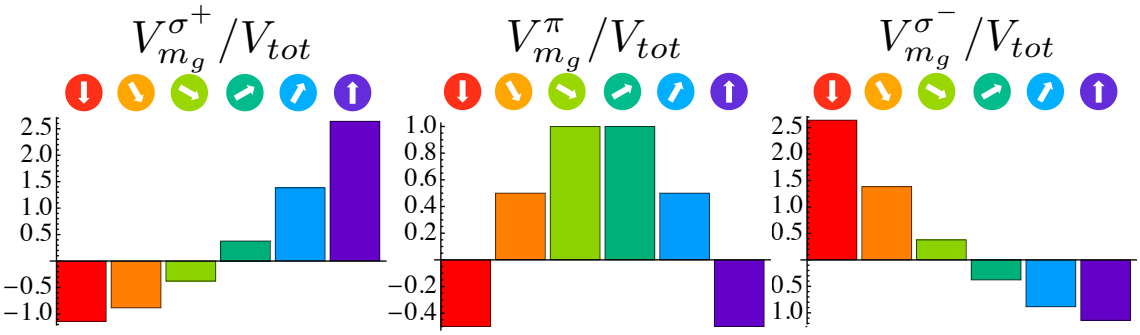

Figure 6.3: Spin-dependent light shift for polarization $q = \sigma^+, \pi, \sigma^-$ at detuning $\Delta = 1.876$ GHz. All values are normalized to the light shift V_{tot} induced by a "uniform" polarization $\hat{\boldsymbol{\varepsilon}} = 1/\sqrt{3}(\hat{\boldsymbol{\varepsilon}}_+ + \hat{\boldsymbol{\varepsilon}}_- + \hat{\boldsymbol{\varepsilon}}_\pi)$ which is independent from the specific spin state as defined in Eq. (1.43). Note that $V^{\sigma^+}_{m_g} = V^{\sigma^-}_{-m_g}$.

man splitting (207 Hz/Gauss) is exactly linear. For this reason all spin states can be resonantly coupled by the same pairs of Raman beams, as pictorially shown in Fig. 6.1. The only ingredient that breaks down the perfect linearity of the Zeeman splitting is the spin-dependent light shift $V^{(q)}_{m_g}$ defined in Eq. (1.39) for a q-polarized light field (see Fig. 6.7) which acts as a state-dependent energy offset as shown in Eq. (1.50). Although at first sight this feature seems a downside, nevertheless it can be exploited to give access to a wide range of Raman schemes. In the next sections we will show how, by tuning polarization and two-photon detunings, ^{173}Yb turns out to be an incredibly rich system for engineering Raman transitions.

6.2 Raman setup

The most direct way to characterize the Raman couplings and the light shifts of a given configuration is to study the time evolution of the ground-state nuclear spin populations. The Hamiltonian that rules the internal state dynamics is a 3×3 or 6×6 matrix in the $\boldsymbol{\sigma}^+\boldsymbol{\sigma}^-$ or $\boldsymbol{\sigma}^\pm\boldsymbol{\pi}$ case respectively, and it is a generalization of the one shown in Eq. (1.53). In order to focus on the characterization of Raman couplings, in this work we investigated only experimental configurations in which the kinetic energy and the harmonic confinement are negligible compared to the energy scales of the internal state dynamics. This is achieved in two different setups displayed in Fig. 6.4:

(A) In the first setup we set no momentum exchange associated with the Raman process, namely $k_R = 0$. In this way, the Raman coupling does not depend on the momentum state of the atoms and therefore the external motion can be factorized with respect to

the internal state dynamics. The experimental setup (Fig. 6.4a) consists in a single Raman beam modulated using an AOM driven with two frequencies separated by $\Delta\omega/2\pi$ similarly to the setup for the Bragg spectroscopy experiment (section 4.2). Having a double frequency spectrum, the single beam amounts to two co-propagating laser beams which generate the Raman coupling without momentum exchange.

(B) In the second setup we set a small momentum exchange $2k_R \sim 0.3k_F$ using two different Raman beams with two different frequencies, aligned with a total angle $\theta \simeq 16^\circ$ (Fig. 6.4b). At the same time we confine the atoms in a three-dimensional optical lattice with periodicity $d = \lambda_L/2 = 380$ nm with lattice depths $s_x = s_y = s_z \geq 20$, in order to suppress their kinetic energy. Indeed, in a deep lattice the kinetic energy is of the order of the bandwidth $4J$ of the lowest band, where J is tunneling energy (see Eq. 1.66). Since $J/h \leq 5$ Hz at at $s \geq 20$, the atomic motion evolves on longer timescales compared to the ones associated to typical Rabi frequency $\Omega/2\pi \sim 400$ Hz.

In both cases, the Hamiltonian ruling the internal state dynamics can be written in the appropriate rotating-frame as:

$$\hat{H}/\hbar = \sum_\alpha \left(\xi_\alpha - \alpha\delta \right) |\alpha\rangle\langle\alpha| + \frac{1}{2} \left(\Omega_\alpha |\alpha+1\rangle\langle\alpha| + h.c. \right), \tag{6.6}$$

where for simplicity we map the nuclear spin state m_g in the α index, which ranges from 1 to 3 in the $\boldsymbol{\sigma^+\sigma^-}$ scheme or from 1 to 6 in the $\boldsymbol{\sigma^\pm\pi}$ scheme. In this notation ξ_α is the spin-dependent light shift, Ω_α is the two-photon Rabi frequency connecting the states $|\alpha\rangle$ and $|\alpha+1\rangle$ and δ is the detuning with respect to the two-photon resonance.

The single-photon detuning at 1.876 GHz with respect to the ${}^1S_0 \rightarrow {}^3P_1(F_e = 7/2)$ resonance is obtained using a series of AOMs. The radio-frequency setup amounts to

- a 351 MHz AOM in double passage at first order (+702 MHz)
- a 235 MHz AOM in double passage at second order (+940 MHz)
- a 400 MHz AOM in single passage in first order (+400 MHz).

The total frequency shift results in 2.042 GHz that, taking into account the -166 MHz of the laser with respect to the resonance ${}^1S_0 \rightarrow {}^3P_1(F_e = 7/2)$ (see Fig. 2.9), leads to the desired +1.876 GHz. For setup (A) we modulate the 400 MHz AOM by means of two radio-frequencies separated by $\Delta\omega/2\pi$. For setup (B) we split the beam into two optical paths and, on the second beam, we use another 200 MHz AOM in single passage at second order locked in phase with the local oscillator driving the 400 MHz AOM. In this case,

the two beams coming from the two different AOMs are recombined into a polarizing beam splitter and injected into the same polarization-maintaining fiber in order to reduce relative phase fluctuations. Since they have also orthogonal polarization they can be split at the end of the fiber by another polarizing beam splitter.

The starting point for all the measurements in this chapter is a ^{173}Yb spin-polarized degenerate Fermi gas with $N_{\mathrm{at}} \simeq 30000$ atoms at $T/T_F < 0.2$. Quantum degeneracy is achieved by forced evaporation of a $(m_g = -5/2) + (m_g = +5/2)$ nuclear spin mixture in the optical dipole trap with mean geometric frequency $\bar{\omega}/2\pi \sim 80$ Hz. After evaporation, the atoms in the unwanted state are removed by a resonant laser pulse (see section 2.4) and a spin-polarized Fermi gas in either the $m_g = \pm 5/2$ states is left. The Zeeman splitting

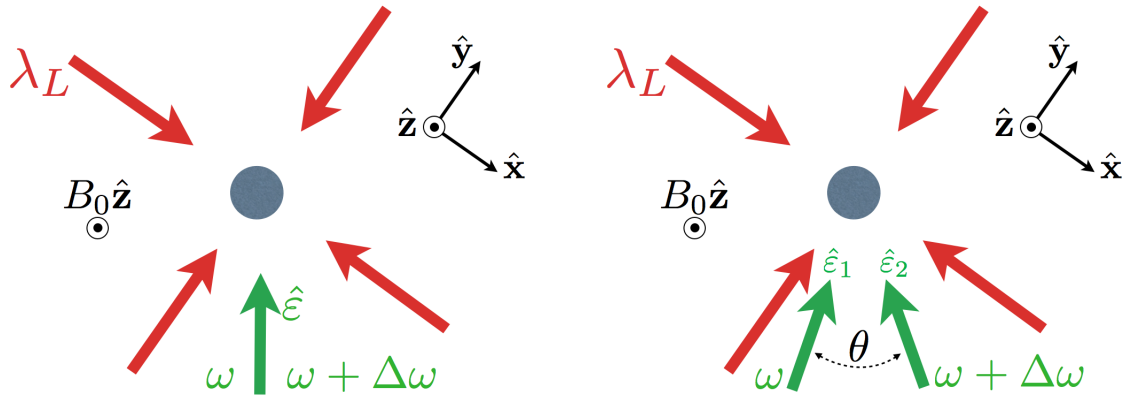

(a) Setup (A) **(b)** Setup (B)

Figure 6.4: Schematic top view of the two optical setups for Raman experiments.

between different nuclear spin components is generated by a bias magnetic field pointing in the $\hat{z}$ direction and also defining the quantization axis of the atoms. Typically the bias magnetic field ranges from of $B_0 = 51.5$ G ($\Delta_Z = 2\pi \times 10.6(6)$ kHz) to a maximum of $B_0 = 153$ Gauss ($\Delta_Z = 2\pi \times 31.6(6)$ kHz).

6.3 The $\sigma\sigma$ scheme

In order to better characterize the system we started from the configuration with fewer states involved, namely the $\boldsymbol{\sigma}^+\boldsymbol{\sigma}^-$ scheme. Given the geometric configuration shown in Fig. 6.4, we cannot use pure σ polarization since the Raman electric field wavevector $\mathbf{k}_R$ is orthogonal to the quantization axis defined by the magnetic field B_0. Therefore, we use

horizontal polarization, which amounts to an equal mixture of $\boldsymbol{\sigma}^+$ and $\boldsymbol{\sigma}^-$ polarization:

$$\hat{\boldsymbol{\varepsilon}}_H = \frac{1}{\sqrt{2}}\left(\hat{\boldsymbol{\varepsilon}}_+ + \hat{\boldsymbol{\varepsilon}}_-\right). \tag{6.7}$$

In order to induce a three-level $\boldsymbol{\sigma}^+\boldsymbol{\sigma}^-$ dynamics we set $\Delta\omega \simeq 2\Delta_Z$ in such a way that unwanted $\boldsymbol{\sigma}^\pm\boldsymbol{\pi}$ processes due to a residual $\boldsymbol{\pi}$ polarization are detuned by Δ_Z with respect to the two-photon resonance. The polarization is actually optimized by setting $\Delta\omega \simeq \Delta_Z$ and minimizing $\boldsymbol{\sigma}^\pm\boldsymbol{\pi}$ processes by tuning the orientation of the wave-plates that define the polarization of the Raman beams. Since the polarization of both beams is horizontal, the atomic sample sees both $\boldsymbol{\sigma}^+$ and $\boldsymbol{\sigma}^-$ polarization components with a double frequency spectrum, giving rise to several possible processes. Nevertheless, in the frame rotating at $2\Delta_Z$, only one transition is resonant since the others are detuned at least by $2\Delta_Z$ (see Fig. 6.5a). These processes are then negligible if the power broadening is lower than the level separation, namely if $\Omega_1 \ll 2\Delta_Z$. Under these conditions, the Hamiltonian can be written in the frame rotating at $2\Delta_Z$ as:

$$\hat{H}/\hbar = \begin{pmatrix} \xi_1 - \delta & \Omega_1/2 & 0 \\ \Omega_1/2 & \xi_2 - 2\delta & \Omega_2/2 \\ 0 & \Omega_2/2 & \xi_3 - 3\delta \end{pmatrix}. \tag{6.8}$$

In this configuration the light shifts ξ_α are strongly asymmetric, as shown in Fig. 6.5b. This effect can be interpreted as a spin-dependent magnetic field changing the resonance

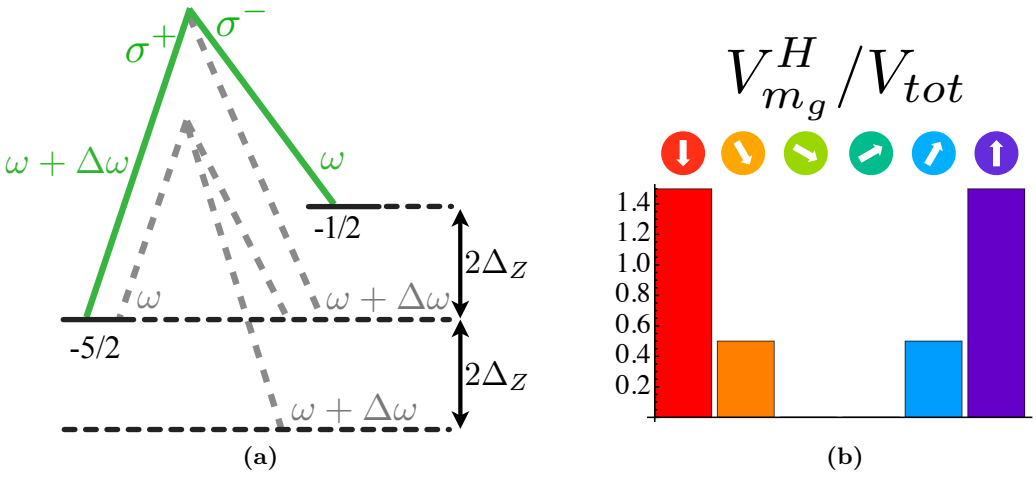

Figure 6.5: **(a)** Level diagram scheme showing all the possible $\sigma^+\sigma^-$ processes. **(b)** Light shifts for polarization $\hat{\varepsilon}_H$ at detuning $\Delta = +1.876$ GHz.

condition between the first two states, which becomes $\Delta\omega = 2\Delta_Z + \Delta\xi$, with $\Delta\xi = \xi_2 - \xi_1$. Therefore, in order to characterize the light shifts in this configuration, we compared the two-photon resonances starting the evolution from a spin-polarized Fermi gas in the two stretched states $m_g = -5/2$ and $m_g = +5/2$ (Fig. 6.6) using setup (B). The resonances

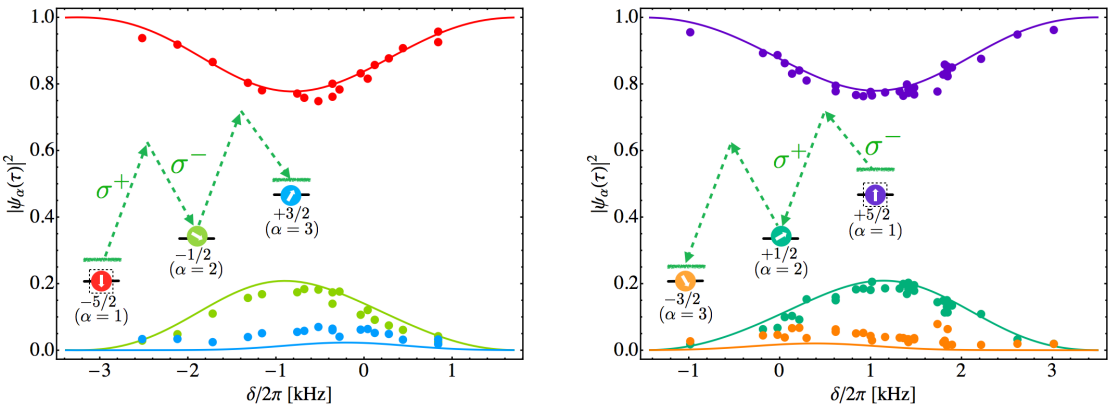

(a) $\alpha = 1 \to m_g = -5/2$ **(b)** $\alpha = 1 \to m_g = +5/2$

Figure 6.6: Two photon-resonances at $P = 48$ μW starting from $m_g = -5/2$ **(a)** or from $m_g = +5/2$ **(b)** measured at $\tau = 400$ μs in setup (B). Solid lines are the fit results (see text). The frequencies on the x-axis are rescaled in the rotating-frame by subtracting $2\Delta_Z = 2\pi \times 21.3(2)$ kHz.

are acquired by letting the system evolve for a given time τ and measuring the relative spin populations $|\psi^2_\alpha(\tau)|$ with OSG detection (see section 2.4.1) as a function of the frequency difference $\Delta\omega$, or equivalently of the detuning $\delta = \Delta\omega - \Delta_Z$ in the rotating-frame. The data points are then fitted by calculating numerically the populations $|\psi^2_\alpha(\tau)|$ with Hamiltonian (6.8) at different detunings, by using just ξ_1 and Ω_1 as fitting parameters. The optimal ξ_1 and Ω_1 are calculated by minimizing the mean squared error between the numerical theoretical evolution and the experimental data. All the other quantities are determined by the proportionalities implied by Eqs. (1.39) and (6.2).

In order to better characterize the system and to assess our model reliability, we measured the light shifts at different Raman powers starting from both stretched states $m_g = -5/2$ and $m_g = +5/2$. As expected, for the $m_g = -5/2$ case, $\Delta\xi = \xi_2 - \xi_1$ is in the opposite direction with respect to Δ_Z leading to an effective lower energy separation. Conversely, in the $m_g = +5/2$ case, $\Delta\xi$ increases the energy separation between the first two states. In particular, for a beam waist of 130 μm and a magnetic field of $B_0 = 51.5$ Gauss, we predict as slopes -16.1 Hz/μW and 19.5 Hz/μW for $m_g = -5/2$ and $m_g = +5/2$ respectively, which are in good agreement with the experimental data (see Fig. 6.7). The asymmetry between the two slopes is caused by the magnetic field effect

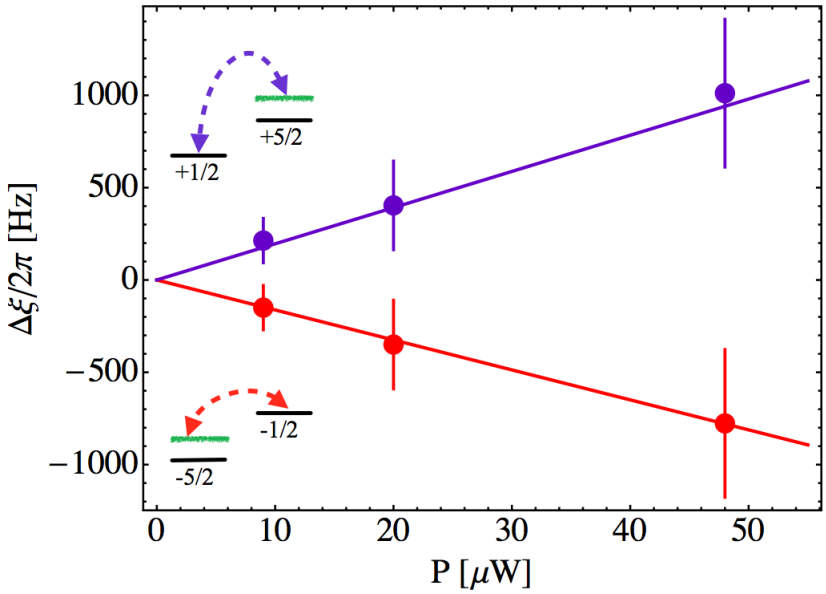

Figure 6.7: Measure of the differential light shift $\Delta\xi = \xi_2 - \xi_1$ as a function of the Raman power in setup (B). Starting the evolution from $m_g = -5/2$ ($m_g = +5/2$) leads to a decrease (increase) in the energy separation between the first two states. Solid lines are theoretical predictions using a $w_0 = 130$ μm beam waist.

on the $^3P_1$ excited state.

We can actually exploit this light shift configuration to restrict the evolution to approximately two states. Indeed, if we set $\delta = \xi_2 - \xi_1$, the first two states are resonant and the third has a light shift $\xi_3 + \xi_1 - 2\xi_2 \simeq 2.5\,\Omega_1$, modulo an irrelevant global energy shift. The exact value of the proportionality to Ω_1 depends on the magnetic field, which causes corrections of the order of 6%. This detuning is enough to let the $\alpha = 3$ state negligibly populated during the evolution, as shown by Rabi dynamics in Fig. 6.8, making this configuration a two-level-like system. In order to measure the system parameters, we fit the data using the Raman evolution based on Hamiltonian (6.8) using Ω_1 as a free parameter and taking light shift ξ_1 obtained by the resonance fit in Fig. 6.6. In particular we simulate numerically the three-level evolution for a set of Ω_1 and choose the one that minimizes the mean squared error with respect to the experimental data points. As in the case of the resonance fit, all the other parameters are determined by the proportionalities implied by Eqs. (1.39) and (6.2).

In order to involve also the third state in the dynamics, it is necessary to have all states with the same light shift. We know from Eq. (1.43) that at zero magnetic field this

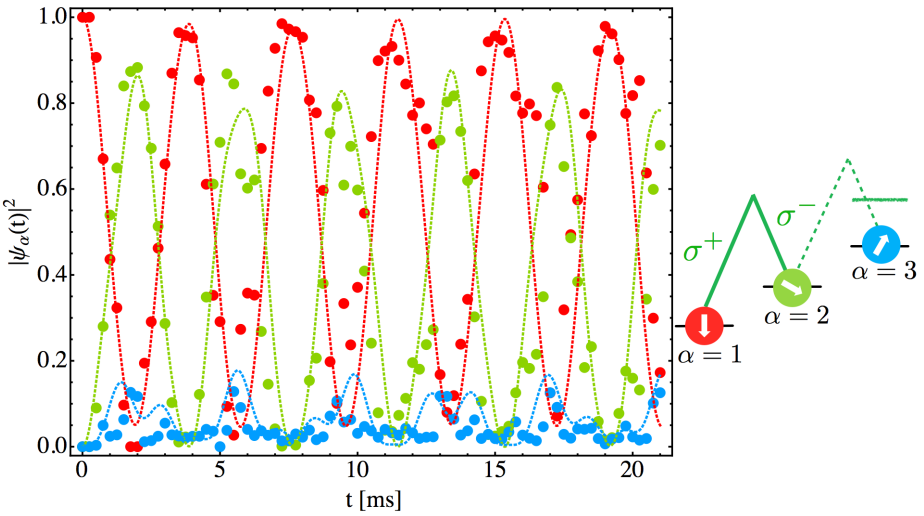

Figure 6.8: Raman evolution with pure horizontal polarization starting from the $m_g = -5/2$ state in setup (B). Dashed lines are the population evolutions fitted using $\xi_1 = 2\pi \times 322.5$ Hz fixed by the resonance fit and letting $\Omega_1 = 2\pi \times 270$ Hz as free parameter. The other parameters are determined by the relations $(\xi_1, \xi_2, \xi_3) = (0, 0, 2.54)\Omega_1$ and $\Omega_2 = 1.36\,\Omega_1$ with $B_0 = 51.5$ Gauss.

condition is fulfilled by using the polarization

$$\hat{\boldsymbol{\varepsilon}}_{tot} = \frac{1}{\sqrt{3}}(\hat{\boldsymbol{\varepsilon}}_+ + \hat{\boldsymbol{\varepsilon}}_- + \hat{\boldsymbol{\varepsilon}}_\pi). \tag{6.9}$$

If, on the one hand, this polarization allows us to resonantly couple all the three states, on the other hand it sets an additional constraint to the validity of the three-level model. Indeed, given the presence of $\boldsymbol{\pi}$ polarization in the Raman beams, $\boldsymbol{\sigma}^{\pm}\boldsymbol{\pi}$ processes have a non-zero probability and are detuned only by Δ_Z. Therefore, the additional condition $\Omega^{\sigma^{\pm}\pi} \ll \Delta_Z$ must be fulfilled to prevent power broadening to excite these unwanted processes. For this reason, we decided to work with higher magnetic field ($B_0 = 153$ Gauss) to relax the constraint on the power broadening and limit the spurious $\boldsymbol{\sigma}^{\pm}\boldsymbol{\pi}$ processes by increasing Δ_Z. The presence of such a large magnetic field breaks the light shifts symmetry (see Eqs. 1.42) and causes a linear dependence of the resonance on the Raman power. The slope is an order of magnitude smaller than the horizontal polarization configuration (2.4 Hz/μW) but it is still measurable and in good agreement with the theoretical prediction of the model (see Fig. 6.10). The Raman evolution in this configuration is displayed in Fig. 6.11, showing that all three states are involved in the coherent dynamics. Also in this case, the evolution is fitted by fixing ξ_1 to the value measured with the resonance fit (see Fig. 6.10) and letting Ω_1 as a free parameter. Especially in the three-level evolution,

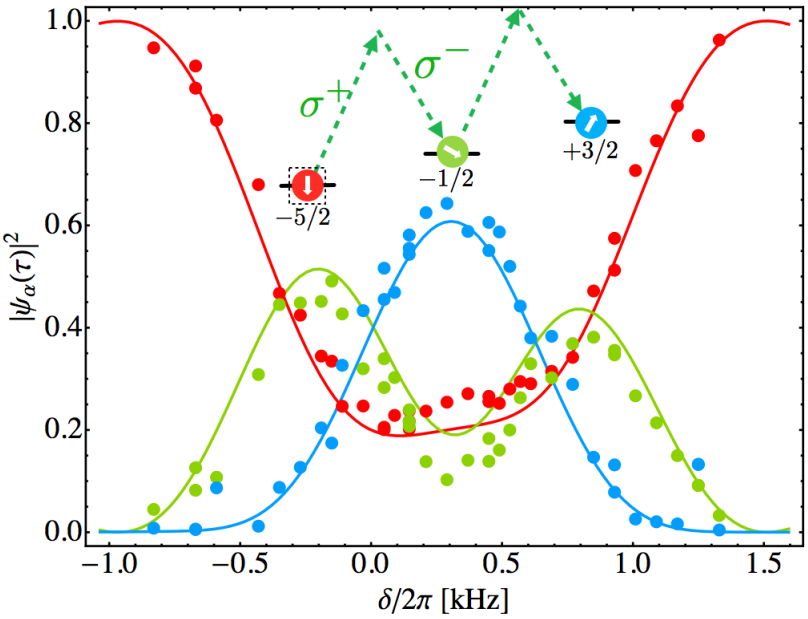

Figure 6.9: Typical two-photon resonance with uniform polarization $\hat{\varepsilon}_{tot}$ and $P = 145$ μW starting from $m_g = -5/2$ taken at $\tau = 800$ μs in setup (B). The frequencies on the x-axis are rescaled in the rotating-frame by subtracting $2\Delta_Z = 2\pi \times 63.3(2)$ kHz.

we observe a damping which depends on the power. We attribute this behaviour mostly to the inhomogeneity of the Raman beam profile, as the atoms in the cloud experience a space-dependent Rabi frequency which leads to a dephasing in the global population evolution. This explanation is supported by the large sensitivity of the Rabi frequency to the alignment of the Raman beams and by the decrease of the damping as a consequence of the beam waist enlargement.

6.4 The $\sigma\pi$ scheme

The possibility to resonantly couple N atomic sublevels has been long investigated in the past regarding both the dynamics [169–172] and coherent population transfer [173–175]. Nowadays, stimulated Raman transitions coupling multi-level atoms open interesting possibilities in quantum simulation of non-abelian gauge fields [30] and synthetic dimensions [47, 48]. In this section we report the techniques developed during this thesis in order to exploit $\boldsymbol{\sigma^{\pm}\pi}$ processes[2] to coherently couple up to six nuclear spin components, exploring

[2]In this section we use the following convention: a $\Omega^{(qq')}$ process indicates a two-photon process where a photon of polarization q is absorbed and a photon of polarization q' is emitted.

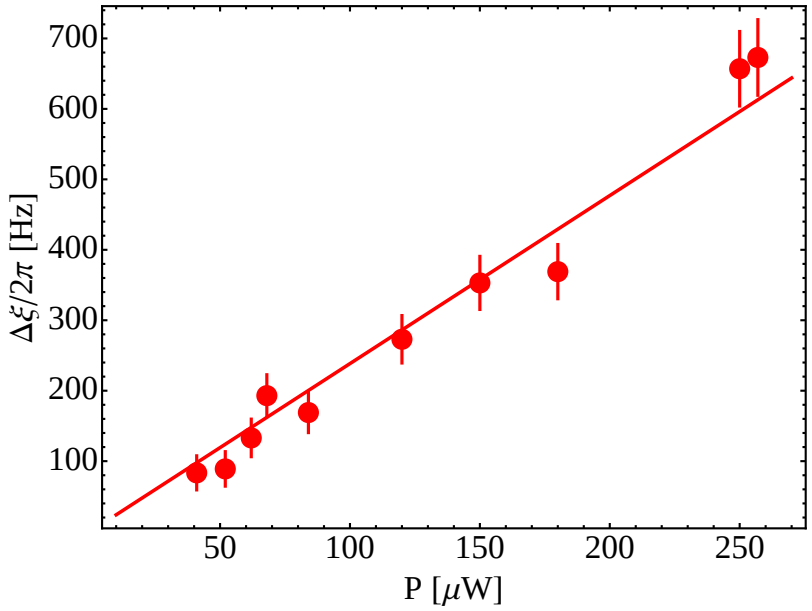

Figure 6.10: Measure of the differential light shift $\Delta\xi = \xi_2 - \xi_1$ as a function of the Raman power with uniform polarization $\hat{\varepsilon}_{tot}$ in setup (B). Solid lines are theoretical predictions considering a $w_0 = 150$ μm beam waist and a $B_0 = 153$ Gauss magnetic field.

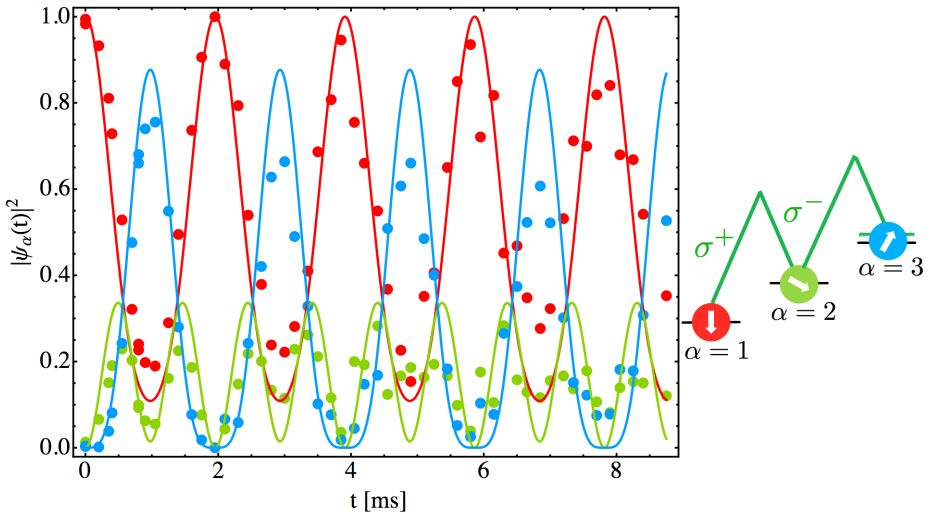

Figure 6.11: Raman evolution with uniform polarization $\hat{\varepsilon}_{tot}$ starting from the $m_g = -5/2$ state in setup (B). Solid lines are the fitted population evolutions with $\xi_1 = 2\pi \times 280$ Hz fixed by the resonance fit and using $\Omega_1 = 2\pi \times 590$ Hz as a free parameter. The other parameters are determined by the relations $(\xi_1, \xi_2, \xi_3) = (0, 0, 0.16)\Omega_1$ and $\Omega_2 = 1.41\,\Omega_1$ with $B_0 = 153$ Gauss.

the rich variety of experimental configurations allowed by the peculiar features of ^{173}Yb.

In order to excite $\Delta m_g = \pm 1$ processes, we set $\Delta\omega = \Delta_Z$ and we always set power and polarization so that the horizontal component $\hat{\boldsymbol{\varepsilon}}_H$ has twice the power of the $\hat{\boldsymbol{\varepsilon}}_\pi$ component. In this way, as explained in section 6.3, the asymmetry between the light shifts is minimized so that all the states are potentially involved in the evolution. Specifically, this means that in the setup (A) we use uniform polarization $\hat{\boldsymbol{\varepsilon}}_{tot}$, whereas in the setup (B) we use one beam with horizontal polarization $\hat{\boldsymbol{\varepsilon}}_H$ and with twice the power of the other beam, which has $\hat{\boldsymbol{\varepsilon}}_\pi$ polarization.

However, in this configuration, setup (A) or setup (B) lead to completely different dynamics due to our specific geometric configuration. Indeed, if we excite Raman processes

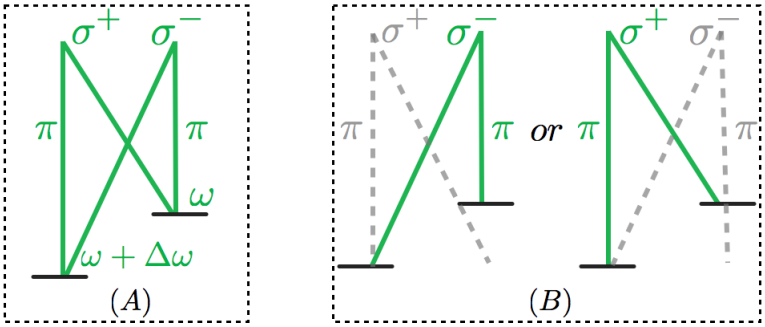

Figure 6.12: Level scheme of resonant processes in the setup (A), where all polarization components have a double frequency spectrum and setup (B), where $\boldsymbol{\sigma}^\pm$ and $\boldsymbol{\pi}$ polarization components have different frequencies. In the latter case there are two possible configurations depending on which polarization component has higher frequency.

in setup (A) by using two co-propagating Raman beams with polarization $\boldsymbol{\varepsilon}_{tot}$, all three polarization components have the same double frequency spectrum leading both $\boldsymbol{\sigma}^\pm\boldsymbol{\pi}$ and $\boldsymbol{\pi}\boldsymbol{\sigma}^\mp$ processes to be resonant, as shown in Fig. 6.12. On the other hand, in setup (B), since $\boldsymbol{\sigma}^\pm$ and $\boldsymbol{\pi}$ polarizations components have different frequencies, only one of the two processes is resonant and the other is detuned by Δ_Z. It shall be noted that, depending on which polarization has higher frequency, we can choose whether to excite the $\boldsymbol{\sigma}^\pm\boldsymbol{\pi}$ or the $\boldsymbol{\pi}\boldsymbol{\sigma}^\mp$ process. This leads to very different dynamics as the Rabi frequencies of the $\Delta m_g = \pm 1$ processes are strongly asymmetric as shown in Fig. 6.13. Moreover, these two amplitudes have opposite signs because of the property (1.35). Indeed, as explained in section 1.2, this relation implies that $\boldsymbol{\sigma}^\pm$ emission and absorption processes between two specific sublevels m_g and m_e have opposite phases while $\boldsymbol{\pi}$ emission and absorption processes have the same phase. Therefore, to correctly assess the phases of the Raman couplings, we have to take into account this property in the single-photon Rabi frequencies,

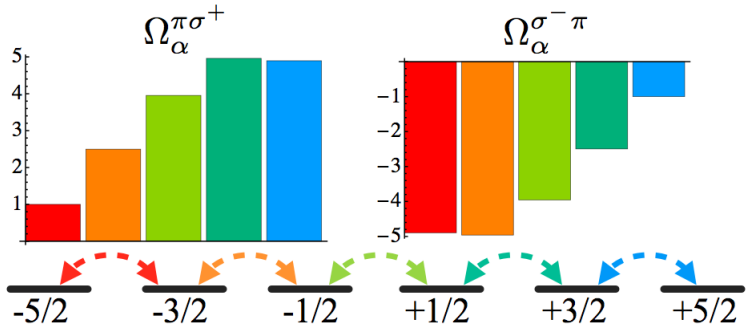

Figure 6.13: Raman amplitudes for $\boldsymbol{\pi\sigma}^+$ ($\boldsymbol{\sigma}^-\boldsymbol{\pi}$) normalized to Ω_1 (Ω_5).

for which the following relation holds:

$$\Omega^*_{\sigma^\pm} = -\Omega_{\sigma^\pm}, \tag{6.10}$$

where the complex conjugate refers to emission. This property affects the Raman amplitudes, whose phase depends on whether the circularly polarized photon is emitted or absorbed and are then related by the relation:

$$\Omega^{\sigma^\pm\pi}_{m_g,m_g+1} = -\Omega^{\pi\sigma^\mp}_{-m_g,-m_g-1}, \tag{6.11}$$

which is crucial to correctly evaluate the Raman amplitudes in setup (A).

In order to verify the strong asymmetry between the two different processes we study the Raman evolution in the setup (B) starting from the two stretched states, similarly to what we did in the $\sigma\sigma$ scheme. In both configurations the $\hat{\boldsymbol{\varepsilon}}_H$ beam was lower in frequency than the $\boldsymbol{\pi}$ beam, meaning that we are exciting the $\boldsymbol{\sigma}^-\boldsymbol{\pi}$ process when starting from $m_g = +5/2$ (see Fig. 6.14) and the $\boldsymbol{\pi\sigma}^+$ process when starting from $m_g = -5/2$ (see Fig. 6.15). Moreover, in order to minimize the asymmetry among the light shifts, the beam with $\hat{\boldsymbol{\varepsilon}}_H$ polarization and frequency ω has twice the power of the beam with π polarization and frequency $\omega + \Delta\omega$. Although there is reasonable agreement at short times, evolutions shown in Figs. 6.14 and 6.15 exhibit a much more evident damping with respect to the $\sigma\sigma$ evolution. As stated before, this is mainly due to the inhomogeneity of the beams profile, but in this case the damping is accentuated by a non perfect balancing of the spin-dependent light shifts that, combined with strong asymmetry among the five non-commensurate Rabi frequencies, leads to a very complex dynamics.

On the other hand, using setup (A) with one Raman beam with a double frequency spectrum, the total Raman amplitude is the result of the two processes $\boldsymbol{\sigma}^-\boldsymbol{\pi}$ and $\boldsymbol{\pi\sigma}^+$ as shown in Fig. 6.16. These two probability amplitudes can interfere differently depending

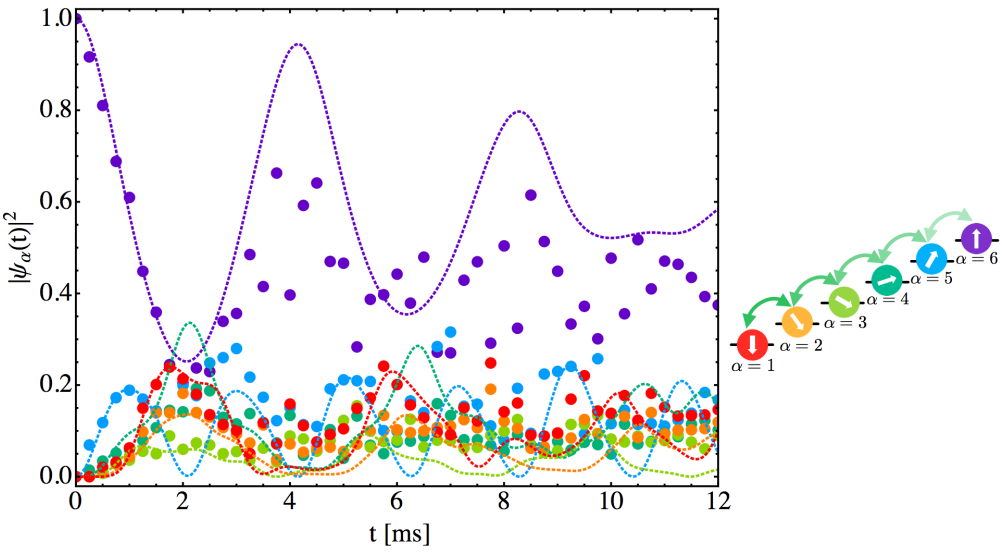

Figure 6.14: Raman evolution starting from $m_g = +5/2$ exploiting $\sigma^-\pi$ processes in setup (B). The dashed lines are the fit results using as free parameters $\Omega_1 = 2\pi \times 262$ Hz, $\xi_1 = 2\pi \times 453$ Hz and detuning $\delta = -2\pi \times 50$ Hz.

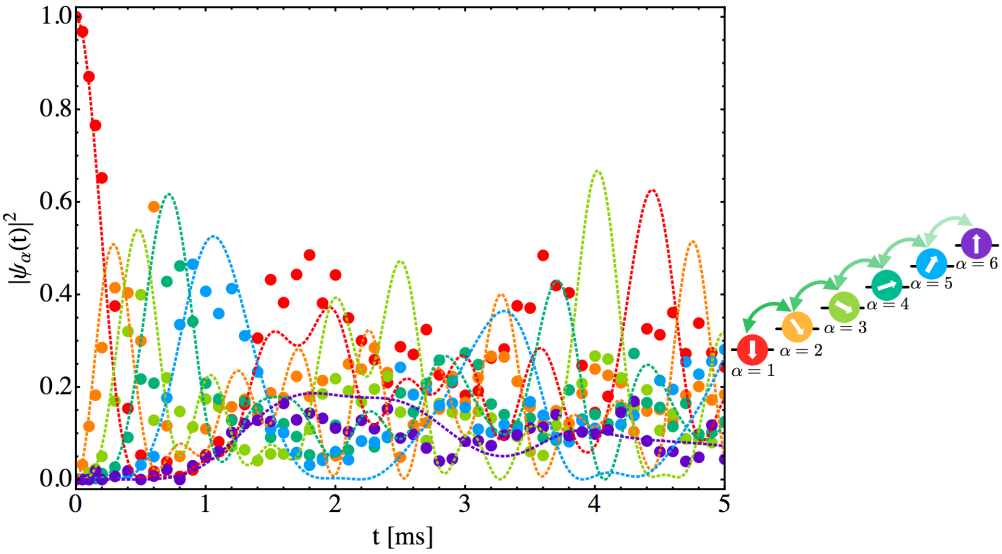

Figure 6.15: Raman evolution starting from $m_g = -5/2$ exploiting $\pi\sigma^+$ processes in setup (B). The dashed lines are the fit results using as free parameters $\Omega_1 = 1246$ Hz, $\xi_1 = 283$ Hz and detuning $\delta = 153$ Hz.

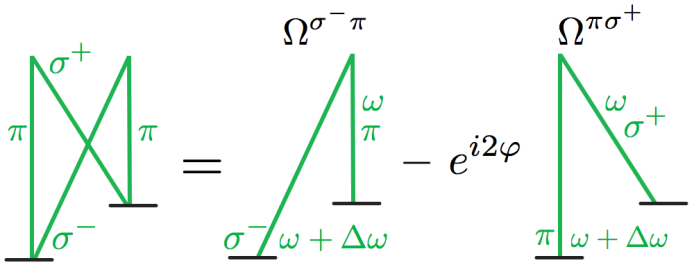

Figure 6.16: Level diagram of the two resonant processes compounding the total Raman amplitude.

on the relative phase φ between the $\hat{\boldsymbol{\varepsilon}}_\pm$ and the $\hat{\boldsymbol{\varepsilon}}_\pi$. As a matter of fact, the polarization

$$\hat{\boldsymbol{\varepsilon}}_{tot}^{(\varphi)} = \frac{1}{\sqrt{3}}(\hat{\boldsymbol{\varepsilon}}_+ + \hat{\boldsymbol{\varepsilon}}_- + e^{i\varphi}\hat{\boldsymbol{\varepsilon}}_\pi), \tag{6.12}$$

still leads to symmetric light shift coefficients, but features the phase φ as an additional degree of freedom. The reason why this phase determines the interference between the two processes relies in the single-photon Rabi frequencies compounding the Raman amplitudes namely:

$$\begin{aligned} \Omega^{\pi\sigma^\pm} &\propto e^{i\varphi}\frac{\Omega_\pi \Omega^*_{\sigma^\pm}}{\Delta} \\ \Omega^{\sigma^\mp\pi} &\propto e^{-i\varphi}\frac{\Omega_{\sigma^\mp} \Omega^*_{\pi}}{\Delta} \end{aligned} \tag{6.13}$$

These phase relations are imprinted in the Raman amplitudes yielding the following total coupling, apart from an irrelevant global phase:

$$\Omega^{(\varphi)} \propto \frac{\Omega_{\sigma^\mp}\Omega_\pi}{\Delta} - e^{i2\varphi}\frac{\Omega_\pi \Omega_{\sigma^\pm}}{\Delta}. \tag{6.14}$$

Therefore, by opportunely turning a $\lambda/4$ waveplate on the Raman beam in setup (A) we can have access to very different configurations indicated in Fig 6.17. In the case of $\varphi = 0$ the two processes interfere destructively and in the particular case of the coupling between $m_g = -1/2$ and $m_g = +1/2$ states, the symmetry relation (6.4) implies:

$$\Omega^{(\varphi=0)}_{-1/2,+1/2} = \Omega^{\sigma^\mp\pi}_{-1/2,+1/2} - \Omega^{\sigma^\pm\pi}_{-1/2,+1/2} = \Omega^{\sigma^\mp\pi}_{-1/2,+1/2} - \Omega^{\sigma^\mp\pi}_{+1/2,-1/2} = 0. \tag{6.15}$$

This leads to a peculiar configuration in which the Hilbert space of the internal states is divided in two completely separated subsets because of quantum interference. Therefore, starting from one of the stretched states, the evolution is limited to the first three states

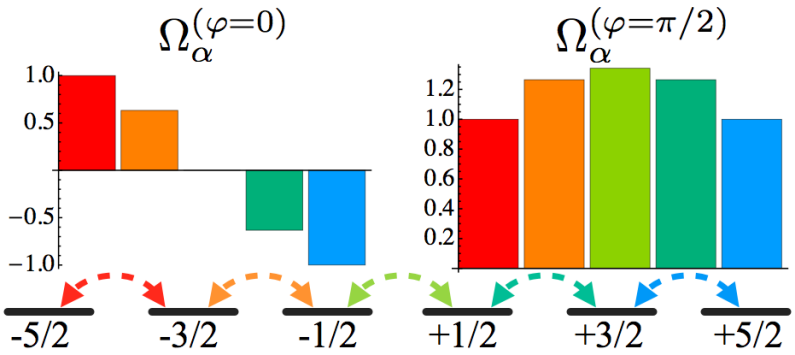

Figure 6.17: Total Raman couplings Ω_α in the setup (A) normalized to the first Rabi frequency Ω_1 in the totally symmetric ($\varphi = \pi/2$) and anti-symmetric ($\varphi = 0$) configuration.

as shown in Fig. 6.18. On the other hand, by setting $\varphi = \pi/2$, Eq. (6.4) gives rise to a totally symmetric configuration where $\Omega^{(\varphi=\pi/2)}_{m_g,m_g+1} = \Omega^{(\varphi=\pi/2)}_{-m_g-1,-m_g}$, as shown in Fig. 6.17. In this configuration all six states are coherently coupled (see Fig. 6.19). In this case, we also included a damping coefficient τ to take into account the beam inhomogeneity effect.

6.5 Conclusions and Outlook

The work described in this chapter demonstrates the possibility to create coherent couplings between nuclear spin states and shows how the peculiar features of ^{173}Yb offer a broad variety of different Raman configurations, which have been fully characterized. Indeed, exploiting the large hyperfine splitting of the $^3P_1$ manifold with respect to its narrow linewidth, we achieved a large ratio between Rabi frequencies and inelastic scattering rate. With this setup, we observed long coherence times in the $\sigma\sigma$ system but still some improvements need to be carried out to fully master the $\sigma\pi$ configuration. The Raman system has been characterized using the two different configurations in which the external motion of the atoms can be factorized with respect to the internal state dynamics. In such a system, the possibility to resonantly couple more than two internal states leads to fascinating ideas, like the interpretation of the nuclear spin states as singly addressable sites of a synthetic lattice [47] where Raman couplings can be viewed as synthetic tunneling along an additional "extra-dimension".

The natural prosecution of this work is the study of the interplay between the kinetic energy and the resonant Raman couplings among the atomic internal states, which will be treated in detail in the PhD thesis of my coworker Marco Mancini [49]. Indeed, during

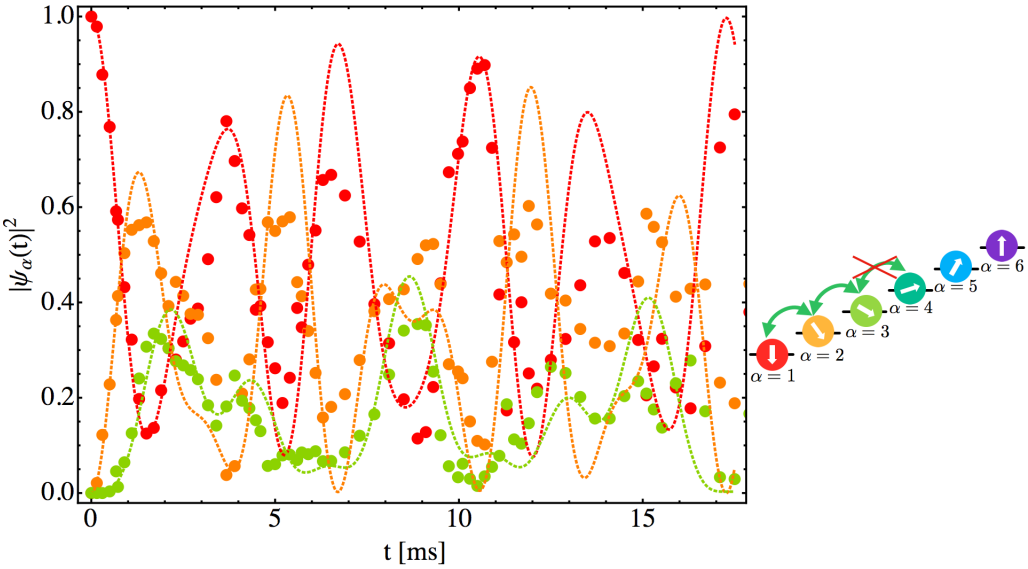

Figure 6.18: Raman evolution with $\varphi = 0$ in setup (A). The dashed lines are the fit results using as free parameter $\Omega_1 = 325$ Hz, $\xi_1 = 104$ Hz and detuning $\delta = 121$ Hz.

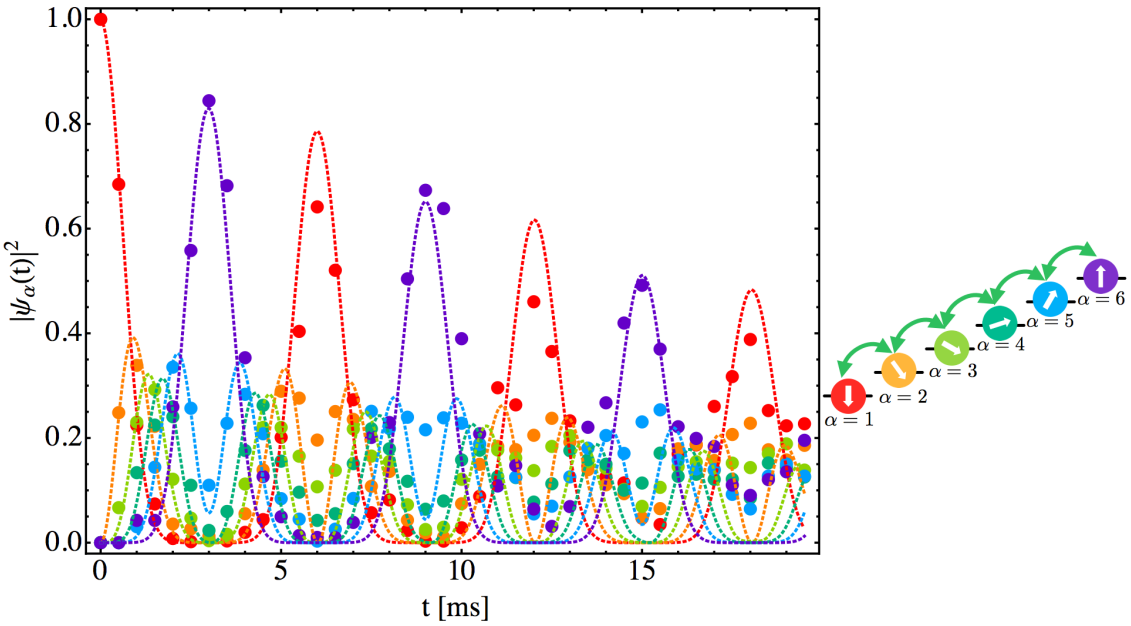

Figure 6.19: Raman evolution with $\varphi = \pi/2$ in setup (A). The dashed lines are the fit results using as free parameters $\Omega_1 = 362$ Hz, $\xi_1 = 158$ Hz and detuning $\delta = 36$ Hz and $\tau = 25$ ms.

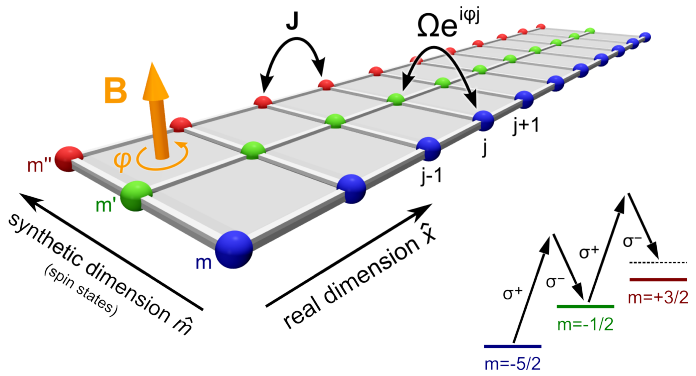

Figure 6.20: Two-dimensional synthetic lattice: an optical lattice along a real direction $\hat{x}$ with tunneling J, and by a laser-induced hopping between spin states along a synthetic direction m. By inducing a complex tunneling $\Omega_{1,2}e^{i\varphi j}$ along $\hat{m}$, the atom wavefunction acquires a phase ' per plaquette, mimicking the effect of a transverse magnetic field B on charged particles.

the preparation of this thesis, this experimental setup has been used to realize synthetic gauge fields with fermions in optical lattices, following the scheme proposed by Celi et al. in Ref. [48]. In particular, using the synthetic dimension approach, a momentum-dependent Raman coupling (setup (B)), combined with a tunneling energy J comparable with the Rabi frequency Ω_α, allowed the implementation of an artificial magnetic field in a two-dimensional synthetic lattice [50, 176] (see Fig. 6.20). In such a system, the different periodicity of the Raman pattern λ_R with respect to the one of the "real" lattice λ_L yields a non-zero Peierls phase $\varphi = 2\pi(\lambda_L/\lambda_R)$, associated to the synthetic tunneling Ω_α. This system is described by the Hamiltonian [50]:

$$\begin{aligned}\hat{H} &= \sum_j \sum_\alpha \left[-J(\hat{c}^\dagger_{j,\alpha}\hat{c}_{j+1,\alpha} + \text{h.c.})\right] \\ &+ \sum_j \sum_\alpha \left[\frac{\Omega_\alpha}{2}(e^{i\varphi j}\hat{c}^\dagger_{j,\alpha}\hat{c}_{j,\alpha+1} + \text{h.c.}) + \xi_\alpha n_{j,\alpha}\right] \end{aligned} \tag{6.16}$$

where $c^\dagger_{j,\alpha}(c_{j,\alpha})$ are fermionic creation (annihilation) operators on the site (j,α) in the real (j) and synthetic (α) dimension, and $n_{j,\alpha} = c^\dagger_{j,\alpha}c_{j,\alpha}$. The tunneling J along the real direction can be tuned by changing the intensity of the optical lattice beams while the dynamics along the synthetic dimension is controlled by the Rabi frequency Ω_α. Besides the tunneling terms, the state-dependent light shifts ξ_α provide an energy offset along the "extra-dimension". This system allowed the direct detection of chiral edge states with ultracold neutral fermions pierced by an artificial gauge field.

In the future, by exploiting $\sigma\sigma$ and $\sigma\pi$ schemes, we can apply this approach to ladder systems with a tunable number of sites, providing a setting for the investigation of both edge and bulk 2D topological matter, complementary to recent works on Chern insulators [177]. In addition, this system can be used to simulate non-trivial topologies [178] by engineering boundary conditions along the synthetic dimensions. Moreover, we could investigate in a controlled manner the combined effect of interactions and synthetic gauge fields, a fundamental ingredient for fractional quantum Hall physics [179], potentially leading to the realization of novel states of matter in ladder systems such as, e.g., chiral Mott insulator states.

Conclusions and outlook

This PhD thesis investigates a broad range of physical phenomena exploiting the unique features of ultracold fermionic ^{173}Yb. The possibility to combine a large-spin fermion featuring highly symmetric interactions with long-lived electronic states and coherent Raman transitions, makes this atom a pristine playground for quantum simulation and, in perspective, for quantum information [180–182].

We described a new and versatile vacuum apparatus, which enabled us to trap and cool both fermionic ^{173}Yb and bosonic ^{174}Yb isotopes to quantum degeneracy. By developing all-optical manipulation and detection techniques, it has been possible to precisely control and probe both the external motion of the atoms as well as their internal states. In particular, we used a wide variety of atomic physics tools, ranging from the implementation of optical lattices, the coherent addressing of an ultra-narrow clock transition and the realization of two-photon Raman couplings between nuclear spin states. This brought us to investigate three different lines of research:

- In a first set of experiments, we developed all-optical techniques to detect and initialize the spin distribution with a high degree of accuracy. Using these tools and exploiting the highly symmetric interactions between ground-state atoms, we realized a new many-body system, namely a one-dimensional liquid of fermions with $SU(N)$ symmetry. We characterized this system by studying its static and dynamic properties as a function of the number of spin components [31] and providing the first experimental observation of the so-called "high-spin bosonization" [34].
- In a second set of experiments, we exploited the coherent addressing of the $^3P_0$ metastable state using an ultra-narrow laser at 578 nm. This enabled us to study the interactions of two atoms trapped in a deep 3D optical lattice in two different long-lived electronic orbitals. We directly measured the spin-exchange energy by observing for the first time coherent orbital magnetization dynamics and exploited this new observable to determine the scattering length a_{eg}^{+} associated to the electronic symmetric state [35].

- In a third line of research, we fully characterize several Raman configurations to coherently couple the nuclear spin states of ^{173}Yb. This characterization allowed the creation of an effective lattice dynamics in a finite-sized "extra dimension". By using this innovative approach, after the completion of this thesis, it was possible to realize synthetic magnetic fields for effectively-charged fermions and to demonstrate the emergence of chiral edge states propagating along the edges of the system, thus providing a direct evidence of a prominent feature of quantum Hall physics in condensed-matter systems [50, 176].

Outlook

During this thesis, quite diverse kinds of experiments have been carried out and, for this reason, specific outlooks were already given at the end of each chapter. In the future, these different lines of research may give rise to exciting and fruitful cross-talks. For example, the study of $SU(N)$ one-dimensional many-body systems can be extended by studying the spin sector of low-momentum excitations employing spin-dependent light shifts provided by the Raman light. By selecting two spin components, which display light shift equal in modulus and opposite in sign, in principle we could access the spin dynamical structure factor of an interacting liquid of fermions. Another interesting possibility is to study strongly correlated fermions in one dimension using the long-lived excited state $|e\rangle$. In this system charge and spin collective modes associated to different electronic states are predicted and the presence of the exchange interaction leads to the onset of four separated collective modes [126]. Raman light can be used also to enhance the contrast of spin-exchange oscillations. Indeed, a spin-dependent light shift can be used as an effective magnetic field that mixes the $|eg^+\rangle$ and $|eg^-\rangle$ collisional channels. Optical control of the collisional mixing would lead to a significant enhancement of spin-exchange oscillations contrast.

In the long run, several improvements to the experimental setup are on the way. The high-optical-access glass cell has been conceived to implement single-site imaging and addressing of ^{173}Yb atoms in an optical lattice with a high-resolution objective. Indeed undoubtedly the future of ultracold atoms experiments points towards the local probing of the atomic sample. In the past years, this unprecedented degree of control has been achieved for bosonic ^{87}Rb [183–185] and ^{174}Yb [186] and more recently also for fermionic ^{40}K [187, 188] and ^{6}Li [189]. Implementing such a high degree of control on ^{173}Yb is a challenge that is worth taking and that could lead to major achievements in the investigation of quantum many-body systems.

Appendix A

Ytterbium atomic properties

Ytterbium is a rare alkaline-earth-like metal, strongly diamagnetic, collocated in the Lanthanides series. The atomic number is $Z = 70$ and it has several stable isotopes, both bosonic and fermionic, reported in table A.1 with their relative abundance, nuclear spin and nuclear magnetic moment in units of the nuclear magneton μ_N. In table A.2 the s-wave scattering lengths for all the possible inter-isotope two-body collisions are reported.

Table A.1: Ytterbium isotopes properties

Isotope	Relative abundance (%)	Nuclear spin	μ/μ_N
^{168}Yb	0.13	0	0
^{170}Yb	3.05	0	0
^{171}Yb	14.3	1/2	+0.4919
^{172}Yb	21.9	0	0
^{173}Yb	16.12	5/2	-0.6776
^{174}Yb	31.8	0	0
^{176}Yb	12.7	0	0

The electronic configuration of the ground state is $[\mathrm{Xe}]4f^{14}6s^2$ and since it has two electrons in the outer shell, similarly to Helium, the first excited levels can be separated in triplet ($S = 1$) and singlet ($S = 0$) states. The level scheme with the excited states used in this work is indicated in Fig. A.1. All the relevant transitions used in the calculation of optical potentials, starting from the $^1S_0$ and from the $^3P_0$ states are reported in tables A.3 and A.4. In table A.3, it is worth noting that the intercombination ($\Delta S = 0$) $^1S_0 \rightarrow {}^3P_1$ transition at 555.8 nm is forbidden in LS-coupling but it is nevertheless observed with

Table A.2: Ytterbium scattering lenghts in a_0 units [75]

	^{168}Yb	^{170}Yb	^{171}Yb	^{172}Yb	^{173}Yb	^{174}Yb	^{176}Yb
^{168}Yb	252	117	89	65	39	2	-359
^{170}Yb		64	36	-2	-81	-518	209
^{171}Yb			-3	-84	-578	429	142
^{172}Yb				-600	418	200	106
^{173}Yb					200	139	80
^{174}Yb						105	54
^{176}Yb							-24

a quite narrow line ($\Gamma = 2\pi \times 182$ kHz). Indeed, for large atomic number ($Z = 70$ in the Yb case), the LS-coupling approximation is inaccurate since the spin-orbit interaction is not negligible compared to the Coulomb repulsion between electrons and consequently the total spin S is not a good quantum number anymore. The same argument applies to

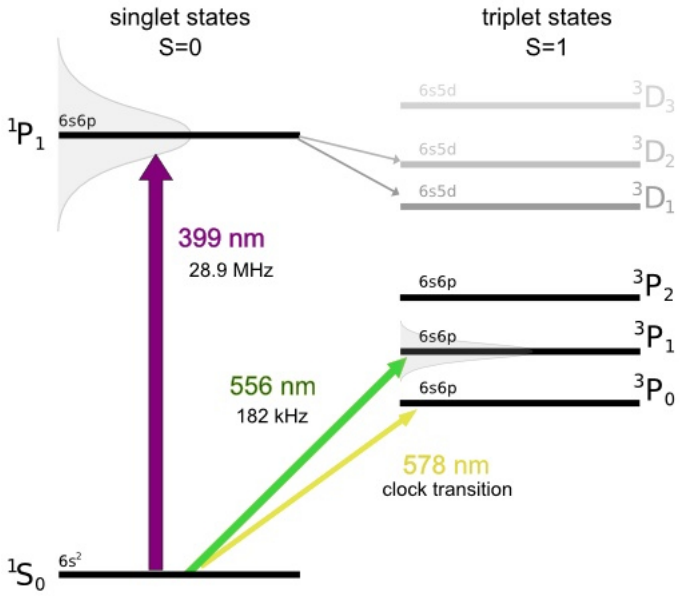

Figure A.1: Levels scheme of Yb first excited states.

the particular case of the $6s6p\,(^3P_0)$ state, which is connected to the ground state by a $J = 0 \to J' = 0$ transition that should be forbidden to all orders. However in fermionic isotopes, the hyperfine interaction between the nuclear magnetic moment and electrons admixes this state with the atomic levels with total angular momentum $J = 1$, thus opening an electric-dipole branch to the ground state. The true eigenstate of the atomic

system is then a linear combination of pure LS-coupling states $|^{2S+1}P_J\rangle_0$:

$$|^3P_0\rangle = \alpha|^3P_0\rangle_0 + \beta|^3P_1\rangle_0 + \gamma|^1P_1\rangle_0, \tag{A.1}$$

with the mixing coefficient $\beta, \gamma \ll 1$ depending on the hyperfine interaction [147]. Hence the small but finite mixing with the dipole allowed state $|^1P_1\rangle_0$ causes a finite dipole matrix element, which corresponds to a 26 s lifetime for the $^3P_0$ state.

Table A.3: Ytterbium $^1S_0$ energy levels and linewidths

States	Energy [cm^{-1}]	λ [nm]	τ [ns]	$\Gamma/2\pi$ [MHz]	Branching Ratio
$6s6p\,(^3P_1)$	17992.007[a]	555.802	870[a]	0.1829	-
$6s6p\,(^1P_1)$	25068.222[a]	398.911	5.46[a]	29.12	-
$(7/2, 5/2)\,j = 1$	28857.014[a]	346.536	14.6[b,c]	10.90	-
$(5/2, 5/2)\,j = 1$	37414.59[a]	267.275	70[a]	2.067	-
$6s7p\,(^3P_1)$	38174.17[b,c]	261.957	120[b,c]	1.326	0.8
$6s7p\,(^1P_1)$	40563.97[a]	246.524	10[a]	15.91	0.65
$6s8p\,(^3P_1)$	43659.38[b]	229.046	140[b]	1.136	-
$6s8p\,(^1P_1)$	44017.60[b]	227.182	50[b]	3.183	-

Table A.4: Ytterbium $^3P_0$ energy levels and linewidths

States	Energy [cm^{-1}]	λ [nm]	τ [ns]	$\Gamma/2\pi$ [MHz]	Branching Ratio
$6s5d\,(^3D_1)$	7200.663[b]	1388.76	380[b]	0.423	0.639
$6s7s\,(^3S_1)$	15406.253[d]	649.087	14[d]	11.36	0.15
$6s6d\,(^3D_1)$	22520.281[b]	444.044	21[b]	7.01	0.582
$6s8s\,(^3S_1)$	24326.601[d]	411.073	34[d]	4.68	0.135
$6p^2\,(^1P_1)$	26516.981[b]	377.117	15[b]	10.61	0.35
$6s7d\,(^3P_1)$	27022.941[b]	370.056	38[b]	4.19	0.56

[a] Ref.[190] [b] Ref. [191] [c] Ref. [192] [d] Ref. [193]

Appendix B

^{173}Yb Clebsch-Gordan coefficients

Table B.1: Clebsch-Gordan coefficient for $(^1S_0 \rightarrow {}^{2S+1}P_1)$ π transition

m_g	-5/2	-3/2	-1/2	+1/2	+3/2	+5/2
$F' = \frac{7}{2}$	$-\sqrt{\frac{2}{21}}$	$-\frac{1}{3}\sqrt{\frac{10}{7}}$	$-\sqrt{\frac{2}{21}}$	$-\sqrt{\frac{2}{21}}$	$-\frac{1}{3}\sqrt{\frac{10}{7}}$	$-\sqrt{\frac{2}{21}}$
$F' = \frac{5}{2}$	$\sqrt{\frac{5}{21}}$	$\sqrt{\frac{3}{35}}$	$\sqrt{\frac{1}{105}}$	$-\sqrt{\frac{1}{105}}$	$-\sqrt{\frac{3}{35}}$	$-\sqrt{\frac{5}{21}}$
$F' = \frac{3}{2}$	0	$\frac{2}{3\sqrt{5}}$	$\sqrt{\frac{2}{15}}$	$\sqrt{\frac{2}{15}}$	$\frac{2}{3\sqrt{5}}$	0

Table B.2: Clebsch-Gordan coefficient for $(^1S_0 \rightarrow {}^{2S+1}P_1)$ σ^+ transition

m_g	-5/2	-3/2	-1/2	+1/2	+3/2	+5/2
$F' = \frac{7}{2}$	$\frac{1}{3\sqrt{7}}$	$\frac{1}{\sqrt{21}}$	$\sqrt{\frac{2}{21}}$	$\frac{1}{3}\sqrt{\frac{10}{7}}$	$\sqrt{\frac{5}{21}}$	$\frac{1}{\sqrt{3}}$
$F' = \frac{5}{2}$	$-\sqrt{\frac{2}{21}}$	$-\frac{4}{\sqrt{105}}$	$-\sqrt{\frac{6}{35}}$	$-\frac{4}{\sqrt{105}}$	$-\sqrt{\frac{2}{21}}$	0
$F' = \frac{3}{2}$	$\frac{\sqrt{2}}{3}$	$\sqrt{\frac{2}{15}}$	$\sqrt{\frac{1}{15}}$	$\frac{1}{3\sqrt{5}}$	0	0

Appendix C

Luttinger Liquid explicit derivations

Anomalous commutator

In order to compute the commutator $[\hat{\rho}_{qr}, \hat{\rho}^{\dagger}_{-q'r}]$, it is needed to take care of normal ordering to avoid infinities in the sum $\sum_k$ on occupied states:

$$\begin{aligned}
[\hat{\rho}_{qr}, \hat{\rho}^{\dagger}_{-q'r}] &= \sum_k \left(\hat{a}^{\dagger}_{k+q-q',r} \hat{a}_{k,r} - \hat{a}^{\dagger}_{k-q',r} \hat{a}_{k-q,r} \right) \\
&= \sum_k \left(: \hat{a}^{\dagger}_{k+q-q',r} \hat{a}_{k,r} : - : \hat{a}^{\dagger}_{k-p',r} \hat{a}_{k-q,r} : \right) \\
&\quad + \sum_k \left(\langle 0 | \hat{a}^{\dagger}_{k+q-q',r} \hat{a}_{k,r} | 0 \rangle - \langle 0 | \hat{a}^{\dagger}_{k-q',r} \hat{a}_{k-q,r} | 0 \rangle \right) \\
&= \sum_k \left(\langle 0 | \hat{a}^{\dagger}_{k+q-q',r} \hat{a}_{k,r} | 0 \rangle - \langle 0 | \hat{a}^{\dagger}_{k-q',r} \hat{a}_{k-q,r} | 0 \rangle \right) \\
&= \delta_{qq'} \sum_k \left(\langle 0 | \hat{a}^{\dagger}_{k,r} \hat{a}_{k,r} | 0 \rangle - \langle 0 | \hat{a}^{\dagger}_{k-q,r} \hat{a}_{k-q,r} | 0 \rangle \right), \qquad \text{(C.1)}
\end{aligned}$$

where $\sum_k \langle 0 | \hat{a}^{\dagger}_{k,r} \hat{a}_{k,r} | 0 \rangle = \sum_k n_{k,r}$ is the sum of occupied states of species r with $n_{k,r} = 1(0)$ if the state is occupied (empty). From the quantization of momentum $q = 2\pi n/L$, with

integer $n > 0\,(n < 0)$ for $r = R(L)$ the commutator can be recast as:

$$\begin{aligned}\left[\hat{\rho}^{\dagger}_{qr}, \hat{\rho}^{\dagger}_{-q'r}\right] &= \delta_{qq'} \sum_{k \leq k_F} (n_{k,r} - n_{k-q,r}) \\ &= \delta_{qq'} \left(\sum_{k \leq k_F} n_{k,r} - \sum_{k \leq k_F - q} n_{k,r} \right) \\ &= -\delta_{qq'} \sum_{k_F - q \leq k \leq k_F} n_{k,r} \\ &= -\delta_{qq'} \frac{qrL}{2\pi}, \end{aligned} \tag{C.2}$$

where $r = +1(-1)$ for right and left-movers respectively.

Back-scattering g_1 processes in the spinless case

The back-scattering processes in g-ology are characterized by the coupling constant g_1 and are described by the Hamiltonian (C.3):

$$\hat{H}^{(2)}_{int} = \frac{1}{2L} \sum_{||q| - 2k_F| < \Lambda} V(q) \sum_{k,k'} (\hat{a}^{\dagger}_{k+q,R} \hat{a}_{k,L} \hat{a}^{\dagger}_{k'-q,L} \hat{a}_{k',R} + L \leftrightarrow R). \tag{C.3}$$

However for spinless fermions, the process g_1 is identical to a process g_2 up to a minus sign. This can be understood intuitively by switching the final states in Fig. 3.5c: since the particles are indistinguishable, one obtains a g_2 process. This simplification is not possible if the spin degree of freedom is taken into account. In that case, the equivalence between g_1 and g_2 processes holds only for parallel spins but opposite spins give rise to a spin-flip term, which cannot be expressed in terms of density fluctuation operators (see section 3.2.4). More formally, by approximating $k \simeq k_F$, $k' \simeq -k_F$ and $q \simeq 2k_F + q'$ for the first term in the brackets and $k \simeq -k_F$, $k' \simeq k_F$ and $q \simeq -2k_F + q'$ for the second $L \leftrightarrow R$ term, the interaction term can be recast as:

$$\hat{a}^{\dagger}_{k_F+q',R} \hat{a}_{-k_F,L} \hat{a}^{\dagger}_{-k_F-q',L} \hat{a}_{-k_F,R} = -\hat{a}^{\dagger}_{k_F+q',R} \hat{a}_{k_F,R} \hat{a}^{\dagger}_{-k_F-q',L} \hat{a}_{-k_F,L}, \tag{C.4}$$

Hence (3.17) can be reformulated as:

$$\hat{H}^{(2)}_{int} \simeq -\frac{1}{2L} \sum_{|q'| < \Lambda} V(2k_F) \underbrace{(\hat{\rho}_{-q,R} \hat{\rho}_{q,L} + \hat{\rho}_{-q,L} \hat{\rho}_{q,R})}_{g_2}. \tag{C.5}$$

Appendix D

Bragg scattering

In this Appendix we will give a phenomenological illustration of the physics behind Bragg scattering at $T = 0$ following references [138] and [194]. The interaction Hamiltonian in a Bragg experiment is

$$\hat{H}_{Bragg} = \frac{V_0}{2} e^{-\eta t} \left(\hat{\rho}^{\dagger}_{\mathbf{q}} e^{-i\omega t} + \hat{\rho}_{\mathbf{q}} e^{i\omega t} \right) \tag{D.1}$$

where

$$\hat{\rho}_{\mathbf{q}} = \int d^3\mathbf{r} e^{-i\mathbf{q}\cdot\mathbf{r}} \hat{\rho}(\mathbf{r}) = \sum_i e^{-i\mathbf{q}\cdot\hat{\mathbf{r}}_i}$$

is the $\mathbf{q}$ Fourier component of the particle density operator $\hat{\rho}(\mathbf{r}) = \hat{\Psi}^{\dagger}(\mathbf{r})\hat{\Psi}(\mathbf{r})$ (see Eq. 3.6) and

$$V_0 = \frac{3\pi c^2 \Gamma}{\omega_0^3} \frac{I}{\Delta}$$

is the light shift potential defined in Eq. (1.25). The factor $e^{-\eta t}$ with $\eta = 0^+$, ensures that the system is governed by the unperturbed Hamiltonian at $t = -\infty$. The transition probability from the ground state $|0\rangle$ to an exact excited state $|n\rangle$ of the many-body system with energy E_n is then related to the matrix element:

$$\langle n|\hat{H}_{Bragg}|0\rangle = \frac{V_0}{2} \left(\langle n|\hat{\rho}^{\dagger}_{\mathbf{q}}|0\rangle e^{-i\omega t} + \langle n|\hat{\rho}_{\mathbf{q}}|0\rangle e^{i\omega t} \right) \tag{D.2}$$

Assuming $T = 0$, the system is initially in its ground state and therefore it cannot release energy to the probe ($\hat{\rho}_{\mathbf{q}}|0\rangle = 0$). In this special case, according to Fermi golden rule, the

excitation probability per unit time is:

$$\begin{aligned} P(\mathbf{q},\omega) &= \left(\frac{2\pi}{\hbar}\right)\sum_n |\langle n|\hat{H}_{Bragg}|0\rangle|^2\delta\left(\hbar\omega - E_n - E_0\right) \\ &= \left(\frac{2\pi}{\hbar}\right)\frac{|V_0|^2}{4}\sum_n |\langle n|\hat{\rho}^\dagger_{\mathbf{q}}|0\rangle|^2\delta\left(\hbar\omega - E_n - E_0\right) \\ &\propto |V_0|^2 S(\mathbf{q},\omega) \end{aligned} \tag{D.3}$$

where:

$$S(\mathbf{q},\omega) = \sum_n |\langle n|\hat{\rho}^\dagger_{\mathbf{q}}|0\rangle|^2\delta\left(\hbar\omega - E_n - E_0\right) \tag{D.4}$$

is the dynamical form factor defined in Eq. (4.12).

In the more general case of a spin-dependent potential, the interaction Hamiltonian in a Bragg experiment is

$$\hat{H}_{Bragg} = \sum_\sigma \frac{V_\sigma}{2} e^{-\eta t}\left(\hat{\rho}^\dagger_{\mathbf{q},\sigma}e^{-i\omega t} + \hat{\rho}_{\mathbf{q},\sigma}e^{i\omega t}\right) \tag{D.5}$$

where $\hat{\rho}_\sigma(\mathbf{r}) = \hat{\Psi}^\dagger_\sigma(\mathbf{r})\hat{\Psi}_\sigma(\mathbf{r})$ and V_σ is the light shift potential felt by a spin σ particle. Making the above assumptions, the relevant matrix element can be written as:

$$\langle n|\hat{H}_{Bragg}|0\rangle = \frac{V_\uparrow}{2}\langle n|\hat{\rho}^\dagger_{\mathbf{q},\uparrow}|0\rangle e^{-i\omega t} + \frac{V_\downarrow}{2}\langle n|\hat{\rho}^\dagger_{\mathbf{q},\downarrow}|0\rangle e^{-i\omega t} \tag{D.6}$$

Taking the modulus squared we get:

$$\begin{aligned} |\langle n|\hat{H}_{Bragg}|0\rangle|^2 &= \frac{|V_\uparrow|^2}{4}|\langle n|\hat{\rho}^\dagger_{\mathbf{q},\uparrow}|0\rangle|^2 + \frac{|V_\downarrow|^2}{4}|\langle n|\hat{\rho}^\dagger_{\mathbf{q},\downarrow}|0\rangle|^2 \\ &+ \frac{V_\uparrow V_\downarrow}{4}\left[\langle 0|\hat{\rho}_{\mathbf{q},\downarrow}|n\rangle\langle n|\hat{\rho}^\dagger_{\mathbf{q},\uparrow}|0\rangle + \langle 0|\hat{\rho}_{\mathbf{q},\uparrow}|n\rangle\langle n|\hat{\rho}^\dagger_{\mathbf{q},\downarrow}|0\rangle\right] \end{aligned} \tag{D.7}$$

Then, we can define:

$$S_{\sigma\sigma'}(\mathbf{q},\omega) = \sum_n \langle 0|\hat{\rho}_{\mathbf{q},\sigma}|n\rangle\langle n|\hat{\rho}^\dagger_{\mathbf{q},\sigma'}|0\rangle\delta\left(\hbar\omega - E_n - E_0\right) \tag{D.8}$$

which is the dynamical structure factor related to the response of the system to a spin dependent excitation. In the particular case of a two-component balanced spin mixture ($N_\uparrow = N_\downarrow$), we get [195] $S_{\uparrow\uparrow} = S_{\downarrow\downarrow}$ and $S_{\uparrow\downarrow} = S_{\downarrow\uparrow}$. Therefore, the probability per unit

time that the many-body system is excited is

$$\begin{aligned} P(\mathbf{q},\omega) &= \left(\frac{2\pi}{\hbar}\right)\sum_n |\langle n|\hat{H}_{Bragg}|0\rangle|^2\delta\left(\hbar\omega - E_n - E_0\right) \\ &\propto \left(|V_\uparrow|^2 + |V_\downarrow|^2\right) S_{\uparrow\uparrow}(\mathbf{q},\omega) + 2V_\uparrow V_\downarrow S_{\uparrow\downarrow}(\mathbf{q},\omega). \end{aligned} \tag{D.9}$$

It shall be noted that having $V_\uparrow = \pm V_\downarrow$ gives access to the charge (density) and spin dynamical structure factors, namely:

$$S_{c,s} = 2(S_{\uparrow\uparrow} \pm S_{\uparrow\downarrow}). \tag{D.10}$$

Bibliography

[1] M. H. Anderson, J. R. Ensher, M. R. Matthews, C. E. Wieman, and E. A. Cornell. *Observation of Bose-Einstein Condensation in a Dilute Atomic Vapor*. Science **269**, 198–201 (1995).

[2] K. B. Davis, M. O. Mewes, M. R. Andrews, N. J. van Druten, D. S. Durfee, D. M. Kurn, and W. Ketterle. *Bose-Einstein Condensation in a Gas of Sodium Atoms*. Phys. Rev. Lett. **75**, 3969–3973 (1995).

[3] B. DeMarco and D. S. Jin. *Onset of Fermi Degeneracy in a Trapped Atomic Gas*. Science **285**, 1703–1706 (1999).

[4] A. G. Truscott, K. E. Strecker, W. I. McAlexander, G. B. Partridge, and R. G. Hulet. *Observation of Fermi Pressure in a Gas of Trapped Atoms*. Science **291**, 2570–2572 (2001).

[5] I. Buluta and F. Nori. *Quantum Simulators*. Science **326**, 108–111 (2009).

[6] R. P. Feynman. *Simulating physics with computers*. International Journal of Theoretical Physics **21**, 467–488 (1982).

[7] M. Greiner, O. Mandel, T. Esslinger, T. Hänsch, and I. Bloch. *Quantum phase transition from a superfluid to a Mott insulator in a gas of ultracold atoms*. Nature **415**, 39–44 (2002).

[8] R. Grimm, M. Weidemuller, and Y. B. Ovchinnikov. *Optical Dipole Traps for Neutral Atoms*. Advances In Atomic, Molecular, and Optical Physics **42**, 95 – 170 (2000).

[9] C. Chin, P. Julienne, and E. Tiesinga. *Feshbach resonances in ultracold gases*. Rev. Mod. Phys. **82**, 1225–1286 (2010).

[10] D. Jaksch, C. Bruder, J. Cirac, C. Gardiner, and P. Zoller. *Cold Bosonic Atoms in Optical Lattices*. Phys. Rev. Lett. **81**, 3108–3111 (1998).

[11] I. Bloch, J. Dalibard, and W. Zwerger. *Many-body physics with ultracold gases*. Rev. Mod. Phys. **80**, 885–964 (2008).

[12] I. Bloch, J. Dalibard, and S. Nascimbène. *Quantum simulations with ultracold quantum gases*. Nature Physics **8**, 267–276 (2012).

[13] T. Fukuhara, Y. Takasu, M. Kumakura, and Y. Takahashi. *Degenerate Fermi Gases of Ytterbium*. Phys. Rev. Lett. **98**, 030401 (2007).

[14] A. V. Gorshkov, M. Hermele, V. Gurarie, C. Xu, P. S. Julienne, J. Ye, P. Zoller, E. Demler, M. D. Lukin, and a. M. Rey. *Two-orbital SU(N) magnetism with ultracold alkaline-earth atoms*. Nature Physics **6**, 289–295 (2010).

[15] M. Hermele, V. Gurarie, and A. Rey. *Mott Insulators of Ultracold Fermionic Alkaline Earth Atoms: Underconstrained Magnetism and Chiral Spin Liquid*. Phys. Rev. Lett. **103**, 135301 (2009).

[16] M. A. Cazalilla, A. F. Ho, and M. Ueda. *Ultracold gases of ytterbium: ferromagnetism and Mott states in an SU(6) Fermi system*. New Journal of Physics **11**, 103033 (2009).

[17] M. A. Cazalilla and A. M. Rey. *Ultracold Fermi gases with emergent SU(N) symmetry*. Reports on Progress in Physics **77**, 124401 (2014).

[18] F. F. Assaad. *Phase diagram of the half-filled two-dimensional* SU(N) *Hubbard-Heisenberg model: A quantum Monte Carlo study*. Phys. Rev. B **71**, 075103 (2005).

[19] D. Banerjee, M. Bögli, M. Dalmonte, E. Rico, P. Stebler, U.-J. Wiese, and P. Zoller. *Atomic Quantum Simulation of* $\mathbf{U}(N)$ *and* SU(N) *Non-Abelian Lattice Gauge Theories*. Phys. Rev. Lett. **110**, 125303 (2013).

[20] A. Rapp, G. Zaránd, C. Honerkamp, and W. Hofstetter. *Color Superfluidity and "Baryon" Formation in Ultracold Fermions*. Phys. Rev. Lett. **98**, 160405 (2007).

[21] E. Zohar, J. I. Cirac, and B. Reznik. *Cold-Atom Quantum Simulator for SU(2) Yang-Mills Lattice Gauge Theory*. Phys. Rev. Lett. **110**, 125304 (2013).

[22] L. Mazza, A. Bermudez, N. Goldman, M. Rizzi, M. A. Martin-Delgado, and M. Lewenstein. *An optical-lattice-based quantum simulator for relativistic field theories and topological insulators*. New Journal of Physics **14**, 015007 (2012).

[23] L. Tagliacozzo, A. Celi, P. Orland, M. W. Mitchell, and M. Lewenstein. *Simulation of non-Abelian gauge theories with optical lattices*. Nature Communications **4**, 2615 (2013).

[24] C. W. Hoyt, Z. W. Barber, C. W. Oates, T. M. Fortier, S. a. Diddams, and L. Hollberg. *Observation and absolute frequency measurements of the* $^1S_0$-$^3P_0$ *optical clock transition in neutral ytterbium.* Phys. Rev. Lett. **95**, 083003 (2005).

[25] N. Hinkley, J. A. Sherman, N. B. Phillips, M. Schioppo, N. D. Lemke, M. Pizzocaro, C. W. Oates, and A. D. Ludlow. *An Atomic Clock with* 10^{-18} *Instability.* Science **341**, 1215–1218 (2013).

[26] M. Boyd, T. Zelevinsky, A. Ludlow, S. Blatt, T. Zanon-Willette, S. Foreman, and J. Ye. *Nuclear spin effects in optical lattice clocks.* Phys. Rev. A **76**, 022510 (2007).

[27] B. J. Bloom, T. L. Nicholson, J. R. Williams, S. L. Campbell, M. Bishof, X. Zhang, W. Zhang, S. L. Bromley, and J. Ye. *An optical lattice clock with accuracy and stability at the* 10^{-18} *level.* Nature **506**, 71–75 (2014).

[28] A. Derevianko and H. Katori. *Colloquium: Physics of optical lattice clocks.* Rev. Mod. Phys. **83**, 331–347 (2011).

[29] F. Gerbier and J. Dalibard. *Gauge fields for ultracold atoms in optical superlattices.* New Journal of Physics **12**, 033007 (2010).

[30] J. Dalibard, F. Gerbier, G. Juzeliūnas, and P. Öhberg. *Colloquium: Artificial gauge potentials for neutral atoms.* Rev. Mod. Phys. **83**, 1523–1543 (2011).

[31] G. Pagano, M. Mancini, G. Cappellini, P. Lombardi, F. Schäfer, H. Hu, X.-J. Liu, J. Catani, C. Sias, M. Inguscio, and L. Fallani. *A one-dimensional liquid of fermions with tunable spin.* Nature Physics **10**, 198–201 (2014).

[32] C. N. Yang. *Some Exact Results for the Many-Body Problem in one Dimension with Repulsive Delta-Function Interaction.* Phys. Rev. Lett. **19**, 1312–1315 (1967).

[33] F. D. M. Haldane. *"Luttinger liquid theory" of one-dimensional quantum fluids. I. Properties of the Luttinger model and their extension to the general 1D interacting spinless Fermi gas.* Journal of Physics C: Solid State Physics **14**, 2585 (1981).

[34] C. N. Yang and Y.-Z. You. *One-Dimensional w -Component Fermions and Bosons with Repulsive Delta Function Interaction.* Chinese Physics Letters **28**, 020503 (2011).

[35] G. Cappellini, M. Mancini, G. Pagano, P. Lombardi, L. Livi, M. Siciliani de Cumis, P. Cancio, M. Pizzocaro, D. Calonico, F. Levi, C. Sias, J. Catani, M. Inguscio, and L. Fallani. *Direct Observation of Coherent Interorbital Spin-Exchange Dynamics.* Phys. Rev. Lett. **113**, 120402 (2014).

[36] G. Cappellini. PhD thesis, European Laboratory for Non-linear Spectroscopy (LENS) (in preparation).

[37] A. Thobe. *Ultracold Yb Gases with Control over Spin and Orbital Degrees of Freedom Spin and Orbital Degrees of Freedom*. PhD thesis, Universität Hamburg (2014).

[38] F. Scazza. *Probing SU(N)-symmetric orbital interactions with ytterbium Fermi gases in optical lattices*. PhD thesis, Ludwig-Maximilians-Universität München (2015).

[39] A. Dareau, M. Scholl, Q. Beaufils, D. Döring, J. Beugnon, and F. Gerbier. *Doppler spectroscopy of an ytterbium Bose-Einstein condensate on the clock transition*. Phys. Rev. A **91**, 023626 (2015).

[40] F. Scazza, C. Hofrichter, M. Höfer, P. C. De Groot, I. Bloch, and S. Fölling. *Observation of two-orbital spin-exchange interactions with ultracold SU(N)-symmetric fermions*. Nature Physics **10**, 779–784 (2014).

[41] V. Galitski and I. B. Spielman. *Spin-orbit coupling in quantum gases*. Nature **494**, 49–54 (2013).

[42] Y.-J. Lin, K. Jiménez-García, and I. B. Spielman. *Spin-orbit-coupled Bose-Einstein condensates*. Nature **471**, 83–86 (2011).

[43] Y.-J. Lin, R. L. Compton, K. Jiménez-García, J. V. Porto, and I. B. Spielman. *Synthetic magnetic fields for ultracold neutral atoms*. Nature **462**, 628–632 (2009).

[44] Y.-J. Lin, R. Compton, a. Perry, W. Phillips, J. Porto, and I. Spielman. *Bose-Einstein Condensate in a Uniform Light-Induced Vector Potential*. Phys. Rev. Lett. **102**, 130401 (2009).

[45] Y.-J. Lin, R. L. Compton, K. Jiménez-García, W. D. Phillips, J. V. Porto, and I. B. Spielman. *A synthetic electric force acting on neutral atoms*. Nature Physics **7**, 531–534 (2011).

[46] K. Jiménez-García, L. LeBlanc, R. Williams, M. Beeler, a. Perry, and I. Spielman. *Peierls Substitution in an Engineered Lattice Potential*. Phys. Rev. Lett. **108**, 225303 (2012).

[47] O. Boada, a. Celi, J. Latorre, and M. Lewenstein. *Quantum Simulation of an Extra Dimension*. Phys. Rev. Lett. **108**, 133001 (2012).

[48] A. Celi, P. Massignan, J. Ruseckas, N. Goldman, I. B. Spielman, G. Juzeliunas, and M. Lewenstein. *Synthetic Gauge Fields in Synthetic Dimensions*. Phys. Rev. Lett. **112**, 043001 (2014).

[49] M. Mancini. PhD thesis, Università degli studi di Firenze (in preparation).

[50] M. Mancini, G. Pagano, G. Cappellini, L. Livi, M. Rider, J. Catani, C. Sias, P. Zoller, M. Inguscio, M. Dalmonte, and L. Fallani. *Observation of chiral edge states with neutral fermions in synthetic Hall ribbons.* (2015).

[51] C. Cohen-Tannoudji. *Atomic motion in laser light.* Les Houches session LIII (1992).

[52] C. Cohen-Tannoudji and G. Grynberg. *Atom-photon interactions: basic processes and applications*, Volume 1. Wiley (1998).

[53] R. Loudon. *The Quantum Theory of Light.* Oxford University Press (2001). ISBN 978-0-19-850176-3.

[54] D. A. Steck. *Quantum and Atom Optics.* (2007).

[55] T. Loftus. *Laser Cooling and Trapping of atomic Ytterbium.* PhD thesis, University of Oregon (2001).

[56] N. W. Ashcroft and D. N. Mermin. *Solid State Physics.* Saunders College Publishing, Fort Worth, TX (1976).

[57] E. Duchon, Y. Loh, and N. Trivedi. *Optical lattice emulators: Bose and Fermi Hubbard models.* arXiv preprint arXiv:1311.0543 pages 1–75 (2013).

[58] M. Greiner, I. Bloch, O. Mandel, T. Hänsch, and T. Esslinger. *Exploring Phase Coherence in a 2D Lattice of Bose-Einstein Condensates.* Phys. Rev. Lett. **87**, 160405 (2001).

[59] M. Köhl, H. Moritz, T. Stöferle, K. Günter, and T. Esslinger. *Fermionic Atoms in a Three Dimensional Optical Lattice: Observing Fermi Surfaces, Dynamics, and Interactions.* Phys. Rev. Lett. **94**, 080403 (2005).

[60] H. Müller, S.-W. Chiow, and S. Chu. *Atom-wave diffraction between the Raman-Nath and the Bragg regime: Effective Rabi frequency, losses, and phase shifts.* Phys. Rev. A **77**, 023609 (2008).

[61] B. Deh, C. Marzok, S. Slama, C. Zimmermann, and P. W. Courteille. *Bragg spectroscopy and Ramsey interferometry with an ultracold Fermi gas.* Applied Physics B **97**, 387–396 (2009).

[62] J. Dalibard. *Collisional dynamics of ultra-cold atomic gases.* Proceedings of the International School of Physics "Enirco Fermi", Course CLXI pages 1–29 (1999).

[63] W. Ketterle and M. W. Zwierlein. *Making, probing and understanding ultracold Fermi gases*. In M. Inguscio, W. Ketterle, and C. Salomon, editors, *Proceedings of the International School of Physics "Enrico Fermi", Course CLXIV, Varenna, 20 - 30 June 2006*, number June 2006, pages 20–30. IOS Press, Amsterdam (2006).

[64] J. J. Sakurai. *Modern Quantum Mechanics*. Addison-Wesley Reading, Massachusetts (1995).

[65] K. Huang. *Statistical Mechanics*. John Wiley and sons, Inc., New York (1987).

[66] K. Huang and C. N. Yang. *Quantum-mechanical many-body problem with hard-sphere interaction*. Physical Review **105**, 767–775 (1957).

[67] M. Olshanii. *Atomic Scattering in the Presence of an External Confinement and a Gas of Impenetrable Bosons*. Phys. Rev. Lett. **81**, 938–941 (1998).

[68] E. Haller, M. Mark, R. Hart, and J. Danzl. *Confinement-induced resonances in low-dimensional quantum systems*. Phys. Rev. Lett. **104**, 153203 (2010).

[69] T. Bergeman, M. Moore, and M. Olshanii. *Atom-Atom Scattering under Cylindrical Harmonic Confinement: Numerical and Analytical Studies of the confinement induced resonance*. Phys. Rev. Lett. **91**, 163201 (2003).

[70] G. Astrakharchik, D. Blume, S. Giorgini, and L. Pitaevskii. *Interacting Fermions in Highly Elongated Harmonic Traps*. Phys. Rev. Lett. **93**, 050402 (2004).

[71] D. M. Stamper-Kurn and M. Ueda. *Spinor Bose gases: Symmetries, magnetism, and quantum dynamics*. Rev. Mod. Phys. **85**, 1191–1244 (2013).

[72] A. Widera, F. Gerbier, S. Fölling, T. Gericke, O. Mandel, and I. Bloch. *Coherent collisional spin dynamics in optical lattices*. Phys. Rev. Lett. **95**, 190405 (2005).

[73] A. Widera, F. Gerbier, S. Folling, T. Gericke, O. Mandel, and I. Bloch. *Precision measurement of spin-dependent interaction strengths for spin-1 and spin-2 ^{87}Rb atoms*. New Journal of Physics **8**, 152 (2006).

[74] J. S. Krauser, J. Heinze, N. Fläschner, S. Götze, O. Jürgensen, D.-S. Lühmann, C. Becker, and K. Sengstock. *Coherent multi-flavour spin dynamics in a fermionic quantum gas*. Nature Physics **8**, 813–818 (2012).

[75] M. Kitagawa, K. Enomoto, K. Kasa, Y. Takahashi, R. Ciuryo, P. Naidon, and P. Julienne. *Two-color photoassociation spectroscopy of ytterbium atoms and the precise determinations of s-wave scattering lengths*. Phys. Rev. A **77**, 012719 (2008).

[76] F. Gerbier, A. Widera, S. Fölling, O. Mandel, T. Gericke, and I. Bloch. *Interference pattern and visibility of a Mott insulator.* Phys. Rev. A **72**, 053606 (2005).

[77] F. Gerbier, A. Widera, S. Fölling, O. Mandel, T. Gericke, and I. Bloch. *Phase coherence of an atomic Mott insulator.* Phys. Rev. Lett. **95**, 050404 (2005).

[78] T. Gericke, F. Gerbier, A. Widera, S. Foelling, O. Mandel, and I. Bloch. *Adiabatic loading of a Bose-Einstein condensate in a 3D optical lattice.* Journal of Modern Optics **54**, 735–743 (2007).

[79] H. Metcalf and P. Van Der Straten. *Laser Cooling and Trapping.* Springer (1999).

[80] G. Pagano. *Raffreddamento e Intrappolamento di atomi di Itterbio.* Master's thesis, Università La Sapienza (2011).

[81] B. Zimmermann, T. Müller, J. Meineke, T. Esslinger, and H. Moritz. *High-resolution imaging of ultracold fermions in microscopically tailored optical potentials.* New Journal of Physics **13**, 043007 (2011).

[82] T. L. Gustavson, a. P. Chikkatur, a. E. Leanhardt, a. Görlitz, S. Gupta, D. E. Pritchard, and W. Ketterle. *Transport of Bose-Einstein condensates with optical tweezers.* Phys. Rev. Lett. **88**, 020601 (2002).

[83] S. Schmid, G. Thalhammer, K. Winkler, F. Lang, and J. H. Denschlag. *Long distance transport of ultracold atoms using a 1D optical lattice.* New Journal of Physics **8**, 159–159 (2006).

[84] A. Ashkin, G. Boyd, and J. Dziedzic. *Resonant optical second harmonic generation and mixing.* Quantum Electronics, IEEE Journal of **2**, 109–124 (1966).

[85] T. Hansch and B. Couillaud. *Laser frequency stabilization by polarization spectroscopy of a reflecting reference cavity.* Optics Communications **35**, 441–444 (1980).

[86] A. Yamaguchi. *Metastable State of Ultracold and Quantum Degenerate Ytterbium Atoms.* PhD thesis, Kyoto University (2008).

[87] B. Fröhlich, T. Lahaye, B. Kaltenhäuser, H. Kübler, S. Müller, T. Koch, M. Fattori, and T. Pfau. *Two-frequency acousto-optic modulator driver to improve the beam pointing stability during intensity ramps.* The Review of scientific instruments **78**, 043101 (2007).

[88] E. Black. *An introduction to Pound–Drever–Hall laser frequency stabilization.* American Journal of Physics **69**, 79 (2001).

[89] G. Insero. *Realizzazione di un Apparato Sperimentale per il rallentamento di un fascio atomico di Itterbio* (2010).

[90] W. Phillips and H. Metcalf. *Laser Deceleration of an Atomic Beam.* Phys. Rev. Lett. **48**, 596–599 (1982).

[91] T. E. Barrett, S. W. Dapore-Schwartz, M. D. Ray, and G. P. Lafyatis. *Slowing atoms with σ^- polarized light.* Phys. Rev. Lett. **67**, 3483–3486 (1991).

[92] C. Fort. *Intrappolamento e raffreddamento di atomi di cesio tramite luce laser: misure spettroscopiche.* PhD thesis, Università di Firenze (1995).

[93] T. Kuwamoto, K. Honda, Y. Takahashi, and T. Yabuzaki. *Magneto-optical trapping of Yb atoms using an intercombination transition.* Phys. Rev. A **60**, R745–R748 (1999).

[94] R. Maruyama. *Optical Trapping of Ytterbium Atoms.* PhD thesis, University of Washington (2003).

[95] K.-A. Suominen. *Theories for cold atomic collisions in light fields.* Journal of Physics B: Atomic, Molecular and Optical Physics **29**, 5981–6007 (1996).

[96] J. Weiner and P. S. Julienne. *Experiments and theory in cold and ultracold collisions.* Rev. Mod. Phys. **71**, 1–85 (1999).

[97] L. F. Livi. *Trasporto ottico di atomi freddi a lunga distanza* (2012).

[98] Y. Castin and R. Dum. *Bose-Einstein Condensates in Time Dependent Traps.* Phys. Rev. Lett. **77**, 5315–5319 (1996).

[99] Y. B. Ovchinnikov, J. H. Müller, M. R. Doery, E. J. D. Vredenbregt, K. Helmerson, S. L. Rolston, and W. D. Phillips. *Diffraction of a Released Bose-Einstein Condensate by a Pulsed Standing Light Wave.* Phys. Rev. Lett. **83**, 284–287 (1999).

[100] S. Gupta, A. E. Leanhardt, A. D. Cronin, and D. E. Pritchard. *Coherent manipulation of atoms with standing light waves.* Comptes Rendus de l'Academie des Sciences - Series {IV} - Physics **2**, 479 – 495 (2001).

[101] S. Taie, Y. Takasu, S. Sugawa, R. Yamazaki, T. Tsujimoto, R. Murakami, and Y. Takahashi. *Realization of a SU(2) × SU(6) System of Fermions in a Cold Atomic Gas.* Phys. Rev. Lett. **105**, 190401 (2010).

[102] S. Stellmer, R. Grimm, and F. Schreck. *Production of quantum-degenerate strontium gases.* Phys. Rev. A **87**, 013611 (2013).

[103] J. M. Luttinger. *An Exactly Soluble Model of a Many-Fermion System.* Journal of Mathematical Physics **4**, 1154 (1963).

[104] D. C. Mattis and E. H. Lieb. *Exact Solution of a Many-Fermion System and Its Associated Boson Field.* J. Math. Phys. **6**, 304–312 (1965).

[105] T. Giamarchi. *Quantum Physics in One Dimension.* (2004).

[106] G. Giuliani and G. Vignale. *Quantum theory of the electron liquid.* Cambridge University Press (2005).

[107] H. J. Schulz, G. Cuniberti, and P. Pieri. *Fermi liquids and Luttinger liquids.* In *Field theories for low-dimensional condensed matter systems*, pages 9–81. Springer (2000).

[108] A. Recati, P. Fedichev, W. Zwerger, and P. Zoller. *Spin-Charge Separation in Ultracold Quantum Gases.* Phys. Rev. Lett. **90**, 020401 (2003).

[109] A. Recati, P. O. Fedichev, W. Zwerger, and P. Zoller. *Fermi one-dimensional quantum gas: Luttinger liquid approach and spin-charge separation.* Journal of Optics B: Quantum and Semiclassical Optics **5**, S55 (2003).

[110] M. Ogata and H. Shiba. *Bethe-ansatz wave function, momentum distribution, and spin correlation in the one-dimensional strongly correlated Hubbard model.* Phys. Rev. B **41**, 2326–2338 (1990).

[111] V. Cheianov, H. Smith, and M. Zvonarev. *Low-temperature crossover in the momentum distribution of cold atomic gases in one dimension.* Phys. Rev. A **71**, 033610 (2005).

[112] M. D. Girardeau. *Permutation Symmetry of Many-Particle Wave Functions.* Phys. Rev. **139**, B500–B508 (1965).

[113] B. Paredes, A. Widera, V. Murg, O. Mandel, S. Folling, I. Cirac, G. V. Shlyapnikov, T. W. Hansch, and I. Bloch. *Tonks-Girardeau gas of ultracold atoms in an optical lattice.* Nature **429**, 277–281 (2004).

[114] T. Kinoshita, T. Wenger, and D. S. Weiss. *Observation of a one-dimensional Tonks-Girardeau gas.* Science **305**, 1125–8 (2004).

[115] H. Bethe. *Zur Theorie der Metalle.* Zeitschrift fuer Physik **71**, 205–226 (1931).

[116] X.-W. Guan, M. T. Batchelor, and C. Lee. *Fermi gases in one dimension: From Bethe ansatz to experiments.* Rev. Mod. Phys. **85**, 1633–1691 (2013).

[117] E. H. Lieb and W. Liniger. *Exact analysis of an interacting Bose gas. 1. The General solution and the ground state.* Phys.Rev. **130**, 1605–1616 (1963).

[118] V. Cheianov and M. Zvonarev. *Nonunitary Spin-Charge Separation in a One-Dimensional Fermion Gas.* Phys. Rev. Lett. **92**, 176401 (2004).

[119] G. a. Fiete and L. Balents. *Green's function for magnetically incoherent interacting electrons in one dimension.* Phys. Rev. Lett. **93**, 226401 (2004).

[120] G. a. Fiete. *Colloquium: The spin-incoherent Luttinger liquid.* Rev. Mod. Phys. **79**, 801–820 (2007).

[121] G. Zürn, F. Serwane, T. Lompe, a. N. Wenz, M. G. Ries, J. E. Bohn, and S. Jochim. *Fermionization of Two Distinguishable Fermions.* Phys. Rev. Lett. **108**, 075303 (2012).

[122] B. Sutherland. *Further results for the many-body problem in one dimension.* Phys. Rev. Lett. **20**, 98–100 (1968).

[123] E. Orignac and R. Citro. *Response functions in multicomponent Luttinger liquids.* Journal of Statistical Mechanics: Theory and Experiment **2012**, P12020 (2012).

[124] X.-W. Guan, Z.-Q. Ma, and B. Wilson. *One-dimensional multicomponent fermions with δ-function interaction in strong- and weak-coupling limits: κ-component Fermi gas.* Phys. Rev. A **85**, 033633 (2012).

[125] X. W. Guan, J. Y. Lee, M. T. Batchelor, X. G. Yin, and S. Chen. *Universal Tomonaga-Luttinger liquid phases in one-dimensional strongly attractive SU(N) fermionic cold atoms.* Phys. Rev. A **82**, 021606 (2010).

[126] E. Szirmai. *Two-orbital physics of high-spin fermionic alkaline-earth atoms confined in a one-dimensional chain.* Phys. Rev. B **88**, 195432 (2013).

[127] X.-J. Liu and H. Hu. *Collective mode evidence of high-spin bosonization in a trapped one-dimensional atomic Fermi gas with tunable spin.* Annals of Physics **350**, 84–94 (2014).

[128] T. Kinoshita, T. Wenger, and D. S. Weiss. *A quantum Newton's cradle.* Nature **440**, 900–3 (2006).

[129] E. Haller, R. Hart, M. J. Mark, J. G. Danzl, L. Reichsöllner, M. Gustavsson, M. Dalmonte, G. Pupillo, and H.-C. Nägerl. *Pinning quantum phase transition for a Luttinger liquid of strongly interacting bosons.* Nature **466**, 597–600 (2010).

[130] H. Moritz, T. Stöferle, K. Günter, M. Köhl, and T. Esslinger. *Confinement induced molecules in a 1D fermi gas.* Phys. Rev. Lett. **94**, 210401 (2005).

[131] Y.-A. Liao, A. S. C. Rittner, T. Paprotta, W. Li, G. B. Partridge, R. G. Hulet, S. K. Baur, and E. J. Mueller. *Spin-imbalance in a one-dimensional Fermi gas.* Nature **467**, 567–9 (2010).

[132] S. Tan. *Large momentum part of a strongly correlated Fermi gas.* Annals of Physics **323**, 2971 – 2986 (2008).

[133] S. Tan. *Energetics of a strongly correlated Fermi gas.* Annals of Physics **323**, 2952 – 2970 (2008).

[134] M. Barth and W. Zwerger. *Tan relations in one dimension.* Annals of Physics **326**, 2544 – 2565 (2011).

[135] J. Stenger, S. Inouye, A. P. Chikkatur, D. M. Stamper-Kurn, D. E. Pritchard, and W. Ketterle. *Bragg Spectroscopy of a Bose-Einstein Condensate.* Phys. Rev. Lett. **82**, 4569–4573 (1999).

[136] M. Kozuma, L. Deng, E. Hagley, J. Wen, R. Lutwak, K. Helmerson, S. Rolston, and W. Phillips. *Coherent Splitting of Bose-Einstein Condensed Atoms with Optically Induced Bragg Diffraction.* Phys. Rev. Lett. **82**, 871–875 (1999).

[137] N. Fabbri, M. Panfil, D. Clément, L. Fallani, M. Inguscio, C. Fort, and J.-S. Caux. *Dynamical structure factor of one-dimensional Bose gases: Experimental signatures of beyond-Luttinger-liquid physics.* Phys. Rev. A **91**, 043617 (2015).

[138] P. Nozières and D. Pines. *The theory of quantum liquids.* Westview Press (1994) (1999).

[139] P. Vignolo, A. Minguzzi, and M. Tosi. *Light scattering from a degenerate quasi-one-dimensional confined gas of noninteracting fermions.* Phys. Rev. A **64**, 023421 (2001).

[140] C. Menotti and S. Stringari. *Collective oscillations of a one-dimensional trapped Bose-Einstein gas.* Phys. Rev. A **66**, 043610 (2002).

[141] X.-J. Liu, P. Drummond, and H. Hu. *Signature of Mott-Insulator Transition with Ultracold Fermions in a One-Dimensional Optical Lattice.* Phys. Rev. Lett. **94**, 136406 (2005).

[142] E. Lipparini and S. Stringari. *Sum rules and giant resonances in nuclei.* Physics Reports **175**, 103 – 261 (1989).

[143] S. Stringari. *Collective Excitations of a Trapped Bose-Condensed Gas.* Phys. Rev. Lett. **77**, 2360–2363 (1996).

[144] I. Carusotto. *Bragg scattering and the spin structure factor of two-component atomic gases.* Journal of Physics B: Atomic, Molecular and Optical Physics **39**, S211 (2006).

[145] S. Hoinka, M. Lingham, M. Delehaye, and C. J. Vale. *Dynamic Spin Response of a Strongly Interacting Fermi Gas.* Phys. Rev. Lett **109**, 050403 (2012).

[146] Z. Barber, J. Stalnaker, N. Lemke, N. Poli, C. Oates, T. Fortier, S. Diddams, L. Hollberg, C. Hoyt, a. Taichenachev, and V. Yudin. *Optical Lattice Induced Light Shifts in an Yb Atomic Clock.* Phys. Rev. Lett. **100**, 103002 (2008).

[147] S. Porsev, A. Derevianko, and E. Fortson. *Possibility of an optical clock using the* $6^1S_0 \rightarrow 6^3P_0$ *transition in* $^{171,173}Yb$ *atoms held in an optical lattice.* Phys. Rev. A **69**, 021403 (2004).

[148] G. Cappellini, P. Lombardi, M. Mancini, G. Pagano, M. Pizzocaro, L. Fallani, and J. Catani. *A compact ultranarrow high-power laser system for experiments with 578 nm ytterbium clock transition.* Review of Scientific Instruments **86**, 073111 (2015).

[149] V. A. Dzuba and A. Derevianko. *Dynamic polarizabilities and related properties of clock states of ytterbium atom.* J. Phys. B: At. Mol. Opt. Phys **43**, 11 (2009).

[150] R. H. Dicke. *Coherence in Spontaneous Radiation Processes.* Phys. Rev. **93**, 99–110 (1954).

[151] T. Sleator, T. Pfau, V. Balykin, O. Carnal, and J. Mlynek. *Experimental demonstration of the optical Stern-Gerlach effect.* Phys. Rev. Lett. **68**, 1996–1999 (1992).

[152] T. Busch, B. G. Englert, K. Rzazewski, and M. Wilkens. *Two cold atoms in a harmonic trap.* Foundations of Physics **28**, 549–559 (1998).

[153] M. Köhl, K. Günter, T. Stöferle, H. Moritz, and T. Esslinger. *Strongly Interacting Atoms and Molecules in a 3D Optical Lattice.* J. Phys. B: At. Mol. Opt. Phys. **39**, S47–S56 (2006).

[154] F. Deuretzbacher, K. Plassmeier, D. Pfannkuche, F. Werner, C. Ospelkaus, S. Ospelkaus, K. Sengstock, and K. Bongs. *Heteronuclear molecules in an optical lattice: Theory and experiment.* Phys. Rev. A **77**, 032726 (2008).

[155] J. Mentink and S. Kokkelmans. *Two interacting atoms in an optical lattice site with anharmonic terms.* Phys. Rev. A **79**, 1–9 (2009).

[156] E. L. Bolda, E. Tiesinga, and P. S. Julienne. *Effective-scattering-length model of ultracold atomic collisions and Feshbach resonances in tight harmonic traps.* Phys. Rev. A **66**, 013403 (2002).

[157] J. S. Krauser, U. Ebling, N. Fläschner, J. Heinze, K. Sengstock, M. Lewenstein, a. Eckardt, and C. Becker. *Giant spin oscillations in an ultracold Fermi sea.* Science **343**, 157–60 (2014).

[158] S. Trotzky, P. Cheinet, S. Fölling, M. Feld, U. Schnorrberger, a. M. Rey, a. Polkovnikov, E. a. Demler, M. D. Lukin, and I. Bloch. *Time-resolved observation and control of superexchange interactions with ultracold atoms in optical lattices.* Science **319**, 295–299 (2008).

[159] P. Coleman. *Heavy Fermions: Electrons at the Edge of Magnetism.* In H. Kronmuller and S. Parkin, editors, *Handbook of magnetism and advanced magnetic materials*, page 30. Wiley, 2007 edition (2007).

[160] M. Foss-Feig, M. Hermele, and A. M. Rey. *Probing the Kondo lattice model with alkaline-earth-metal atoms.* Phys. Rev. A **81**, 051603 (2010).

[161] M. Anderlini, P. J. Lee, B. L. Brown, J. Sebby-Strabley, W. D. Phillips, and J. V. Porto. *Controlled exchange interaction between pairs of neutral atoms in an optical lattice.* Nature **448**, 452–6 (2007).

[162] L. W. Cheuk, A. T. Sommer, Z. Hadzibabic, T. Yefsah, W. S. Bakr, and M. W. Zwierlein. *Spin-Injection Spectroscopy of a Spin-Orbit Coupled Fermi Gas.* Phys. Rev. Lett. **109**, 095302 (2012).

[163] P. Wang, Z. Q. Yu, Z. Fu, J. Miao, L. Huang, S. Chai, H. Zhai, and J. Zhang. *Spin-orbit coupled degenerate Fermi gases.* Phys. Rev. Lett. **109**, 095301 (2012).

[164] M. Aidelsburger, M. Atala, S. Nascimbène, S. Trotzky, Y.-a. Chen, and I. Bloch. *Experimental Realization of Strong Effective Magnetic Fields in an Optical Lattice.* Phys. Rev. Lett. **107**, 255301 (2011).

[165] M. Aidelsburger, M. Atala, M. Lohse, J. T. Barreiro, B. Paredes, and I. Bloch. *Realization of the Hofstadter hamiltonian with ultracold atoms in optical lattices.* Phys. Rev. Lett. **111**, 185301 (2013).

[166] H. Miyake, G. A. Siviloglou, C. J. Kennedy, W. C. Burton, and W. Ketterle. *Realizing the Harper Hamiltonian with Laser-Assisted Tunneling in Optical Lattices.* Phys. Rev. Lett. **111**, 185302 (2013).

[167] M. Aidelsburger, M. Lohse, C. Schweizer, M. Atala, J. T. Barreiro, S. Nascimbene, N. R. Cooper, I. Bloch, and N. Goldman. *Measuring the Chern number of Hofstadter bands with ultracold bosonic atoms*. Nature Physics **11**, 162–166 (2015).

[168] R. Wei and E. J. Mueller. *Magnetic-field dependence of Raman coupling in alkali-metal atoms*. Phys. Rev. A **87**, 042514 (2013).

[169] J. H. Eberly, B. W. Shore, Z. Białynicka-Birula, and I. Białynicki-Birula. *Coherent dynamics of N-level atoms and molecules. I. Numerical experiments*. Phys. Rev. A **16**, 2038–2047 (1977).

[170] Z. Białynicka-Birula, I. Białynicki-Birula, J. H. Eberly, and B. W. Shore. *Coherent dynamics of N-level atoms and molecules. II. Analytic solutions*. Phys. Rev. A **16**, 2048–2054 (1977).

[171] R. J. Cook and B. W. Shore. *Coherent dynamics of N-level atoms and molecules. III. An analytically soluble periodic case*. Phys. Rev. A **20**, 539–544 (1979).

[172] B. W. Shore and R. J. Cook. *Coherent dynamics of N-level atoms and molecules. IV. Two- and three-level behavior*. Phys. Rev. A **20**, 1958–1964 (1979).

[173] B. W. Shore, J. Martin, M. P. Fewell, and K. Bergmann. *Coherent population transfer in multilevel systems with magnetic sublevels. I. Numerical studies*. Phys. Rev. A **52**, 566–582 (1995).

[174] J. Martin, B. W. Shore, and K. Bergmann. *Coherent population transfer in multilevel systems with magnetic sublevels. II. Algebraic analysis*. Phys. Rev. A **52**, 583–593 (1995).

[175] J. Martin, B. W. Shore, and K. Bergmann. *Coherent population transfer in multilevel systems with magnetic sublevels. III. Experimental results*. Phys. Rev. A **54**, 1556–1569 (1996).

[176] B. K. Stuhl, H.-I. Lu, L. M. Aycock, D. Genkina, and I. B. Spielman. *Visualizing edge states with an atomic Bose gas in the quantum Hall regime*. ArXiv e-prints (2015).

[177] G. Jotzu, M. Messer, R. Desbuquois, M. Lebrat, T. Uehlinger, D. Greif, and T. Esslinger. *Experimental realisation of the topological Haldane model*. Nature **515**, 14 (2014).

[178] O. Boada, A. Celi, J. Rodriguez-Laguna, J. Latorre, and M. Lewenstein. *Quantum simulation of non-trivial topology*. New Journal of Physics **17**, 045007 (2015).

[179] S. Barbarino, L. Taddia, D. Rossini, L. Mazza, and R. Fazio. *Magnetic crystals and helical liquids in alkaline-earth fermionic gases.* ArXiv e-prints (2015).

[180] A. J. Daley. *Quantum Computing and Quantum Simulation with Group-II atoms.* Quantum Information Processing (2011).

[181] A. Daley. *Quantum computing and quantum simulation with group-II atoms.* Quantum Information Processing pages 865–884 (2011).

[182] A. Daley, M. Boyd, J. Ye, and P. Zoller. *Quantum Computing with Alkaline-Earth-Metal Atoms.* Phys. Rev. Lett. **101**, 170504 (2008).

[183] W. S. Bakr, a. Peng, M. E. Tai, R. Ma, J. Simon, J. I. Gillen, S. Fölling, L. Pollet, and M. Greiner. *Probing the Superfluid-to-Mott-Insulator Transition at the Single-Atom Level.* Science **329**, 547–550 (2010).

[184] J. F. Sherson, C. Weitenberg, M. Endres, M. Cheneau, I. Bloch, and S. Kuhr. *Single-atom-resolved fluorescence imaging of an atomic Mott insulator.* Nature **467**, 68–72 (2010).

[185] C. Weitenberg, M. Endres, J. F. Sherson, M. Cheneau, P. Schauss, T. Fukuhara, I. Bloch, and S. Kuhr. *Single-spin addressing in an atomic Mott insulator.* Nature **471**, 319–24 (2011).

[186] M. Miranda, R. Inoue, Y. Okuyama, A. Nakamoto, and M. Kozuma. *Site-resolved imaging of ytterbium atoms in a two-dimensional optical lattice.* Phys. Rev. A **91**, 063414 (2015).

[187] E. Haller, J. Hudson, A. Kelly, D. A. Cotta, B. Peaudecerf, G. D. Bruce, and S. Kuhr. *Single-atom imaging of fermions in a quantum-gas microscope.* Nature Physics **advance online publication** (2015).

[188] L. W. Cheuk, M. A. Nichols, M. Okan, T. Gersdorf, V. V. Ramasesh, W. S. Bakr, T. Lompe, and M. W. Zwierlein. *Quantum-Gas Microscope for Fermionic Atoms.* Phys. Rev. Lett. **114**, 193001 (2015).

[189] M. F. Parsons, F. Huber, A. Mazurenko, C. S. Chiu, W. Setiawan, K. Wooley-Brown, S. Blatt, and M. Greiner. *Site-Resolved Imaging of Fermionic* ^{6}Li *in an Optical Lattice.* Phys. Rev. Lett. **114**, 213002 (2015).

[190] Y. Ralchenko. *NIST atomic spectra database.* Mem. S.A.It. Suppl. **8**, 96–102 (2005).

[191] K. Blagoev and V. Komarovskii. *Lifetimes of Levels of Neutral and Singly Ionized Lanthanide Atoms.* Atomic Data and Nuclear Data Tables **56**, 1 – 40 (1994).

[192] C. Bowers, D. Budker, E. Commins, D. DeMille, S. Freedman, a. T. Nguyen, S.-Q. Shang, and M. Zolotorev. *Experimental investigation of excited-state lifetimes in atomic ytterbium*. Phys. Rev. A **53**, 3103–3109 (1996).

[193] M. Baumann, M. Braun, A. Gaiser, and H. Liening. *Radiative lifetimes and g_J factors of low-lying even-parity levels in the Yb I spectrum*. Journal of Physics B: Atomic and Molecular Physics **18**, L601–L604 (1999).

[194] A. Brunello, F. Dalfovo, L. Pitaevskii, S. Stringari, and F. Zambelli. *Momentum transferred to a trapped Bose-Einstein condensate by stimulated light scattering*. Phys. Rev. A **64**, 063614 (2001).

[195] R. Combescot, S. Giorgini, and S. Stringari. *Molecular signatures in the structure factor of an interacting Fermi gas*. Europhysics Letters (EPL) **75**, 695–701 (2006).